The properties of galaxies and active galactic nuclei using panchromatic fitting

Author:
Soumyadeep DAS

Supervised by:
Prof. D.J.B. SMITH
Prof. M.J. HARDCASTLE

Centre for Astrophysics Research
School of Physics, Astronomy and Mathematics
University of Hertfordshire

Submitted to the University of Hertfordshire in partial fulfilment of the requirements of the degree of Doctor of Philosophy.

August 2025

Abstract

This thesis investigates the evolving nature of galaxy populations from the early Universe to the present day using broadband spectral energy distribution (SED) fitting of both real and simulated datasets, incorporating photometry and spectroscopy. Our analysis is performed with the new-generation energy-balance Bayesian forward-modelling SED fitting code PROSPECTOR, which treats photometry and spectroscopy on an equal footing and includes the capability to model AGN contributions to galaxy SEDs, both of which are critical to this work.

First, we investigate the nature of the faint radio source population. Recent efforts have combined fits from multiple SED-fitting codes to account for the host galaxy and any active nucleus that may be present. We show that it is possible to produce similar-quality classifications using a single energy-balance SED fitting code, PROSPECTOR, to model up to 26 bands of UV–far-infrared aperture-matched photometry for ∼31,000 sources in the ELAIS-N1 field from the LOFAR Two-Metre Sky Survey (LoTSS) Deep fields first data release. One of a new generation of SED-fitting codes, PROSPECTOR accounts for potential contributions from radiative active galactic nuclei (AGN) when estimating galaxy properties, including star formation rates (SFRs) derived using non-parametric star formation histories. Combining this information with radio luminosities, we classify 92 per cent of the radio sources as a star-forming galaxy, high-/low-excitation radio galaxy, or radio-quiet AGN and study the population demographics as a function of 150 MHz flux density, luminosity, SFR, stellar mass, redshift and apparent r-band magnitude. Finally, we use PROSPECTOR SED fits to investigate the SFR–150 MHz luminosity relation for a sample of ∼133,000 3.6 μm-selected $z < 1$ sources, finding that the stellar mass dependence is significantly weaker than previously reported, and may disappear altogether at $\log_{10}(\mathrm{SFR}/M_{\odot}\,\mathrm{yr}^{-1}) > 0.5$.

Second, we develop a fully Bayesian spectrophotometric classification framework that combines LoTSS DR1 photometry with DESI EDR spectroscopy for 6,038 radio sources. Leveraging the full posterior distributions from PROSPECTOR, we derive probabilistic classifications based on mid-IR excess, emission-line diagnostics, and radio-excess criteria, enabling both maximum-likelihood and confidence-threshold classifications. Comparing our 90 per cent reliability classifications (P_{90}) with the photometric maximum-likelihood classifications and the spectroscopic

probabilistic classifications from previous studies demonstrates the advantages of a joint photometric–spectroscopic approach. In particular, the inclusion of emission-line and mid-IR information reveals populations of radiative-mode AGN that are missed by photometric or spectroscopic methods alone. While this thesis presents initial results from this framework, forthcoming spectroscopic datasets from surveys such as WEAVE-LOFAR and ORCHIDSS will allow for a substantial expansion of this approach, enabling a more comprehensive understanding of the faint radio source population.

Finally, we explore the recovery of burstiness, η, defined as the log of the ratio of the short-term star formation rate (averaged over the last 10 Myr) to the intermediate-scale star formation rate (averaged over the last $\sim$100 Myrs) using UV-to-mid IR photometry from an idealised data set based on *Hubble* plus *James Webb Space Telescope* NIRCam and MIRI imaging. We generate synthetic photometry for 1,380 galaxies spanning $4.64 \leq z \leq 10$ from the SPHINX^{20} cosmological radiation-hydrodynamic simulations and use PROSPECTOR to infer physical galaxy properties, including η, under two non-parametric star formation history (SFH) priors: a continuity prior and a bursty-continuity prior. While the former prefers constant SFHs, the latter is more flexible, and is capable of modelling short-term variability in SFHs. We find that the choice of SFH prior exerts a strong and often undue influence on the inferred parameters, with individual η estimates remaining unreliable irrespective of the prior used. While there is some success in recovering the average η for samples of galaxies, our results reveal strong redshift-dependent biases and systematic effects arising from photometric band selection and wavelength coverage. These limitations highlight the difficulty of identifying galaxies undergoing bursts of star formation or temporary quenching events using photometry alone, underscoring the need for spectroscopic information to break degeneracies and improve the fidelity of burstiness recovery.

Together, the results presented in this thesis demonstrate the power and flexibility of modern Bayesian SED fitting frameworks for studying galaxy populations across cosmic time. By unifying photometric and spectroscopic information, developing probabilistic classification methods, and stress-testing the recovery of recent star formation activity, this work lays the foundation for exploiting forthcoming spectroscopic datasets to obtain a more complete and physically motivated understanding of galaxy evolution, the nature of the faint radio source population, and the role of AGN across the history of the Universe.

Declaration

I declare that no part of this work is being submitted concurrently for another award of the University or any other awarding body or institution. This thesis contains a substantial body of work that has not previously been submitted successfully for an award of the University or any other awarding body or institution.

The following parts of this submission have been published previously and/or undertaken as part of a previous degree or research programme:

1. Chapter 2: this has been published as Das et al., 2024, *Monthly Notices of the Royal Astronomical Society*, **531**, 977.

Except where indicated otherwise in the submission, the submission is my own work and has not previously been submitted successfully for any award.

Acknowledgements

This thesis has truly been a team effort, and it would not have been possible without the unwavering support of so many wonderful people throughout my PhD, especially during the demanding process of writing this thesis. I begin by expressing my deepest gratitude to my parents. I am where I am today because of them and have no words to describe how fortunate I have been to receive such unconditional love and support. My supervisor, Prof. Daniel J. B. Smith, has been an outstanding mentor throughout, encouraging me to take initiative in my projects, pursue my ideas, and develop as an independent researcher. He has fostered a spirit of collaboration within the group that led to multiple co-authored papers and, through his dad-jokes and cheerful demeanor, has created an environment where, despite inevitable setbacks, research has remained both engaging and enjoyable. Dan's ideas have been to this thesis what walkers are to MCMC – exploring the parameter space of science cases and steadily moving towards the thesis goals while ensuring that even seemingly minor objectives were not overlooked. The process of making Dan reasonably happy has been both challenging and fun in equal measure. I am particularly grateful for his support during some of the most difficult periods of my life that coincided with this PhD; it is largely due to his guidance that I retained my passion for this work and was ultimately able to bring it to completion. I am thankful to my second supervisor, Prof. Martin Hardcastle, for his invaluable guidance and constant support. His suggestions have consistently offered much-needed perspective. Together, Dan and Martin have provided an exemplary supervisory team. I am also grateful to Prof. Preeti Kharb (NCRA) for her encouragement and mentorship, which began even before the start of this PhD, and for being one of the strongest voices urging me to keep going despite the hardships in life.

I am thankful to everyone at the University of Hertfordshire for creating a friendly, warm, and caring work environment. I owe much to my "siblings-in-science" – the so-called Danlings: Marina Arnaudova, Shravya Shenoy, Alyssa Drake, Paul Haskell, and Luke Holden. Your company made the day-to-day frustrations of research not only bearable but often enjoyable. I am grateful for the countless discussions in which no idea was too big or too small and, as our co-authored publications show, were always a good use of our time. I would also like to thank James McGarry, Kasia Novak, Tracy Garratt, and Matthew Doherty for making the University livelier with their kindness, passionate discussions, and memes. To Vito Graffagnino: my sincere thanks and regards, good sir, for being a true gentleman and ensuring that all the computing needs of this thesis were always met.

On a more personal note, I feel incredibly lucky to have a partner as supportive as Mahima. Your steady presence and relentless positivity have kept me going through the final, most demanding stretch of this thesis. During my most fragile times, your presence gave me strength and made sure I never felt alone. I cannot put into words how much your presence has meant to me. Thank you. I am grateful to my extended family for their unwavering support. It would be remiss to

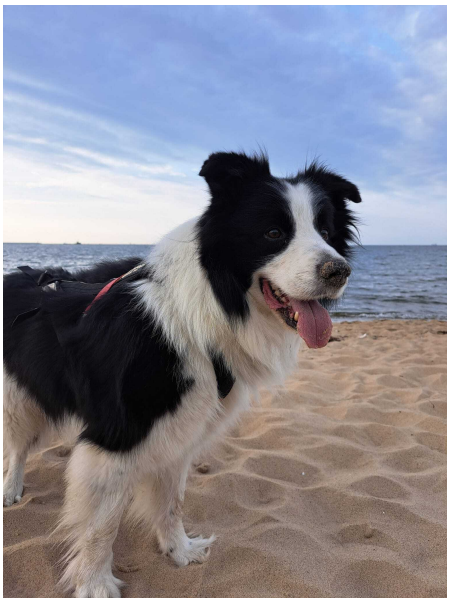

FIGURE 1: Riky.

not mention my grandparents – Tulsi Narayan Das, Jharna Das, Chandra Madhab Das, Gita Rani Das; the guardian *Dases* – Swapan, Susmita, Ratan, Sujita, Dibyendu, Moumita; and the younglings – Shreya, Sunetra, and Ditsa. I am thankful to my friends Pranav Roy, Madhuri Ganji, Vishal Shrivastava, Thashmika Bandara, Jay Pandya, Jaya Acharya, and Michael Shima, who brought much-needed balance to this intense period of life. It has been a pleasure organising trips with you, and I look forward to many more in the future. To my boys in India – Anant Raj, Tarush Tiwari, Abhishek Kavrani, and Pranjal – you have been my lifeline. Even so far from home, I never felt alone, and I feel truly blessed to have held on to such friendships across time and distance. And to Yash Jain, thanks for making Europe feel like a second home. I am grateful to Laura Matouskova (and more importantly, Riky; see Fig. 1), for being a constant source of joy through their antics, and to my friends in the BeetRootBandits DotA guild, for ensuring it was never all work and no games.

Finally, to my father: one of my earliest memories of you is seeing the comet from your lap. You are the reason I took up astronomy. You left us too soon. I have never been particularly religious or spiritual, but now I want to believe that when people pass, they live among the stars, so that every time I look at the night sky, I can see you. And to my mother: you are the bravest and kindest person I know. Someday I hope to become even half the son you believe me to be. Once the defense is done and the corrections are made, I hope never to open this thesis again. May this be the shallow grave where all the pain of the past six months is finally laid to rest.

Contents

Abstract i

Acknowledgements iv

Contents vi

List of Figures ix

List of Tables xvii

List of Abbreviations xviii

1 Introduction 1

1.1 The early Universe . . . 2
1.1.1 The Big Bang and the epoch of inflation . . . 2
1.1.2 The cosmic dark ages and the formation of the first stars . . . 3
1.1.3 The epoch of reionisation . . . 5
1.2 Galaxies in the early Universe . . . 6
1.2.1 Evolution of star formation histories and galaxy morphologies . . . 6
1.2.2 Formation of the first black holes . . . 11
1.2.3 Further growth via dynamical evolution and interactions . . . 12
1.3 Feedback processes in galaxies . . . 12
1.3.1 Stellar feedback . . . 13
1.3.2 AGN feedback . . . 14
1.3.2.1 Radiatively-efficient AGN feedback . . . 16
1.3.2.2 Radiatively-inefficient mode of AGN feedback . . . 17
1.4 Probing the deep fields in the sky with radio surveys . . . 17
1.4.1 Overview of the radio continuum emission in galaxies . . . 17
1.4.2 Radio sky surveys . . . 18
1.4.3 The faint radio source population . . . 21
1.4.3.1 Classification of the faint radio source population . . . 22
1.4.4 Massively multiplexed spectroscopic surveys . . . 23
1.5 SED modelling . . . 26
1.5.1 Stellar population synthesis . . . 26
1.5.1.1 Simple Stellar Populations . . . 27
1.5.1.2 Composite Stellar Population . . . 28
1.5.1.3 Star formation history . . . 29

1.5.2 Dust . . . 30
1.5.2.1 Dust attenuation . . . 30
1.5.2.2 Dust emission . . . 31
1.5.3 AGN torus . . . 32
1.5.4 Nebular emission . . . 34
1.5.5 The fitting process . . . 35
1.5.6 Contemporary SED fitting programs . . . 37
1.6 Structure of this thesis . . . 38

2 The LOFAR Two-metre Sky Survey: The nature of the faint source population and SFR-radio luminosity relation using Prospector 41
2.1 Introduction . . . 41
2.2 Data . . . 45
2.2.1 Multi-wavelength data . . . 45
2.2.2 Radio Observations . . . 46
2.2.3 Datasets for SED fitting . . . 46
2.3 SED fitting . . . 48
2.3.1 Comparison of physical parameters . . . 52
2.4 Radio source classification . . . 56
2.4.1 Identification of radiative-mode AGN . . . 57
2.4.2 Identification of radio-excess sources . . . 60
2.4.3 Final classifications . . . 65
2.5 Stellar mass dependence in the SFR–150 MHz radio luminosity relation . . . 72
2.5.1 Determining stellar mass dependence using Prospector SED fits . . . 72
2.5.2 The influence of passive galaxies . . . 74
2.6 Conclusions . . . 76

3 LoTSS Deep Fields: A novel Bayesian approach for classifying radio sources fitting photometry and spectroscopy using Prospector 78
3.1 Data . . . 81
3.1.1 Radio observations . . . 81
3.1.2 Multiwavelength photometry . . . 81
3.1.3 Spectroscopic data . . . 82
3.1.4 Sample selection . . . 83
3.2 SED modelling . . . 84
3.2.1 Model construction . . . 84
3.2.2 Estimating parameters from the posterior distribution . . . 87
3.3 Probabilistic source classification . . . 91
3.3.1 Identification of radiative-mode AGN based on mid-IR excess . . . 93
3.3.2 Identification of radiative-mode AGN based on emission line rations . . . 97
3.3.3 Identification of radio-excess AGN . . . 98
3.3.3.1 Radio-excess AGN identification through the SFR–150 MHz relation . . . 99
3.3.3.2 Using the Hα line luminosity–150 MHz radio luminosity relation . . . 100
3.3.3.3 Combining SFR- and Balmer-line -based radio-excess classification methods . . . 102

3.3.4 Combined spectrophotometric classification of radio sources in the LoTSS deep field EN1 . . . 103
3.4 Discussion . . . 105
3.4.1 Comparison with photometric classification . . . 108
3.4.2 Comparison with probabilistic spectroscopic classification . . . 111
3.5 Conclusion . . . 114

4 Measuring the recent histories of high-redshift galaxies using *HST* and *JWST* photometry with Prospector SED fitting 118
4.1 Data . . . 121
4.2 SED Modelling . . . 124
4.3 Results and discussion . . . 129
4.3.1 Estimation of physical parameters . . . 129
4.3.2 Recovery of the burstiness parameter . . . 132
4.3.2.1 Dependence on redshift . . . 134
4.3.3 Influence of different multi-wavelength coverage . . . 137
4.4 Conclusions . . . 140

5 Conclusions and Future Work 142
5.1 Plans for the future . . . 145
5.1.1 Future Directions for the current projects . . . 146
5.1.1.1 Joint spectrophotometric studies of the faint radio source population . . . 146
5.1.1.2 Spectrophotometric study of burstiness in high-redshift galaxies 147
5.1.2 Plans for improving the SED fitting framework . . . 148
5.1.2.1 Reducing the time required for joint spectrophotometric fitting 148
5.1.2.2 Improving emission line fitting . . . 149
5.2 Additional research not included in this thesis . . . 149
5.3 Concluding remarks . . . 150

A Assessment of Prospector derived SFRs 152
A.1 Comparison with spectroscopically measured SFRs . . . 152
A.2 Star forming main sequence . . . 153

Bibliography 154

List of Figures

1.1 An illustration showcasing the key milestones in the evolution of the Universe from the post- Big Bang inflationary phase (towards the left-hand side) to the present day (due right) according to the ΛCDM model (adapted from Robertson et al., 2010). 3

1.2 Temperature anisotropies in the all-sky map of the cosmic microwave background, measured by the European Space Agency's *PLANCK* Mission (*PLANCK* Legacy Release 2018; Planck Collaboration et al., 2020). 4

1.3 The cosmic star formation rate density (CSFRD) calculated using FUV (top-right panel), IR (bottom-right panel), and FUV+IR (left panel) rest-frame flux measurements. The fluxes are empirically converted to instantaneous star formation rate (SFR) valid for the Salpeter (1955) IMF. The CSFRD shows a peak at $z \approx 2$ (reproduced from Madau and Dickinson, 2014). 7

1.4 The expected (red) and the observed (blue) galaxy luminosity function, highlighting the disagreements at the low- and high- mass ends, potentially due to stellar and AGN feedback, respectively (adapted from Silk, 2011). 14

1.5 Illustration of the central engines in radiative-mode (left) and jet-mode (right) AGN. Radiative-mode AGN feature a geometrically-thin, optically-thick accretion disk producing luminous UV radiation that powers broad- and narrow-line regions, often obscured from some viewing angles by a dusty torus. In contrast, jet-mode AGN host a geometrically-thick, radiatively-inefficient accretion flow, with most energy released via large-scale radio jets. A truncated thin disk may persist at larger radii, contributing weakly to low-ionization narrow-line emission (reproduced from Heckman and Best, 2014). 18

1.6 The core of the LOFAR telescope, known as the superterp, in the Netherlands (Image credits: LOFAR/ASTRON, adapted from `https://www.jb.man.ac.uk/news/2011/LOFAR-pulsars/`). 20

1.7 The redshift-luminosity plane, as sampled by the three tiers of the WEAVE-LOFAR survey. Blue triangles, red diamonds, and black points represent the deep ($S_{150\ \mathrm{MHz}} > 100\ \mu$Jy), mid ($S_{150\ \mathrm{MHz}} > 1$ mJy), and wide ($S_{150\ \mathrm{MHz}} > 10$ mJy) tiers, respectively. While the left-hand panel shows all the targets, the right-hand panel only shows those sources for which successful redshift measurements are expected based on simulations (obtained from Smith et al., 2016). 25

1.8 Schematic representation of the contribution of different physical components to the SED of an unobscured AGN, compared to that of a star-forming galaxy (adapted from Harrison, 2014; Hickox and Alexander, 2018). 27

1.9 Schematic AGN SED illustrating the approximate shape and extent of key components. Dashed lines show intrinsic AGN emission, dash-dotted lines indicate reprocessed emission, and the dotted line represents starlight from an elliptical host. The hatched region marks wavelengths heavily absorbed by the IGM (adapted from Collinson et al., 2017). 33
1.10 Comparison of the smooth AGN templates (left-hand panel) from Fritz et al. (2006) and the clumpy AGN templates (right-hand panel) from Nenkova et al. (2008a). This figure is reproduced from Feltre et al. (2012). 34

2.1 (Left panel) 150 MHz radio luminosity coverage of the radio-detected and the $z < 1$ SWIRE-selected source samples used in this work. (Right panel) Histogram showing the number count of sources binned by 150 MHz luminosity for the two data samples. Sources with radio luminosity less than 10^{17} W Hz^{-1} (including radio non-detections) were arbitrarily assigned to the lowest radio luminosity bin at $\log_{10}(L_{150}/\mathrm{W\ Hz^{-1}}) = 17$. The blue data points below the lower limit of the purple distribution represent sources with $< 5\sigma$ 150 MHz radio flux measurements. Including these sources is key to leveraging the low S/N measurements in a statistical manner. 47
2.2 SED fits (left-hand panels) and recovered star formation histories (right-hand panels) for two example radio sources. ILTJ161528.25+544449.9, at a redshift of 1.8, with an estimated $\log_{10}(f_{\mathrm{AGN},16}) = 0.32$ (indicating the likely presence of radiative-mode AGN), is shown in the top panels. Meanwhile, ILTJ161146.91+553623.4, at $z = 0.4$ with $\log_{10}(f_{\mathrm{AGN},16}) = -4.33$ (implying a likely lack of radiative-mode AGN activity), is displayed in the bottom panels. In left-hand panels the photometry is shown with black dots and error bars, while solid lines represent SED fits randomly drawn from the DYNESTY chains. In all panels, red lines indicate fits with an AGN component included, while blue lines refer to fits without AGN. 53
2.3 Median likelihood estimates of stellar mass (top-left), star formation rate averaged over the last 100 Myrs (top-right), specific star formation rate averaged over the last 100 Myrs (bottom left), and dust luminosity (bottom-right) with associated uncertainties from MAGPHYS (plotted along the y-axis) compared with those obtained from PROSPECTOR (plotted along the x-axis). The sources in each plot are colour coded by the logarithm of the 16$^{\mathrm{th}}$ percentile of AGN fraction estimated by PROSPECTOR. At the bottom of each panel, we plot the difference between the MAGPHYS and PROSPECTOR estimates ($\Delta X = \log_{10}(X_{\mathrm{MAGPHYS,median}}) - \log_{10}(X_{\mathrm{PROSPECTOR,median}})$, where X represents the physical parameter estimates). In the insets we show the distribution of this difference (ΔX), with the blue histogram representing sources with $\log_{10}(f_{\mathrm{AGN},16}) < -2$ and the orange filled histogram representing sources with $\log_{10}(f_{\mathrm{AGN},16}) > -2$. 54
2.4 Comparison of the median likelihood estimates of stellar mass (left-hand panel) and the average star formation rate in the last 100 Myrs (right-hand panel) from PROSPECTOR with the consensus estimates from B23. The error bars along the x-axis represent the uncertainties in the PROSPECTOR estimates; however, uncertainties are not available for the consensus estimates from B23. The difference between the B23 consensus and PROSPECTOR estimates (as the Δ parameter, see Figure 2.3) are plotted at the bottom of each panel. Histograms depicting the distribution of the Δ parameters are shown in the insets. The blue histograms represent sources with $\log_{10}(f_{\mathrm{AGN},16}) < -2$, while the orange filled histograms represent sources with $\log_{10}(f_{\mathrm{AGN},16}) > -2$. 56

2.5 (Top panel) Histogram showing the distribution of $\log_{10}(f_{\mathrm{AGN,16}})$. (Middle panel) Comparison of χ^2 arising from PROSPECTOR fits with AGN component included (χ^2_{AGN}) along the x-axis against the χ^2 from fits without AGN ($\chi^2_{\mathrm{No\ AGN}}$). Sources classified as AGN using previous optical/spectroscopic/X-ray studies are represented as red points. (Bottom panel) Histogram showing the distribution of $\chi^2_{\mathrm{No\ AGN}}/\chi^2_{\mathrm{AGN}}$. A majority of sources classified as AGN in previous works produce better fits when AGN templates are included in the physical model. 59

2.6 Stacked two dimensional heatmap showing the SFR–$L_{150\ \mathrm{MHz}}$ plane, constructed by summing over the PDFs of sources in the SWIRE-selected sample. The thick red curve represents the median likelihood SFR–$L_{150\ \mathrm{MHz}}$ relation. The accompanying thin red curves indicate the 16$^{\mathrm{th}}$ and 84$^{\mathrm{th}}$ percentiles of the $L_{150\,\mathrm{MHz}}$ distribution at each SFR, respectively. The blue and green solid lines represent the single slope and broken power law relations from G18. The black and magenta solid lines represent the best fit relations from S21 and B23 respectively. 63

2.7 Maximum likelihood 150 MHz radio luminosities of the radio-detected sample plotted as a function of the PROSPECTOR estimated median SFRs. The best-fit SFR–$L_{150\ \mathrm{MHz}}$ relation (obtained from the SWIRE-detected sample and therefore including radio non detections) and the radio-excess cut-off used in our work (blue) and in B23 (orange) are overplotted. 65

2.8 Venn diagrams showing the number of sources in each class (star-forming galaxies, radio-quiet AGN, low- or high-excitation radio galaxy) that have been identified by our method (pink), by B23 (yellow) and by both (overlap region). . . . 66

2.9 Sources classified as SFG (in black), RQ-AGN (orange), LERG (blue), HERG (purple), and the sources marked unclassified (in green), represented as the fraction of total sources. We show the distribution of sources in each galaxy class as a function of (top-left panel) PROSPECTOR median likelihood stellar mass estimates, (top-right panel) PROSPECTOR median likelihood SFR estimates, (centre-left panel) 150 MHz radio flux density, (centre-right panel) 150 MHz radio luminosity, (bottom-left panel) redshift, and (bottom-right panel) optical r-band magnitude. The dotted lines with open squares represent the fractions of sources in each galaxy class from B23. In the top-left and top-right panels, we plot the B23 source fractions against the B23 consensus stellar mass and SFR estimates, respectively. The distribution of the whole sample as a function of the respective quantities is shown in the background, as a normalised grey histogram with peak being equal to unity. 68

2.10 Distribution of the different source classes in the stellar mass–SFR plane: the shaded 2D histogram represents the SFGs, the overlaid purple and blue contours represent the RQ AGN and LERGs, respectively, and the cyan circles denote the HERGs. In the bottom panel, the solid orange line and the shaded orange region represent the Schreiber et al. (2015) parametrisation of the main sequence converted to our adopted Kroupa (2001) IMF with the typical 0.3 dex scatter around it. Contour levels are selected to encompass 5, 50, and 90 per cent of the corresponding sample. 69

2.11 The relationship between radio luminosity at 150 MHz and the dependence on stellar mass and star formation rate (SFR), derived for the 85,162 $z < 1$ SWIRE-selected sources excluding known/likely AGN. Stellar mass and SFRs are estimated through PROSPECTOR SED fits. In the top left-hand panel, the median likelihood 150 MHz radio luminosity - SFR plot is shown for different stellar mass bins. The different coloured lines represent distinct stellar mass bins, as indicated in the colour-bar to the right. The top right-hand panel illustrates the median likelihood stellar mass vs 150 MHz radio luminosity plots for different SFR bins, with colours again relative to the bar to the right. Similarly, in the bottom left-hand panel, the stellar mass-adjusted radio luminosity - SFR plot is displayed for varying stellar mass bins, using the best fit values from Equation 2.2. Finally, the bottom right-hand panel exhibits the SFR-adjusted radio luminosity vs stellar mass plot for different SFR bins. 75

3.1 Transmission curves of the LoTSS UV–far-IR filters used in this work are shown, with a sample galaxy SED redshifted to $z = 0$ and $z = 1$ overplotted to illustrate the photometric coverage of typical galaxy spectral features. The galaxy was selected at random from the 6,038 galaxies in our sample. The yellow-shaded region indicates the approximate range of wavelengths sampled by the DESI EDR spectroscopy used in this work. 83

3.2 The logarithm of the ratio of uncertainties obtained from PROSPECTOR posterior PDFs to those obtained from the FASTSPECFIT catalogue is plotted as a function of the median likelihood fluxes estimated in this work. The panels show (top-left) Hβ, (top-right) [OIII], (bottom-left) Hα, and (bottom-right) [NII]. There is a clear indication of a flux-dependent systematic bias in the uncertainties estimated from the PROSPECTOR PDFs. The best-fit straight line, which is used to correct for this bias, is shown as a dot-dashed red line in each plot. 89

3.3 The blue-shaded histograms show the distribution of reduced chi-squares ($\overline{\chi}^2$) calculated for the two BPT emission line pairs: (left-hand panel) Hβ + [OIII], and (right-hand panel) Hα + [NII]. The uncertainties in the distribution, estimated using bootstrapping, are represented by the blue bars. The solid red curves depict the best-fit standardised reduced chi-squared PDFs for each line-pair. 90

3.4 Comparison of the median-likelihood parameter estimates (clockwise from the top-left panel: current stellar mass, SFR averaged over 10 Myrs, SFR averaged over 100 Myrs, AGN fraction parameter, and the specific SFR averaged over 100 Myrs) obtained from the spectrophotometric PROSPECTOR fits used in this work (along the x-axis) with those from the PROSPECTOR photometry-only fits by D24 (along the y-axis). Typical uncertainties are indicated by the error bar in the lower right of each panel. The plots are colour-coded by redshift, as shown by the colourbar at the top. 91

3.5 Comparison of the median-likelihood flux estimates for the four BPT emission lines: (top-left) Hβ, (top-right) [OIII], (bottom-left) Hα, and (bottom-right) [NII]. Fluxes calculated using PROSPECTOR, after applying corrections, are plotted on the x-axis, while those reported in the FASTSPECFIT catalogue are on the y-axis. The plots are colour-coded by redshift, with error bars shown as gray lines. Only sources with a 3σ detection in each line in both works are considered. 92

3.6 The distribution of the posterior probabilities of radio sources hosting radiative AGN ($\mathcal{P}_{\rm AGN,MIR}$) is shown without *a priori* restrictions (top panels), after applying a likelihood ratio prior (middle panels), and after applying the modified likelihood ratio prior (bottom panels). The left-hand columns show the distribution of the $\mathcal{P}_{\rm AGN,MIR}$ vs z plane. The lack of redshift evolution in $\mathcal{P}_{\rm AGN,MIR}$ supports the interpretation that the distributions are driven by model degeneracies rather than physical effects. The histograms in the right-hand columns demonstrate how the introduction of physically motivated priors enables more secure classification of sources hosting radiative-mode AGN. 95

3.7 BPT diagram, colour-coded by the probabilities of sources belonging to the SFG ($\mathcal{P}_{\rm BPT,SFG}$), LINER ($\mathcal{P}_{\rm BPT,LINER}$), and Seyfert ($\mathcal{P}_{\rm BPT,Seyfert}$) classes, shown in the left-hand, centre, and right-hand panels, respectively. Overlaid are the Kewley et al. (2001), Kauffmann et al. (2003), and Cid Fernandes et al. (2010) demarcation lines. 97

3.8 Distribution of $\log_{10}(L_{150}) - \log_{10}(\psi)$ (top-left panel) and $\log_{10}(L_{150}) - \log_{10}(L_{\rm H}\alpha)$ (bottom-left panel). The blue-shaded histogram in each panel represents the full source population, the navy-outlined histogram denotes the SFG population – obtained by reflecting the left-hand side of the full distribution about its peak, and the orange histogram shows the residual population, which is predominantly composed of radio-excess AGN. The right-hand panels show the Gamma cumulative distribution function (Γ-CDF) fits to the probability functions defined by Eqn. 3.8 (top) and Eqn. 3.13 (bottom). The uncertainties, represented by the shaded pink regions, are computed through bootstrapping. 102

3.9 The typical SEDs of the P_{90}-classified sources in the (top-left panel) SFG, (top-right panel) RQ AGN, (centre-left) LERG, and (centre-right) HERG classes. Unclassified sources are in the bottom panel. The solid orange line in each panel represents the median unattenuated stellar SED, the solid green line shows the median AGN model, and the solid blue line indicates the median full UV–FIR SED. The shaded regions denote the scatter between the $16^{\rm th}$ and $84^{\rm th}$ percentile SEDs. 106

3.10 Sources in the four galaxy classes: SFGs (shaded gray histogram), RQ AGN (magenta points), LERGs (blue points), and HERGs (green points with black outlines), shown relative to the main sequence of star forming galaxies, with the stellar mass – SFR plane. The solid orange line and the shaded orange region depict the Schreiber et al. (2015) parametrisation of the main sequence, converted Kroupa (2001) IMF, with the typical 0.3 dex scatter. The left-hand panel displays stellar masses and SFRs from D24, colour-coded by their classifications, while the right-hand panel presents results from this chapter's spectrophotometric fitting, colour-coded according to the P_{90} classifications. 107

3.11 Distributions of the SFGs (shaded gray histogram), RQ AGN (magenta points), LERGs (blue points), and HERGs (green points with black outlines) in the redshift-150 MHz radio luminosity plane. The colourbar to the right denotes the number of SFGs. 108

3.12 Distribution of the different AGN classes in the BPT plane. SFGs are denoted by the shaded gray histogram (with the colourbar to the right-hand side denoting the number of SFGs). The RQ AGN, LERGs, and HERGs are represented by the magenta, blue, and green points with black outlines, respectively. The BPT plane includes the Kewley et al. (2001), Kauffmann et al. (2003), and Cid Fernandes et al. (2010) demarcation lines. Only sources with 3σ detections are shown in this figure. 109

3.13 Confusion matrices comparing the probabilistic classifications from this work with the photometry-only classifications from D24. The comparison between our P_{90} and ML classifications and the D24 classifications is shown in the top and bottom rows, respectively. In each case, the left-hand panel shows the number of sources, while the right-hand panel shows the percentage agreement between the two classification schemes. In each cell of the right-hand panel, the top value includes unclassified sources, while the parenthesis-enclosed value below excludes them. The total number of sources in each class (from this work) is indicated at the top of each row. 111

3.14 The K-band (2.2μm) normalised full UV-FIR SEDs (blue), unattenuated stellar SEDs (orange), and AGN models (green), for sources corresponding to the confusion matrix in top rows of Fig. 3.13. The thicker dashed lines denote the median SEDs and their respective components. 112

3.15 Confusion matrices comparing the spectrophotometric classifications from this work with the spectroscopy-only classifications from A25. Both classifications are >90 per cent purity limited. The left panel shows source counts; the right shows percentage agreement between classifications. In each right-hand cell, the top value includes unclassified sources, while the value in parentheses excludes them. The total number of sources in each class (from this work) is shown at the top. 114

3.16 The K-band (2.2μm) normalised full UV–FIR SEDs (blue), unattenuated stellar SEDs (orange), and AGN models (green) for sources corresponding to the confusion matrix in Fig. 3.15. The thicker dashed lines represent the median SEDs and their respective components. 115

4.1 Histograms showing the distributions of the true physical parameters covered in the SPHINX Public Data Release Version 1 (SPDRv1) sample. The panels show the total stellar mass formed, the stellar metallicity in the units of solar metallicity, the star formation rate averaged over 10 and 100 Myrs, and the burstiness parameter η. 121

4.2 (Top) Location of the SPHINX^{20} galaxies relative to the galaxy star formation rate–stellar mass relation, shown as the difference between the true 100 Myr averaged SFR and the SFR expected for a source with the same stellar mass and redshift using the Schreiber et al. (2015) parametrisation (converted to our adopted Kroupa, 2001 IMF) as a function of the true stellar mass. The grey shaded region indicates the canonical ±0.3 dex width of the so-called 'main-sequence'. (Bottom) Burstiness parameter η vs total stellar mass, demonstrating the stochasticity of SFHs of SPHINX^{20} galaxies. In both panels the points are colour coded by redshift relative to the colour bar located to the right. 122

4.3 SED of a sample SPHINX^{20} galaxy, selected at random, and redshifted to $z = 4.64, 5, 6, 7, 8, 9$, and 10 (from topmost panel to bottom). Transmission curves of the *HST*, *JWST* NIRCam, and *JWST* MIRI filters, listed in Table 4.1, are shown as blue, yellow, and pink shaded regions, respectively, to demonstrate the coverage they provide to the SEDs (and the accompanying spectral features) at each redshift. 125

4.4 SED of the same SPHINX^{20} galaxy as in Fig. 4.3 at $z = 4.64, 5, 6, 7, 8, 9$, and 10, with the y-axis range adjusted to highlight the continuum features. Transmission curves of the *HST*, *JWST* NIRCam, and *JWST* MIRI filters are shown as blue, yellow, and pink shaded regions, respectively. 126

4.5 SED fits and recovered SFHs for sources randomly selected at $z = 4.64$ and $z = 8$, with varying degrees of burstiness. The plots for each source are presented in two panels: the top panel shows the SED fits, and the bottom panel shows the SFH. The top two rows show sources at $z = 4.64$ with temp-quenched, constant, and bursty SFHs (in the left-, middle- and right-hand columns, respectively) while the third and fourth rows show sources at $z = 8$. Median likelihood SEDs and SFHs from the CSFH fitting are denoted by dashed blue lines, while those assuming a BSFH prior are denoted by dot-dashed magenta lines, with associated uncertainties indicated by the shaded area. The input photometry is shown with black outlined squares and error bars, overlaid on the true SPHINX^{20} spectra (in grey). 130

4.6 Comparison of median likelihood estimates from PROSPECTOR (plotted along the y-axis) – total stellar mass (left-hand panels), SFR averaged over 10 Myrs (middle panels), and the SFR averaged over 100 Myrs (right-hand panels) versus the true values (along the x-axis), along with the typical uncertainties which are indicated by the error bar to the lower right in each panel. The top panels (A to C) show estimates using the bursty prior, while the bottom panels (D to F) show results with the continuity SFH prior. Plots are coloured according to their redshift, relative to the colour-bar at the right. 131

4.7 Burstiness parameter (η) recovered using the bursty SFH prior (left) and continuity SFH prior (right), colour-coded by redshift relative to the colour-bar to the right. For each prior, the top panel shows the median-likelihood η estimates vs the true values, overlaid with a 1:1 line surrounded by shading indicating the typical η uncertainty estimated as a function of true η. The middle and bottom panels display $\Delta\eta$ (i.e. the difference between the median likelihood estimate and the truth) as a function of true η in the units of dex and the actual uncertainty (σ_η), respectively. 132

4.8 The true (black dashed line) and recovered (magenta and blue shading, showing the BSFH and CSFH values, respectively) distribution of burstiness parameter, η. 133

4.9 The average recovered η as a function of true η, at redshifts of $z = 4.64, 5, 6, 7$, and $z \geq 8$ (as indicated in the legend). The left-hand panels show the recovery of η using the BSFH prior, while the right-hand panels use the CSFH prior. The solid lines show the median values at each redshift, with shaded regions representing the scatter within each bin. Each panel includes a one-to-one line, plotted as a dashed gray line. η from the bursty SFH prior shows a weak correlation with the true values, while those from the continuity prior are generally consistent with 0 ± 0.2 dex, irrespective of the true values. The coloured histograms on the top of the plot shows the source count in each η bin at each redshift. The bottom panel shows $\Delta\eta = \eta_{\rm recovered} - \eta_{\rm true}$ in each redshift bin. . . 134

4.10 Similar to Fig. 4.9, but showing the median η recovery (using the BSFH prior) when all galaxies are artificially shifted to $z = 6$ to force the same photometric coverage in each band (right-hand panels). The left-hand panels show the sources from the fiducial run with BSFH for comparison. Only one randomly selected direction from all the SPHINX^{20} haloes is used to make these plots. . . 135

4.11 We show $\chi = \left(\frac{F_{\nu,\text{PROSPECTOR best fit}} - F_{\nu,\text{obs}}}{\sigma_{F_{\nu,\text{obs}}}}\right)$, computed between input and PROSPECTOR best-fit photometry, as a function of observed-frame wavelength across different redshift bins. The top panel shows the sources from the fiducial BSFH run, while the bottom panel shows the results where the input SEDs were redshifted to $z = 6$ prior to fitting. The solid lines denote the median χ value, while the shaded regions denote the spread between 16$^{\text{th}}$ and 84$^{\text{th}}$ percentile bounds within a wavelength range. Only one direction is shown per halo. We find that there is a consistent trend in χ across all redshift ranges as a function of rest-frame wavelength, which indicates that certain spectral features are fit better than others – a limitation of photometry-only fitting process. However, we do not find a clear dependence of χ on redshift, that could explain the observed redshift-biases in η recovery. 137

4.12 Comparison of median likelihood estimates from the BSFH prior (plotted along the y-axis) – total stellar mass (left-hand panels), SFR averaged over 10 Myrs (middle panels), and the SFR averaged over 100 Myrs (right-hand panels) versus the true values (along the x-axis), along with the typical uncertainties which are shown as error bars to the lower-right, for the three sets of fits: NIRCam-only (blue), NIRCam + MIRI (magenta), and *HST* + NIRCam + MIRI (green). Scatter plots for NIRCam only and NIRCam + MIRI fits are shown here, those for the fiducial fits can be found in Fig. 4.6. The solid lines with the shaded regions show the median likelihood estimate and the uncertainties calculated using bootstrap resampling. 138

4.13 The median likelihood η was estimated with the bursty prior using the NIRCam-only (blue), NIRCam + MIRI (magenta), and *HST* + NIRCam + MIRI (green) filter configurations. The solid lines with shaded regions denote the median η with uncertainties estimated through bootstrapping. The scattered blue and magenta points also show the spread of the corresponding η values vs the true values. The scatter for *HST* + NIRCam + MIRI is not included, it can be seen instead in Fig. 4.7. Typical uncertainties are also shown in the corresponding colours. The lower panel shows $\Delta\eta$ (= median likelihood estimate − true) as a function of the true η for the different sets of fits. The histogram to the right of the top panel shows the distributions of median likelihood η values from the three sets of fits. 138

A.1 Comparison of PROSPECTOR estimated median likelihood SFRs (averaged over 10 Myrs) with the Balmer corrected Hα SFRs. The solid black line denotes the ideal 1:1 relation. The red dashed line represents the best-fit deviation of the PROSPECTOR estimated SFRs from the Hα SFRs, while the bottom panel shows the difference of the PROSPECTOR SFR estimates of the individual sources from Hα SFRs, in units of the (propagated) uncertainties. 153

A.2 Stellar mass vs SFR plots for ∼120,000 SWIRE-selected sources using estimates obtained from PROSPECTOR (top panel) and MAGPHYS (bottom panel) SED fits. The blue shaded region represents the region enclosed by the Schreiber et al. (2015) parametrisation of the main sequence of star forming galaxies between $0 < z < 1$, converted to our adopted Kroupa (2001) IMF. 154

List of Tables

2.1 Description of the PROSPECTOR parameters used in the final model. † The PROSPECTOR models use the total stellar mass formed in a source as a free parameter, which is larger than the currently surviving stellar mass. We use the latter for analysis purposes throughout this work. 51

2.2 The number of star forming galaxies, radio-quiet AGN, low-excitation radio galaxies, and high-excitation galaxies, identified in the ELAIS N1 deep field using our classification scheme, along with uncertainties calculated using bootstrap resampling. B23 classification results are also included for comparison. . 66

3.1 Description of the PROSPECTOR parameters used in the final model. Similar to Chapter 2, † denotes the total stellar mass formed in a source which is used as a free parameter, and is larger than the currently surviving stellar mass. 85

3.2 The number of star forming galaxies, radio-quiet AGN, low/high-excitation galaxies, identified after setting a 90 per cent purity threshold (P_{90}), and using maximum-likelihood (ML) classification approach, out of a total of 5,401 sources that could be classified by either method. Poisson uncertainties are reported. The percentages of the 5,401 sources that fall into each class are quoted below, with the accompanying parentheses giving the percentages relative to the number of sources that could be classified using that method (i.e. excluding unclassified sources). For comparison, D24 classifications are also presented. While the ML classification allows for the classification of approximately twice as many sources as the P_{90} classification, the latter is more reliable. 105

3.3 Number of sources in each class from this work and the spectroscopic classifications of A25, both limited to a >90 per cent probability threshold. The values correspond to a total of 3,704 sources common to both datasets for which the necessary conditions for classification were met. As in Table 3.2, Poisson uncertainties are reported, and the number of sources in each class is given both as a percentage of the total 3,704 sources compared here and as a percentage of the sources classified as SFG, RQ AGN, LERG, or HERG (i.e., excluding unclassified sources). 114

4.1 *HST*, *JWST* NIRCam, and *JWST* MIRI photometric filters used in this work. Check marks indicate whether that filter was used in that programme. 127

4.2 Details of the PROSPECTOR parameters used in our SED model, including the choice of prior. 129

4.3 Goodness of physical parameter (= recovered − true) recovery using PROSPECTOR BSFH prior using different sets of photometric filters, quantified by the median $\Delta \log_{10}$ parameter, its standard deviation, and typical uncertainty on $\log_{10}$ parameter. . . 140

List of Abbreviations

ΛCDM	Λ cold dark matter
AGB	Asymptotic giant branch
AGN	Active galactic nuclei
AIPS	Astronomical Image Processing System
ALMA	Atacama Large Millimeter/submillimeter Array
APERTIF	APERture Tile In Focus
ASKAP	Australian Square Kilometre Array Pathfinder
ATHENA	Advanced Telescope for High ENergy Astrophysics
BAGPIPES	Bayesian Analysis of Galaxies for Physical Inference and Parameter EStimation
BAO	Baryon acoustic oscillations
BaSTI	Bag of Stellar Tracks and Isochrones
BBB	Big Blue Bump
BC03	Bruzual and Charlot (2003) model
BEAGLE	BayEsian Analysis of GaLaxy sEds
BH	Black hole
BLR	Broad line region
BOSS	Baryon Oscillation Spectroscopic Survey
BPASS	Binary Population and Spectral Synthesis
BPT	Baldwin-Phillips-Terlevich
BSFH	Bursty star formation history
CASA	Common Astronomy Software Applications
CDF	Cumulative distribution function
CEERS	Cosmic Evolution Early Release Science
CGM	Circumgalactic medium
CIGALE	Code Investigating GALaxy Emission

CMB	Cosmic microwave background
COBE	Cosmic Background Explorer
CPU	Central Processing Unit
CRE	Cosmic-ray electrons
CSFH	Continuity star formation history
CSFRD	Cosmic star formation rate density
CSP	Composite stellar population
DEC	Declination
DESI	Dark Energy Spectroscopic Instrument
DM	Dark matter
E-ELT	European Extremely Large Telescope
EDFN	Euclid Deep Field North
EDR	Early data release
EELG	Extreme emission line galaxies
ELAIS-N1	European Large Area ISO Survey Northern Field 1
EMU	Evolutionary Map of the Universe
EoR	Epoch of reionisation
ERS	Early Release Science
ESO	European Southern Observatory
EUV	Extreme ultraviolet
EVN	European VLBI Network
EW	Equivalent Width
FFT	Fast Fourier transform
FIRC	Far-infrared radio correlation
FIRE	Feedback In Realistic Environments
FIRST	Faint Images of the Radio Sky at Twenty-Centimeters
FIR	Far-infrared
FSPS	Flexible Stellar Population Synthesis
FUV	Far-ultraviolet
FWHM	Full width at half maximum
GHz	Gigahertz
GLASS	Grism Lens-Amplified Survey from Space
HBA	High Band Antennas

HERG	High excitation radio galaxy
HSC-SSP	Hyper Suprime-Cam Subaru Strategic Program
HST	Hubble space telescope
IFU	Integral field unit
IGM	Intergalactic medium
IMF	Initial mass function
IRAC	Infrared Array Camera
IRTF	Infrared Telescope Facility
IR	Infrared
ISM	Interstellar medium
ISRF	Interstellar radiation field
JADES	JWST Advanced Deep Extragalactic Survey
JWST	James Webb space telescope
LBA	Low Band Antennas
LERG	Low excitation radio galaxy
LF	Luminosity function
LINER	Low-ionization Nuclear Emission-line Region
LISA	Laser Interferometer Space Antenna
LMC	Large Magellanic Cloud
LMT	Large Millimeter Telescope
LOFAR	LOw-Frequency ARray
LoLSS	Low Band Antenna Sky Survey
LoTSS	LOFAR Two Metre Sky Survey
LSF	Line spread function
LSKSP	LOFAR Surveys Key Science project
MAGPHYS	Multi-wavelength Analysis of Galaxy Physical Properties
MCMC	Markov Chain Monte Carlo
MERLIN	Multi-Element Radio Linked Interferometer Network
MESA	Modules for Experiments in Stellar Astrophysics
MHz	Megahertz
MIGHTEE	MeerKAT International Gigahertz Tiered Extragalactic Explorations Survey
MILES	Medium-resolution Isaac Newton Telescope library of empirical spectra
MIPS	Multiband Imaging Photometer

MIRI	Mid-Infrared Instrument
MIR	Mid infrared
MIST	MESA Isochrones and Stellar Tracks
ML	Maximum-likelihood
MMSS	Massively-multiplexed spectroscopic surveys
MOONS	Multi-Object Optical and Near-infrared Spectrograph
MOS	Multi Object Spectroscopy
MPA-JHU	Max Planck Institute for Astrophysics- Johns Hopkins University
MS	Main sequence
MW	Milky Way
NASA	National Aeronautics and Space Administration
NGSL	HST/STIS next generation spectral library
NIRCAM	Near-Infrared Camera
NIR	Near infrared
NLR	Narrow line region
NRAO	National Radio Astronomy Observatory
NUV	Near infrared
NVSS	NRAO VLA Sky Survey
ORCHIDSS	Optical, Radio Continuum and HI Deep Spectroscopic Survey
PACS	Photodetector Array Camera and Spectrometer
PAH	Polycyclic aromatic hydrocarbon
PARSEC	PAdova and TRieste Stellar Evolution Code
PDF	Probability density function
PFS	Prime Focus Spectrograph
Pop. III	Population III
Pop. II	Population II
QSO	Quasi-stellar object
RASCAS	RAdiative SCattering in Astrophysical Simulations
RA	Right ascension
REX	Radio excess
RLF	Radio luminosity functions
RL	Radio loud
RMS	Root mean square

RQ-AGN	Radio quiet AGN
RST	Nancy Grace Roman Space Telescope
SBI	SBI
SDSS	Sloan Digital Sky Survey
SED	Spectral energy distribution
SERVS	Spitzer Extragalactic Representative Volume Survey
SEY	Seyfert
SFG	Star forming galaxy
SFH	Star formation history
SFMS	Star forming main sequence
SFR	Star formation rate
SKA	Square Kilometre Array
SMBH	Supermassive black hole
SMC	Small Magellanic Cloud
SMF	Stellar mass function
SNe	Supernovae
SNR	Signal to noise ratio
SPIRE	Spectral and Photometric Imaging REceiver instrument
***Spitzer*/IRAC**	Infrared Array Camera for the *Spitzer* Space Telescope
SPS	Stellar population synthesis
SQ	Stephen's quintet
SSP	Single stellar population
STIS	Space Telescope imaging spectrograph
SWIRE	SIRTF Wide - Area Infrared Extragalactic Survey
UKIDSS-DXS	UK Infrared Deep Sky Survey Deep Extragalactic Survey
UV	Ultraviolet
VAC	Value added catalogue
VLA-COSMOS	VLA Cosmic Evolution Survey
VLASS	VLA Sky Survey
VLA	Karl G. Jansky Very Large Array
VLBI	Very Long Baseline Interferometry
VLT	Very Large Telescope
WAVES	Wide Area VISTA Extragalactic Survey

WEAVE	William Herschel Telescope Enhanced Area Velocity Explorer
WFC	Wide Field Camera
WHT	William Herschel Telescope
WISE	Wide-field Infrared Survey Explorer
WMAP	Wilkinson Microwave Anisotropy Probe
WST	Wide-field Spectroscopic Telescope
XID	XMM identification
XMM-Newton	X-ray Multi-Mirror Mission
XSL	X-shooter library

Chapter 1

Introduction

"So much universe, and so little time."

–Terry Pratchett

One of the core objectives of astrophysics is to understand how galaxies have formed and evolved over cosmic time. Galaxies are the fundamental building blocks of the Universe, acting as sanctuaries where stars are born, black holes grow, and increasingly heavy metals are formed and propagated throughout the Universe (Abel et al., 2002; Somerville and Davé, 2015). Emission of photons from galaxies is powered by a complex interplay of processes, such as the birth and death of stars, absorption and emission by dust and the interstellar medium (ISM), and accretion on to the supermassive black hole (SMBH), which can drive outflows and jets (Kennicutt, 1998a; Kennicutt and Evans, 2012; Calzetti, 2001; Draine, 2003; Galliano et al., 2018; Heckman and Best, 2014; Fabian, 2012; Netzer, 2015; Hardcastle and Croston, 2020). All of this information, along with physical properties such as the stellar mass and rate of star formation, is encoded in the spectral energy distribution (SED) of the galaxy. Decoding the SEDs and extracting this information requires robust observations to constrain physically-motivated models, a statistical framework capable of breaking model degeneracies, and a computational infrastructure to support the entire process (Walcher et al., 2011; Conroy, 2013; Smith and Hayward, 2015; Pacifici et al., 2023). This thesis investigates an approach to decoding galaxy SEDs across a wide range of redshifts (z) by exploring different combinations of model parameters and working with both observed and simulated data of varying sensitivities, wavelength coverage, and resolutions. We aim to gain a deeper understanding of galaxy evolution and to explore the nature and composition of different galaxy populations.

1.1 The early Universe

1.1.1 The Big Bang and the epoch of inflation

Through the theory of nucleosynthesis, Gamow (1946) postulated that the Universe began as a very hot and dense state of singularity, which then began to expand with a *Big Bang*. The coincidental discovery of the cosmic microwave background (CMB; Penzias and Wilson, 1965) radiation independently validated the theoretical predictions of Gamow (1946), thereby laying the foundation of standard Big Bang cosmology (see Tsujikawa, 2003, for an overview). The prevailing cosmological theoretical framework describing the initial stages of the Universe and the formation of structure within it is the Λ cold dark matter (ΛCDM; Peebles, 1984; Davis et al., 1985) model (see Bull et al., 2016, for a detailed review). According to the ΛCDM model, the Universe is spatially flat and undergoing accelerated expansion. The present-day ΛCDM Universe consists of approximately 70 per cent "dark energy", 25 per cent cold[1] dark matter (DM) particles, and 5 per cent baryonic matter (Peebles and Ratra, 2003; Planck Collaboration et al., 2016; Bullock and Boylan-Kolchin, 2017). Dark energy is a homogeneous form of energy that is believed to drive the accelerating expansion of the Universe. Observational evidence for dark energy comes from observations of Type Ia supernovae (SNe), baryon acoustic oscillations (BAO), weak gravitational lensing, and the distribution and abundance of galaxy clusters in the Universe (see Li et al., 2013; Weinberg et al., 2013, and references therein).

Fig. 1.1, adapted from Robertson et al. (2010), provides a schematic illustration of the key milestones in the evolution of the Universe, tracing its history from the Big Bang to the present day. The Universe underwent an epoch of exponential expansion, known as "inflation", between $\sim 10^{-36}$ and $\sim 10^{-32}$ seconds after the Big Bang (Guth, 1981; Jones and Lambourne, 2004; Baumann, 2009). During this epoch, the temperature dropped by a factor of $\sim 10^6$ (see Gibbons et al., 1983), and microscopic quantum fluctuations were stretched to macroscopic scales. The post-inflationary Universe marked a phase of further expansion, albeit at a slower rate, and continued to cool. The baryons at this stage were coupled to the electromagnetic radiation field through Thomson scattering, forming a hot, dense, and nearly homogeneous plasma (Kolb and Turner, 1990; Weinberg, 2008). This tightly coupled primordial plasma persisted until ~380,000 years after the Big Bang ($z \approx 1,100$), when the Universe cooled sufficiently for electrons and

[1] Here, cold refers to the low velocities, when compared to the speed of light (Davis et al., 1985).

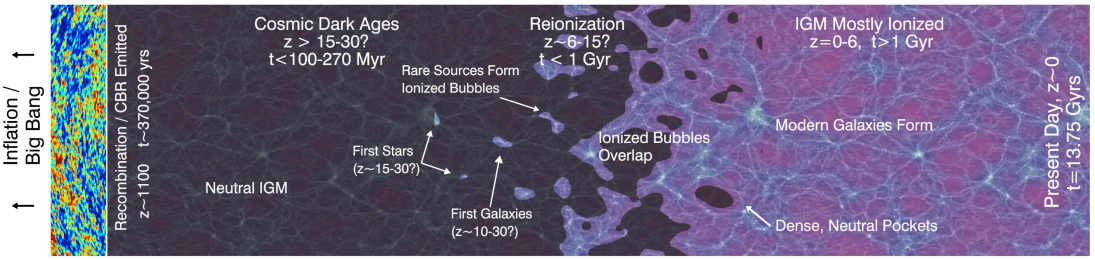

FIGURE 1.1: An illustration showcasing the key milestones in the evolution of the Universe from the post- Big Bang inflationary phase (towards the left-hand side) to the present day (due right) according to the ΛCDM model (adapted from Robertson et al., 2010).

protons to combine, forming neutral Hydrogen (termed the epoch of "recombination"). Recombination caused a drastic drop in the density of free electrons, and led to the photon scattering rate falling below the rate of Hubble expansion, decoupling them from the baryonic matter, and producing the CMB radiation. The CMB follows a blackbody spectrum with a present-day temperature of 2.725 K (Fixsen, 2009). As the oldest light in the Universe, it provides a snapshot of the Universe at the time of recombination. Observations by the *Cosmic Background Explorer* (*COBE*; Smoot et al., 1992) satellite, the *Wilkinson Microwave Anisotropy Probe* (*WMAP*; Kogut et al., 2003; Spergel et al., 2003, 2007) satellite, and the *PLANCK* mission (Planck Collaboration et al., 2020) have revealed tiny variations (or anisotropies) in the temperature of the CMB (see Fig. 1.2), which are believed to correspond to the fluctuations in the density of matter in the early universe, and therefore represent the seeds of all structures in the Universe.

1.1.2 The cosmic dark ages and the formation of the first stars

The post-recombination Universe was predominantly neutral and composed mainly of Hydrogen, Deuterium, Helium, and Lithium atoms, along with a few simple molecules (Harwit and Spaans, 2003). The period between recombination and the formation of the first radiating sources (such as stars and galaxies) is referred to as the "dark ages" (Cimatti et al., 1997). This period, lasting from ∼0.6 Myrs ($z \approx 1,100$) to $100-200$ Myrs ($z \approx 15-30$) after the Big Bang, was characterised by a complete absence of electromagnetic radiation, making it extremely challenging to directly probe this period and to reconstruct the precise conditions that eventually led to the emergence of the first luminous sources in the Universe.

According to the ΛCDM model, structure formation in the Universe proceeded in a "hierarchical" or "bottom-up" manner, where smaller structures coalesced to form larger and larger structures (see White and Rees, 1978, for a review). Prior to the epoch of reionisation, small-scale

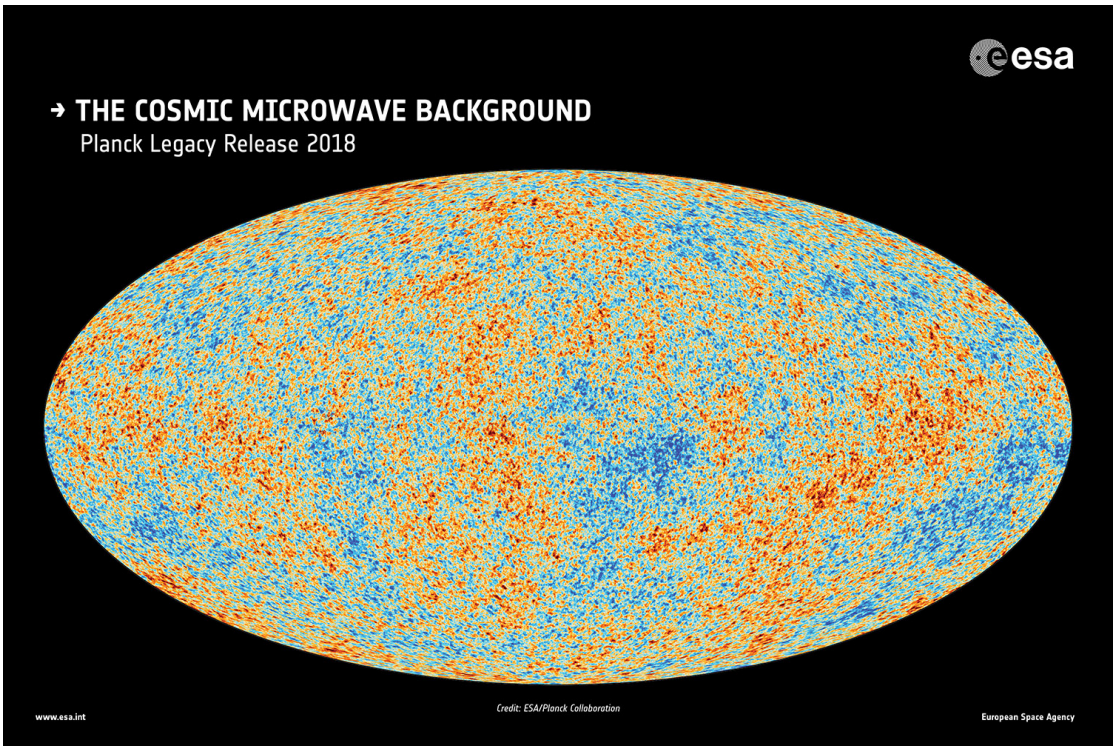

FIGURE 1.2: Temperature anisotropies in the all-sky map of the cosmic microwave background, measured by the European Space Agency's *PLANCK* Mission (*PLANCK* Legacy Release 2018; Planck Collaboration et al., 2020).

density perturbations existed in non-baryonic DM, which evolved into pockets of over-dense regions and subsequently collapsed gravitationally to form larger halos (see Bergström, 2000). However, the radiation pressure exerted upon the coupled baryon-photon plasma prevented it from undergoing a similar collapse until photons decoupled, at which point baryons began to assimilate onto the existing DM haloes. Throughout the dark ages, smaller haloes merged to form progressively larger ones. Simulations by Abel et al. (2002) and Nakamura and Umemura (2001) have demonstrated that once sufficient baryonic matter had accumulated in these haloes and a critical density threshold was reached, the gas was heated through compression, leading to the formation of molecular Hydrogen. This molecular Hydrogen then collided with neutral Hydrogen in the densest regions of the halo, lowering the temperature and pressure, and causing further contraction into gravitationally bound clumps, ultimately leading to the formation of the first stars. The first generation of stars, known as Population III (or Pop. III) stars, are believed to have formed from predominantly metal-free primordial gas in DM haloes with masses $\sim 10^6\ M_\odot$ at $z \approx 20-30$ (see Bromm et al., 2009; Klessen, 2019; Klessen and Glover, 2023, and references therein). Numerical simulations have shown that these stars did not form in isolation; rather, they were often part of stellar systems and clusters (e.g., Clark et al., 2011a,b; Greif et al., 2011; Stacy and Bromm, 2013). While the precise characteristics of these stars and

their initial mass function (IMF) remain a matter of active research, the IMF is thought to have been top-heavy (i.e., more massive stars per unit star formation compared to present-day trends), spanning a wide range of masses (Bromm and Larson, 2004). Massive Pop. III stars ($> 15\ M_{\odot}$) are believed to have ended their lives as SNe, thereby enriching the ISM with metals and laying the foundation for the formation of metal-enriched Population II (Pop. II) stars (Whalen et al., 2013a,b). Although a comprehensive understanding of Pop. III stars is beyond the scope of this thesis, it is important to note that they played a critical role in the chemical enrichment of the Universe and in assembling the first galaxies (Bromm and Yoshida, 2011; Karlsson et al., 2013).

1.1.3 The epoch of reionisation

Theoretical models (e.g. Seager et al., 2000) and detailed measurements of the CMB (e.g., from the *WMAP* mission, see Spergel et al., 2003, 2007) have shown that the intergalactic medium (IGM) in the post-recombination Universe was composed primarily of neutral Hydrogen gas. However, observations of the Gunn-Peterson effect show that the IGM was in an ionised state at $z \sim 6$. The Gunn-Peterson effect (Gunn and Peterson, 1965; Scheuer, 1965; Becker et al., 2001) refers to the spectral features associated with Lyman-α (Lyα) absorption of neutral Hydrogen observed in bright, high-z quasi-stellar objects (QSOs), and is therefore widely used as a measure of the neutral Hydrogen fraction in the IGM. Thus, the IGM transitioned from a neutral state to an ionised state at some point in the past, a period which is known as the epoch of "reionisation" (EoR). While observations have shown that the reionisation process was complete by $z \sim 6$ (see McGreer et al., 2015; Robertson et al., 2015; Planck Collaboration et al., 2020), the beginning of this process is presently not well constrained, with works such as Fan et al. (2006a) suggesting that reionisation started as early as $z \sim 14$. Reionisation is believed to have been driven by photons arising primarily from Pop. III stars; however, the role of other source classes (e.g., the first galaxies, active galactic nuclei or AGN, and mini-QSOs powered by intermediate-mass black holes), as well as demographics of these sources remains poorly understood (Sokasian et al., 2004; Ciardi and Ferrara, 2005; Furlanetto et al., 2006; Benson et al., 2006; Mutch et al., 2016; Wise, 2019).

1.2 Galaxies in the early Universe

Early galaxies played a pivotal role in the reionisation and chemical enrichment of the IGM (see White and Rees, 1978; Blumenthal et al., 1984). Yet, the precise nature of these sources, the initial conditions that governed their formation, and the epoch in which they emerged remain open questions in astrophysics. For several decades, numerical simulations have served as the primary means of investigating these issues. However, this landscape is now shifting with the advent of high-redshift observations from past, current, and upcoming facilities, such as the *Hubble Space Telescope* (*HST*; Williams et al., 1996), the Infrared Array Camera (IRAC) for the *Spitzer* Space Telescope (*Spitzer*/IRAC; Fazio et al., 2004), the Atacama Large Millimeter/submillimeter Array (ALMA; Wootten and Thompson, 2009), the *James Webb Space Telescope* (*JWST*; Gardner et al., 2006, 2023), and the European Extremely Large Telescope (E-ELT; Gilmozzi and Spyromilio, 2007; Gullieuszik et al., 2016). Within the hierarchical structure formation paradigm, the first generation of stars preceded the first galaxies, with feedback from stellar processes playing a crucial role in shaping early galaxy formation (see Ceverino and Klypin, 2009; Bromm and Yoshida, 2011, and references therein). While DM haloes with masses of $\sim 10^6 M_\odot$ have been shown to be capable of hosting Pop. III stars, numerical simulations (e.g., Wise and Abel, 2007, 2008; Greif et al., 2008) suggest that more massive haloes ($\gtrsim 10^8 M_\odot$) were required to gravitationally confine and re-virialise gas that had been heated by stellar photoionisation and accelerated by SNe. In this section, we look at some insights from simulations and observations that underpin our current understanding of formation and characteristics of galaxies in the earliest epochs of the Universe.

1.2.1 Evolution of star formation histories and galaxy morphologies

While the first-generation Pop. III stars are believed to have formed in pre-galactic DM haloes, numerical simulations (e.g. Greif et al., 2010) and observations (e.g. Vanzella et al., 2023) indicate that the metal-poor Pop. II stars began forming within early galaxies. The fundamental process of star formation in these galaxies was similar to that in pre-galactic DM haloes (see Section 1.1.2): gas within the halo cooled sufficiently and collapsed into its dense central regions, where self-gravity began to dominate over the halo's gravitational potential. As in the local Universe, stellar feedback played a key role in regulating star formation in early galaxies; however, the exact mechanisms involved and their relative importance remain active areas of research. Numerical simulations suggest that Pop. III stars can ionise the surrounding IGM, drive

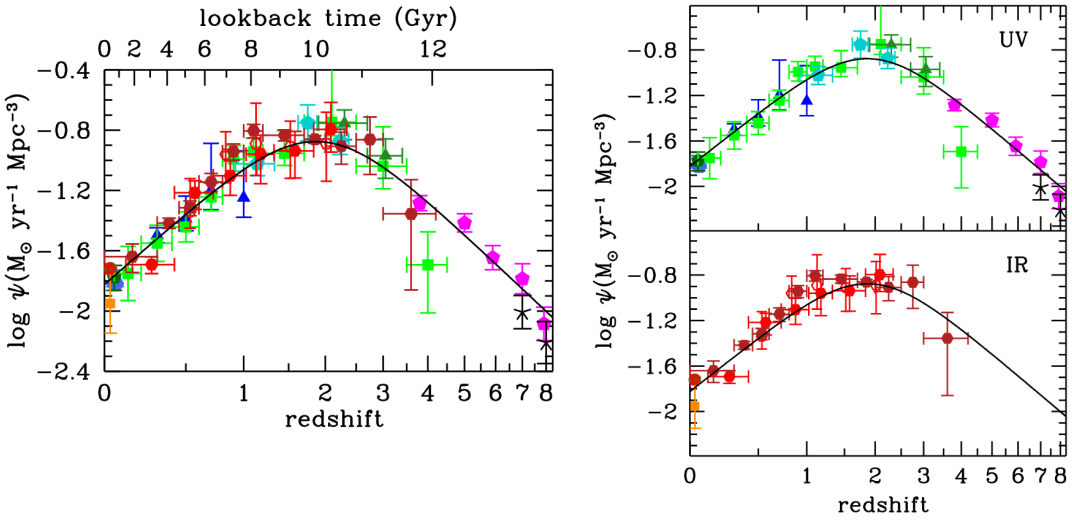

FIGURE 1.3: The cosmic star formation rate density (CSFRD) calculated using FUV (top-right panel), IR (bottom-right panel), and FUV+IR (left panel) rest-frame flux measurements. The fluxes are empirically converted to instantaneous star formation rate (SFR) valid for the Salpeter (1955) IMF. The CSFRD shows a peak at $z \approx 2$ (reproduced from Madau and Dickinson, 2014).

stellar winds, and trigger SNe, thereby injecting energy and momentum into the IGM. These feedback processes can heat and expel gas from low-mass haloes, thereby suppressing further star formation, while simultaneously contributing to the chemical enrichment of the IGM. We elaborate on stellar feedback in Section 1.3.1, but note here that such mechanisms are crucial for explaining the low star formation efficiencies observed at high redshifts. The efficiency of star formation also depends on the ability of the halo gas to cool and condense (Reed et al., 2005; Bromm and Yoshida, 2011). Under conditions of efficient cooling, this can lead to a runaway collapse, causing the gas cloud to fragment into small, highly dense cores that reach the critical pressure and density required to ignite nuclear fusion. Unlike pre-galactic haloes, which cool solely via Hydrogen transitions, the halo gas in early galaxies was enriched with heavier elements and dust produced by Pop. III SNe (e.g. Heger et al., 2002), and could therefore cool efficiently through additional processes (e.g., Carbon or Oxygen fine-structure line transitions and dust cooling; see Bromm et al., 2001; Bromm and Larson, 2004). The stellar IMF in early galaxies is believed to have been top-heavy, forming more massive stars relative to Milky Way (MW) -like galaxies in the local Universe (Marks et al., 2012; Guo et al., 2024; Cameron et al., 2024).

The cosmic star formation rate density (CSFRD; Madau, 1997; Madau and Dickinson, 2014) is a key metric that describes the evolution of the galaxy population across cosmic time. The CSFRD shows a broad peak around $z \approx 2-3$, often referred to as "cosmic noon", followed

by a steady decline toward the present day (Fig. 1.3). This turnover marks a transition in the dominant modes of star formation and morphology. Galaxies at $z \gtrsim 3$ are frequently observed to have clumpy, irregular, and turbulent morphologies, often lacking cold discs (e.g., Elmegreen et al., 2007; Guo et al., 2015). In contrast, galaxies in the local Universe typically display well-ordered, thin, rotationally-supported star-forming discs. These morphological differences are likewise reflected in the star formation histories (SFHs) of galaxies, which encode the build-up of stellar mass over their lifetimes (e.g., Wuyts et al., 2011; Snyder et al., 2015; Cano-Díaz et al., 2019; Peterken et al., 2021; Orr et al., 2021). In its simplest form, the SFH of a galaxy can be modelled as an exponentially declining function, following an initial period of constant or rising star formation. This formulation is motivated by the principle that star formation is regulated by the availability of cold gas. Under the assumption of a closed-box model with no inflows or outflows, the star formation rate (SFR) depends linearly on the gas density and declines exponentially as the gas reservoir is depleted (Schmidt, 1959; Kennicutt, 1998a,b; Noeske et al., 2007; Tinsley, 1980). This formulation of the SFH, referred to as the "exponentially declining" SFH, is parametrised as (see Carnall et al., 2019):

$$\mathrm{SFR}(t) \propto \begin{cases} \exp\left(-\frac{t-T_0}{\tau}\right) & t > T_0, \\ 0 & t < T_0. \end{cases} \tag{1.1}$$

Here, the SFR reaches a maximum at a time $t = T_0$ in the galaxy's lifetime and subsequently declines exponentially with a timescale parameter τ. The exponentially declining SFH and its variations have been shown to effectively describe the average SFH of star-forming galaxies (SFGs) in the low-redshift Universe, where SFHs are predominantly smooth and show little evidence of SFR variability (e.g., Noeske et al., 2007; Rodighiero et al., 2014; Shivaei et al., 2015). However, the majority of galaxies at $z > 4$ exhibit spectral features indicative of variability (or "stochasticity") in their SFHs, such as bursts of star formation and rapid quenching events occurring on timescales < 100 Myrs. For example, Endsley et al. (2021) reported high equivalent-width (EW) Hα and [OIII] + Hβ emission features in the *Spitzer*/IRAC spectra of high-redshift galaxies. These galaxies, referred to as extreme emission line galaxies (EELGs), represent low-mass systems with very young stellar populations and moderately low metallicities, undergoing short-lived, intense bursts of star formation (e.g., Maseda et al., 2013; Amorín et al., 2015). While EELGs are rare at low redshifts, they are believed to make up a significant fraction of SFGs at $z > 6$ (Boyett et al., 2022). Studies of low-mass dwarf galaxies (e.g., Domínguez et al., 2015; Emami et al., 2019; Asada et al., 2024) have shown that bursty SFHs

can also occur at low redshifts ($z < 2$). Preliminary observations from *JWST* have significantly advanced the study of star formation activity in the early Universe, providing the clearest evidence to date for bursty SFHs at high redshifts (e.g., Endsley et al., 2024; Looser et al., 2025; Stark et al., 2025). *JWST* observations have helped create a statistical sample of EELGs exhibiting rapidly rising SFRs (e.g., Boyett et al., 2022; Asada et al., 2023; Jones et al., 2023; Williams et al., 2023; Asada et al., 2024). High-resolution spectroscopic studies of both individual systems and large samples, such as those by Strait et al. (2023), Looser et al. (2024a), and Endsley et al. (2024), have shown strong signatures of ongoing rapid quenching, weak emission lines, and/or prominent Balmer breaks. These observations also indicate that galaxies in the early Universe underwent a radical transformation over cosmic time: at high redshifts, galaxies were typically low-mass systems exhibiting stochastic or bursty SFHs and irregular, turbulent morphologies, whereas as the Universe evolved, a significant fraction of these systems developed into more massive, dynamically settled galaxies characterised by well-ordered morphologies (including thin discs) and smoother, more continuous star formation activity.

Understanding the origin of bursty SFHs in early galaxies, and how some of these evolve into smooth SFHs, has historically been extremely challenging to address using observations alone, as it requires insight into interdependent physical processes operating at galactic and sub-galactic scales (e.g., feedback, turbulence, and galaxy-galaxy interactions) that have remained unresolved even by the most cutting-edge telescopes over the past decades. As a result, such studies have relied heavily on numerical modelling and simulations (see Naab and Ostriker, 2017, for a review). Of particular relevance are cosmological hydrodynamic zoom-in simulations, which explicitly model the physics of gravitationally bound clouds (GBCs) within the ISM, along with the associated stellar feedback processes that regulate star formation on sub-galactic scales (e.g., Rodighiero et al., 2011; Hopkins et al., 2014; Caputi et al., 2017; Ma et al., 2018; Faucher-Giguère, 2018; Garrison-Kimmel et al., 2018; Hopkins et al., 2023; Gurvich et al., 2023). Several scenarios have been proposed to explain the rapid bursts and quenching events, some of which are listed below:

1. Through analytical modelling (e.g. Ferrara and Tolstoy, 2000) and zoom-in simulations (e.g., Muratov et al., 2015; Sparre et al., 2017), it has been shown that one of the primary reasons for bursty star formation in low-mass galaxies is their shallow potential wells. These wells are unable to prevent the thermal and mechanical feedback from stellar populations from rapidly expelling gas, thereby quenching star formation. These studies have also demonstrated that through accretion of sufficient gas via interactions with

the galaxy's environment and neighbouring galaxies, star formation can be rekindled. As galaxies grow in mass and develop deeper gravitational potentials, stellar feedback becomes less effective at driving large-scale outflows, allowing for a more continuous regulation of star formation (e.g. Bassini et al., 2023).

2. The short dynamical timescales (< 20 Myrs) in the small, low-mass galaxies at $z > 6$ allow star formation to proceed rapidly and efficiently, leading to an overproduction of stars before SNe feedback can effectively regulate it. This is much more modest in the MW-mass galaxies in the low-redshift Universe, helping explain the prevalence of bursty star formation in the early Universe (see Orr et al., 2019; Faucher-Giguère, 2018; Furlanetto and Mirocha, 2022).

3. Works such as Martig et al. (2009) and Yu et al. (2023) indicate that morphological quenching (i.e., the transformation of a galactic disc into a spheroidal geometry through accretion, mergers, and/or instabilities) can rapidly shut down star formation in high-redshift sources. In turn, the spheroidal discs can fragment into clumps and reinitiate star formation if their densities become sufficiently high due to the infall of gas.

4. Semi-analytic models and N-body simulations show that gas accretion onto galaxies also plays an important role in driving bursty star formation. Gas accretion proceeds via two distinct modes: "hot-mode accretion", in which gas is shock-heated to the virial temperature of the DM halo during mergers or infall, and "cold-mode" accretion, where gas flows along cosmic filaments without ever being heated to virial temperatures (see Katz et al., 2003; Kereš et al., 2005; Dekel et al., 2009; Silk et al., 2014, and references therein). While hot-mode accretion is more prevalent in the present Universe, cold-mode accretion was the dominant mode of accretion in the high-redshift, low-mass haloes. Works such as Dekel et al. (2009), van de Voort et al. (2011), and Stern et al. (2021) suggest that cold-mode accretion led to efficient star formation, thus explaining the high incidence of starbursts in the early galaxies. Cold-mode accretion was also capable of forming spheroids and halting star formation, and subsequently fragmenting them into clumps and restarting star formation, as discussed earlier.

While these works have demonstrated that the cumulative effect of these processes results in bursty SFHs and could potentially lead to smoother SFHs, the relative importance of each individual mechanism, as well as the identification of additional missing physical processes, remains an open and active area of research.

1.2.2 Formation of the first black holes

Detections of high-z quasars have confirmed the existence of supermassive black holes (SMBHs) with masses in the range $\sim 10^8 - 10^9\ M_\odot$ as early as $z \sim 6-7$ (Fan et al., 2006b; Willott et al., 2007; Jiang et al., 2009; Mortlock et al., 2011; Bañados et al., 2014; Venemans et al., 2013, 2015; Wu et al., 2015). The formation of such massive objects within the first billion years after the Big Bang presents a major challenge to current models of black hole growth. It is now widely believed that the growth of black holes was hierarchical, wherein smaller, low-mass ($M_{\rm BH} \sim 100 - 600\ M_\odot$) "seed" black holes (BHs) first formed, and subsequently grew to a billion solar masses through accretion and mergers (see review by Volonteri, 2010; Latif and Ferrara, 2016; Inayoshi et al., 2020, and references therein). Through theoretical modelling and numerical simulations, several mechanisms have been proposed to explain the formation of seed BHs. One of the leading theories is that the core-collapse of Pop. III stars led to the formation of seed BHs at $z \approx 20-50$. These objects had typical masses of up to a few hundred solar masses and are referred to as stellar-mass BHs. They are thought to have grown primarily via gas accretion at near Eddington limits (Madau and Rees, 2001; Haiman and Loeb, 2001). However, simulations by Hosokawa et al. (2011) and Stacy et al. (2012) suggest that their growth may have been stunted by inefficient accretion in shallow potential wells and feedback from their host galaxies. Thus, for the stellar mass BHs to grow into SMBHs, multiple episodes of super-Eddington accretion are required (e.g., Madau et al., 2014; Volonteri et al., 2016). Another proposed scenario involves runaway collisions and core collapse in dense, compact stellar clusters, forming seed BHs with masses of the order of a few thousand solar masses (Begelman and Rees, 1978; Devecchi and Volonteri, 2009). Such BH seed models have an advantage over stellar mass BH models as they require less extreme growth histories to reach SMBH masses by $z \sim 6-7$. Lastly, it has also been suggested that direct collapse of massive metal-poor gas clouds in atomic cooling haloes can form intermediate mass black holes (IMBHs; Loeb and Rasio, 1994; Begelman et al., 2006; Lodato and Natarajan, 2006; Wise et al., 2019; Greene et al., 2020) with $M_{\rm BH} \sim 10^4 - 10^6\ M_\odot$. Distinguishing between these seeding pathways remains a major goal in high-redshift astrophysics. Advent deep surveys and high-resolution data from next-generation facilities such as the *JWST*, the upcoming *Nancy Grace Roman Space Telescope* (RST; Mosby et al., 2020), *Advanced Telescope for High Energy Astrophysics* (ATHENA; Barcons et al., 2012; Barret et al., 2020) and *Laser Interferometer Space Antenna* (*LISA*; Amaro-Seoane et al., 2017) missions is expected to place strong observational constraints on the formation channels of the

earliest black holes by probing the demographics, host galaxies, and environments of early AGN (Volonteri et al., 2021).

1.2.3 Further growth via dynamical evolution and interactions

In addition to the processes described above, galaxies also evolve through "secular" processes. These are slow processes (happening over timescales greater than the dynamical time) and are driven by intrinsic factors, such as disc heating by stellar scattering, bar-driven instabilities, and interactions among stars, gas, and spiral structures (see Kormendy and Kennicutt, 2004; Kormendy, 2013). Secular processes are believed to become dominant in the later stages of a galaxy's evolution, redistributing mass and angular momentum within the galaxy, and can lead to significant morphological transformations, including the formation of pseudo-bulges and the thickening of galactic discs (e.g. Sellwood, 2014). It is worth noting that galaxies and their haloes do not exist in isolation. Rather, they also accrete material from the intergalactic medium and undergo mergers with other systems, such as galaxies or clusters of galaxies (Lacey and Cole, 1993; Springel et al., 2005; De Lucia and Blaizot, 2007). Major mergers, i.e., the mergers between comparable-mass haloes, can lead to significant morphological changes, and potentially trigger star bursts and AGN activity. Minor mergers, in contrast, are less disruptive: satellite galaxies orbiting within DM haloes gradually lose stars, gas, and DM due to tidal stripping and spiral inward due to dynamical friction. If the host halo contains a hot gas component, satellites may also undergo ram-pressure stripping, where gas is removed due to the drag from motion through the intra-halo medium (Boselli and Gavazzi, 2006; Mayer et al., 2006).

1.3 Feedback processes in galaxies

Cooling of baryons within DM haloes is predicted to be highly efficient in the ΛCDM hierarchical structure formation paradigm (Mo et al., 2010), leading to the expectation that the majority of baryonic matter should condense into stars. However, observational evidence indicates that only a small fraction of baryons (≈10 per cent) are found in the form of cold gas or stars (see Somerville and Davé, 2015, and references therein). This discrepancy between theoretical expectations and observations highlights the need for additional physical processes in galaxy formation models that regulate gas temperature and baryonic content, thereby suppressing star formation.

A key observational constraint on models of galaxy formation is provided by the luminosity function (LF), $\Phi(L)$, and the stellar mass function (SMF), $\Phi(M)$, which quantify the number density of galaxies as a function of luminosity and stellar mass, respectively, at a given epoch. In the absence of baryonic physics, the hierarchical assembly of DM haloes in the standard ΛCDM cosmology predicts that both the LF and SMF should follow steep, nearly power-law distributions. These distributions are commonly parametrised by the Schechter function (Press and Schechter, 1974; Schechter, 1976), which provides a good empirical fit to the observed galaxy population across a wide range of masses and luminosities. The functional form of the LF is given by:

$$\Phi(L)\mathrm{d}L = \Phi^{\star}\left(\frac{L}{L^{\star}}\right)^{\alpha}\exp\left(-\frac{L}{L^{\star}}\right)\mathrm{d}\left(\frac{L}{L^{\star}}\right) \tag{1.2}$$

This function combines a power law slope (α) at the faint end ($L \ll L^{\star}$) and has an exponential cutoff at the bright end ($L \gg L^{\star}$), where $L^{\star}$ is the characteristic luminosity and $\Phi^{\star}$ is the normalisation density at $L^{\star}$. The SMF is also parametrised similarly (see, e.g., Cimatti et al., 2020). However, the observed LFs and SMFs deviate from the model predictions at both the low- and high-mass ends (see Fig. 1.4). These discrepancies imply the presence of mass-dependent feedback mechanisms that preferentially suppress star formation in both low-mass and high-mass systems. It is now widely accepted that stellar feedback and AGN-driven processes are the primary reasons behind this discrepancy. We discuss both in this section.

1.3.1 Stellar feedback

At the low-mass end, the observed flattening of the SMF relative to the halo mass function suggests that star formation is inefficient in low-mass galaxies, which is attributed to stellar feedback processes (White and Rees, 1978; Benson et al., 2003). Stellar feedback processes inject mass, momentum, and energy into the ISM, thereby preventing gas from cooling or ejecting it altogether, and consequently suppressing star formation. The most common forms of feedback are photoionisation flows and stellar winds, both driven by highly energetic photons from young, massive stars (e.g. O- and OB-type stars; see Lamers and Cassinelli, 1999; Osterbrock and Ferland, 2006; Hopkins et al., 2012; Walch et al., 2012; Kim et al., 2013; Rosen et al., 2014). These processes deliver both radiative and mechanical feedback to the surrounding gas (Luisi et al., 2021). Additionally, SNe driven shocks and winds, stochastic heating and jets produced by the accretion of gas onto star forming giant molecular clouds (GMCs), and the cumulative radiation pressure from all of the above processes further contribute to the suppression

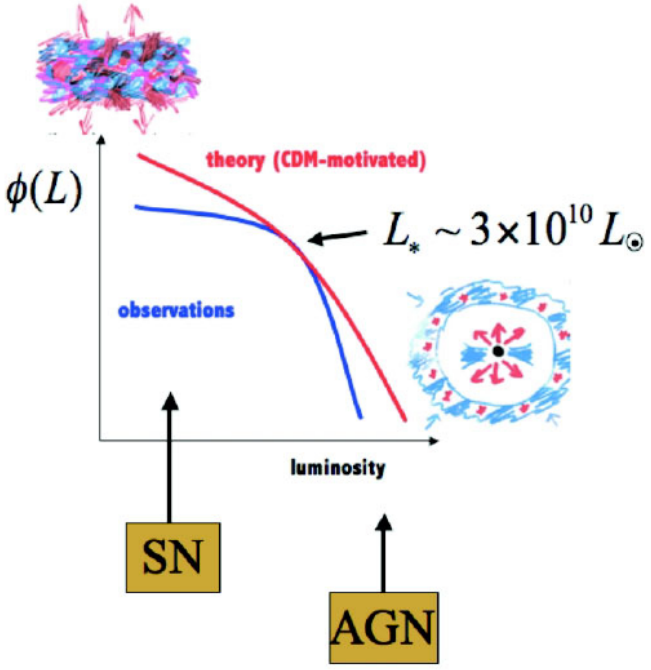

FIGURE 1.4: The expected (red) and the observed (blue) galaxy luminosity function, highlighting the disagreements at the low- and high- mass ends, potentially due to stellar and AGN feedback, respectively (adapted from Silk, 2011).

of star formation (see Dale, 2015, for a review). This picture is supported by both semi-analytic models and hydrodynamical simulations, which find that including strong stellar feedback is essential to reproduce the shape of the LF and SMF at low masses (see Hopkins et al., 2012, 2014; Somerville and Davé, 2015; Hayward and Hopkins, 2017, and references therein).

1.3.2 AGN feedback

At the high-mass end of the galaxy SMF, the sharp decline in the number density of bright and massive galaxies cannot be explained by stellar feedback alone. The deep gravitational potential wells of massive galaxies are usually sufficient to retain the gas injected with radiative and mechanical feedback from stellar processes. Furthermore, radiative cooling times in these systems are much shorter than their ages, especially in group and cluster environments, which in the absence of additional feedback processes would lead to rapid gas condensation, thus fuelling continued star formation (McNamara and Nulsen, 2007, 2012; Morganti, 2017). Consequently, galaxy formation models that include only stellar feedback typically overpredict the masses and SFRs of the most massive galaxies (e.g., Bower et al., 2006; Croton et al., 2006). To resolve this discrepancy, an additional feedback mechanism is required. ISM gas is heated and/or expelled by the injection of energy and momentum from accretion onto SMBHs at galactic centres

– a process known as AGN feedback – which thereby quenches star formation and suppresses further galaxy growth (e.g., Fabian, 2012; Heckman and Best, 2014). AGN feedback is now a standard ingredient in galaxy formation models and has been shown to be critical for reproducing the observed turnover in the SMF at high stellar masses, as well as the observed colours, morphologies, and quenching of massive galaxies (Somerville and Davé, 2015).

Feedback from AGN occurs in two principal modes – radiatively efficient (traditionally known as radiative or quasar mode) and radiatively inefficient (also called radio or jet mode) – depending on the efficiency of mass accretion onto the SMBH relative to the Eddington limit (Fabian, 2012; Heckman and Best, 2014). Assuming spherical symmetry, the force due to radiation pressure ($F_{\rm rad}$) exerted on a fully ionised Hydrogen plasma at a distance r from a black hole of mass $M_{\rm BH}$ and total luminosity L is given by:

$$F_{\rm rad} = \frac{L\sigma_{\rm T}}{4\pi r^2 c}, \tag{1.3}$$

where $\sigma_{\rm T}$ is the Thomson scattering cross-section and c is the speed of light. The gravitational force on the plasma ($F_{\rm grav}$) is given by:

$$F_{\rm grav} = \frac{GM_{\rm BH}m_{\rm p}}{r^2}, \tag{1.4}$$

where G is the gravitational constant and $m_{\rm p}$ is the mass of a proton. Accretion can proceed as long as $F_{\rm grav} > F_{\rm rad}$, with the limiting condition for accretion being $F_{\rm grav} = F_{\rm rad}$. The maximum luminosity at which a black hole can be powered by steady-state accretion over a long period of time, known as the Eddington luminosity ($L_{\rm Edd}$; Eddington, 1921; Rybicki and Lightman, 1979; Netzer, 2015), is given by:

$$L_{\rm Edd} = \frac{4\pi c G M_{\rm BH} m_{\rm p}}{\sigma_{\rm T}} \simeq 1.26\times10^{38}\left(\frac{M_{\rm BH}}{M_\odot}\right) \text{ergs s}^{-1}, \tag{1.5}$$

Given the radiative efficiency of the AGN $\epsilon_{\rm rad}$, the Eddington mass accretion rate $\dot{M}_{\rm Edd}$ is defined as:

$$\dot{M}_{\rm acc} = \frac{L_{\rm Edd}}{\epsilon_{\rm rad} c^2}\,. \tag{1.6}$$

For a black hole with luminosity $L_{\rm BH}$, the Eddington ratio $f_{\rm Edd}$ is defined as:

$$f_{\rm Edd} = \frac{L_{\rm BH}}{L_{\rm Edd}} = \frac{\dot{M}_{\rm acc}}{\dot{M}_{\rm Edd}}\,. \tag{1.7}$$

If accretion is spherically symmetric, then the $\dot{M}_{\rm Edd}$ represents the maximum accretion rate up to which hydrostatic equilibrium can be sustained. For the vast majority of cases, the observed AGN luminosities are sub-Eddington ($L_{\rm BH} < L_{\rm Edd}$; e.g. King and Pounds, 2015). However, super-Eddington luminosities and mass accretion rates are possible when accretion is not spherically symmetric, e.g., in the presence of a geometrically thick accretion disc (e.g., Abramowicz et al., 1980; McKinney et al., 2014; Sadowski et al., 2014; Jin et al., 2017; Jiang et al., 2019).

1.3.2.1 Radiatively-efficient AGN feedback

This mode of feedback occurs when there is efficient accretion of mass onto the SMBH ($10^{-2} < f_{\rm Edd} < 1$). In this regime, the SMBH is surrounded by a geometrically thin, optically thick accretion disc (Fig. 1.5, left-hand panel). The accretion disc is enveloped by a hot corona. The nuclear region is embedded within multiple gaseous components: dense gas clouds located on scales of light-days to light-years (referred to as the broad-line region, or BLR), lower-density circumnuclear gas on scales of $\sim 100 - 1000$ pc (known as the narrow-line region, or NLR), and a dusty, toroidal structure composed of molecular gas (Antonucci, 1993; Urry and Padovani, 1995; Frank et al., 2002; Heckman and Best, 2014; Netzer, 2015). The potential energy of the infalling gas is efficiently converted into electromagnetic radiation, making these sources extremely luminous. The thermal emission from the hot accretion disc spans the ultraviolet (UV) to visible wavelengths. The photons from the accretion disc undergo inverse-Compton scattering in the hot corona and are upscattered to X-ray wavelengths (Haardt and Maraschi, 1991; Tombesi et al., 2013; Fabian et al., 2015). The dusty molecular gas absorbs a fraction of the radiation from the accretion disc and soft X-ray from the corona and re-emits it as thermal radiation in the MIR wavelengths (Pier and Krolik, 1992, 1993; Barvainis, 1987; Mor et al., 2009). Photoionisation of the BLR gas by the radiation from the disc and corona leads to UV, optical, and near-infrared (NIR) permitted emission lines (velocity dispersion $\sim 10^3$ km s^{-1}). In contrast, photoionisation of the NLR gas produces UV, optical, and IR forbidden and permitted emission-lines (velocity dispersion $\sim 10^2$ km s^{-1}). In these systems, the dominant mode of feedback is radiative feedback due to the high luminosities, e.g., photoionisation heating, and heating via winds driven by accretion disc photons (known as AGN winds). However, mechanical feedback, i.e., displacement of gas by outflows, is also important. Cold, star-forming gas is heated and often expelled from the dense central regions of the galaxy, suppressing star formation (Fabian, 2012; Heckman and Best, 2014; King and Pounds, 2015). This process simultaneously disrupts the inflow of gas onto the SMBH, making this phase of AGN activity inherently self-regulating.

1.3.2.2 Radiatively-inefficient mode of AGN feedback

Jet or radio mode feedback occurs in systems with inefficient accretion, typically characterised by Eddington ratios $f_{\rm Edd} \lesssim 10^{-2}$. As shown in the right-hand panel of Fig. 1.5, the accretion discs are geometrically thick, with inflow times shorter than cooling times, and are known as advection-dominated or radiatively inefficient accretion flows (ADAFs/RIAFs; see Narayan and Yi, 1995b,a; Quataert, 2001; Narayan, 2005; Ho, 2008). These sources produce powerful, often collimated jets composed of relativistic plasma, which emit radio synchrotron radiation (see Morganti, 2017; Hardcastle and Croston, 2020, and references therein). The precise mechanism responsible for generating these jets remains an open question, although magnetic fields are widely believed to play a crucial role in their formation and collimation (Blandford and Znajek, 1977; Blandford and Payne, 1982; Hughes, 1991; Meier, 2001). As these jets propagate, they interact mechanically with the surrounding medium, as evidenced by cavities in the diffuse X-ray emission surrounding massive elliptical galaxies that coincide with radio lobes (McNamara and Nulsen, 2007, 2012). The jets displace molecular gas as they pass through it and inject mechanical energy that heats the medium. This mechanical feedback is widely regarded as the primary mechanism preventing runaway cooling flows in galaxy cluster-scale structures, thereby regulating and suppressing further star formation (Fabian, 2012; Voit et al., 2015; Cimatti et al., 2020).

1.4 Probing the deep fields in the sky with radio surveys

1.4.1 Overview of the radio continuum emission in galaxies

Since the serendipitous discovery of radio emission from the MW by Jansky (1933) and Reber (1940) almost a century ago, radio astronomy has evolved into a fundamental pillar of astrophysics, transitioning from a means to study the rarest, most-powerful sources in the Universe (e.g., giant radio galaxies and quasars; see Kellermann, 1980) to becoming one of the primary probes of SFGs up to very high redshifts (see reviews by Casey et al., 2009; Padovani, 2016). Radio emission in galaxies is a combination of (i) non-thermal synchrotron radiation, emitted by relativistic particles (predominantly cosmic-ray electrons) that are subject to acceleration perpendicular to their velocity, due to supernova remnants of short-lived massive ($M > 8\ M_{\odot}$) stars, and/or due to jets produced by accretion onto SMBHs; and (ii) the thermal free-free emission,

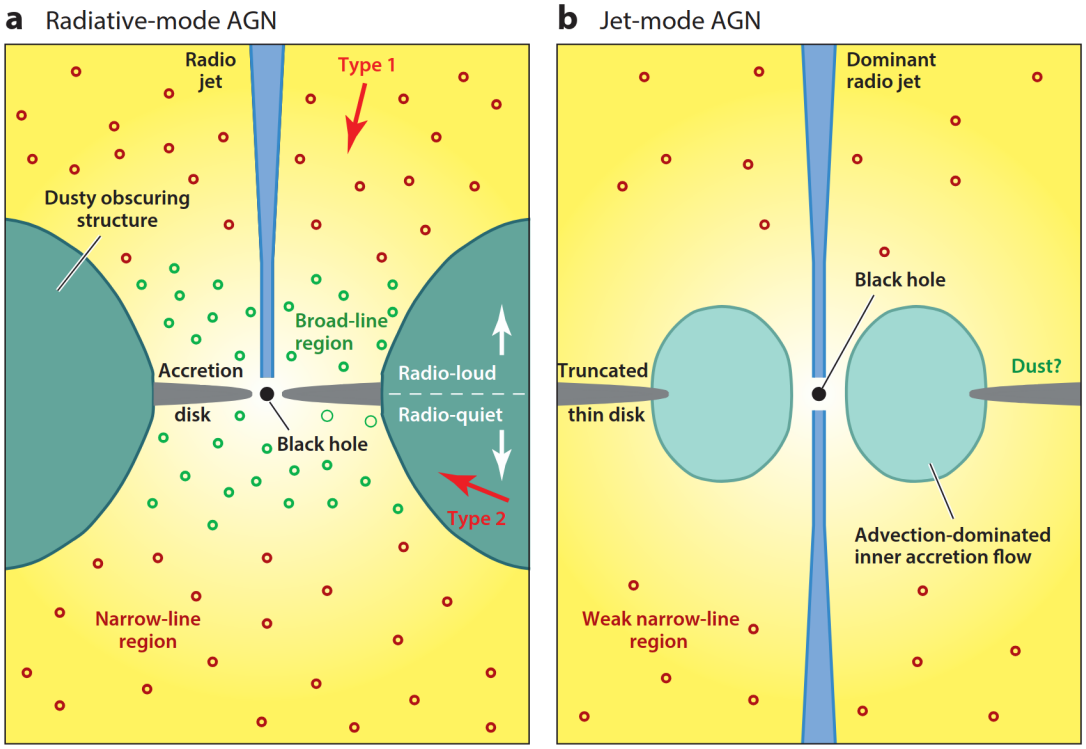

FIGURE 1.5: Illustration of the central engines in radiative-mode (left) and jet-mode (right) AGN. Radiative-mode AGN feature a geometrically-thin, optically-thick accretion disk producing luminous UV radiation that powers broad- and narrow-line regions, often obscured from some viewing angles by a dusty torus. In contrast, jet-mode AGN host a geometrically-thick, radiatively-inefficient accretion flow, with most energy released via large-scale radio jets. A truncated thin disk may persist at larger radii, contributing weakly to low-ionization narrow-line emission (reproduced from Heckman and Best, 2014).

produced by scattering of free electrons by ionised Hydrogen (HII) regions in the ISM (refer to Condon and Ransom, 2016, for detailed descriptions of both). As noted by Condon and Ransom (2016), the contribution of free-free emission to the total radio emission of galaxies decreases with frequency: it dominates the continuum at $\nu \sim 30-300$ GHz, accounts for about 10 per cent of the continuum at $\nu \sim 1$ GHz, and is practically negligible at $<$ GHz frequencies.

1.4.2 Radio sky surveys

The radio luminosity function, defined as the space density of sources as a function of radio luminosity, spans several orders of magnitude (e.g. Condon, 1996). This, combined with the fact that radio observations are unaffected by dust, lays the foundation for observing different classes of extragalactic sources across a wide redshift range (see Jackson, 2004, for a review). Since the early decades of radio astronomy, radio continuum surveys have been highly impactful in cataloguing distant extragalactic sources, with minimal confusion from nearby stars, despite their

low angular resolution and modest sensitivities (e.g., the Third Cambridge, or 3C catalogue, Edge et al., 1959, and the revised 3CR catalogue Bennett, 1962). A summary of the historical radio sky surveys can be found in Condon (1999). In the last couple of decades, advancements in aperture synthesis techniques, low-noise receivers, and high-speed data transmission (see Garrett, 2012, for a review) have enabled surveys like the Karl G. Jansky Very Large Array (VLA; Perley et al., 2011) Sky Survey (VLASS; Lacy et al., 2016) to match optical resolutions with remarkable survey speeds. The construction of the Square Kilometre Array (SKA; Rawlings et al., 2004; Dewdney et al., 2009) has ushered in a new era of technological capabilities, which has benefited the design of current and upcoming surveys. These developments mark a transformative phase in radio astronomy, laying the groundwork for comprehensive studies of galaxy evolution, AGN activity, and the cosmic energy budget across cosmic time.

GHz and sub-GHz radio frequencies are especially valuable, as they offer a reliable means to study sources at the faint end (< 1 mJy) of the radio luminosity function (commonly referred to as the "faint radio source population", e.g., Bonzini et al., 2013; Padovani et al., 2015). These frequencies are highly sensitive to cosmic-ray electrons originating in aged plasma, making them a powerful tool for studying "dying" radio galaxies and fossil radio plasma (e.g. Murgia et al., 2011). Being largely unaffected by thermal free-free emission, they provide a clean window to observe synchrotron emission from galaxies while simultaneously probing star formation and BH accretion processes. Additionally, they play an integral role in observing the redshifted 21 cm EoR signal and in characterising the foreground noise (such as diffuse Galactic emission) that has long plagued EoR studies (e.g., Jelić et al., 2014; Koopmans, 2017). These science cases have driven the design and execution of a new generation of radio sky surveys, such as the LOw-Frequency ARray (LOFAR; van Haarlem et al., 2013) Two Metre Sky Survey (LoTSS; Shimwell et al., 2017, 2019, 2022), MeerKAT[2] International Gigahertz Tiered Extragalactic Explorations Survey (MIGHTEE; Jarvis et al., 2016; Heywood et al., 2022), the VLA Cosmic Evolution Survey (VLA-COSMOS; Scoville et al., 2007) 3 GHz Large Project (Smolčić et al., 2017b), and the Australian Square Kilometre Array Pathfinder (ASKAP; Johnston et al., 2007) Evolutionary Map of the Universe (EMU; Norris et al., 2011, 2021; Gürkan et al., 2022).

Among the aforementioned surveys, LoTSS is of particular relevance to this thesis. LOFAR is a low-frequency radio interferometer, which consists of 51 individual stations (with around

[2] http://www.ska.ac.za/meerkat

FIGURE 1.6: The core of the LOFAR telescope, known as the superterp, in the Netherlands (Image credits: LOFAR/ASTRON, adapted from https://www.jb.man.ac.uk/news/2011/LOFAR-pulsars/).

8,000 antennas) distributed across Europe[3]. The inner core of LOFAR, known as the "superterp" (Fig. 1.6), is situated in the Netherlands. LOFAR stations are analogous to the dish antennas used in interferometers, such as the VLA. However, unlike a physical and steerable dish, the LOFAR stations consist of small, stationary, omni-directional dipole antennas. In each station, the signals received by the antennas are combined using analog and digital beamforming techniques, programmatically achieving functions such as tracking and pointing (van Haarlem et al., 2013; Thompson et al., 2017). LOFAR antennas are of two types: the High Band Antennas (HBA), which can operate at frequencies of 110−240 MHz, and Low Band Antennas (LBA), which can operate at 10−90 MHz. LOFAR by design is particularly well-suited for large-area sky surveys, such as LoTSS, which is being conducted using the HBA at 120−168 MHz. LoTSS is part of the LOFAR Surveys Key Science Projects (LSKSP; Röttgering et al., 2011), and is complemented by the very wide area 42−66 MHz LOFAR Low Band Antenna Sky Survey (LoLSS; de Gasperin et al., 2021). LoTSS consists of two survey modes. The first is the wide-area survey (LoTSS-wide), which aims to image the complete Northern sky at a resolution

[3] https://www.lofar.inaf.it/index.php/en/

of 6 arcseconds (equivalent to that obtained using the Dutch LOFAR stations) and a sensitivity of ~ 100 μJy beam^{-1} (Shimwell et al., 2017, 2022). As noted in the second data release (DR2; Shimwell et al., 2022), LoTSS-wide has completed imaging of 5,634 square degrees (~ 27 per cent) of the Northern sky, cataloguing 4,396,228 radio sources, which is the largest catalogue of radio sources released to date. The second, the LoTSS deep fields survey (LoTSS-deep; Tasse et al., 2021; Sabater et al., 2021; Kondapally et al., 2021; Duncan et al., 2021; Best et al., 2023), is taking repeated 8 hour observations of "deep fields", which are small patches of the sky with extensive wide-field UV, optical, and infrared (IR) coverage. Currently four deep fields are being surveyed: European Large Area ISO Survey Northern Field 1 (ELAIS-N1; Oliver et al., 2000), the Boötes field (Jannuzi and Dey, 1999), the Lockman Hole (Lockman et al., 1986), and the Euclid Deep Field North (EDFN; Euclid Collaboration et al., 2022; Bondi et al., 2024). LoTSS-deep aims to reach noise levels of 10–15 μJy beam^{-1} over a combined sky area of at least 30 deg^2. This sensitivity allows the detection of MW-like galaxies at $z > 1$, SFGs with high SFRs ($\gtrsim 100\,M_\odot$ yr^{-1}) at $z > 5$ (e.g. Smith et al., 2016), and radio-quiet quasars out to $z \sim 6$ (Gloudemans et al., 2021). LoTSS-deep is expected to detect over 100,000 AGN and SFGs, and allow for the detailed studies of their key properties such as luminosity, redshift, stellar mass and environment (Best et al., 2023).

1.4.3 The faint radio source population

The earliest evidence for the presence of a faint radio source population emerged from the observed flattening of the Euclidean-normalised 1.4 and 5 GHz radio luminosity functions (RLFs) at sub-mJy flux densities (see Condon and Mitchell, 1984; Windhorst et al., 1984, 1985, and review by Padovani, 2016). These results were in tension with the view that the radio sky was predominantly composed of luminous radio galaxies and radio quasars. The observed flattening was attributed to a population of "blue" radio galaxies, which became increasingly important at $1 < S_{1.4\,\mathrm{GHz}} < 10$ mJy, and often exhibited irregular morphologies indicative of galaxy interactions or mergers (Windhorst et al., 1985). However, determining the precise nature of this population remained elusive for several decades, primarily due to the limited angular resolution and sensitivity of early radio surveys, and the inherent difficulty in obtaining redshifts for such optically faint sources using traditional optical and NIR spectroscopy.

1.4.3.1 Classification of the faint radio source population

Over the years, a number of different approaches have been adopted to classify the faint radio source population, each aiming to disentangle the diverse physical processes contributing to their radio emission. Early radio surveys, such as the VLA Faint Images of the Radio Sky at Twenty-cm (FIRST; Becker et al., 1994; Helfand et al., 2015) and the NRAO VLA Sky Survey (NVSS; Condon et al., 1998), classified sources based on their large-scale radio morphology and spectral properties. Classical double-lobed or core-jet morphologies indicated radio-loud AGN (Fanaroff and Riley, 1974), while compact or diffuse emission was seen as more typical of SFGs or radio-quiet AGN. The radio spectral index (α, where $S_\nu \propto \nu^\alpha$) helped distinguish between flat-spectrum cores (often AGN-dominated) and steep-spectrum lobes or star-forming regions (e.g. Muxlow et al., 2005). Thresholds in radio luminosity, such as $L_{1.4\ \mathrm{GHz}} > 10^{24}$ W Hz^{-1}, have also been used to distinguish between radio-loud and radio-quiet populations (Tadhunter, 2016). With the advent of deep optical spectroscopic surveys, emission-line diagnostics such as the Baldwin-Phillips-Terlevich (BPT; Baldwin et al., 1981) diagram have become invaluable for distinguishing radiative-mode AGN from SFGs. Several studies, such as Mauch and Sadler (2007), Best and Heckman (2012), Sabater et al. (2019), and Drake et al. (2024), have used large spectroscopic samples to classify radio sources in the local Universe. Radio-loud AGN were found predominantly in red, early-type hosts, whereas radio sources in blue, late-type galaxies were more likely to be star-formation-driven. The launch of *Spitzer* helped AGN identification via mid-IR colour-colour diagrams. AGN exhibit redder IRAC colours due to hot dust emission from the torus, allowing classification using templates such as the "Donley wedge" (Lacy et al., 2004; Stern et al., 2005; Donley et al., 2012). This method is especially powerful for detecting obscured AGN that may not be apparent in optical or X-ray data. Deep X-ray observations, such as those from the Chandra X-ray observatory (*Chandra*; Weisskopf et al., 2000) and the X-ray multi-mirror mission (*XMM-Newton*; Jansen et al., 2001), have revealed populations of AGN with minimal radio emission. Sources with $L_{\mathrm{Xray}} \gtrsim 10^{42}$ erg s^{-1} are typically classified as AGN. X-ray data therefore identify radiatively efficient, radio-quiet AGN not captured by radio morphology or MIR diagnostics (Szokoly et al., 2004; Alexander et al., 2005; Hickox et al., 2009). The joint availability of radio and FIR observations has facilitated the separation of AGN from SFGs through the "far-infrared radio correlation" (FIRC) observed in SFGs (e.g., van der Kruit, 1971; de Jong et al., 1985; Helou et al., 1985; Yun et al., 2001; Jarvis et al., 2010; Bourne et al., 2011; Smith et al., 2014; Magnelli et al., 2015; Delhaize et al., 2017; Read et al., 2018; Molnár

et al., 2021; Delvecchio et al., 2021; McCheyne et al., 2022), wherein both radio and FIR emission can be traced back to stellar origins. Radio AGN can therefore be identified as sources that deviate significantly from this otherwise tight correlation. A complementary approach is available when direct estimates of SFRs exist alongside radio measurements, for example using the linear relationship between 150 MHz radio luminosity and SFRs (the so-called "SFR–$L_{150\ \mathrm{MHz}}$ relation"; Brown et al., 2017; Calistro Rivera et al., 2017; Gürkan et al., 2018; Read et al., 2018; Wang et al., 2019; Smith et al., 2021; Heesen et al., 2022). In this context, radio AGN are identified as sources whose radio luminosity significantly exceeds what is expected from star formation alone (e.g., Hardcastle et al., 2016; Williams et al., 2018; Hardcastle et al., 2019; Smolčić et al., 2017a; Calistro Rivera et al., 2017; Best et al., 2023; Das et al., 2024).

1.4.4 Massively multiplexed spectroscopic surveys

Large optical spectroscopic surveys are fundamental to the study of galaxy populations. High signal-to-noise ratio (SNR) optical spectra enable detailed emission-line diagnostics, offering crucial insights into stellar populations, gas-phase conditions, galaxy kinematics, and nuclear activity (e.g., Erb et al., 2003; Brinchmann et al., 2004; Iwata et al., 2005; Mármol-Queraltó et al., 2011; Best and Heckman, 2012; Heckman and Best, 2014; Belli et al., 2015; Wu et al., 2018; Drake et al., 2024). These surveys are particularly valuable for studying the nature of sources detected in radio continuum surveys, as, in addition to providing several diagnostic approaches (e.g., Mauch and Sadler, 2007; Buttiglione et al., 2009; Best and Heckman, 2012; Heckman and Best, 2014; Sabater et al., 2019; Drake et al., 2024), spectroscopic surveys provide accurate redshift measurements for radio source populations with unmatched reliability (see Best et al., 1999; Brookes et al., 2008; Duncan et al., 2021, and references therein). Among these, "massively-multiplexed spectroscopic surveys" (MMSS) stand out for their ability to obtain thousands of spectra simultaneously in a single exposure, using multi-fiber or integral field spectrographs over wide fields of view. This enables the efficient acquisition of large, statistically robust samples across cosmologically significant volumes. The Sloan Digital Sky Survey (SDSS; York et al., 2000) and the Dark Energy Spectroscopic Instrument (DESI; DESI Collaboration et al., 2016a,b) are two of the most influential examples, having revolutionised our understanding of galaxy evolution and large-scale structure by collecting millions of high-quality spectra across vast areas of the sky. SDSS uses two multi-object spectrographs mounted on the 2.5 m wide-angle optical telescope at Apache Point Observatory in New Mexico, USA, consisting of a total of 1,000 fibers covering the wavelength range $3,600 - 10,400$ Å at a spectral

resolution of $\lambda/\Delta\lambda \approx 2,000$. DESI, on the other hand, is mounted on the 4 m Mayall Telescope at Kitt Peak National Observatory in Tucson, Arizona, and is equipped with 10 identical spectrographs, each with 500 fibres. DESI covers $3,600 < \lambda < 9,800$ Å with spectral resolutions ranging from $\lambda/\Delta\lambda \approx 2,000$ to $5,000$. DESI aims to obtain spectroscopic observations of 40 million extragalactic sources (DESI Collaboration et al., 2024). However, both these surveys have limited completeness for radio-selected samples. Of the 4.2 million radio-detected sources in the second data release of LoTSS (LoTSS DR2; Hardcastle et al., 2023), ~7.1 per cent have spectra from SDSS and ~9.5 per cent[4] from the first data release of DESI (DESI DR1; DESI Collaboration et al., 2016a, 2025), with ~2.4 per cent of the sources observed in both programmes.

Over the past decade, spectroscopic surveys have increasingly been designed to operate in synergy with radio continuum surveys. One of the most prominent examples of this is the WEAVE-LOFAR survey (Smith et al., 2016), that has been designed to provide targeted coverage of radio sources in the LoTSS survey. The WEAVE-LOFAR survey is being conducted using the William Herschel Telescope Enhanced Area Velocity Explorer (WEAVE; Dalton et al., 2012; Dalton, 2016; Jin et al., 2024), a state-of-the-art spectroscopic instrument on the 4-m William Herschel Telescope (WHT) in La Palma. WEAVE's multi-object spectrograph (MOS) includes 960 fibers with 1.3" diameter, offering full coverage across $3,660 < \lambda < 9,590$ Å in its "low resolution" mode ($\lambda/\Delta\lambda \sim 5,000$), and in three wavelength windows between $4,525 < \lambda < 6,431$ Å in its "high-resolution" mode ($\lambda/\Delta\lambda \sim 20,000$). WEAVE-LOFAR is expected to obtain low resolution spectra of over one million radio detected sources in LoTSS. It has been designed to operate in a three-tier "wedding cake" strategy: deep ($S_{150\ \mathrm{MHz}} > 100\ \mu$Jy), mid ($S_{150\ \mathrm{MHz}} > 1$ mJy), and wide ($S_{150\ \mathrm{MHz}} > 10$ mJy); thus providing spectroscopic data for large statistical samples of both radio-bright and radio-faint sources (Fig. 1.7). Additionally, WEAVE includes deployable mini-IFUs and a large IFU (LIFU) for spatially resolved spectroscopy of nearby radio sources under less favourable observing conditions.

In the Southern hemisphere, the Wide Area VISTA Extragalactic Survey (WAVES; Driver et al., 2016, 2019) will be conducted with the 4-metre Multi-Object Spectroscopic Telescope (4MOST) instrument (de Jong et al., 2012, 2019) on the VISTA telescope at ESO's Paranal Observatory. 4MOST is also a massively-multiplexed facility, simultaneously operating in a low resolution

[4]We match the RA and DEC coordinates of the sources in the DESI DR1 primary redshift catalogue (https://data.desi.lbl.gov/doc/organization/) with those from Hardcastle et al. (2023)'s catalogue using a nearest-neighbour algorithm with a maximum 1.5 arcsec separation, finding ~398,000 common sources.

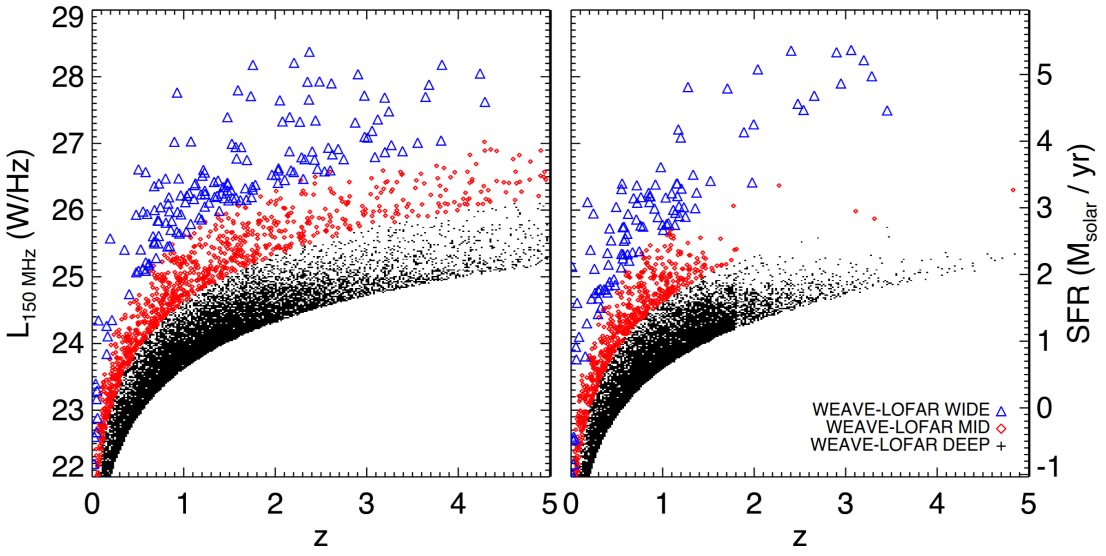

FIGURE 1.7: The redshift-luminosity plane, as sampled by the three tiers of the WEAVE-LOFAR survey. Blue triangles, red diamonds, and black points represent the deep ($S_{150\ MHz} > 100\ \mu$Jy), mid ($S_{150\ MHz} > 1$ mJy), and wide ($S_{150\ MHz} > 10$ mJy) tiers, respectively. While the left-hand panel shows all the targets, the right-hand panel only shows those sources for which successful redshift measurements are expected based on simulations (obtained from Smith et al., 2016).

spectroscopy mode (LRS; 1,624 fibers, $3,700 < \lambda < 9,500$ Å, $\lambda/\Delta\lambda \sim 6,500$) and a high resolution spectroscopy mode (HRS; 812 fibers, $3,926 < \lambda < 6,790$ Å, $\lambda/\Delta\lambda \sim 20,000$). WAVES aims to obtain spectra for ∼1.6 million galaxies to $r < 22$, extending four magnitudes deeper than SDSS, albeit over smaller areas (∼70 deg^2 for WAVES-DEEP and up to 1200 deg^2 for WAVES-WIDE). An extension to WAVES, the Optical, Radio Continuum and HI Deep Spectroscopic Survey (ORCHIDSS; Duncan et al., 2023), is designed to provide spectroscopy for radio and HI-selected sources from deep MeerKAT surveys. Over the coming decades, several next-generation multi-object spectrographs will further expand the reach of massively multiplexed spectroscopy. These include the Prime Focus Instrument (PFS; Tamura, 2016) on the 8.2 m Subaru telescope ($\sim 2,400$ fibers, $0.38-1.26\ \mu$m, $\lambda/\Delta\lambda \sim 2,300-4,300$), the Multi-Object Optical and Near-infrared Spectrograph (MOONS; Cirasuolo and MOONS Consortium, 2016) on ESO's 8.2 m Very Large Telescope (VLT) with 1,000 fibers, $0.645-1.8\ \mu$m, $\lambda/\Delta\lambda \sim 4,000-6,000$ (low-resolution mode) and $\lambda/\Delta\lambda > 9,000$ (high-resolution mode), and the Wide-field Spectroscopic Telescope (WST; Bacon et al., 2024; Mainieri et al., 2024), which will be a 12.4 m telescope with a MOS, consisting of $\sim 20,000$ low-resolution and $\sim 2,000$ high-resolution fibers across $3,700-9,700$ Å. These instruments will offer a transformative increase in survey speed, depth, and spectral resolution, paving the way for detailed, statistical studies of galaxy populations at all redshifts.

1.5 SED modelling

A galaxy's SED is the sum of the emission arising from the different physical processes within the galaxy, and therefore encodes information about its stellar population (e.g., stellar mass, IMF, and SFH), dust content, and potential AGN activity (see Fig. 1.8). The most common technique used to recover this information is SED fitting, in which the observed SEDs are compared to templates or physically-motivated models. The galaxy properties are then inferred either by identifying the model that best fits the observed data or by marginalising over a posterior probability distribution (see reviews by Walcher et al., 2011; Smith and Hayward, 2015; Conroy, 2013; Pacifici et al., 2023). The past several decades have seen rapid progress in the development of SED fitting techniques, primarily focussing on the far-ultraviolet (FUV) to the far-infrared (FIR) wavelength ranges. Early SED fitting approaches were often empirical and involved combining stellar spectra until a fit was obtained through trial and error or basic minimisation techniques (e.g., Spinrad and Taylor, 1971; Faber, 1972). The development of stellar population synthesis (SPS) models marked a shift from empirical matching to physically motivated modelling, in which stellar evolution theory was used to constrain stellar populations as a function of age and metallicity (Tinsley, 1968, 1972; Tinsley and Gunn, 1976; Bruzual A., 1983; Bruzual and Charlot, 2003). Over the past four decades, efforts have focused on developing physically motivated models for the various components of galaxy SEDs, spanning the UV-to-FIR wavelength range (e.g., Tinsley and Gunn, 1976; Draine and Lee, 1984; O'Connell, 1999; da Cunha et al., 2008; Groves et al., 2008; Noll et al., 2009). In this section, we look at the different physical processes powering emission in galaxies, and discuss how they are treated during SED fitting.

1.5.1 Stellar population synthesis

The principal stellar contribution to galaxy SEDs is the radiation from the photospheres of O to M spectral-type stars, which, in the absence of dust, is concentrated in the UV-NIR wavelength range (Bruzual and Charlot, 2003; Smith et al., 2012; Cimatti et al., 2020). Young, massive stars emit predominantly in the UV, tracing recent star formation, while older, cooler stars contribute more significantly at optical and NIR wavelengths. Stellar emission also gives rise to absorption and emission features, such as the Balmer and Paschen series from Hydrogen, metal absorption lines (e.g., Ca II $\lambda 3,969$ and K $\lambda 3,934$), and molecular bands like TiO in late-type stars (for an overview, see Sánchez Almeida et al., 2012, and references therein). The shape of the stellar

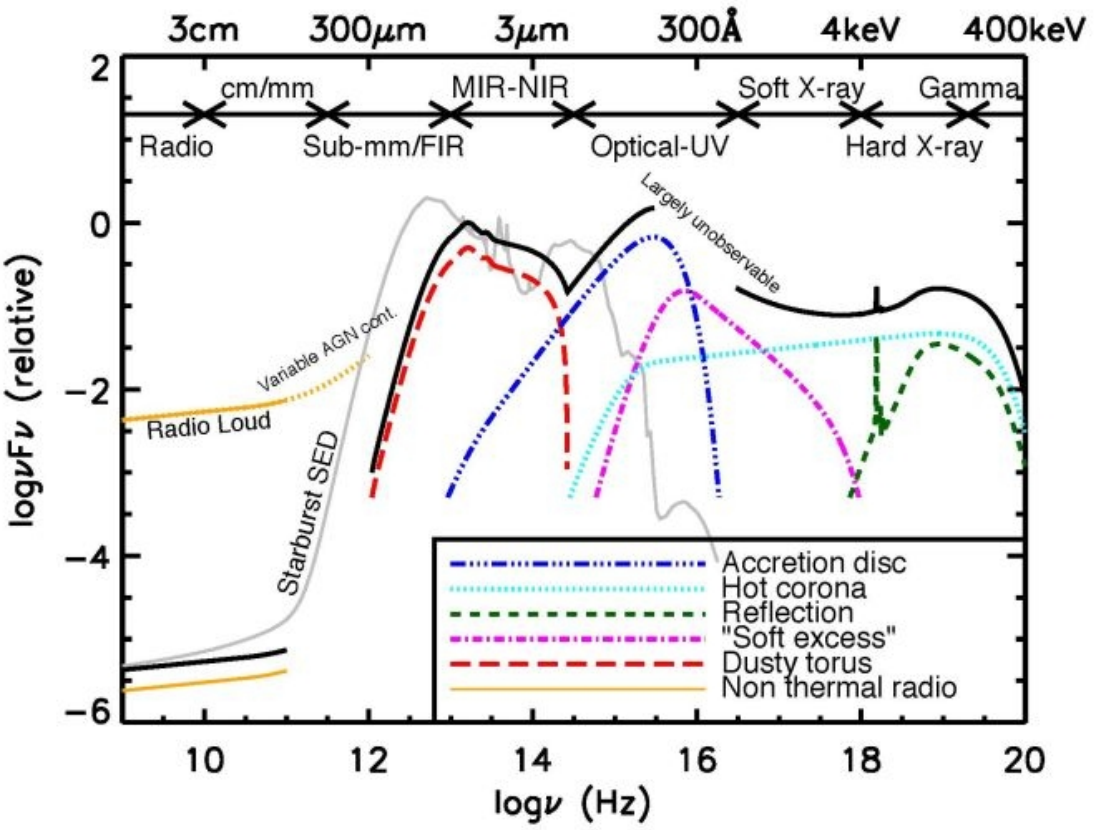

FIGURE 1.8: Schematic representation of the contribution of different physical components to the SED of an unobscured AGN, compared to that of a star-forming galaxy (adapted from Harrison, 2014; Hickox and Alexander, 2018).

continuum in galaxy SEDs is primarily determined by the ages and metallicities of the stellar populations, together with the effects of dust extinction. SPS provides the theoretical framework for modelling a galaxy's stellar emission, based on the basic tenet that a stellar population can be decomposed into a sum of instantaneous starbursts (referred to as "simple stellar population", or SSPs), after accounting for dust attenuation (see Charlot and Bruzual A, 1991; Bruzual A. and Charlot, 1993). In this section, we discuss the different aspects of SPS modelling.

1.5.1.1 Simple Stellar Populations

SSPs are the fundamental building blocks of SPS modelling, and are defined as an idealised single-age, co-evolving stellar population with a single metallicity and abundance pattern (Silva et al., 1998; Cid Fernandes et al., 2005; Conroy et al., 2009; Conroy, 2013). The spectrum of a single SSP ($f_{\rm SSP}$), as a function of initial mass M, age t, and metallicity Z, is given as:

$$f_{\rm SSP}(t,Z) = \int_M \phi(M)_{t,Z}\ f_{\rm star}(M,t,Z)\ dM, \tag{1.8}$$

where $\phi(M)$ represents the SMF, and $f_{\rm star}$ is a stellar spectrum. In the SPS framework, the SMF is constructed using an IMF, which encodes the distribution of stellar masses at the onset of star formation activity, and an interpolated grid of stellar isochrones (defined as the loci of stars with the same ages and chemical compositions, but potentially spanning a range of different masses, on the Hertzsprung-Russell diagram; see Walcher et al., 2008). Several popular stellar isochrone libraries are used in SPS modelling, such as the Padova (Bertelli et al., 1994; Girardi et al., 2000; Marigo et al., 2008), the Geneva (Schaller et al., 1992; Meynet and Maeder, 2000), the Bag of Stellar Tracks and Isochrones (BaSTI; Pietrinferni et al., 2004, 2013), the *MESA* Isochrones and Stellar Tracks (MIST; Dotter, 2016; Choi et al., 2016), and the TRieste Stellar Evolution Code (PARSEC; Bressan et al., 2012) models. Stellar spectra are obtained from stellar spectral libraries, given the masses, ages, and metallicities. Stellar spectral libraries can be divided into two broad categories: (i) "theoretical", which are based on models of stellar atmospheres and radiative transfer (e.g., Martins et al., 2005; Munari et al., 2005; Coelho et al., 2005, 2007), and (ii) "empirical", which are composed of observed stellar spectra, e.g., the STELIB stellar library (Le Borgne et al., 2003), the *HST*/STIS Next generation spectral library (NGSL; Gregg et al., 2006), the medium-resolution Isaac Newton Telescope library of empirical spectra (MILES; Sánchez-Blázquez et al., 2006), the Infrared Telescope Facility Spectral library (IRTF; Rayner et al., 2009), and the X-shooter library (XSL; Chen et al., 2011).

1.5.1.2 Composite Stellar Population

Composite stellar populations (CSPs) are constructed by summing over the contributions of SSPs spanning a broad range of ages and metallicities, while also accounting for the effects of dust attenuation and emission (discussed in Section 1.5.2). By integrating the spectral contributions of individual SSPs over the age of the stellar population (t') and metallicity (Z), the SED of the CSP is defined as (see Conroy, 2013, equation 2).

$$f_{\rm CSP}(t) = \int_{t'=0}^{t'=t} \int_{Z=0}^{Z=Z_{\rm max}} {\rm SFR}(t-t')\, P(Z, t-t')\, f_{\rm SSP}(t', Z)\, \exp^{-\tau_d(t')} + A f_{\rm dust}(t', Z)\, dt'\, dZ, \tag{1.9}$$

where ${\rm SFR}(t)$ gives the SFR as a function of time (so-called SFH), $P(Z,t)$ is the time-dependent metallicity distribution function, $\tau_d(t')$ is the optical depth that is used to model the time dependent dust attenuation, and the function $f_{\rm dust}(t', Z)$ incorporates dust emission. A is a normalisation constant that is set by balancing the luminosity absorbed by dust and that which is re-radiated. A common simplification adopted in the construction of CSPs is to assume a single

value for metallicity, thereby replacing $P(Z,t)$ with a simple δ function (see Walcher et al., 2008; Conroy, 2013). The remaining components of this model are discussed in the subsequent sections.

1.5.1.3 Star formation history

Modelling the SFH of galaxies is one of the most critical aspects of the SED fitting process. Works such as Simha et al. (2014); Diemer et al. (2017); Carnall et al. (2019) have shown that galaxy SFHs can be reasonably approximated by relatively simple functions of time – by using the so-called "parametric SFHs". The simplest of these is the exponential SFH, which, under the assumption of a closed-box model, postulates that SFR is proportional to the availability of cold gas, resulting in an exponentially declining SFR over time (see also Section 1.2.1). However, real SFHs are complex, and variations of the exponential SFH, such as the delayed-exponential form or linear combinations of multiple exponential components, are commonly used in SED fitting (see Carnall et al., 2019, for a detailed list). Often, additional modifications, such as inclusion of empirical templates or delta-function components to model starbursts, are required to capture stochastic or bursty star formation episodes (e.g. da Cunha et al., 2008; Rocca-Volmerange et al., 2013; Johnson et al., 2021).

Parametric SFH models, however, have several drawbacks. First, assuming a functional form for the SFH *a priori* can potentially exclude entire classes of plausible solutions, thereby introducing biases in the resulting parameter estimates (Carnall et al., 2019; Leja et al., 2019). Second, parametric SFH models often struggle to deal with complex features in the SFH, such as episodes of star-burst activity, sudden quenching and rejuvenation, etc., leading to further biases in the parameter estimates (Simha et al., 2014). For instance, Lower et al. (2020) reported a bias of up to 0.4 dex in stellar masses estimated using parametric SFHs, compared to models in which no functional form is assumed (so-called "non-parametric SFH models"). Similarly, Haskell et al. (2024) fitted a sample of galaxies from cosmological zoom-in simulations and found that parametric SFHs can lead to biases of up to 1 dex in the derived SFRs, as well as underestimation of the associated uncertainties.

So-called "non-parametric" SFH models address most of the shortcomings of parametric SFHs. In the non-parametric treatment, the lifetime of a galaxy is split into age bins, with either pre-defined or adaptive widths. The fitting procedure directly infers a physical parameter tied to the star formation happening in each bin, such as the fraction of the total stellar mass formed

in each bin, or the SFR or sSFR in each bin (e.g., Cid Fernandes et al., 2005; Ocvirk et al., 2006; Tojeiro et al., 2007; Leja et al., 2017). Analytical prior distributions, such as the Dirichlet and Student's–t distributions, are used to ensure correlations between adjacent time bins in non-parametric SFHs. Non-parametric SFH models provide greater flexibility in capturing the full diversity of complex SFHs (e.g., Iyer and Gawiser, 2017; Leja et al., 2019; Lower et al., 2020; Ciesla et al., 2023). They have been shown to yield more robust estimates of galaxy properties, e.g., providing more realistic uncertainty estimates than parametric SFHs (e.g., Leja et al., 2019; Das et al., 2024), and mitigating some of the biases inherent in results derived from parametric forms (e.g., Suess et al., 2022; Jain et al., 2024; Haskell et al., 2024). However, this flexibility comes at a computational cost: non-parametric models typically involve a larger number of free parameters and require the generation of a greater number of model SEDs to effectively constrain the broader space of possible SFH behaviours (Leja et al., 2019; Lower et al., 2020).

1.5.2 Dust

Interstellar dust is composed of carbonaceous and silicate granules, and can be divided into three principal components: small dust grains (≈ 0.01 μm in size), larger dust grains ($\approx 0.01 - 0.25$ μm), and polycyclic aromatic hydrocarbons or PAHs (see Stein and Soifer, 1983; Draine, 2003, for a review). Dust plays a crucial role in shaping a galaxy's SED by attenuating the UV-NIR light from stellar populations, subsequently re-radiating the absorbed light at IR and sub-mm wavelengths in the form of a modified black body spectrum (see Li and Draine, 2001; Draine, 2003; Salim and Narayanan, 2020; Cimatti et al., 2020).

1.5.2.1 Dust attenuation

In its fundamental form, starlight along a line of sight is absorbed and scattered when it passes through a column of dust – a phenomenon known as "extinction". Dust extinction along a line of sight depends on the properties of dust grains in the column (e.g. their composition and size) as well as the column density. By comparing the expected spectrum without dust (from numerical models) to the observed spectrum of individual stars in the MW and Large and Small Magellanic Clouds (LMC and SMC, respectively) along multiple lines of sight, average extinction curves have been obtained (see Calzetti, 2001; Li, 2007; Salim and Narayanan, 2020, and references therein). Dust "attenuation" aggregates the effect of extinction over the entire galaxy, and depends not only on grain properties but also on the relative geometry between stars

and dust. Attenuation thus also incorporates the contribution of unobscured stars whose light is scattered into the line of sight. And while extinction measurements can only be performed in nearby objects where individual lines of sight can be resolved, attenuation information can be obtained for sources up to high redshifts.

Modelling of dust attenuation forms a core part of the SED fitting process. One of the most popular dust attenuation models is the two-component Charlot and Fall (2000) model, which comprises of separate birth cloud and diffuse dust screens to account for the differential attenuation of starlight from younger and older stellar populations. Birth cloud refers to the dense molecular clouds and HII regions shrouding the young stars. This obscuration diminishes as the stars age and move away from their birth clouds. Additionally, the clouds themselves disperse with time. Light from young stars is heavily attenuated by the birth cloud in addition to the diffuse dust and ISM in the galaxy (referred to as the diffuse dust screen). In contrast, the light from older stars experiences relatively modest attenuation only from the diffuse dust. This framework has been highly effective in modelling the dust reddening of galaxies up to high redshifts. Over the years, significant efforts have been made to improve upon the Charlot and Fall (2000) model, such as modelling the 2,175 Å absorption feature (Kriek and Conroy, 2013), adopting steeper slopes (e.g., Reddy et al., 2015; Boquien et al., 2022), and exploring the dependence of the curve slopes on metallicity (e.g. Shivaei et al., 2020) and stellar mass (e.g. Salim et al., 2018). Further efforts are ongoing to improve upon dust attenuation modelling using numerical simulations, SED fitting, and observations from facilities such as ALMA and *JWST* (e.g., Lower et al., 2020; Markov et al., 2023; Shapley et al., 2023; Fisher et al., 2025).

1.5.2.2 Dust emission

Dust emission, spanning MIR to sub-mm wavelengths, arises from the heating of dust grains by stellar radiation, including both direct emission from young, massive stars and the interstellar radiation field (ISRF), which represents the integrated light from a galaxy's total stellar population (see Draine and Li, 2001; Draine, 2003; Blain et al., 2002; Galliano et al., 2018, and references therein). Numerical simulations (e.g. Cen and Kimm, 2014) have shown that it can account for up to 90 per cent of the total bolometric luminosity in SFGs. A source's dust emission depends on the size and optical properties of the dust grains, as well as on the spectrum and intensity of the ISRF. The $\approx$0.01 μm dust granules absorb UV photons from the massive, short-lived OB stars, reaching temperatures of $100-200$ K (known as "warm dust"; see Cimatti

et al., 2020). The larger $\approx 0.01-0.25$ μm dust granules are heated by the general ISRF, reaching equilibrium temperatures of $15-25$ K, and emitting at $\lambda > 60$ μm (referred to as "cold dust"; see Li, 2005). PAHs give rise to strong MIR emission spectral features at 3.2, 6.2, 7.7, 8.6, and 11.3 μm (Mathis et al., 1983; Stein and Soifer, 1983; Draine and Li, 2007).

Sophisticated models are available to predict dust emission across IR wavelengths, given the grain size distributions, their optical properties, and the intensity and spectral shape of the ISRF (see Silva et al., 1998; Dale et al., 2001; Popescu et al., 2000; Jonsson, 2006; Piovan et al., 2006; Groves et al., 2008; Popescu et al., 2011). These models typically require a large number of input parameters, including assumptions about the dust composition, grain heating mechanisms, and the spatial distribution of stars and dust, which necessitate full radiative transfer calculations. As a result, they are computationally intensive and often too complex to be applied directly in SED fitting of large galaxy samples. To address this limitation, simplified models have been developed. A widely adopted strategy in SED fitting is the use of empirical or semi-empirical IR templates. For example, template libraries based on the models of Dale et al. (2001) and Chary and Elbaz (2001) reproduce the observed IR SEDs of SFGs and ultraluminous infrared galaxies (ULIRGs) across a range of total IR luminosities, effectively collapsing a high-dimensional model into a one-parameter family characterised by IR luminosity. In addition to templates, physically motivated phenomenological models are also employed. For instance, da Cunha et al. (2008) model the IR emission as a sum of multiple modified blackbody components representing thermal dust emission at different temperatures, combined with a stochastic component from small grains and empirically derived PAH templates. Similarly, Draine and Li (2007) construct the IR SED using three key parameters: the minimum intensity of the stellar radiation field, the fraction of dust mass exposed to radiation fields stronger than this minimum, and the mass fraction of PAHs. Crucially, many SED fitting frameworks link dust attenuation and emission through the principle of "energy-balance" (e.g., da Cunha et al., 2008; Haskell et al., 2023). This principle enforces the conservation of energy between absorbed starlight and re-emitted IR emission, such that only combinations of stellar population models and IR templates or dust emission models that are energetically consistent are permitted.

1.5.3 AGN torus

AGN undergoing radiatively efficient accretion of matter onto SMBHs make several notable contributions to the SED of their host galaxies (see Padovani et al., 2017, for an overview):

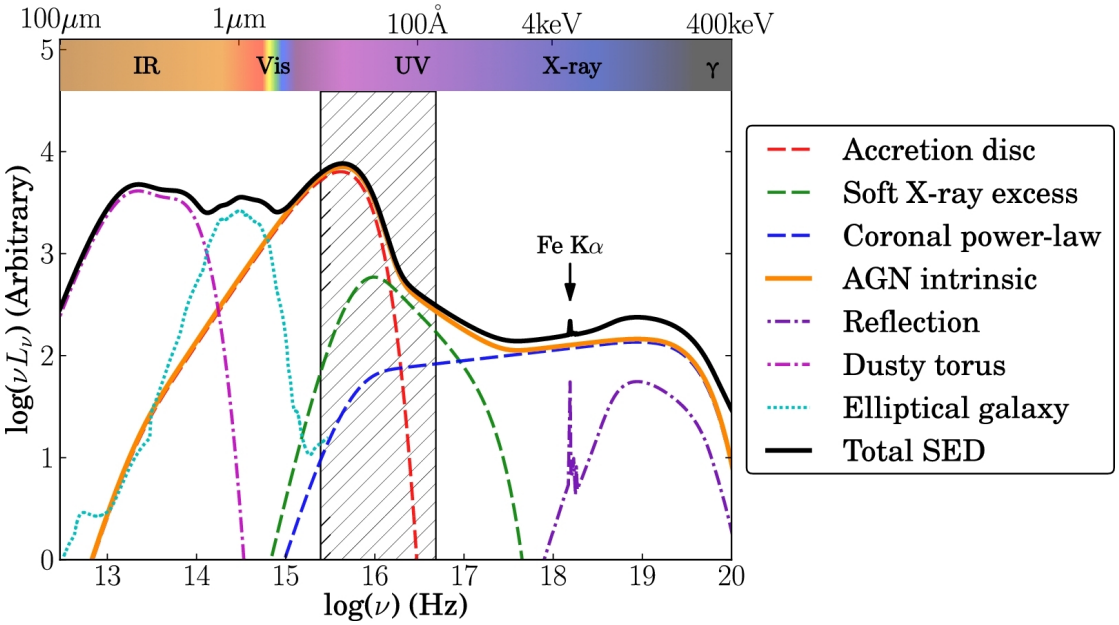

FIGURE 1.9: Schematic AGN SED illustrating the approximate shape and extent of key components. Dashed lines show intrinsic AGN emission, dash-dotted lines indicate reprocessed emission, and the dotted line represents starlight from an elliptical host. The hatched region marks wavelengths heavily absorbed by the IGM (adapted from Collinson et al., 2017).

(i) the "Big Blue Bump" (BBB; Mathews and Ferland, 1987; Sanders et al., 1989; Elvis et al., 1994; Shang et al., 2005; Richards et al., 2006; Krawczyk et al., 2013) in the UV – optical SED (peaking in the extreme ultraviolet, or EUV, around 100 – 912 Å), thought to arise due to thermal emission from the accretion disc, (ii) MIR emission produced by the heating of the dusty torus by UV – optical radiation from the nuclear region (e.g., Barvainis, 1987; Pier and Krolik, 1993; Mor et al., 2009), (iii) a complex X-ray component comprising of a power-law tail (PLT) from inverse Compton (IC) scattering by a hot, optically thin corona (e.g., Haardt and Maraschi, 1991; Tombesi et al., 2013), a hard X-ray reflection bump from the accretion disc (George and Fabian, 1991), and, possibly arising from further reflection or upscattering (Arnaud et al., 1985; Crummy et al., 2006; Done et al., 2012). Fig. 1.9 presents a schematic diagram, adapted from Collinson et al. (2017), illustrating the various AGN SED components described above.

Since this thesis is focused on the UV – FIR SEDs of galaxies, we restrict our discussion of AGN modelling to the MIR emission driven by the AGN torus. Thermal emission from the AGN torus is concentrated in the $\sim 3-30$ μm range, overlapping with the wavelength range of dust emission heated by starlight. In the absence of AGN torus models, SED fitters attribute the entire MIR emission to hot dust, potentially leading to biased estimates of galaxy properties when radiative-mode AGN is present (e.g., overestimation of specific SFRs by up to 0.6 dex; see Salim et al., 2016). Given that AGN are prevalent in the galaxy population (up to 40 per cent of SFGs display

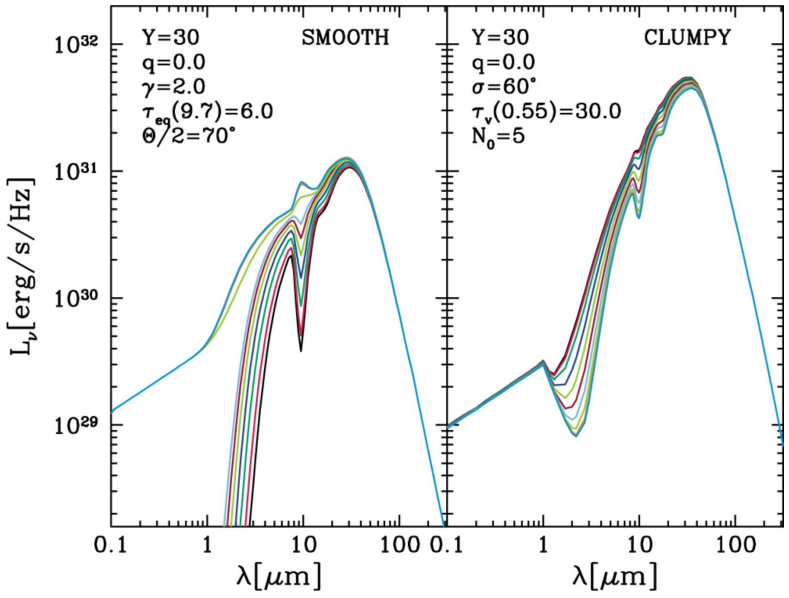

FIGURE 1.10: Comparison of the smooth AGN templates (left-hand panel) from Fritz et al. (2006) and the clumpy AGN templates (right-hand panel) from Nenkova et al. (2008a). This figure is reproduced from Feltre et al. (2012).

some degree of AGN activity; see Kauffmann et al., 2003; Juneau et al., 2013; Kirkpatrick et al., 2015), it is crucial that the contribution of AGN torus emission to galaxy SEDs is properly accounted for. AGN torus emission has been typically modelled either as a "clumpy" dust distribution (CLUMPY models; Nenkova et al., 2008a,b) or as a continuous (a.k.a., "smooth") distribution (Fritz et al., 2006). These models are generally parametrised by the torus geometry (e.g., opening angle, radial extent, inclination), optical depth, and the distribution of dust clouds or density. There are several notable differences between the two sets of models (see Feltre et al., 2012, for a detailed comparison): clumpy torus models are generally more complex than smooth torus models, produce broader IR SEDs, and predict weaker silicate features as well as a less prominent transition between type I and type II AGN (Fig. 1.10). Ultimately, the choice of model depends on the specific science goals, and different codes therefore adopt either model set or use a hybrid approach that attempts to strike a balance between the two (e.g. Calistro Rivera et al., 2016).

1.5.4 Nebular emission

In SED modelling, nebular emission is generally assumed to arise from ionising photons emitted by young, massive stars, which are absorbed and reprocessed by the surrounding gas (e.g., Osterbrock and Ferland, 2006; Byler et al., 2017). Modern SED fitting frameworks therefore couple nebular emission prescriptions with SPS models, enabling self-consistent predictions of

emission-line strengths based on physical parameters tied to the underlying stellar populations, such as metallicity, ionisation parameter, and the shape of the ionising spectrum. For example, photoionisation model grids generated with CLOUDY (Ferland et al., 2013; Byler et al., 2017) often use stellar populations from SPS models such as BPASS (Eldridge et al., 2017) or `FSPS` (Conroy et al., 2009) as the ionising sources. Nebular emission models are typically parameterised by (i) a continuum component arising from free-free, free-bound, and two-photon processes, and (ii) line emission produced by radiative recombination and collisionally excited fine-structure transitions. The impact of nebular emission is particularly significant at high redshift, where galaxies host large fractions of young stellar populations and exhibit low metallicities. In this regime, strong emission lines can contribute as much as 20–60 per cent of the flux in broadband filters (see Anders and Fritze-v. Alvensleben, 2003; Schaerer and de Barros, 2009, 2012).

1.5.5 The fitting process

At its core, SED fitting compares observed SEDs to a pre-computed library of model SEDs and constrains physical parameters through this process (see reviews by Walcher et al., 2011; Conroy, 2013; Pacifici et al., 2023). SED fitting codes either take a deterministic approach, returning a single best-fitting model, or adopt a probabilistic approach, yielding a probability distribution function (PDF) over the model parameters. Bayes' theorem provides the probability of a set of model parameters describing the observed data, under the assumption that the specified prior conditions are valid. The posterior probability $\mathcal{L}(\Theta|D)$, i.e., the likelihood that the model parameters Θ fit the data D is defined as:

$$\mathcal{L}(\Theta|D) = \frac{\mathcal{L}(D|\Theta) \times \mathcal{L}(\Theta)}{\mathcal{L}(D)}, \tag{1.10}$$

where, $\mathcal{L}(\Theta)$ encodes the prior information on the model parameters (referred to as the prior distribution) and $\mathcal{L}(D|\Theta)$ is the likelihood that the data D are described by the model Θ (known as the likelihood function). The likelihood function is typically given by the chi-squared (χ^2) metric calculated between the observed and model fluxes, under the assumption of independent Gaussian errors. The denominator $\mathcal{L}(D)$ is the marginal likelihood (also called the Bayesian evidence) that describes the likelihood of all the models given the data. For each observed galaxy, the posterior PDFs of individual parameters are obtained by marginalising over all other parameters in the library. The resulting PDFs provide robust estimates of parameters, typically

via the median and the width (in σ units) of the PDF. This approach naturally integrates all available measurements, and incorporates non-linear physical processes (e.g., those due to dust) in a self-consistent manner (see Walcher et al., 2011).

The vast majority of modern SED fitters use Bayesian inference, since these offer several advantages over frequentist approaches (see Pacifici et al., 2023, for a summary of different SED fitting codes). First, Bayesian inference methods include prior distributions on the models, which not only place physical constraints on the model parameters but also fold in model reliability. This is especially important when dealing with low SNR data or working in under-constrained regimes (e.g. at high redshifts or with low-luminosity galaxies). Second, Bayesian inference deals with full posterior distributions instead of the point estimates typical of frequentist approaches. This is crucial for obtaining realistic uncertainties on parameters, capturing degeneracies between parameters (e.g., age-dust-metallicity, see Bell and Kennicutt, 2001; Calzetti, 2013; Leja et al., 2017), and allowing for robust marginalisation over nuisance parameters. The marginal likelihoods, together with the Bayesian evidence, quantify the relative support for different models, thus enabling formal model comparison.

Central to Bayesian SED fitting is the efficient exploration of the posterior probability space. This involves sampling different parameters within the bounds of their respective priors to generate models, obtaining the SEDs associated with these models, and then evaluating the likelihood of each model by comparing the model SEDs to the observed data. SED fitters typically use two approaches: (i) assembling a comprehensive library of model SEDs corresponding to different combinations of parameters on a discrete grid spanning a wide range of plausible physical values; and (ii) calculating the SED for each model on the fly, without relying on a predefined grid, through Bayesian forward modelling. The former approach is fast (since the SEDs are pre-computed), easily parallelisable, and allow for simple interpolation between grid points. However, they involve a large overhead for storing the pre-computed libraries, and are not as flexible as on-the-fly approaches. On-the-fly approaches can accommodate more complex or custom physical models easily, and do not need to rebuild the parameter grid every time the model definitions are changed. The flexibility offered by on-the-fly methods comes at the cost of speed, which can be several orders of magnitude slower than the grid-based methods. The choice of the sampling method is therefore subjective to the science cases and resource availability. Bayesian forward modelling has been widely performed through the use of Markov Chain Monte Carlo (MCMC; Foreman-Mackey et al., 2013) techniques, where several "walkers" stochastically traverse the parameter space. In the recent decades, nested sampling techniques have become

increasingly common for forward modelling. In nested sampling (Skilling, 2004) and dynamic nested sampling (Higson et al., 2019), the posterior is partitioned into concentric contours of increasing likelihood, and samples are drawn within each contour. Because the volume of these iso-likelihood contours decreases as the likelihood increases, regions with higher likelihoods are sampled more densely than those with lower likelihoods. A weight parameter, defined as a function of the contour volume, quantifies the relative importance of each region. Nested sampling techniques mitigate the potential biases introduced by the initial positions of MCMC walkers, and are better suited to deal with cases where the likelihood space is pathologically complex or has highly multi-modal features (see Speagle, 2020).

1.5.6 Contemporary SED fitting programs

Over the past two decades, a diverse suite of SED fitting codes has been developed to infer the physical properties of galaxies from multiwavelength photometry and spectroscopy. These codes vary in their implementation, particularly in their treatment of SFHs, sampling strategies, statistical frameworks, and physical modelling components. In this section, we summarise the distinguishing features of several widely used SED fitting codes in extragalactic astronomy: AGNFITTER Calistro Rivera et al. (2016), Bayesian Analysis of Galaxies for Physical Inference and Parameter EStimation (BAGPIPES; Carnall et al., 2018), BayEsian Analysis of GaLaxy sEds (BEAGLE; Chevallard and Charlot, 2016), Code Investigating GALaxy Emission (CIGALE; Noll et al., 2009; Boquien et al., 2019; Dey et al., 2022), The Dense Basis SED fitting code (DENSE BASIS; Iyer and Gawiser, 2017; Iyer et al., 2019), LEPHARE (Arnouts et al., 1999; Ilbert et al., 2006), Multi-wavelength Analysis of Galaxy Physical Properties (MAGPHYS; da Cunha et al., 2008, 2015), PROSPECT (Robotham et al., 2020; Thorne et al., 2023), and PROSPECTOR (Leja et al., 2017; Johnson et al., 2021).

All of the listed codes employ Bayesian inference, except for LEPHARE, which uses traditional χ^2 minimisation. Uncertainties in LEPHARE must therefore be estimated via bootstrap resampling, whereas Bayesian codes return posterior distributions with full marginalisation over model parameters and priors. Regarding the inference framework used in the Bayesian codes, CIGALE, DENSE BASIS, LEPHARE, and MAGPHYS use grid-based approaches. The remaining codes use Bayesian forward modelling – AGNFITTER uses MCMC, while BAGPIPES, BEAGLE, and PROSPECTOR can use both MCMC and nested sampling. The treatment of

SFHs is another point of differentiation. DENSE BASIS uses non-parametric SFHs exclusively, and uses Gaussian regression processes to compute SFHs (Iyer et al., 2019). BAGPIPES and PROSPECTOR allow both parametric and non-parametric SFHs. The remaining codes listed here use parametric SFHs. MAGPHYS superimposes random bursts to the parametric SFHs in order to model stochastic SFHs. The treatment of physical processes such as dust, stellar populations, and AGN varies across codes. Most use different IMF (e.g., Kroupa, 2001 and Chabrier, 2003), SPS models (e.g., Bruzual and Charlot, 2003 or BC03, and FSPS), dust attenuation and emission models, and nebular emission models. Emission from AGN tori is incorporated in AGNFITTER, CIGALE, MAGPHYS (in more recent updates, see Chang et al., 2017; Battisti et al., 2019), PROSPECT, and PROSPECTOR, typically using templates such as those by Fritz et al. (2006) or Nenkova et al. (2008a). AGNFITTER is explicitly optimised for AGN studies and does not enforce energy balance, unlike most others. PROSPECT supports evolving stellar metallicities, unlike other codes which assume fixed metallicity per galaxy. BAGPIPES, BEAGLE, and PROSPECTOR can fit both photometry and spectroscopy, while the rest support only photometry. PROSPECTOR further can perform self-consistent spectrophotometric calibration by treating both photometry and spectra on an equal footing (Leja et al., 2017; Johnson et al., 2021). While SED fitting codes have traditionally focussed on the UV–FIR wavelength range (or subsets thereof), ongoing efforts aim to expand their coverage. For instance, the most recent versions of CIGALE (Dey et al., 2022; Yang et al., 2022) and PROSPECT (Thorne et al., 2023) have explored the simultaneous fitting of FUV–radio SEDs. CIGALE has also introduced models to account for X-ray emission from galaxies and AGN (Yang et al., 2022). Each of these codes has its advantages and limitations, and there is no single "best" SED fitting code (see Pacifici et al., 2023, for a detailed comparison of these codes). Ultimately, the onus lies with the user to select an appropriate code that aligns with their scientific objectives and available computational resources.

1.6 Structure of this thesis

The overarching aim of this thesis is to investigate the evolving nature of galaxy populations from the early Universe to the present day, using broadband SED fitting. We work with both real and simulated datasets, incorporating photometry and spectroscopy. Our analysis is carried out using the SED fitting code PROSPECTOR, which offers several features essential to our science goals. In particular, it treats photometry and spectroscopy on an equal footing and includes the

capability to model AGN contributions to galaxy SEDs, both of which are critical to this work. The structure of this thesis is summarised in the subsequent paragraphs.

In Chapter 2 (published as Das et al., 2024), we use PROSPECTOR, to model up to 26 bands of UV–FIR aperture-matched photometry for ∼31,000 sources in the ELAIS-N1 field from the LOFAR Two-Metre Sky Survey (LoTSS) Deep fields first data release. Combining the parameter estimates from the SED fits with LoTSS 150 MHz radio luminosities, we produce maximum likelihood classifications for 92 per cent of the radio sources as a star-forming galaxy, high-/low-excitation radio galaxy, or radio-quiet AGN and study the population demographics as a function of 150 MHz flux density, luminosity, SFR, stellar mass, redshift and apparent r-band magnitude. We also used PROSPECTOR SED fits to investigate the SFR–150 MHz luminosity relation for a sample of ∼133,000 3.6 μm-selected $z < 1$ sources, finding that the stellar mass dependence is significantly weaker than previously reported, and may disappear altogether at $\log_{10}(\mathrm{SFR}/M_{\odot}\,\mathrm{yr}^{-1}) > 0.5$.

In Chapter 3, we use PROSPECTOR to simultaneously model UV–FIR photometry and DESI early data release spectroscopy in the ELAIS-N1 field, one of the LoTSS deep fields, producing spectrophotometric fits for 6,038 radio-selected galaxies. Building on Chapter 2, we develop a fully Bayesian classification scheme that combines photometry and spectroscopy, alongside LoTSS DR1 radio data, to probabilistically classify faint radio sources into SFG, RQ AGN, LERG, and HERG classes. We compare our results to both the photometry-only classification from Chapter 2 and spectroscopy-only classifications from Arnaudova et al. (2025). We show that spectrophotometric classification outperforms either method alone by classifying more sources, and is better at identifying obscured AGN via their mid-IR excess. Finally, we discuss scaling this approach to handle large datasets from surveys like WEAVE-LOFAR.

In Chapter 4, we investigate recent findings that galaxy properties derived from SED fitting can be biased by the details of their recent star formation histories. We use PROSPECTOR to model *Hubble* and *JWST* NIRCam- and MIRI-like synthetic photometry of $4.64 < z < 10$ sources from the SPHINX^{20} cosmological radiation-hydrodynamic simulation suite. We focus on the recovery of burstiness, η, defined as the log of the ratio of the short-term star formation rate (averaged over the last 10 Myr) to the intermediate-scale star formation rate (averaged over the last ∼100 Myrs). Our results show that the SFH prior exerts a strong and undue influence on the inferred parameters. Regardless of the SFH prior used, the inferred values of η for individual sources remain unreliable. However, the average burstiness of the sample of galaxies can be

recovered with relative success. This work serves as a stress-test of recovering recent SFH trends using photometry-only fits, and we highlight the need for spectroscopy to obtain reliable estimates.

Finally, in Chapter 5, we distill the findings of this thesis, and lay down a plan of action for future works.

Throughout this thesis, we assume a standard cosmology with $H_0 = 70\,\mathrm{km\,s^{-1}\,Mpc^{-1}}$, $\Omega_\mathrm{M} = 0.3$, and $\Omega_\mathrm{vac} = 0.7$. All magnitudes are quoted in the AB system (Oke and Gunn, 1983) unless otherwise stated.

Chapter 2

The LOFAR Two-metre Sky Survey: The nature of the faint source population and SFR-radio luminosity relation using Prospector

"I'm sure the universe is full of intelligent life. It's just been too intelligent to come here."
–Arthur C. Clarke

2.1 Introduction

Understanding the evolution of galaxies from the early stages of the Universe to the present is one of the key goals in modern astrophysics. Two critical aspects of the evolutionary pathway of galaxies are the build-up of stellar mass over cosmic time (i.e., the star formation history or SFH; see review by Madau and Dickinson, 2014), and feedback from active galactic nuclei (AGN; see reviews by McNamara and Nulsen, 2007; Fabian, 2012; Heckman and Best, 2014; Hardcastle and Croston, 2020). Radio observations are particularly important for conducting simultaneous studies of both star formation and nuclear activity in galaxies, being virtually unaffected by the dust obscuration that plagues shorter wavelengths (e.g. Condon and Ransom, 2016; Smith et al., 2016). Radio emission in galaxies is a combination of two principal components (e.g. Condon, 1992): thermal free-free emission (which contributes significantly only at frequencies above

$\sim$ 1 GHz), and non-thermal synchrotron radiation. The synchrotron component dominates at low frequencies, and is powered by (i) the acceleration of cosmic rays by supernova remnants of short-lived massive stars (Blumenthal and Gould, 1970; Condon, 1992; Condon and Ransom, 2016) and (ii) jets and lobes produced by the central supermassive black hole (SMBH; see reviews by Bridle and Perley, 1984; Padovani et al., 2017; Hardcastle and Croston, 2020) if the galaxy hosts an AGN.

AGN activity can be separated into two fundamental modes based on the efficiency of matter accretion onto the SMBH (see Hardcastle et al., 2007; Best and Heckman, 2012; Janssen et al., 2012; Heckman and Best, 2014; Mingo et al., 2014; Tadhunter, 2016; Hardcastle and Croston, 2020, and references therein). Radiatively efficient AGN activity (also known as "radiative-mode" or "quasar-mode") is known to form geometrically thin, optically thick accretion disks (e.g. Shakura and Sunyaev, 1973). The optical/near-infrared emission in radiative-mode AGN is primarily due to the presence of a hot, obscured accretion disk. This emission ionizes the surrounding gas, resulting in broad emission lines and high-excitation forbidden lines that are stronger than those produced by the significantly softer radiation field in young stellar populations (Filippenko et al., 1993; Ho, 2008; Kormendy and Ho, 2013). Radiative-mode AGN have also been observed to exhibit powerful radio jets (e.g. Tadhunter, 2016; Hardcastle and Croston, 2020). Jetted radiative-mode AGN are called high-excitation radio galaxies (HERGs), while those lacking radio jets (or possessing weak radio jets, e.g., Jarvis et al., 2019; Gürkan et al., 2019; Macfarlane et al., 2021) are called radio-quiet AGN (RQ AGN). On the other hand, radiatively inefficient AGN activity (often referred to as "jet-mode" or "radio-mode") is believed to form geometrically thick, optically thin disks (e.g., Narayan and Yi, 1995b), and exhibits bipolar relativistic jets. These sources typically lack strong forbidden lines in the optical wavelengths, or signs of AGN activity at other wavelengths (e.g. Laing et al., 1994; Evans et al., 2006; Kondapally et al., 2022), and are referred to as low-excitation radio galaxies (LERGs).

Deep radio surveys, such as the LOFAR Two Metre Sky Survey (LoTSS; Shimwell et al., 2017, 2019, 2022), MeerKAT[1] International Gigahertz Tiered Extragalactic Explorations Survey (MIGHTEE; Jarvis et al., 2016; Heywood et al., 2022), the Karl G. Jansky Very Large Array (VLA; Perley et al., 2011) Cosmic Evolution Survey (VLA-COSMOS; Scoville et al., 2007) 3 GHz Large Project (Smolčić et al., 2017b), and the Australian Square Kilometre Array Pathfinder (ASKAP; Johnston et al., 2007) Evolutionary Map of the Universe (EMU; Norris et al., 2011, 2021; Gürkan et al., 2022) survey have enabled studies of the faint radio source

[1] http://www.ska.ac.za/meerkat

population up to high redshifts. Unlike the radio bright population (which is predominantly composed of luminous AGN and radio-loud quasi-stellar objects, e.g. Condon, 1989; Prandoni et al., 2001; Simpson et al., 2006; Padovani, 2016; Hardcastle and Croston, 2020; Fanaroff et al., 2021), the faint radio population is a heterogeneous mixture of star forming galaxies (SFGs), RQ AGN, and low-luminosity radio galaxies (e.g., Windhorst, 2003; Jackson, 2005; Rosario et al., 2013; Padovani et al., 2015; Padovani, 2016). Previous studies, including those by Mauch and Sadler (2007), Best and Heckman (2012), and Sabater et al. (2019), used large spectroscopic samples to classify radio AGN in the local Universe. However, in many of the surveys mentioned above (including VLA-COSMOS, EMU, MIGHTEE, and LoTSS), complete spectroscopic coverage is not currently available. To a large extent, however, this lack of spectroscopic coverage has been mitigated through the integration of radio astronomy with multi-wavelength data sets. This integration has enabled works such as Smolčić et al. (2017a) and Whittam et al. (2022) to classify faint radio sources using a combination of different criteria, including their X-ray luminosity, mid-IR colour, UV–far-IR spectral energy distribution (SED), and dust extinction-corrected near-UV optical colour.

By design, LoTSS is particularly well-suited to joint radio and multiwavelength studies. The LoTSS wide area second data release (DR2; Shimwell et al., 2022; Hardcastle et al., 2023) observations reach a typical RMS sensitivity of $\sim 83 \mu$Jy beam^{-1} RMS at 144 MHz over 43 per cent of the extragalactic northern sky that is covered by the DESI Legacy Surveys programme (Dey et al., 2019). Additionally, the LoTSS deep fields (Tasse et al., 2021; Sabater et al., 2021; Kondapally et al., 2021; Duncan et al., 2021; Best et al., 2023) data release 1 (DR1) observations reach noise levels of $20-35 \mu$Jy beam^{-1} over at least 25 deg^2, a factor of $2-4\times$ deeper compared to the LoTSS wide survey, with extensive wide-field UV, optical, and infrared coverage. Of particular relevance to this work, Best et al. (2023, hereafter B23) performed SED fitting of about 80,000 radio-detected LoTSS deep fields sources using four codes; MAGPHYS (da Cunha et al., 2008), BAGPIPES (Carnall et al., 2018), CIGALE (Noll et al., 2009; Boquien et al., 2019), and AGNFITTER (Calistro Rivera et al., 2016). There are two principal differences in these codes. Firstly, the CIGALE and AGNFITTER models account for the contribution of AGN to the SED while MAGPHYS and BAGPIPES do not. Secondly, MAGPHYS, BAGPIPES, and CIGALE assume energy balance between dust attenuation and emission, while the version of AGNFITTER used in B23 does not. By comparing the results from these different SED fitting codes, B23 identified galaxies hosting radiative-mode AGN and derived optimised consensus estimates of the stellar mass and SFR. Furthermore, they identified galaxies with radio luminosity exceeding

that expected on the basis of the star formation processes alone. Using this information, B23 classified the radio sources as either SFGs, RQ AGN, LERGs, or HERGs.

Energy balance SED fitting represents the state-of-the-art for estimating the physical properties of galaxies from photometry at high-redshift (and subsequently classifying them). However, due to the computational resources required, and because obtaining scientifically-usable results from even a single code is not trivial, using multiple SED fitting codes to perform galaxy classifications may not be optimal.

In this work, we explore the viability of using a single SED fitting code to classify galaxies on the basis of their multi-wavelength photometry (following the approach adopted by B23) and use our new SED fitting results to revisit the stellar mass-dependence previously reported in the SFR–150 MHz[2] radio luminosity relation (e.g., Gürkan et al., 2018, hereafter G18, and Smith et al., 2021, hereafter S21). To do this, we use the SED fitting code PROSPECTOR (Leja et al., 2017; Johnson et al., 2021) as (i) it can model varying contributions of nebular emission and AGN to galaxy SEDs, and (ii) it is capable of modelling multi-wavelength photometry and spectroscopy on an equal footing. Even though PROSPECTOR can not model the radio SEDs of galaxies (cf. e.g. CIGALE, Dey et al., 2022, MAGPHYS, da Cunha et al., 2015, and PROSPECT, Robotham et al., 2020; Thorne et al., 2023), these aforementioned attributes are particularly useful in the context of this work, since radio-selected sources are known to be rich in both AGN and emission lines (e.g. Netzer, 1990; Simpson et al., 2006). While the current work will focus on the photometric classification (since spectra exist for only a minority of the sources in the LoTSS deep fields; e.g. Sabater et al., 2019; Duncan et al., 2021, Drake et al. *in preparation*), the ability to model spectra simultaneously with PROSPECTOR will become particularly useful in the coming years as we build up complete spectroscopy for sources in the LoTSS deep fields with the WEAVE-LOFAR survey (Smith et al., 2016).

This paper is structured as follows: in Section 2.2, we describe the datasets used in this work. In Section 2.3, we discuss the process of SED fitting using PROSPECTOR. In Section 2.4, we outline the criteria that we use to identify sources hosting radiative-mode and/or radio-loud AGN, summarise our classification scheme, and look into the demographics of the different galaxy classes as a function of a number of physical parameters. We also use our parameter estimates to revisit the relation between star formation rate and 150 MHz radio luminosity. In

[2]The central frequency of the LoTSS Deep Fields data varies slightly between the fields: it is 144 MHz in Boötes and Lockman Hole, and 146 MHz in ELAIS-N1. In this paper, we will refer to the LoTSS frequency as 150 MHz.

Section 2.5, we look into the stellar mass-dependent calibration of the SFR–150 MHz radio luminosity relation. Finally, in Section 2.6 we summarise the key findings of this work.

Throughout this work, we assume a standard cosmology with $H_0 = 70\,\mathrm{km\,s^{-1}\,Mpc^{-1}}$, $\Omega_\mathrm{M} = 0.3$, and $\Omega_\mathrm{vac} = 0.7$. All magnitudes are quoted in the AB system (Oke and Gunn, 1983) unless otherwise stated.

2.2 Data

Of the four LoTSS deep fields, the ELAIS-N1 region has the most sensitive 150 MHz data in LoTSS DR1, making it ideal for studying faint star-forming galaxies. ELAIS-N1 also benefits from some of the deepest wide-field optical, near-IR and mid-IR surveys. In this work, we focus on the $6.7\,\mathrm{deg}^2$ of this field where the best ancillary data are available.

2.2.1 Multi-wavelength data

Kondapally et al. (2021) generated 26 bands of aperture-matched photometry by combining aperture- and galactic extinction-corrected fluxes from UV to the mid-IR wavelengths with far-IR photometry measured using the XID+ tool (Hurley et al., 2017; McCheyne et al., 2022). UV–mid IR fluxes come from the following: *Spitzer* Adaptation of the Red-sequence Cluster Survey (SpARCS) u-band (Wilson et al., 2009; Muzzin et al., 2009); Panoramic Survey Telescope and Rapid Response System (PanSTARRS) g,r,i,z,y bands (Kaiser et al., 2010; Chambers et al., 2016); g, r, i, z, y, and the narrow-band NB921 data from Hyper-Suprime-Cam (HSC; Miyazaki et al., 2012, 2018) Subaru Strategic Program (HSC-SSP) public DR1 (Aihara et al., 2018); J- and K-band data from the UK Infrared Deep Sky Survey (UKIDSS) Deep Extragalactic Survey (DXS) DR10 (Lawrence et al., 2007); Infrared Array Camera (IRAC) 3.6–8μm data from the *Spitzer* Wide-Area Infrared Extragalactic Survey (SWIRE; Lonsdale et al., 2003), and 3.6–4.5μm data from the *Spitzer* Extragalactic Representative Volume Survey (SERVS; Mauduit et al., 2012). Duncan et al. (2021) combined state-of-the-art template fitting and machine learning techniques to obtain photometric redshift (photo-z, or z_photo) information for all the optical/near-IR selected sources in the LoTSS deep fields. These photo-zs complemented the spectroscopically-compiled redshifts (spec-z, or z_spec) which were available for a small minority (approximately 0.2 per cent) of the deep field sources. Far-IR photometry used in this work included 24 μm data from the Multiband Imaging Photometer for *Spitzer* (MIPS; Rieke

et al., 2004) instrument on *Spitzer*, 250, 350 and 500 μm data from the Spectral and Photometric Imaging Receiver (SPIRE; Griffin et al., 2010) instrument, and 100 and 160 μm data from Photodetector Array Camera and Spectrometer (PACS; Poglitsch et al., 2010). The latter two were obtained as part of the *Herschel* Multi-tiered Extragalactic Survey (HerMES; Oliver et al., 2012). Duncan et al. (2021) flagged sources with prior identification as AGN based on optical spectra, X-ray properties, or mid-IR colour cuts. We refer the reader to Kondapally et al. (2021), McCheyne et al. (2022) and references therein for further details. This multiwavelength source catalogue contains $\sim$ 2.1 million objects with redshifts up to $z \approx 7$.

2.2.2 Radio Observations

The 150 MHz radio data in the ELAIS-N1 deep field were taken with the LOFAR High Band Antenna (HBA) over a period of many years (totalling 164 hours of on-source integration time in DR1) and includes observations from the Dutch LOFAR stations, reaching spatial resolution (equivalent to the full width at half maximum of the restoring beam) of 6 arcsec with an RMS below 30 μJy beam^{-1}. Away from the bright sources, the central region of ELAIS-N1 reaches RMS as deep as 20 μJy beam^{-1}. Sabater et al. (2021) performed calibration and imaging, and catalogued the extracted sources. Owing to the excellent multiwavelength data coverage in this field, Kondapally et al. (2021) identified optical/near-IR counterparts for over 97 per cent of the radio-detected sources. We refer the reader to Sabater et al. (2021) and Kondapally et al. (2021) for details on source extraction and radio-optical cross-matching.

2.2.3 Datasets for SED fitting

In this work we use two different photometric samples.

1. *Radio-selected sample* - The final cross-matched catalogue in the ELAIS-N1 field contains 31,610 radio sources (Kondapally et al., 2021). We refer to this subset of sources as the "radio-selected sample". Redshift information (spectroscopic and/or photometric) is available for 30,538 of these sources (Duncan et al., 2021). Out of these 30,538 sources, 30,470 satisfied the flag cuts recommended in Kondapally et al. (2021). The flag cuts ensured that these sources lay in the overlapping coverage area of PanSTARRS

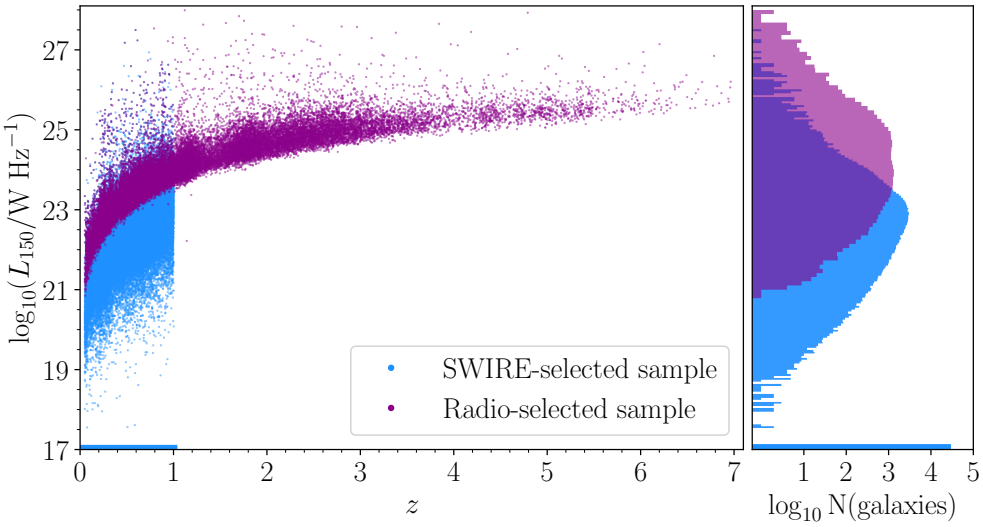

FIGURE 2.1: (Left panel) 150 MHz radio luminosity coverage of the radio-detected and the $z < 1$ SWIRE-selected source samples used in this work. (Right panel) Histogram showing the number count of sources binned by 150 MHz luminosity for the two data samples. Sources with radio luminosity less than 10^{17} W Hz^{-1} (including radio non-detections) were arbitrarily assigned to the lowest radio luminosity bin at $\log_{10}(L_{150}/\mathrm{W\ Hz^{-1}}) = 17$. The blue data points below the lower limit of the purple distribution represent sources with $< 5\sigma$ 150 MHz radio flux measurements. Including these sources is key to leveraging the low S/N measurements in a statistical manner.

i-band, UKIDSS-DXS *K*-band, and *Spitzer*-SWIRE 4.5μm channel, while excluding regions around bright stars as masked in the *Spitzer* data.

2. *SWIRE-selected sample* - The majority of sources in the multiwavelength catalogue were not individually catalogued at 150 MHz by Sabater et al. (2021). Excluding these sources risks biasing the results towards the minority of radio-bright sources. Therefore we also follow the S21 sample definition and select sources with SWIRE 3.6μm flux density exceeding 10 μJy. This roughly corresponds to the 5σ detection threshold in the SWIRE 3.6μm data and is in line with SWIRE webpage[3] recommendations. S21 adopt the SWIRE 3.6μm selection as these data are extremely sensitive and are less susceptible to the influence of dust obscuration and sample biases than samples identified at shorter wavelengths. We restrict this sample to $z < 1$, where Duncan et al. (2021) photo-z estimates are the most reliable, bringing the sample size to 145,162 sources. Finally, we exclude sources at $z < 0.05$ to avoid potential IRAC sources with extended radio emission larger than the LoTSS beam size of 6 arcsec. More than 99.5 per cent of sources at $z < 1$ and over 98 per cent of sources at $z < 0.2$ have an FWHM smaller than 6 arcsec (see S21), therefore this

[3] https://irsa.ipac.caltech.edu/data/SPITZER/SWIRE/

redshift cut does not significantly impact our work. The resulting source sample contains 133,544 sources and is referred to as the "SWIRE-selected sample".

We use the Sabater et al. (2021) flux densities and uncertainties for the 11 per cent of the SWIRE-selected sample that have 150 MHz counterparts in the Kondapally et al. (2021) catalogue. For the remaining sources, we follow S21 and use the flux densities measured at the 150 MHz image pixel coordinates corresponding to each source. For unresolved sources, these values represent the maximum likelihood estimate of the integrated flux density. Figure 2.1 illustrates the different parameter spaces occupied by the two source samples, with the Radio-selected sample shown in purple, and the SWIRE-selected sample shown in light blue. The marginal histogram to the right of Figure 2.1 indicates the sample size as a function of 150 MHz luminosity, with the 150 MHz non-detected sources assigned to the (numerically dominant) lowest luminosity bin if their maximum-likelihood luminosity estimates were lower than this. The individually undetected sources (with S/N < 5, represented by the blue data points below the lower limit of the purple distribution in Figure 2.1) are numerically dominant and together can provide significant analytical insights, making it critical to include these sources in our analysis.

2.3 SED fitting

PROSPECTOR (Leja et al., 2017; Johnson et al., 2021) is an SED fitting code that uses the Flexible Stellar Populations Synthesis (FSPS; Conroy et al., 2009; Johnson et al., 2023) code to model photometric and/or spectroscopic data and infer stellar population properties. It uses the Padova isochrone table (Bertelli et al., 1994; Girardi et al., 2000; Marigo et al., 2008) and the MILES spectral library (Sánchez-Blázquez et al., 2006). The dynamic nested sampling tool DYNESTY (Speagle, 2020) is used to estimate Bayesian posteriors and evidences. We adopt the Initial Mass Function (IMF) from Kroupa (2001). Since PROSPECTOR does not support evolving metallicities (in contrast to, e.g., PROSPECT; Thorne et al., 2022a), and even non-evolving metallicities remain poorly constrained based on photometry alone (e.g. Smith and Hayward, 2018), we set the stellar metallicity at solar. While Thorne et al. (2022a) have shown that the stellar masses and SFRs are not systematically offset by this choice of metallicity, we intend to revisit this choice in future works once WEAVE-LOFAR spectra are available.

Source redshifts have been fixed at spec-z for sources where they are available (5.1 per cent of the radio-detected sample and 1.5 per cent of the SWIRE-selected sample). For the remaining

sources, they were fixed at the photo-z estimates from Duncan et al. (2021). Following B23, neither redshift uncertainties, nor those sources lacking redshift information were considered further. Applying the flags recommended in Kondapally et al. (2021), we ensure that only those sources with the most reliable photo-z are included in our work.[4]

We use the two-component Charlot and Fall (2000) dust attenuation model, which consists of separate birth cloud and diffuse dust screens, to account for the differential attenuation of starlight from younger and older stellar populations. We use the Kriek and Conroy (2013) attenuation curve which is parametrised by the diffuse dust V-band optical depth, the diffuse dust attenuation index, and the ratio of the birth cloud optical depth to the diffuse dust screen optical depth, while energy balance is assumed between dust attenuation and emission (see Leja et al., 2017, for further discussions). The three parameter Draine and Li (2007) dust emission templates are used to describe the shape of the IR SED. Mid-IR emission from the AGN torus is described by the CLUMPY models (Nenkova et al., 2008a,b). These models are parametrised by the $4-20\mu$m AGN luminosity (which is expressed as a fraction of the total stellar bolometric luminosity) and the optical depth of the AGN torus. Nebular lines and continuum emission are calculated through the implementation of the `CLOUDY` photoionization code (Ferland et al., 2013), wherein the ionizing sources are represented by the stellar populations generated using `FSPS` (Byler et al., 2017). This is parametrised by the intensity of the ionizing spectrum, which is denoted by a dimensionless ionization parameter (and kept free in the model), and the gas-phase metallicity. While Leja et al. (2017) demonstrated that gas-phase metallicity is not adequately constrained for individual galaxies using photometry, works such as Bellstedt et al. (2020), Bellstedt et al. (2021) and Thorne et al. (2022b) have highlighted the benefits of modelling galaxies using an evolving metallicity (e.g. for recovering the best estimates of the cosmic star formation history, the CSFH). Since that functionality is not available in `PROSPECTOR`, we have made the pragmatic decision to set the gas-phase metallicity equal to the solar metallicity.

Star formation histories have traditionally been modelled with a number of functional forms (such as constant or exponentially-declining SFHs, commonly referred to as 'parametric' SFHs; e.g. Buat et al., 2008; Maraston et al., 2010; Gladders et al., 2013; Simha et al., 2014; Carnall et al., 2018, 2019, and references therein). Parametric SFHs often struggle to model complex SFH features, such as episodes of star-burst activity, sudden quenching, and rejuvenation (Simha

[4]The outlier fractions – defined as sources with $|z_{\rm spec} - z_{\rm photo}|/(1+z_{\rm spec}) > 0.15$, see Duncan et al. (2021) – for the radio-detected and SWIRE-selected sources, calculated from sub-samples with available spectroscopic redshifts, are 4.3 per cent and 3.2 per cent, respectively. These values fall within the range of the outlier fractions as reported by Duncan et al. (2021): 1.5 to 1.8 per cent for normal galaxies, and from 18 to 22 per cent for sources with identified AGN components.

et al., 2014; Smith and Hayward, 2015; Carnall et al., 2019; Leja et al., 2019). Non-parametric SFHs promise a way out by *not* assuming a specific functional form for the SFH. In its simplest form, the lifetime of the galaxy is divided into discrete time bins and the stellar mass formed in each bin is fitted (e.g., Cid Fernandes et al., 2005; Ocvirk et al., 2006; Tojeiro et al., 2007; Leja et al., 2017). Iyer and Gawiser (2017), Leja et al. (2019), Lower et al. (2020), and Ciesla et al. (2023) have shown that non-parametric SFH models provide the flexibility to describe the full extent of complex SFHs, potentially leading to more robust estimates of galaxy properties and outperforming parametric SFH models, usually at the expense of a few extra free parameters. Given the inability of photometric data to fully constrain SFHs of galaxies (e.g. Smith and Hayward, 2015) the choice of prior distribution plays an important role (e.g. Leja et al., 2019).

In this work, we adopt the PROSPECTOR non-parametric "continuity" prior, which directly fits for $\Delta \log_{10}(\mathrm{SFR})$ between neighbouring time bins using a Student's t-distribution with scale factor $\sigma = 0.3$ and two degrees of freedom ($\nu = 2$). This prior discourages abrupt changes in SFR between adjacent bins, but remains flexible enough to fit starbursts, star-forming and quenched galaxies (Leja et al., 2019; Johnson et al., 2021; Haskell et al., 2024, Das et al. *in preparation*). We divide the SFH up such that the first two and the last time bins are kept the same for all sources, covering $0 < t_l < 10$ Myrs, $10 < t_l < 100$ Myrs, and $0.85t_z < t_l < t_z$, respectively. Here, t_z represents the age of the Universe at the object's redshift, and t_l the lookback time. The remaining period between 100 Myrs and $0.85t_z$ is evenly spaced in logarithmic time. The number of bins is selected such that $\log_{10}(\Delta t_l/\mathrm{GYr}) > 0.02$ for each bin. The number of bins ranges from nine (for the lowest redshift sources) to six (for the highest). Following Smith et al. (2012), an SED fit is deemed acceptable if the best-fit χ^2 is below the 99 per cent confidence threshold for the given number of photometric bands[5].

[5]These limits were derived based on Monte Carlo simulations fit with the MAGPHYS model, and it is unlikely to be strictly applicable for our PROSPECTOR results; we intend to test how well this works in a future investigation.

	Parameter	Description	Prior/Value
Stellar Mass	$\log_{10}(M_\star/M_\odot)$	Total stellar mass formed †	Uniform; between 6.5 to 13.5
Dust attenuation	$\tau_{\lambda,2}$	Diffuse dust V-band optical depth	Uniform; between -1 and 4
	n	Diffuse dust attenuation index	Uniform; between -2 and 0.5
	$\tau_{\lambda,1}/\tau_{\lambda,2}$	The ratio of the optical depth of the birth cloud to the diffuse dust screen optical depth	Clipped normal; mean = 1, variance = 0.3, between 0 and 2
Dust emission	$U_{\rm min}$	The minimum intensity of starlight which heats up the diffuse dust and ISM	Uniform; between 0.1 and 25
	γ_e	Fraction of total dust mass affected by $U_{\rm min}$	Log uniform; between 0.001 and 0.15
	$Q_{\rm PAH}$	The fraction of total dust mass coming from polycyclic aromatic hydrocarbons (PAHs)	Uniform; between 0.1 and 10
AGN	$f_{\rm AGN}$	Total luminosity of the AGN defined as a fraction of total mid-IR ($4-20\mu$m) luminosity	Log uniform; between 10^{-5} and 3
	$\tau_{\rm AGN}$	Optical depth of the AGN torus	Log uniform; between 5 and 150
Nebular Emission	$\log_{10}(U_{\rm gas})$	Gas-phase ionisation parameter	Uniform; between -4 and -1
Fixed Parameters	IMF	Initial mass function	Kroupa (2001)
	z	Redshift	Fixed at spec-z if available, else fixed at photo-z
	$\log_{10}(Z_\odot)$	Stellar metallicity	Fixed at solar.
	$\tau_{\lambda,1}$	Additional optical depth attenuating the light from young stars	Function of $\tau_{\lambda,1}/\tau_{\lambda,2}$
	$k'(\lambda)$	Dust attenuation	Kriek and Conroy (2013) attenuation curve
	$t_{\rm bins}$	Discrete time binning scheme	Fixed, defined in Section 2.3
	$\log_{10}(Z_{\rm gas})$	Gas-phase metallicity	Equal to $\log(Z_\odot)$

TABLE 2.1: Description of the PROSPECTOR parameters used in the final model. † The PROSPECTOR models use the total stellar mass formed in a source as a free parameter, which is larger than the currently surviving stellar mass. We use the latter for analysis purposes throughout this work.

Tests show that with this setup, PROSPECTOR produces good agreement with the spectroscopic SFRs (obtained from dust extinction and aperture corrected Hα emission line measurements) for the small minority of sources in the MPA-JHU catalogue (Brinchmann et al., 2004, see Appendix A.1), and a plausible distribution of derived galaxy properties in the SFR-stellar mass plane relative to the so-called galaxy "main sequence" (e.g. the presence of a main-sequence and distinct clumps of starbursts and quiescent galaxies, as expected from works such as Noeske et al., 2007 and Schreiber et al., 2015), which is shown in Appendix A.2. We intend to further investigate the agreement between PROSPECTOR and spectroscopic SFRs in a future work. Table 2.1 summarises the key PROSPECTOR model parameters and the prior distributions that we adopt for this work.

In Figure 2.2, we present the SED output and the recovered SFH for two radio-selected galaxies: one exhibiting strong MIR emission, due to the presence of a radiative-mode AGN, and another without such emission. Both of these sources were fit twice - once with an AGN component included in the fitting process, and once with any possible AGN contribution neglected. It is evident that the source with a strong MIR emission is better fitted when an AGN template is included in the model, however the impact of the inclusion of AGN on the recovered SFHs is more complex (visible in the top right panel of Figure 2.2). On the other hand, for the source without an obvious MIR excess, the SED fits as well as the recovered SFH from the two sets of fits are virtually indistinguishable whether an AGN component is included or not.

2.3.1 Comparison of physical parameters

The principal physical quantities of interest for this work are the current stellar mass, the SFR and specific SFR (each averaged over the last 10 and 100 Myrs), and the dust luminosity computed between $8 - 1000\mu$m. The current stellar mass refers to the surviving stellar mass after accounting for losses during evolution (e.g. due to AGB winds, supernovae) and is different from the total stellar mass *formed* which is a free parameter in PROSPECTOR models. Throughout this work, the term "stellar mass" will refer to the current stellar mass, unless specified otherwise. For each of these parameters, we construct marginalised PDFs by weighting the output DYNESTY samples (analogous to Markov chains) by their corresponding importance weights. The median likelihood estimates and the 16^{th} and 84^{th} percentile bounds are computed from these PDFs. We compare these parameters to those obtained using the popular SED fitting code MAGPHYS, for sources in the radio selected sample for which both MAGPHYS and

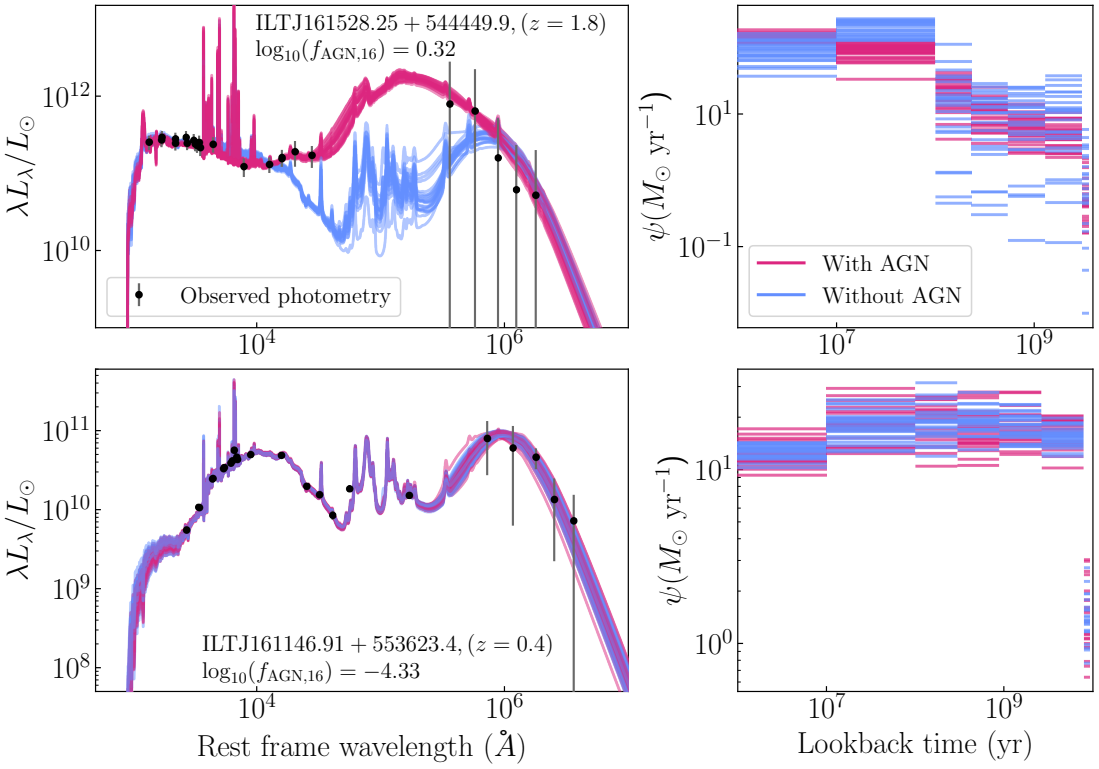

FIGURE 2.2: SED fits (left-hand panels) and recovered star formation histories (right-hand panels) for two example radio sources. ILTJ161528.25+544449.9, at a redshift of 1.8, with an estimated $\log_{10}(f_{\mathrm{AGN},16}) = 0.32$ (indicating the likely presence of radiative-mode AGN), is shown in the top panels. Meanwhile, ILTJ161146.91+553623.4, at $z = 0.4$ with $\log_{10}(f_{\mathrm{AGN},16}) = -4.33$ (implying a likely lack of radiative-mode AGN activity), is displayed in the bottom panels. In left-hand panels the photometry is shown with black dots and error bars, while solid lines represent SED fits randomly drawn from the DYNESTY chains. In all panels, red lines indicate fits with an AGN component included, while blue lines refer to fits without AGN.

PROSPECTOR produced fits that are considered acceptable following the χ^2 based criterion outlined in Smith et al. (2012). As noted above, the MAGPHYS SED fitting of LoTSS Deep Fields galaxies was done by S21 and B23, and we refer the reader to these for a detailed account of the process, highlighting here some key differences. For the stellar SEDs MAGPHYS uses a library of models based on 50,000 exponentially declining SFHs with random bursts superposed, assuming the Chabrier (2003) IMF. It uses the two-component Charlot and Fall (2000) dust model and the principle of energy balance to model the dust emission, neglecting any possible contribution of AGN.

In Figure 2.3, we compare the median likelihood estimates of stellar mass, SFR (averaged over the last 100 Myrs), sSFR, and dust luminosity estimated using MAGPHYS and PROSPECTOR. SFRs have been converted to the Kroupa (2001) IMF where necessary, using the corrections provided in Madau and Dickinson (2014). These plots are colour-coded by the 16$^{\mathrm{th}}$ percentile

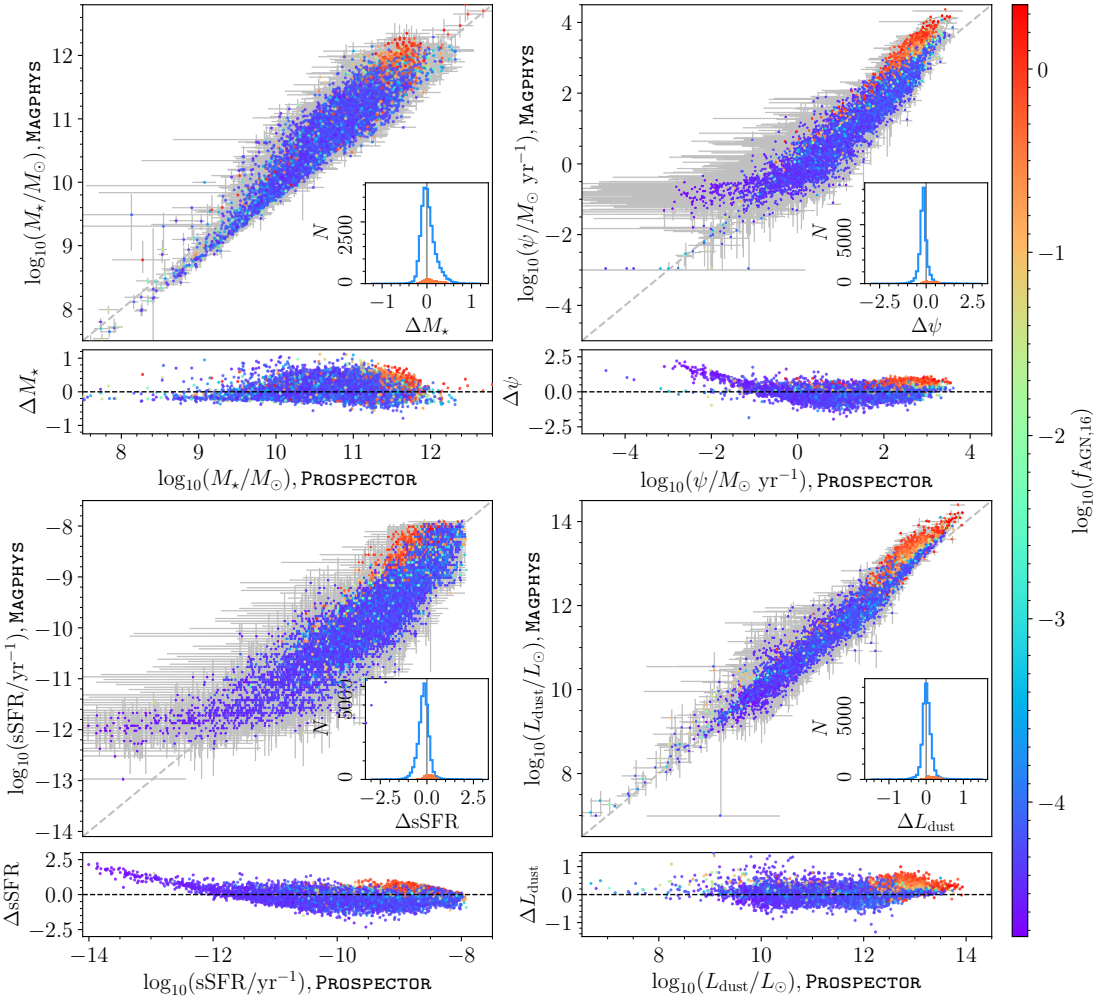

FIGURE 2.3: Median likelihood estimates of stellar mass (top-left), star formation rate averaged over the last 100 Myrs (top-right), specific star formation rate averaged over the last 100 Myrs (bottom left), and dust luminosity (bottom-right) with associated uncertainties from MAGPHYS (plotted along the y-axis) compared with those obtained from PROSPECTOR (plotted along the x-axis). The sources in each plot are colour coded by the logarithm of the 16$^{\mathrm{th}}$ percentile of AGN fraction estimated by PROSPECTOR. At the bottom of each panel, we plot the difference between the MAGPHYS and PROSPECTOR estimates ($\Delta X = \log_{10}(X_{\mathrm{MAGPHYS,median}}) - \log_{10}(X_{\mathrm{PROSPECTOR,median}})$, where X represents the physical parameter estimates). In the insets we show the distribution of this difference (ΔX), with the blue histogram representing sources with $\log_{10}(f_{\mathrm{AGN},16}) < -2$ and the orange filled histogram representing sources with $\log_{10}(f_{\mathrm{AGN},16}) > -2$.

value of the AGN fraction estimated using PROSPECTOR, to emphasize the impact of including AGN templates in the models. The ability of the AGN fraction parameter in SED fitting codes to distinguish between AGN dust emission and dust heated by star formation is strongly dependent on the MIR photometric coverage as well as on the S/N ratio of the MIR observations (Leja et al., 2018). Therefore, it is not uncommon for estimated AGN fractions to have large associated uncertainties (e.g. Ciesla et al., 2015). Following B23, we found the 16$^{\text{th}}$ percentile of the posterior of the AGN fraction to be a more reliable and robust indicator of AGN activity. Therefore, throughout this work, the term AGN fraction will be used to denote the 16$^{\text{th}}$ percentile values ($f_{\text{AGN,16}}$). Figure 2.3 shows that estimates from PROSPECTOR and MAGPHYS are in good general agreement given the uncertainties (sources with high $f_{\text{AGN,16}}$ aside). For the majority of sources, the stellar masses, SFRs and dust luminosities estimated by the two codes are within 0.3 dex of each other. The PROSPECTOR results show that a large number of sources with high median likelihood stellar masses ($M_{\text{star}} > 10^{11}$ M$_{\odot}$), SFRs ($> 10^{2}$ $M_{\odot}$/yr), and dust luminosities ($L_{\text{dust}} > 10^{12}$ $L_{\odot}$), also have high AGN fractions, leading to lower PROSPECTOR estimates of stellar mass, SFR, and dust luminosity than MAGPHYS (which treats stellar emission as the sole origin of emission). Similar trends were observed by Thorne et al. (2022b), who used a method based on PROSPECT AGN fractions[6] to identify AGN hosts. They noted a reduction of up to 2 dex in the estimated SFRs for sources with high PROSPECT AGN fractions when modelled with AGN templates, as opposed to when these sources were fitted without AGN templates. Additionally, PROSPECTOR returns lower median likelihood SFRs with larger error bars than MAGPHYS for galaxies with low SFRs (less than 1 $M_{\odot}$ yr^{-1}). While it may seem tempting to consider these larger error bars as a weakness of using PROSPECTOR with non-parametric SFHs, they are in fact one its major strengths, since previous works (e.g. Pacifici et al., 2023; Haskell et al., 2023) have shown that MAGPHYS uncertainties are likely to be underestimated for such galaxies.

To determine the degree of consistency between our work and B23, in Figure 2.4 we also compare the median likelihood stellar mass and SFR estimates with the "consensus" measurements obtained by B23 (derived for each galaxy by combining the results from four SED fitting codes, as discussed in Section 2.1). We find remarkable agreement, similar to the comparison with MAGPHYS estimates in Figure 2.3, perhaps unsurprisingly since the MAGPHYS estimates (or a median of the MAGPHYS and BAGPIPES estimates) are adopted for the large majority of sources not classified as containing AGN by B23. Nevertheless, the good agreement for the high-stellar

[6] AGN fraction in PROSPECT is defined as the fraction of the total 5–20 μm flux contributed by the AGN component.

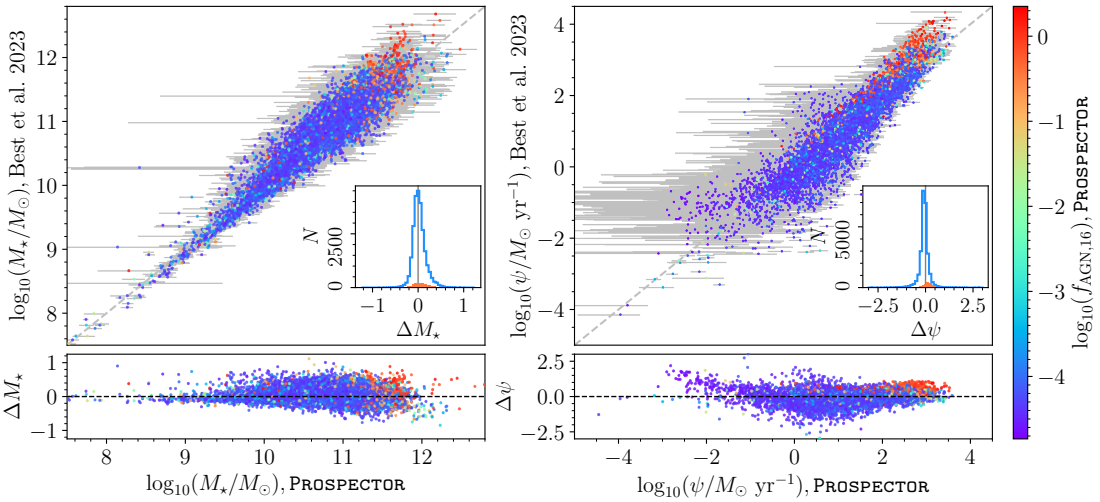

FIGURE 2.4: Comparison of the median likelihood estimates of stellar mass (left-hand panel) and the average star formation rate in the last 100 Myrs (right-hand panel) from PROSPECTOR with the consensus estimates from B23. The error bars along the x-axis represent the uncertainties in the PROSPECTOR estimates; however, uncertainties are not available for the consensus estimates from B23. The difference between the B23 consensus and PROSPECTOR estimates (as the Δ parameter, see Figure 2.3) are plotted at the bottom of each panel. Histograms depicting the distribution of the Δ parameters are shown in the insets. The blue histograms represent sources with $\log_{10}(f_{\mathrm{AGN},16}) < -2$, while the orange filled histograms represent sources with $\log_{10}(f_{\mathrm{AGN},16}) > -2$.

mass and high-SFR sources where AGN are more prevalent is very encouraging. The principal apparent disagreement between the B23 consensus values and the PROSPECTOR estimates appears in the sources with $\log_{10}(\psi_{\mathrm{B23}}/M_\odot\,\mathrm{yr}^{-1}) \lesssim 0$, however this 'difference' is not significant once the error bars are considered. Additionally, PROSPECTOR SED fits indicate that a lower number of radio-detected sources have extremely high SFRs (149 sources with SFR $> 10^3\ M_\odot\ \mathrm{yr}^{-1}$) when compared to both MAGPHYS SED fits (684) and B23 consensus estimates (418). This potentially relieves the tension between the SFR function as derived in works such as Smit et al. (2012), Duncan et al. (2014) and Katsianis et al. (2017), and that calculated in recent studies using SFRs estimated from SED fits (which predict an excess of extremely star forming galaxies, e.g. Gao et al., 2021).

2.4 Radio source classification

In this section, we look into the classification of radio detected sources into the underlying SFG, RQ-AGN, LERG, and HERG population classes. This involves two distinct parts: (i) identifying those sources hosting a radiative-mode AGN (Section 2.4.1) and (ii) identifying

radio-excess sources (Section 2.4.2). In Section 2.4.3, we combine the two criteria to give the overall classification scheme and discuss the characteristics of the various classes.

2.4.1 Identification of radiative-mode AGN

Radiative-mode AGN are typically identified using optical emission-line based diagnostics (e.g. Baldwin et al., 1981; Veilleux and Osterbrock, 1987; Kauffmann et al., 2003; Best and Heckman, 2012; Tanaka, 2012; Comerford et al., 2022) or mid-IR colour-colour cuts (e.g., Lacy et al., 2004; Stern et al., 2005; Donley et al., 2012; Messias et al., 2012). However, these methods are fraught with several caveats. Observations of the Baldwin-Phillips-Terlevich (BPT; Baldwin et al., 1981) emission lines are strongly affected by dust obscuration as well as by redshift effects. Thus the AGN identification methods that rely on optical emission lines are heavily biased against dust-obscured and low luminosity AGN (Padovani et al., 2017; Assef et al., 2018). Furthermore, spectroscopic data are not widely available; B23 report that only 5.1 per cent of the radio-detected ELAIS-N1 deep field sources have associated spectroscopic information, though the WEAVE-LOFAR survey (Smith et al., 2016) will soon offer complete spectroscopic coverage of these sources[7]. Irrespective, selection criteria based on mid-IR colour-cuts often suffer from low signal-to-noise measurements and sample incompleteness, especially when dealing with fainter galaxies. Source samples classified using these broad colour-colour cuts are also likely to be contaminated by a large number of higher-redshift inactive galaxies (Barmby et al., 2006; Georgantopoulos et al., 2008; Gürkan et al., 2014; Donley et al., 2012; Messias et al., 2012).

SED fitting can account for the possible contribution of an AGN whilst simultaneously modelling the host galaxy stars and dust. The AGN fraction parameter in PROSPECTOR directly estimates the fractional contribution of AGN to the total mid-IR ($4-20\mu$m) luminosity, and SED modelling can be used to identify AGN at lower luminosities than mid-IR colour cuts. For example, Leja et al. (2018) identify twice as many AGN using PROSPECTOR in the Brown et al. (2014) galaxy sample than what was achieved using the Stern et al. (2012) colour based selection criteria. Additionally, Thorne et al. (2022b) identified over 91 per cent of the known emission-line AGN in their sample by employing a similar method based on PROSPECT AGN fractions. The top panel of Figure 2.5 shows that the distribution of $f_{\rm AGN,16}$ for the radio-detected

[7]We note that recent Dark Energy Spectroscopic Instrument release (DESI; DESI Collaboration et al., 2016a, 2022) has already improved this situation by obtaining spectra for ∼25 per cent of the ELAIS-N1 radio sources, and these data are being investigated by Arnaudova et al. (*in preparation*).

sample has a prominent peak below 10^{-3} and a long tail above this value. Roughly 92 per cent of the sources have $f_{\mathrm{AGN},16}$ less than 10^{-3}. The tail of this distribution is primarily composed of sources that were marked as AGN by Duncan et al. (2021) on the basis of previous optical, spectroscopic, or X-ray studies. For this latter group, the distribution of $f_{\mathrm{AGN},16}$ is bimodal, with a minimum falling between 10^{-3} and 10^{-2}. We identify those sources with $f_{\mathrm{AGN},16} > 10^{-3}$ as radiative-mode AGN hosts, noting that the total number of SFGs and AGN we classify in this way depends only weakly on the chosen value for f_{AGN} within the limits of 10^{-3} and 10^{-2}.

Leja et al. (2018) and Thorne et al. (2022b) demonstrated that incorporating AGN emission in the galaxy model produces better fits (i.e., lower χ^2) for sources with a significant AGN fraction compared to fits without AGN. Therefore to further improve our ability to identify sources hosting radiative AGN, we produce PROSPECTOR fits with and without the inclusion of an AGN component in the model. Figure 2.2 presents an example where a source with excess MIR emission is better fit when AGN templates are included in the model. Inclusion of AGN templates in the model led to improved fits for 66 per cent of the radio-detected sources (middle panel of Figure 2.5), and 96 per cent of the radio-detected sources which were previously classified as AGN by optical, spectroscopic, or X-ray studies were better fitted when AGN templates were incorporated into the fitting process.

To systematically identify the sources hosting radiative AGN, we consider the distribution of $\chi^2_{\mathrm{No\ AGN}}/\chi^2_{\mathrm{AGN}}$ (where the two terms denote the goodness of the best fit SED omitting and including AGN, respectively), which is shown in the lower panel of Figure 2.5. For values below unity, this distribution can be reasonably well-fit by a Gaussian with standard deviation $\sigma = 0.057$. The sources that show a significant improvement in fits after inclusion of AGN templates are identified as AGN. A fit is considered to have significantly improved if $\chi^2_{\mathrm{No\ AGN}}$ exceeds χ^2_{AGN} by a factor of 1.17, corresponding approximately to 3σ.

Combining the two criteria, we classify a source as a radiative-mode AGN if either of the following two conditions is met:

1. If the fit including AGN in the model is considered acceptable according to the χ^2 criterion described in Section 2.3, and $f_{\mathrm{AGN},16} > 10^{-3}$, or,
2. If $\chi^2_{\mathrm{No\ AGN}} > 1.17\chi^2_{\mathrm{AGN}}$ and $f_{\mathrm{AGN},16} > 10^{-3}$.

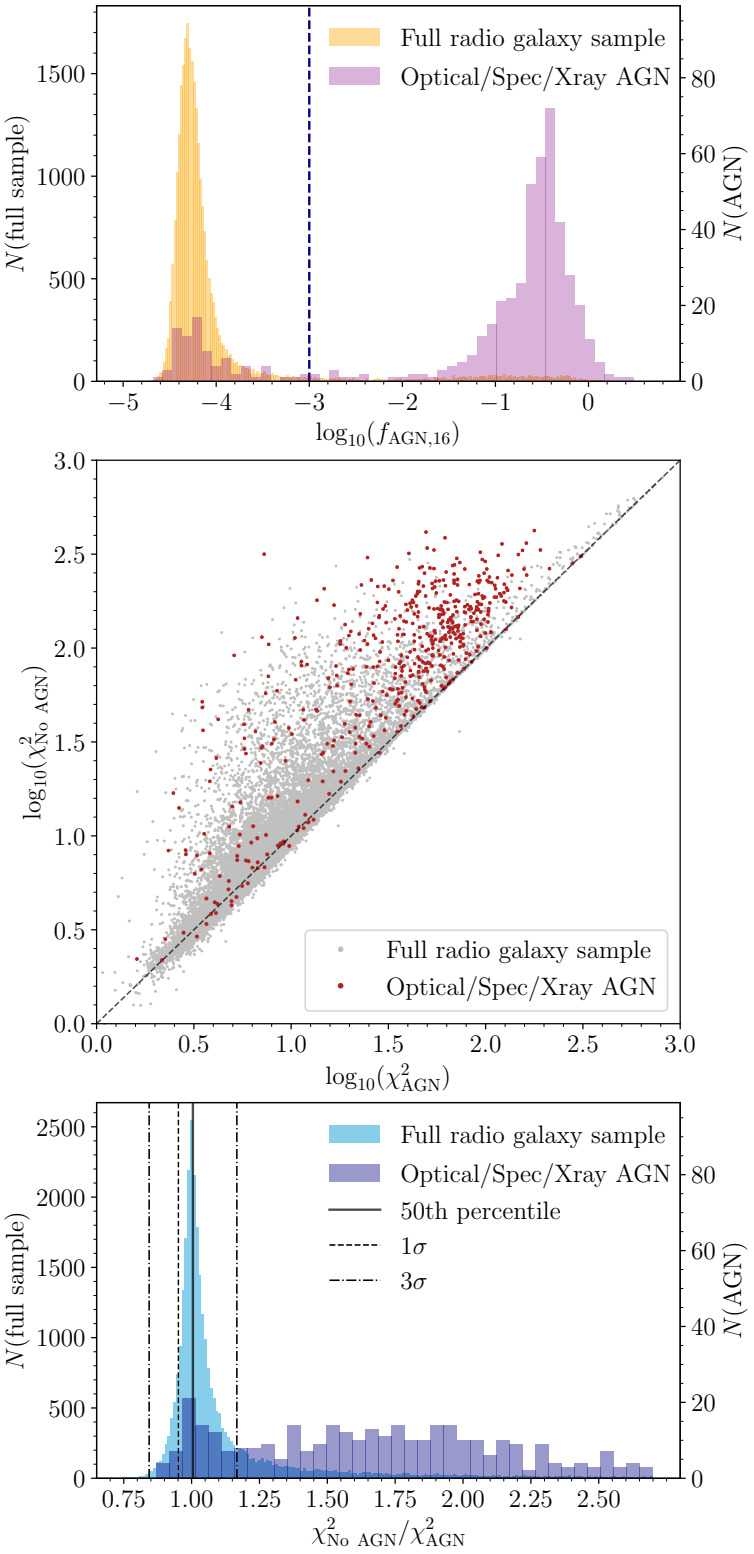

FIGURE 2.5: (Top panel) Histogram showing the distribution of $\log_{10}(f_{\mathrm{AGN},16})$. (Middle panel) Comparison of χ^2 arising from PROSPECTOR fits with AGN component included (χ^2_{AGN}) along the x-axis against the χ^2 from fits without AGN ($\chi^2_{\mathrm{No\ AGN}}$). Sources classified as AGN using previous optical/spectroscopic/X-ray studies are represented as red points. (Bottom panel) Histogram showing the distribution of $\chi^2_{\mathrm{No\ AGN}}/\chi^2_{\mathrm{AGN}}$. A majority of sources classified as AGN in previous works produce better fits when AGN templates are included in the physical model.

We flag sources that were not fitted by PROSPECTOR (owing to either a lack of redshift information or not satisfying the recommended cuts in the LoTSS Deep fields catalogue, following Duncan et al. 2021) as unclassified. Applying the aforementioned criteria, we identify 3,925 (±58) out of the 30,470 radio-selected sources as radiative-mode AGN hosts (where the quoted uncertainties have been obtained by using bootstrap resampling from among our catalogue to generate 10,000 realisations, and calculating the median, 16$^{\text{th}}$, and 84$^{\text{th}}$ percentile bounds of the resulting PDF). In this way, we have identified 82 per cent of the 503 optically-/spectroscopically-/X-ray -identified AGN and 73 per cent of the 1540 AGN selected through the Donley et al. (2012) colour cuts[8]. To assess the performance of our classification scheme, we follow the radiative-AGN selection criteria laid out in B23 and use the data from their MAGPHYS, BAGPIPES, CIGALE, and AGNFITTER catalogues to reproduce their classifications. B23 identified 3,129 out of the 30,470 sources as radiative-mode AGN, identifying 83 per cent and 75 per cent of the optically/spectroscopically/X-ray-identified and Donley et al. (2012) AGN, respectively. Although we identify 3,925 sources as hosting radiative AGN as opposed to the 3,129 sources identified by B23 (i.e., $\sim$ 25 per cent more sources), 84 per cent of the radiative-AGN classified by B23 are also identified as such by our method[9]. It is clear that the results obtained by our method to identify radiative-mode AGN, using a single SED fitting code, are comparable to those obtained using four SED codes in B23.

2.4.2 Identification of radio-excess sources

One of the key tools underpinning our ability to produce robust estimates of SFR and classify radio sources using SED fitting is the relationship between SFR and radio emission in SFGs, thought to arise due to the acceleration of cosmic rays by supernovae. This is further underscored by the well-studied far-infrared radio correlation (FIRC) in SFGs, which has been observed to be linear over several orders of magnitude (e.g. van der Kruit, 1971; de Jong et al., 1985; Helou et al., 1985; Yun et al., 2001; Jarvis et al., 2010; Bourne et al., 2011; Smith et al., 2014; Magnelli et al., 2015; Delhaize et al., 2017; Read et al., 2018; Molnár et al., 2021; Delvecchio et al., 2021; McCheyne et al., 2022). The precise nature of the FIRC, however, depends on a number of factors, such as the balance between the cosmic ray electron (CRE) escape fraction and the optical depth to UV photons (e.g. Lisenfeld et al., 1996; Bell, 2003; Lacki et al., 2010).

[8]Upon using $f_{\text{AGN},16} = 10^{-2}$ as the threshold instead, we identify 3,396 (±52) sources as radiative-mode AGN. We succeed in identifying 80 per cent and 71 per cent of the optically-/spectroscopically-/X-ray -identified and Donley et al. (2012) colour-cut selected AGN, respectively.

[9]If we adopt $f_{\text{AGN},16} > 10^{-2}$ the corresponding value is 80 per cent.

Nevertheless, radio observations provide a potentially highly attractive means of estimating SFRs for galaxies up to high redshifts, and have enabled direct studies of the correlation between SFR and radio luminosity (e.g. Condon, 1992; Cram et al., 1998; Bell, 2003; Brinchmann et al., 2004; Garn et al., 2009; Kennicutt et al., 2009; Davies et al., 2017; Tabatabaei et al., 2017). Free-free emission is a significant contributor to the radio continuum at frequencies in the GHz range and above (Condon, 1992; Murphy et al., 2011). In contrast, low frequency radio observations are largely unaffected by free-free emission. Therefore radio surveys at low frequencies, such as LoTSS, are ideal for studying the relationship between radio luminosity and SFR – provided that very low frequencies, where synchrotron self-absorption becomes significant, are carefully avoided (e.g. Kellermann and Owen, 1988; Condon and Ransom, 2016).

Works such as Brown et al. (2017); Calistro Rivera et al. (2017); Gürkan et al. (2018); Read et al. (2018); Wang et al. (2019); Smith et al. (2021) and Heesen et al. (2022) have used the sensitive LoTSS observations to study the so-called "SFR–$L_{150\ \mathrm{MHz}}$ relation". At 150 MHz, the primary source of radio emission in galaxies is the non-thermal synchrotron radiation arising either due to stellar processes or accretion activities within the central engine, including jets (Padovani et al., 2017). The latter are commonly exhibited by radio-loud active galactic nuclei (RL AGN; e.g. Urry and Padovani, 1995; Wilson and Colbert, 1995; Best et al., 2005; Harrison et al., 2014; Heckman and Best, 2014; Hardcastle et al., 2019; Das et al., 2021). RL AGN can be identified as those sources with a radio luminosity that significantly exceeds what is expected from stellar origin alone (Hardcastle et al., 2016; Williams et al., 2018; Hardcastle et al., 2019; Smolčić et al., 2017a; Calistro Rivera et al., 2017). The SFR–$L_{150\ \mathrm{MHz}}$ relation can be used to predict the radio emission expected from star formation processes alone, if the SFRs are known. In this section, we use the method of S21 to determine the SFR–$L_{150\ \mathrm{MHz}}$ relation for our SWIRE-selected galaxy sample[10]. The main steps of this approach are summarised below, though we refer the reader to S21 for a full discussion of the method.

It is crucial to account for the 150 MHz properties of the sources irrespective of whether or not they are detected in the LoTSS catalogue. Failing to do so risks biasing the results towards the radio-bright sources. We therefore use the PROSPECTOR SED fits for the SWIRE-selected sources. This sample, as demonstrated in Section 2.2.3, includes sources that were not individually catalogued at 150 MHz by Sabater et al. (2021). It is therefore key to getting a true measure of the low frequency radio source population, given that the source counts of radio sources at

[10] B23 used a complementary approach to find the SFR–$L_{150\,\mathrm{MHz}}$ relation, based on a "ridgeline" approach, giving very similar results.

low frequencies are dominated by low luminosity SFGs (e.g. Wilman et al., 2008; de Zotti et al., 2010; Williams et al., 2016; Calistro Rivera et al., 2017; Williams et al., 2019; Mandal et al., 2021; Hale et al., 2023). Excluding objects flagged as AGN by Duncan et al. (2021) and avoiding those for which PROSPECTOR fails to produce acceptable fits, we are left with 120,307 SWIRE-selected galaxies for our analysis. We first obtain the median likelihood SFRs (averaged over 100 Myr) along with asymmetric uncertainties derived using the 16$^{\rm th}$, 50$^{\rm th}$ and 84$^{\rm th}$ percentiles of the derived SFR PDFs, which are equivalent to median $\pm1\sigma$ in the limit of normally distributed data. Next, we use 150 MHz flux densities and uncertainties from the Sabater et al. (2021) catalogue where they exist, and supplement these for the remaining sources with flux densities (and associated RMS uncertainties) measured from the pixel corresponding to the source position in the ELAIS-N1 maps from LoTSS Deep fields DR1. For each source, we then construct a two-dimensional PDF in the SFR–$L_{150\ \rm MHz}$ parameter space with logarithmic axes: 70 equally spaced logarithmic SFR bins between $-3 < \log_{10}(\psi/M_\odot\ \rm yr^{-1}) < 3$ and 180 equally spaced log-bins between $17 < \log_{10}(L_{150\ \rm MHz}/\rm W\ Hz^{-1}) < 26$. This PDF is populated for each source by creating 100 random samples from an asymmetric error distribution, with the median set to the median-likelihood PROSPECTOR SFR estimate and different standard deviations on either side of the median. The standard deviation of the positive wing is taken as the difference between the 84$^{\rm th}$ and 50$^{\rm th}$ percentile bounds of the PROSPECTOR SFR PDF, while the standard deviation of the negative wing is taken as the difference between the 50$^{\rm th}$ and 16$^{\rm th}$ percentile bounds.

For the 150 MHz luminosities we use 100 independent samples from a symmetric normal distribution in linear space, centred on the luminosity obtained from the flux density estimate (either from the catalogue, or from the pixel measurements) assuming the best redshift and a spectral index of $\alpha = 0.7$. The standard deviation on the luminosity distribution is obtained by scaling the uncertainties on the flux density measurements such that the signal-to-noise on the derived luminosity is equal to that on the measured flux densities. The 2D PDFs for each source are then summed, to generate a PDF that accounts for the uncertainties in both the SFR and $L_{150\ \rm MHz}$. To ensure that sources with low S/N and negative radio luminosities were included (since not doing so would censor the distribution and lead to skewed median-likelihood luminosity measurements), we follow S21 and arbitrarily assign samples with $\log_{10}(L_{150\ \rm MHz}) < 17$ to the lowest $L_{150\ \rm MHz}$ such that each source is equally represented in the 2D stacked PDF. Similarly, we arbitrarily assign samples with $\log_{10}(\psi/M_\odot\ \rm yr^{-1}) < -3$ to the lowest log SFR bin. We then calculate the 16$^{\rm th}$, 50$^{\rm th}$, and 84$^{\rm th}$ percentiles of the $L_{150\ \rm MHz}$ distribution in each log SFR bin, with the 50$^{\rm th}$

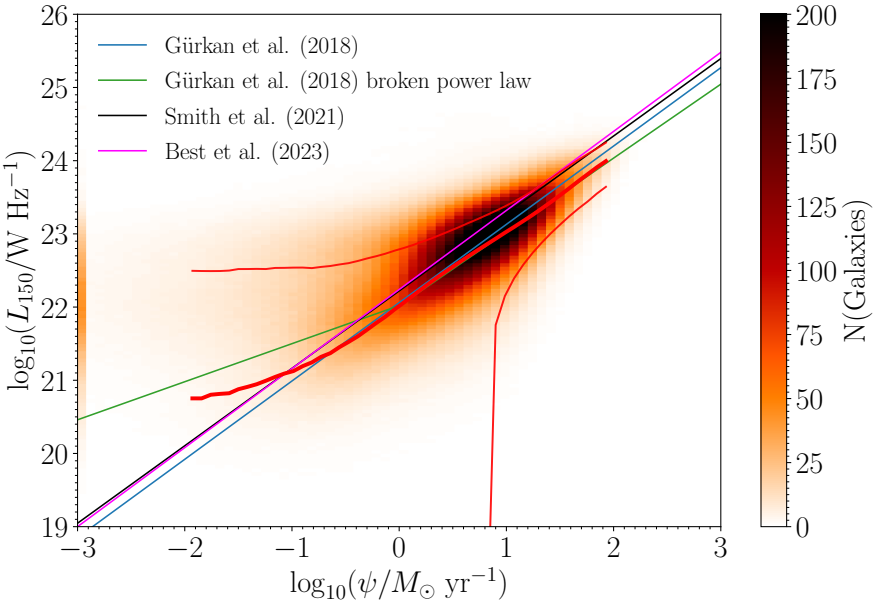

FIGURE 2.6: Stacked two dimensional heatmap showing the SFR–$L_{150\ \mathrm{MHz}}$ plane, constructed by summing over the PDFs of sources in the SWIRE-selected sample. The thick red curve represents the median likelihood SFR–$L_{150\ \mathrm{MHz}}$ relation. The accompanying thin red curves indicate the 16$^{\mathrm{th}}$ and 84$^{\mathrm{th}}$ percentiles of the $L_{150\mathrm{MHz}}$ distribution at each SFR, respectively. The blue and green solid lines represent the single slope and broken power law relations from G18. The black and magenta solid lines represent the best fit relations from S21 and B23 respectively.

percentile values denoting the median likelihood SFR–$L_{150\ \mathrm{MHz}}$ relation.

By fitting a straight line to the stellar mass-independent relation given by G18:

$$L_{150\ \mathrm{MHz}} = L_1\ \psi^{\beta}, \tag{2.1}$$

we obtain a best-fit estimate of $\beta = 1.019 \pm 0.009$ and $\log_{10} L_1 = 22.024 \pm 0.006$. Uncertainties are computed using EMCEE, which was run with 64 walkers and a chain length of 10,000 samples. In comparison, the following best-fit estimates were obtained in past works: $\beta = 1.07 \pm 0.01$ and $\log_{10} L_1 = 22.06 \pm 0.01$ (G18); $\beta = 1.058 \pm 0.007$ and $\log_{10} L_1 = 22.221 \pm 0.008$ (S21); $\beta = 1.08 \pm 0.06$ and $\log_{10} L_1 = 22.24 \pm 0.07$ (B23). Unlike the studies by G18 and S21, our best fit slope is consistent with unity after factoring in uncertainties.

As discussed at length in S21, the SFR–$L_{150\ \mathrm{MHz}}$ relation has significant dispersion, which we must account for in order to identify those sources with a radio excess. To do this, we consider the difference between the 50$^{\mathrm{th}}$ and 84$^{\mathrm{th}}$ percentiles[11] of the $L_{150\mathrm{MHz}}$ distribution for

[11] We have elected to use the 50$^{\mathrm{th}}$ and 84$^{\mathrm{th}}$ percentiles rather than the 16$^{\mathrm{th}}$ and 50$^{\mathrm{th}}$ percentiles since the distribution is asymmetric, with increased scatter on the bottom side due to the lower signal to noise ratio of the fainter sources in the 150 MHz maps.

$\log_{10}(\psi/M_\odot\ \mathrm{yr}^{-1}) > 1.5$, finding $\sigma = 0.289$ dex. This is in good agreement with the results of Cochrane et al. (2023), who found a scatter of 0.3 dex by comparing the shapes of SFR functions for radio- and SED-estimated SFRs. We specifically avoid including sources with SFRs less than $1.5 M_\odot \mathrm{yr}^{-1}$ to mitigate the impact of large uncertainties associated with the best-fit relation at low SFRs (e.g. Figure 2.6).

Using this information, we identify sources that exceed the best-fit SFR–$L_{150\ \mathrm{MHz}}$ relation by 0.867 dex (equivalent to a 3σ excess) as having significant radio-excess (this criterion is indicated by the blue dot-dashed line in Figure 2.7). Additionally, as seen in Section 2.3.1, SED fitting cannot accurately measure the SFRs for sources with very low SFRs, and thus the radio-excess classifications of these sources are likely to be unreliable. To avoid this issue, B23 classified 0.4 per cent of their sources which had SFRs $< 0.01 M_\odot\ \mathrm{yr}^{-1}$ as radio-excess only if their radio luminosities exceeded that expected for a source with SFR $= 0.01 M_\odot\ \mathrm{yr}^{-1}$ by 0.7 dex. If the radio luminosity of such a source was below that value but still surpassed the radio-excess threshold determined by the SED-fitted SFR estimate, then it was designated as Unclassifiable. We follow B23 and similarly mark 0.1 per cent of our sample as Unclassified. Among the 30,470 sources in the radio-selected sample, we identify 5,250 ± 66 sources as having a radio excess (B23 identified 4,786 sources). Uncertainty in the count of radio excess sources is calculated using bootstrapping, in a similar manner that was adopted for radiative-mode AGN identification in Section 2.4.1. The median likelihood SFR estimates from Prospector are lower than the consensus SFRs estimated by B23 for 92 per cent of the sources where the radio-excess classifications differ. In these cases, the radio-excess thresholds calculated for the Prospector results are lower than the thresholds based on B23's results. We therefore classify about 10 per cent more sources as radio-excess than B23.

We mark sources with unacceptable fits according to the χ^2 threshold criterion as "Unclassified", since the Prospector model does not apply and we cannot use the SFR estimates to quantify the expected 150 MHz luminosity. This results in a higher number of sources being flagged as unclassified compared to B23; we have 1,532 compared to 240 (these numbers differ from those shown in Table 2.2 since there the numbers include sources irrespective of whether they have redshifts or are flagged in the cuts recommended by Duncan et al. 2021). Our classifications are in agreement with B23 for 77 per cent of the sources they classified as radio-excess and 90 per cent of the sources they identified as not having a radio excess. While there are non-negligible areas of implied disagreement among the radio-loud classification (e.g. the ∼ 23 per cent of the B23 radio-excess sources not identified using our method which are not apparent in Figure

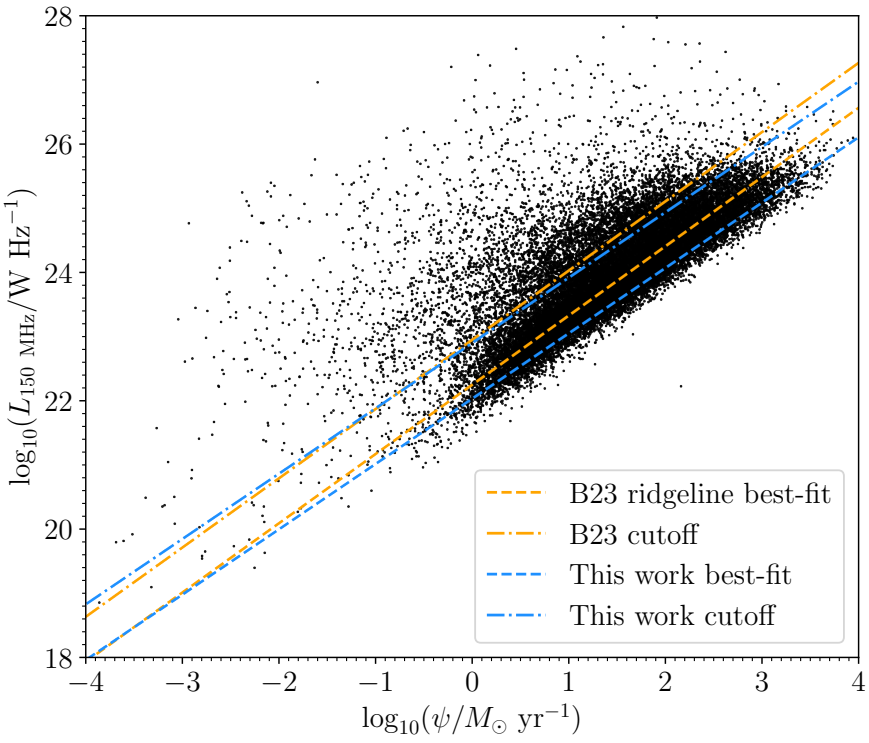

FIGURE 2.7: Maximum likelihood 150 MHz radio luminosities of the radio-detected sample plotted as a function of the PROSPECTOR estimated median SFRs. The best-fit SFR–$L_{150\ \mathrm{MHz}}$ relation (obtained from the SWIRE-detected sample and therefore including radio non detections) and the radio-excess cut-off used in our work (blue) and in B23 (orange) are overplotted.

2.7 since the B23 consensus estimates are not plotted), this type of classification is inherently uncertain: we do not know what the "correct" answer should be for these sources (e.g. Drake et al., 2024). Irrespective, the good general agreement in the radio-AGN classification between the two works offers significant encouragement.

2.4.3 Final classifications

Here, following B23, we combine the radiative-mode and radio-excess AGN classifications discussed in the previous sections to assign each source to one of the five classes: SFG, RQ AGN, LERG, HERG and Unclassified. Specifically:

- sources that have been identified as neither radiative-mode nor having a radio excess are classified as *SFG*;
- those that are identified as radiative-mode AGN hosts, without a radio excess, are classified as *RQ AGN*;

	SFGs	RQ AGN	LERGs	HERGs	Unc.
This work	21257 ± 83	2431 ± 47	4393 ± 61	857 ± 28	2672 ± 49
B23	22720	2779	4287	510	1314

TABLE 2.2: The number of star forming galaxies, radio-quiet AGN, low-excitation radio galaxies, and high-excitation galaxies, identified in the ELAIS N1 deep field using our classification scheme, along with uncertainties calculated using bootstrap resampling. B23 classification results are also included for comparison.

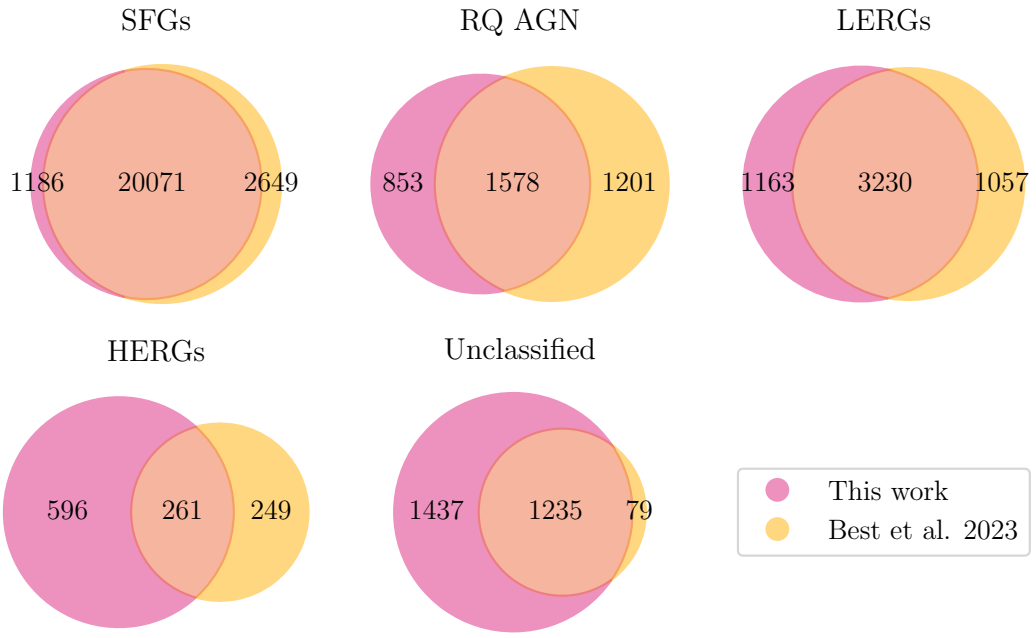

FIGURE 2.8: Venn diagrams showing the number of sources in each class (star-forming galaxies, radio-quiet AGN, low- or high-excitation radio galaxy) that have been identified by our method (pink), by B23 (yellow) and by both (overlap region).

- objects not identified as radiative-mode AGN hosts but showing a significant radio excess are classified as *LERG*;
- hosts of radiative-mode AGN with significant radio excess are classified as *HERG*; and finally
- sources for which we are unable to obtain an acceptable PROSPECTOR SED fit remain *Unclassified*.

The number of sources in each category is shown in Table 2.2, while the degree of overlap between the sources identified following our classification scheme and those presented by B23 is illustrated in Figure 2.8.

Overall, our classification method identifies similar numbers of SFGs (6 per cent lower), RQ AGN (12 per cent lower) and LERGs (2 per cent higher) relative to the results of B23. However, there

are larger differences apparent in the number of HERGs and unclassified sources, where our numbers are 68 and 203 per cent larger. The former change – in the number of HERGs – results primarily from the details of the precise definition of a radio excess that we discussed in Section 2.4.2 relative to B23 (and shown in Figure 2.7). This change represents an increase from 1.6 per cent to 2.7 per cent of the radio-selected catalogue, and though this increase is significant, HERGs remain a small minority of the overall source population, perhaps highlighting the difficulty of this task. In the case of B23, a source is flagged as Unclassified if it fails to produce an acceptable fit in multiple codes. Consequently, they report significantly fewer Unclassified sources compared to our results. While we do not formally classify the sources with unacceptable PROSPECTOR fits, roughly 70 per cent of the sources would be consistent with SFGs, 10 per cent with RQ AGN, 13 per cent with LERGs, and 3 per cent with HERGs, if we were to disregard the checks for fit acceptability. Interestingly, this is in good agreement with the final classification results, indicating that the ability of PROSPECTOR to produce an acceptable fit for a source is approximately independent of the underlying population class. This could suggest that the χ^2 based acceptability criterion we have used on the PROSPECTOR SED fits may be conservative, and we intend to investigate this possibility in a future work.

Similarly to B23, we further examine the demographics of the different AGN classes based on stellar mass, SFR, 150 MHz radio flux density, radio luminosity, redshift, and optical r-band magnitude; these results are shown in Figure 2.9. In each of these figures, our results are shown as the solid lines (coloured according to the classifications as indicated in the legend) and with shaded areas according to the uncertainties implied assuming Binomial statistics (e.g. Cameron, 2011). The corresponding values from the B23 catalogue are shown as squares with dotted lines of the relevant colour, enabling a direct comparison.[12]

The upper panels of Figure 2.9 show the distribution of the different classes based on the median likelihood estimates of stellar mass and SFR from PROSPECTOR. SFGs are the dominant population class for most of the low-to-intermediate stellar mass ranges. At higher stellar masses, the number of AGN sees a steep rise, led by LERGs. Additionally, LERGs dominate the source fractions at SFRs below $\sim 1\ M_{\odot}\,\mathrm{yr}^{-1}$, supporting the view that they are hosted by massive, quiescent galaxies (e.g., Tasse et al., 2008; Smolčić, 2009; Best and Heckman, 2012; Heckman and Best, 2014; Williams et al., 2018). Overall, the stellar mass and SFR demographics in Figure 2.9 are similar to those observed by B23, with the principal differences attributable to the

[12]The B23 results shown in Figure 2.9 do not exactly match those plotted in B23 figure 9, since B23 applied additional cuts in some of their plots, e.g. $z < 2$ for the 150 MHz radio luminosity plot (P. Best, *private communication*), whereas we use the full sample to directly compare with the published catalogue.

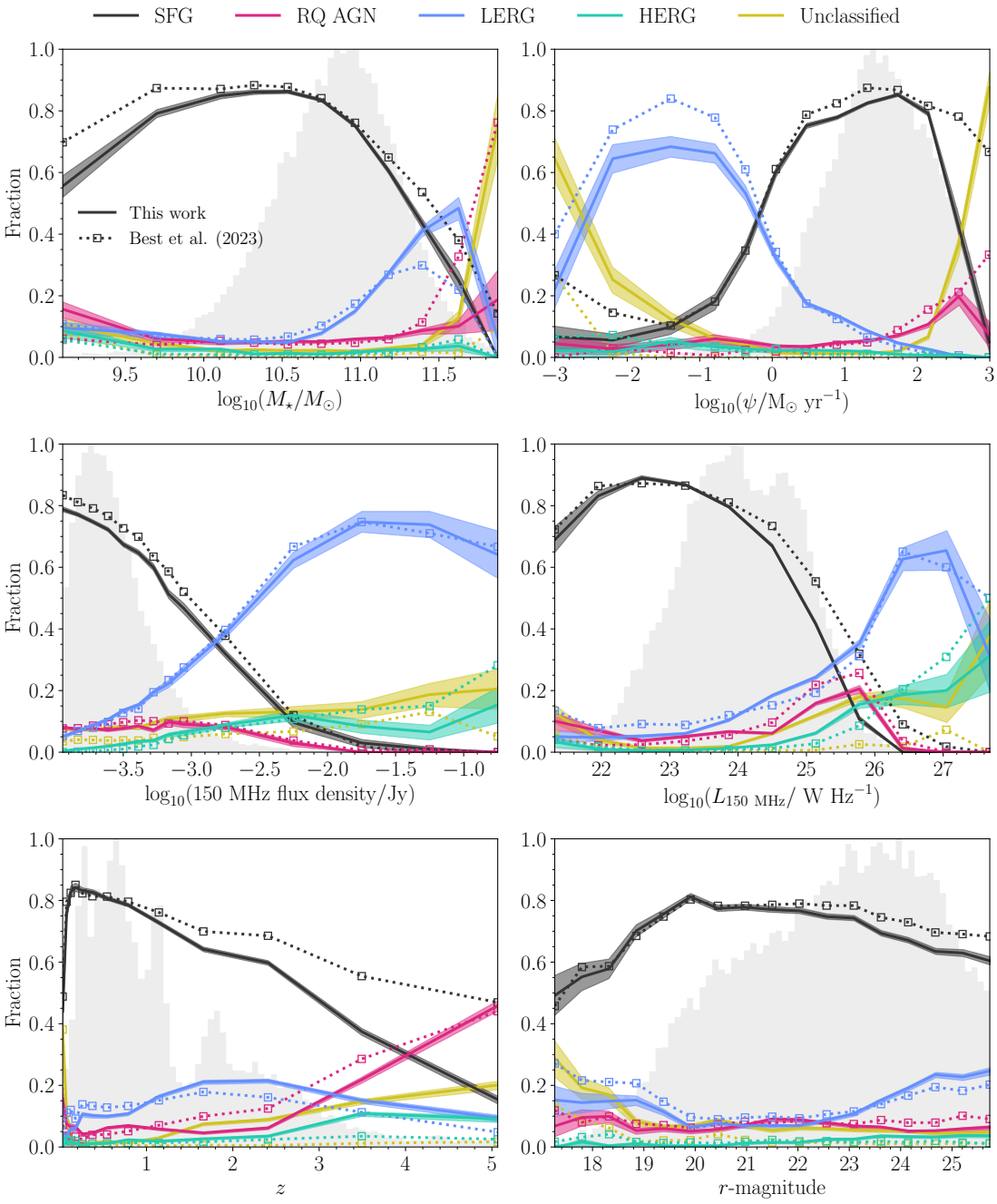

FIGURE 2.9: Sources classified as SFG (in black), RQ-AGN (orange), LERG (blue), HERG (purple), and the sources marked unclassified (in green), represented as the fraction of total sources. We show the distribution of sources in each galaxy class as a function of (top-left panel) PROSPECTOR median likelihood stellar mass estimates, (top-right panel) PROSPECTOR median likelihood SFR estimates, (centre-left panel) 150 MHz radio flux density, (centre-right panel) 150 MHz radio luminosity, (bottom-left panel) redshift, and (bottom-right panel) optical r-band magnitude. The dotted lines with open squares represent the fractions of sources in each galaxy class from B23. In the top-left and top-right panels, we plot the B23 source fractions against the B23 consensus stellar mass and SFR estimates, respectively. The distribution of the whole sample as a function of the respective quantities is shown in the background, as a normalised grey histogram with peak being equal to unity.

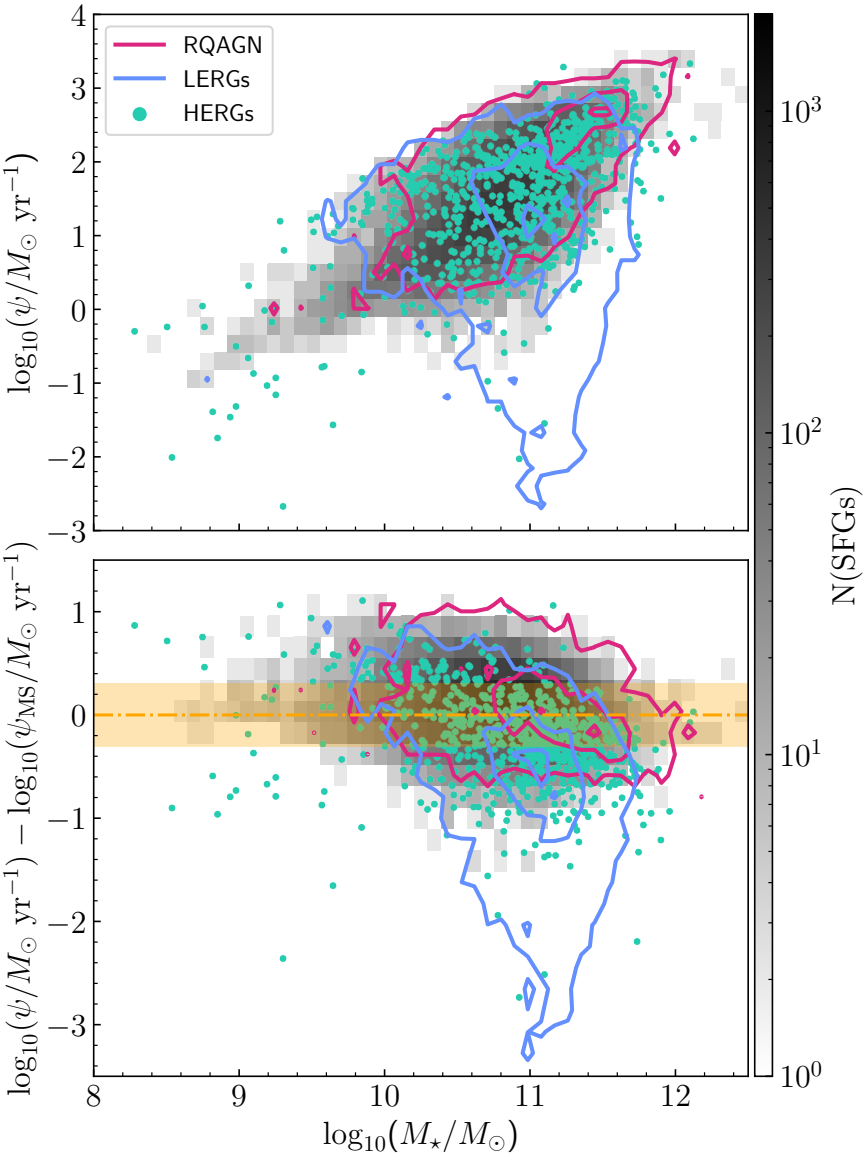

FIGURE 2.10: Distribution of the different source classes in the stellar mass–SFR plane: the shaded 2D histogram represents the SFGs, the overlaid purple and blue contours represent the RQ AGN and LERGs, respectively, and the cyan circles denote the HERGs. In the bottom panel, the solid orange line and the shaded orange region represent the Schreiber et al. (2015) parametrisation of the main sequence converted to our adopted Kroupa (2001) IMF with the typical 0.3 dex scatter around it. Contour levels are selected to encompass 5, 50, and 90 per cent of the corresponding sample.

larger number of Unclassified sources in this work (which become the dominant component at the highest stellar masses and SFRs).

The remaining panels in Figure 2.9 depict the fractions in each class as a function of 150 MHz flux density, luminosity, redshift and r-band magnitude. The demographics of each source type as a function of the 150 MHz radio flux density are generally in agreement with the findings of B23. The LERG and HERG source fractions as functions of 150 MHz radio luminosity follow similar trends as seen in B23. We observe an abundance of LERGs at the highest radio luminosities. It must be noted here that the ELAIS-N1 field may not probe enough volume to reach the very highest radio powers where HERGs dominate. Nevertheless, at the very highest radio luminosities, the HERG fraction sees a steep rise, and the fractions of LERGs and HERGs appear to be roughly equal. This steep rise in HERG fraction strongly hints at HERGs becoming the dominant class at higher luminosities, which is consistent with expectations (e.g., Best and Heckman, 2012; Heckman and Best, 2014; Pracy et al., 2016). The population of RQ AGN remains relatively stable at around 10 per cent below 1 mJy and sees a steady decline above that. Our findings are consistent with B23's results and are lower than the observed fractions of approximately 15-20 per cent reported in studies such as Simpson et al. (2006) and Smolčić et al. (2017a). This difference is likely because of the RQ AGN typically having flatter spectral indices than SFGs (e.g. Gloudemans et al., 2021), and therefore as noted by B23, they are likely to be less prominent at the low frequencies probed by LOFAR than at GHz frequencies and higher. The transition from a sample dominated by star formation to one dominated by radio-loud AGN occurs around 1.6 to 2 mJy, which closely aligns with B23's finding of 1.5 mJy. As noted by those authors, this is consistent with the transition occurring around $200-250\mu$Jy at a higher frequency of 1.4 GHz, assuming typical radio spectral indices (Padovani, 2016; Smolčić et al., 2017a).

We detect radio sources of each class at all redshifts and optical r-band magnitudes. At $z > 1$, we observe lower SFG and RQ-AGN fractions compared to B23, but an increased fraction of LERGs. Our results suggest that SFGs dominate up to redshifts $z \sim 4$, and are subsequently overtaken by RQ AGN. We observe a steeper decline in the SFG fraction with redshift compared to B23, whose classifications suggest a transition from a star-formation dominated sample to an AGN dominated sample at $z \sim 4.5$. We note that the reduced SFG fractions relative to B23 could be caused by (i) a larger number of sources being classified as radio-loud AGN at high redshifts, owing to PROSPECTOR estimating lower SFRs for sources with extreme SFRs (often found at very high redshifts) than B23, therefore having lower radio-excess thresholds, and (ii)

a larger number of potential SFGs being flagged as 'Unclassified' in this work on account of the unacceptable PROSPECTOR SED fit χ^2. The LERG fraction peaks around $z \sim 2$ and subsequently decreases, while RQ-AGN, HERGs and Unclassified sources all increase at $z > 3$. This hints at the existence of an evolutionary relationship between a more energetic, radiative-AGN dominated source population in the early stages of the universe and the jet-mode population at cosmic noon. We draw the attention of the reader to the increase in the fraction of unclassified sources with redshift, with approximately 20 per cent of sources labelled as unclassified at $z = 5$ in our results, and advise caution when using our classifications at high redshifts.

In Figure 2.10, we show the SFR vs stellar mass plane, populated by a shaded 2D histogram showing the number of SFGs at each point colour-coded according to the legend on the right-hand side, which is shared between both the top and bottom panels. In the lower panel, the SFRs have been calculated relative to the so-called "main sequence" relation from Schreiber et al. (2015), converted to our adopted Kroupa (2001) IMF. The typical scatter of ±0.3 dex is indicated by the shaded orange region. Overlaid on the SFGs are contours delineating the locations of the RQ AGN (purple) and LERGs (blue), while the HERGs are represented by cyan circles. The contour levels have been chosen such that they include 5, 50, and 90 per cent of the sample. The SFGs lie broadly around the main sequence as expected, although the observed scatter is slightly greater than the canonical ±0.3 dex reported in literature (e.g. Tacchella et al., 2015). As seen in the bottom panel, a considerable portion of the SFG distribution lies above the main sequence, indicating the presence of a population of starbursts in the radio-detected sample. The RQ AGN occupy a similar region of parameter space as the SFGs, albeit biased towards the high stellar-mass end of the distribution, consistent with our expectations that AGN predominantly reside in higher-mass galaxies (e.g., G18 and Kondapally et al., 2022). Notably, we find a significant population of LERGs ($\sim$ 33 per cent) to lie on or above the main sequence, consistent with the distinct populations of star-forming and quiescent LERGs discussed by Kondapally et al. (2022). At higher stellar masses, LERGs are hosted across all SFRs, whereas at lower stellar masses, only star-forming galaxies host LERGs. This is in agreement with the findings of Kondapally et al. (*in preparation*), and supports their hypothesis that different fuelling mechanisms may be prevalent in different classes of LERGs. Lastly, we observe that 58 per cent of the HERGs lie within the typical 0.3 dex range of the main sequence, with the significant majority of HERGs falling within a 0.6 dex scatter. Our classifications thus align with works such as Best and Heckman (2012), Best et al. (2014), Pracy et al. (2016), and Kondapally et al. (2022), who noted that HERGs were typically hosted by star-forming galaxies.

2.5 Stellar mass dependence in the SFR–150 MHz radio luminosity relation

As discussed in Section 2.4.2, LoTSS data have been extensively used to study the SFR–$L_{150\ \mathrm{MHz}}$ relation. Brown et al. (2017), Wang et al. (2019), and Heesen et al. (2022), found a super-linear relationship (slope greater than unity) between SFR and 150 MHz radio luminosity. G18 found an upturn towards larger radio luminosity at low SFRs, which is in disagreement with calorimetric arguments, and in the opposite direction to the downturn reported by Bell (2003). G18, Read et al. (2018), and S21 also found evidence for a strong stellar mass dependence in the SFR–$L_{150\ \mathrm{MHz}}$ relation. In this section, we seek to address the question of stellar mass-dependence using the SFR and stellar mass estimates from PROSPECTOR.

2.5.1 Determining stellar mass dependence using Prospector SED fits

For this analysis, we focus on the $z < 1$ SWIRE-selected galaxy sample with acceptable PROSPECTOR SED fits. We excluded sources that showed a significant AGN contribution (either radiative mode or radio excess, as defined in Section 2.4.3). We also removed the radio non-detected sources that were flagged as AGN using spectroscopy, X-ray detections, or mid-IR colour-colour cuts by prior studies (Duncan et al., 2021). After applying these cuts, we were left with a sample of 85,162 predominantly star-forming and passive galaxies. Following S21, we extend the stacked PDF method described in Section 2.4.2 to three dimensions. 100 samples are generated for each source along the SFR, stellar mass, and $L_{150\ \mathrm{MHz}}$ axes. We adopt skewed error distributions in log space for SFR and stellar mass using the 16^{th}, 50^{th}, and 84^{th} percentile PROSPECTOR estimates. $L_{150\ \mathrm{MHz}}$ is sampled from a normal distribution in linear space centred at the maximum likelihood estimate and with standard deviation equal to the RMS.[13]

We then create a three-dimensional histogram of the samples, summing over all the sources to create a stacked PDF. We use 50 equally spaced logarithmic stellar mass bins between $7.5 < \log_{10}(M/M_{\odot}) < 11.8$, 60 equally spaced logarithmic SFR bins between $-3 < \log_{10}(\psi/M_{\odot}\ \mathrm{yr}^{-1}) < 3$, and 180 equally spaced logarithmic $L_{150\ \mathrm{MHz}}$ bins between $17 < \log_{10}(L_{150\ \mathrm{MHz}}/\mathrm{W\ Hz}^{-1}) < 26$ and calculate the median $L_{150\ \mathrm{MHz}}$ in each SFR and stellar mass bin. As before, the samples

[13] This does not explicitly account for the negative radio fluxes arising due to the noise; nevertheless, this does not affect our results because any samples with $L_{150\ \mathrm{MHz}} < 10^{17}$ W Hz^{-1} are assigned to the lowest $L_{150\ \mathrm{MHz}}$ bin during PDF construction.

with $L_{150\ \mathrm{MHz}} < 10^{17}$ W Hz^{-1} and SFR $< 10^{-3}$ $M_\odot$ yr^{-1} are arbitrarily assigned to the lowest $L_{150\ \mathrm{MHz}}$ and log SFR bins, respectively.

Similar to G18 and S21, we find clear evidence of stellar mass dependence in the SFR–$L_{150\ \mathrm{MHz}}$ relation (Figure 2.11). In all the panels of Figure 2.11, only the bins populated by a minimum of 15 galaxies are displayed, taking into account that each source is sampled 100 times. The top-left panel of this figure shows the median-likelihood $L_{150\ \mathrm{MHz}}$ as a function of SFR in different stellar mass bins indicated by the colour bar to the right. Interestingly, this plot indicates that the relationship between SFR and $L_{150\ \mathrm{MHz}}$ becomes progressively sub-linear as we move towards higher stellar mass bins. This observation may suggest the influence of non-calorimetric processes, such as the rapid diffusion of CREs within star-forming regions, as discussed by Berkhuijsen et al. (2013) and Heesen et al. (2019), or perhaps the presence of undiagnosed low-luminosity contamination by AGN (as discussed in S21). Furthermore, in contrast to S21 our PROSPECTOR results indicate that the stellar mass dependence (as apparent by the difference between the most- and least-150 MHz luminous stellar mass bins), appears weaker at $\log_{10}(\psi/M_\odot\ \mathrm{yr}^{-1}) > 0.5$ than for the lower SFR galaxies.

The top-right panel of Figure 2.11 displays the median-likelihood $L_{150\ \mathrm{MHz}}$ as a function of stellar mass in different SFR bins. It is immediately clear that there is an increase in $L_{150\ \mathrm{MHz}}$ with stellar mass (consistent with S21 and Heesen et al. 2022). However, in keeping with expectations on the basis of the top-left panel, the gradient of the stellar mass–radio luminosity relation appears to flatten with increasing stellar mass (though the increasingly small stellar mass range probed for the highest SFRs precludes a definitive statement based on visual inspection alone).

To investigate these trends further, we fit our data using the stellar mass dependent form of the SFR–$L_{150\ \mathrm{MHz}}$ relation from G18:

$$L_{150\ \mathrm{MHz}} = L_1\ \psi^\beta \left(\frac{M}{10^{10} M_\odot}\right)^\gamma. \tag{2.2}$$

We use EMCEE with 16 walkers and 10,000 iterations to calculate the uncertainties associated with these fits. The following best fit values are obtained: $\log_{10} L_1 = 22.083 \pm 0.004$, $\beta = 0.778 \pm 0.004$, and $\gamma = 0.334 \pm 0.006$. S21 used simulations to reveal small biases in these estimates, and suggested that the uncertainties are likely to be underestimated (with true uncertainties around $\sigma_\beta = 0.011, \sigma_{\log_{10} L_1} = 0.016$, and $\sigma_\gamma = 0.037$; correcting for these biases will be discussed at length in Shenoy et al. *in preparation*). By way of comparison, S21 obtained best fit estimates of

$\log_{10} L_1 = 22.218 \pm 0.016$, $\beta = 0.903 \pm 0.012$, and $\gamma = 0.332 \pm 0.037$, while G18 found $\log_{10} L_1 = 22.13 \pm 0.01$, $\beta = 0.77 \pm 0.01$, and $\gamma = 0.43 \pm 0.01$. While the exponent of SFR dependence (β) seen in our results is close to that found by G18, the exponent of the stellar mass dependence differs. On the other hand, we see a similar degree of stellar mass dependence to S21, but the SFR dependence differs between the two works. To determine whether incompleteness in our sample selection could be playing a role in our findings, we followed S21 and repeated our analyses using a 95 per cent stellar mass-complete sample of 64,838 sources derived using the method of Pozzetti et al. (2010), finding that our results are statistically unchanged. We therefore conclude that stellar mass completeness does not significantly impact our results.

In the bottom-left panel of Figure 2.11, we plot the stellar mass-adjusted radio luminosity (obtained by dividing the $L_{150\ \mathrm{MHz}}$ data shown in the top panels by the best fit stellar mass-dependent term in Equation 2.2) in an attempt to reveal the SFR–$L_{150\ \mathrm{MHz}}$ relationship with the stellar mass effects accounted for. At $\log_{10}(\psi/M_\odot\ \mathrm{yr}^{-1}) > 0.5$, the $L_{150\mathrm{MHz}}$ values in different stellar mass bins virtually collapse into a single line, while at lower SFRs there is still significant scatter, to a similar degree seen in S21. The differences observed between our results and those of S21, as well as the inferred stellar mass dependence in the SFR–$L_{150\ \mathrm{MHz}}$ relationship, may be partially attributed to the assumed SFH and the various explicit or implicit priors used in the SED fitting process. While the non-parametric continuity prior used in this work has been shown to be flexible enough for modelling a diverse range of galaxy SEDs (Leja et al., 2019; Johnson et al., 2021; Haskell et al., 2024, Das et al. *in preparation*), it is still by no means perfect and may not be uniformly appropriate at all stellar mass scales (e.g. lower mass galaxies are expected to have burstier SFHs; Hopkins et al., 2023). Moreover, the apparent 'break' in the SFR–$L_{150\ \mathrm{MHz}}$ relation might suggest the requirement for additional physics.

2.5.2 The influence of passive galaxies

Our findings in Section 2.5.1 point towards a more pronounced dependence on stellar mass in the SFR–$L_{150\ \mathrm{MHz}}$ relationship at $\log_{10}(\mathrm{SFR}) < 0.5 M_\odot \mathrm{yr}^{-1}$. To investigate a possible cause, we repeat our previous analysis after excluding any quiescent galaxies, which we identify as follows. For each source, we calculate the SFR expected based on the parametrisation of the star-formation rate – stellar mass relation from Schreiber et al. (2015), and identify those 7,081 galaxies with PROSPECTOR SFR lower than < 0.6 dex below the relation as passive galaxies[14].

[14] We choose a looser cutoff than the typical ±0.3 dex scatter associated with the MS (e.g. Tacchella et al., 2022a; Haskell et al., 2023) in order to account for the large uncertainties associated with very low SFRs.

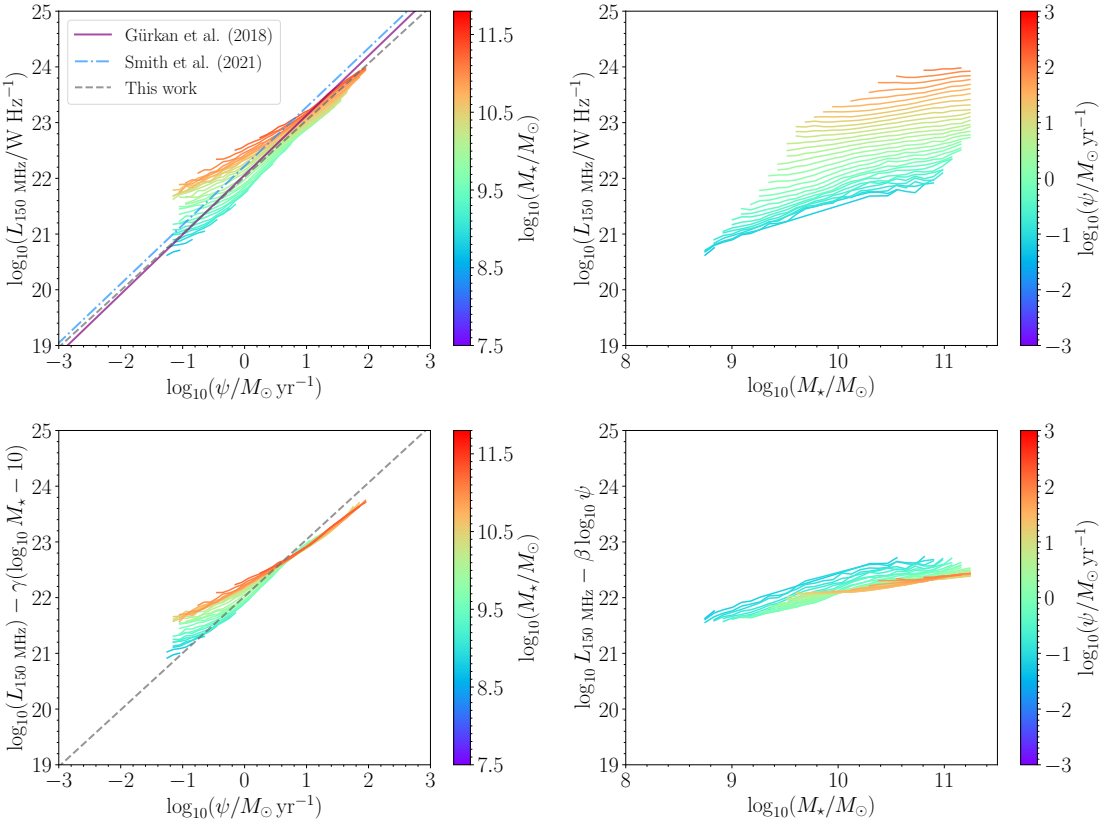

FIGURE 2.11: The relationship between radio luminosity at 150 MHz and the dependence on stellar mass and star formation rate (SFR), derived for the 85,162 $z < 1$ SWIRE-selected sources excluding known/likely AGN. Stellar mass and SFRs are estimated through PROSPECTOR SED fits. In the top left-hand panel, the median likelihood 150 MHz radio luminosity - SFR plot is shown for different stellar mass bins. The different coloured lines represent distinct stellar mass bins, as indicated in the colour-bar to the right. The top right-hand panel illustrates the median likelihood stellar mass vs 150 MHz radio luminosity plots for different SFR bins, with colours again relative to the bar to the right. Similarly, in the bottom left-hand panel, the stellar mass-adjusted radio luminosity - SFR plot is displayed for varying stellar mass bins, using the best fit values from Equation 2.2. Finally, the bottom right-hand panel exhibits the SFR-adjusted radio luminosity vs stellar mass plot for different SFR bins.

The results appear similar – and the best-fit parameters obtained using Equation 2.2 to fit the data after correcting for biases ($\log_{10} L_1 = 22.085 \pm 0.004$, $\beta = 0.783 \pm 0.005$, and $\gamma = 0.338 \pm 0.006$) are consistent with the values derived in Section 2.5.1. This is not unexpected since the star-forming galaxy population is vastly numerically dominant, and we are using median-likelihood $L_{150\,\mathrm{MHz}}$ values in each bin. Excluding the 7,081 quiescent galaxies in this way results in an apparently reduced scatter in the 150 MHz radio luminosity–SFR relation. The apparent reduction in scatter, however, can be attributed purely to the smaller sample size (since fewer bins meet the minimum occupancy threshold of 15 galaxies, especially at low SFRs) rather than a difference in the relationship between luminosity and SFR for passive galaxies, for example.

2.6 Conclusions

In this work, we have used Prospector (Leja et al., 2017; Johnson et al., 2021) to estimate the physical properties of sources over 6 deg^2 of the ELAIS-N1 field. Prospector offers substantial advantages compared to other SED fitting codes, namely, the inclusion of AGN on an even footing with the stellar population synthesis, the implementation of non-parametric star formation histories, the modelling of nebular emission lines and the use of a dynamic nested sampling framework to efficiently sample multi-modal parameter spaces and produce realistic uncertainties alongside the source properties. The main conclusions of this work are as follows:

1. We successfully produce radio source classifications for 92 per cent of the 31,610 150 MHz sources in the ELAIS-N1 field of the LoTSS first data release. Each source is classified as either a star-forming galaxy, radio-quiet AGN, high-excitation radio galaxy (HERG) or low-excitation radio galaxy (LERG).

2. We have shown that our classifications are of a quality which is similar to those produced using four codes in a previous work. This was possible because the inclusion of AGN models in Prospector – on an even footing with the stellar population synthesis – enables us to build on previous work (e.g. Best et al., 2023) by identifying sources that are the likely hosts of radiative mode AGN, as well as those for which there is a radio excess above that expected on the basis of the Prospector SFR.

3. We used Prospector to estimate the physical properties of 133,000 3.6 μm-selected sources, and revisited the relationship between a source's SFR and its radio luminosity.

4. Our best-fit SFR–$L_{150\ \mathrm{MHz}}$ relations are:

   - $\log_{10} L_{150\ \mathrm{MHz}} = (22.024 \pm 0.006) + (1.019 \pm 0.009)\ \log_{10}(\psi / M_\odot\ \mathrm{yr}^{-1})$ for the stellar mass independent case, and
   - $\log_{10}\ L_{150\ \mathrm{MHz}} = (22.083 \pm 0.004) + (0.778 \pm 0.004) \log_{10}(\psi / M_\odot\ \mathrm{yr}^{-1}) + (0.334 \pm 0.006) \log_{10}(M / 10^{10} M_\odot)$ if we assume the stellar mass-dependent form adopted in previous works (e.g. G18 and S21).

5. We found that, using Prospector to fit exactly the same input photometry as used by previous works (e.g. S21), the form of the stellar mass dependence in the SFR–$L_{150\,\mathrm{MHz}}$ relation differs from what had previously been observed using MAGPHYS for the SED

fitting. The PROSPECTOR results indicate a far-tighter relation, with lower scatter especially at $\log_{10}(\psi/M_{\odot}\,\mathrm{yr}^{-1}) > 0.5$ when the stellar mass effects are accounted for.

This work has focused on SED modelling using only photometric data, and it is clear that even using all available codes and every photometric band there can still be significant doubt over what the "correct" classification is for any particular radio source. The most reliable radio source classifications require spectroscopy (e.g. Best and Heckman, 2012, Drake et al. *in preparation*). In this context, it is timely that the WEAVE instrument (Dalton, 2016; Jin et al., 2023) has started collecting data, and the initial batch of over a million spectra of LOFAR-selected sources will be available in the coming months as part of the WEAVE-LOFAR survey (Smith et al., 2016). This will ultimately include every source in the ELAIS-N1 field brighter than ∼100 μJy. PROSPECTOR is uniquely placed to deal with the WEAVE-LOFAR data since it can deal with photometry and spectra on an equal footing. We are hopeful that including the WEAVE spectra in our modelling will allow us to put stronger constraints on the physical parameters (e.g. SFRs) obtained for ELAIS-N1 sources, and significantly improve the accuracy of galaxy classifications. There are great opportunities for this kind of galaxy analysis given the range of new and forthcoming data sets in the era of massively-multiplexed spectroscopic surveys such as 4MOST (de Jong et al., 2019), Subaru-PFS (Greene et al., 2022) and MOONS (Cirasuolo and MOONS Consortium, 2016), for studying new samples from e.g. *Euclid*, LMT/TolTEC (Pope et al., 2019; Wilson et al., 2020) as well as the SKA (Rawlings et al., 2004).

Chapter 3

LoTSS Deep Fields: A novel Bayesian approach for classifying radio sources fitting photometry and spectroscopy using Prospector

"It is far better to grasp the Universe as it really is than to persist in delusion, however satisfying and reassuring."

–Carl Sagan

Radio emission in galaxies is a combination of thermal free-free emission and non-thermal synchrotron radiation (Condon, 1992). The synchrotron component is powered by a combination of star formation activity – through the acceleration of cosmic rays by supernova remnants (Blumenthal and Gould, 1970; Condon, 1992; Condon and Ransom, 2016); and through jets and outflows driven by accretion onto the central supermassive black hole – if the galaxy is host to an active galactic nucleus (AGN; e.g., Bridle and Perley, 1984; Padovani et al., 2017; Hardcastle and Croston, 2020). Synchrotron emission therefore provides a means to study the links between star-formation activity and black hole accretion up to high redshifts, unobstructed by dust (Casey et al., 2009; Condon and Ransom, 2016; Smith et al., 2016).

While the radio-bright population is dominated by luminous AGN and radio-loud quasi-stellar objects (QSOs; Condon, 1989; Prandoni et al., 2001; Simpson et al., 2006; Padovani, 2016;

Hardcastle and Croston, 2020; Fanaroff et al., 2021), the faint radio population is a heterogeneous mixture of star-forming galaxies (SFGs), radio-quiet AGN (RQ AGN), and low-luminosity radio galaxies (Windhorst, 2003; Jackson, 2005; Rosario et al., 2013; Padovani et al., 2015; Padovani, 2016; Best et al., 2023; Das et al., 2024). Understanding the nature of the faint radio source population is therefore critical for studying the role of star formation and black hole accretion in driving galaxy evolution across cosmic time. Radio sky surveys, such as the LOFAR Two-Metre Sky Survey (LoTSS; Shimwell et al., 2017, 2019, 2022) and MeerKAT[1] International Gigahertz Tiered Extragalactic Explorations Survey (MIGHTEE; Jarvis et al., 2016; Heywood et al., 2022), have enabled studies of the faint radio source population out to high redshifts (see reviews by Padovani, 2016; Magliocchetti, 2022, and references therein).

For the vast majority of faint sources, radio observations lack the angular resolution to distinguish between synchrotron emission originating from star formation activity and that produced by AGN outflows (e.g., Ocran et al., 2017; Sabater et al., 2019). Historically, classification efforts have relied on complementing radio observations with ancillary data – ideally spectroscopy, long considered the gold standard for classifying radio sources in the local Universe (e.g., Mauch and Sadler, 2007; Best and Heckman, 2012; Sabater et al., 2019; Drake et al., 2024), as a galaxy's spectrum encodes the signatures of the different emission mechanisms. However, for the majority of deep radio surveys, full spectroscopic coverage is still not available. This lack of spectroscopy is often mitigated by using multi-wavelength information, such as X-ray luminosity, mid-IR colours, analysis of the UV–far-IR spectral energy distribution (SED), or dust extinction-corrected near-UV optical colours, to constrain the types of sources detected (e.g., Smolčić et al., 2017a; Whittam et al., 2022; Best et al., 2023; Das et al., 2024).

The LoTSS deep fields are particularly well suited to joint radio and multiwavelength studies, owing to LOFAR's exceptional survey speed and sensitivity, as well as the extensive ancillary UV–IR data coverage provided by a wide range of surveys (see Section 3.1.2). 150 MHz radio images from LOFAR are obtained at an angular resolution of 6 arcsec (corresponding to the full width at half maximum of the restoring beam) when using the Dutch stations, and reach 0.3 arcsec when including the international baselines (Morabito et al., 2022; Best et al., 2023). This chapter focuses on the ELAIS-N1 field, one of the four LoTSS deep fields, which contains the deepest radio observations in the first data release of the LoTSS deep fields (DR1; Tasse et al., 2021; Sabater et al., 2021; Kondapally et al., 2021; Duncan et al., 2021; Best et al., 2023), reaching RMS noise levels below 30 μJy beam^{-1} over a 10 deg^2 area and as low as

[1] http://www.ska.ac.za/meerkat

20 μJy beam^{-1} in the deepest regions. Significant spectroscopic coverage of the radio-detected sources in the LoTSS deep fields is already available from the early data release of the Dark Energy Spectroscopic Instrument (DESI EDR; DESI Collaboration et al., 2016a, 2022). The LoTSS deep fields will also be covered imminently by the WEAVE-LOFAR survey, which aims to obtain spectra for all sources in the deep fields (with an expected 100 per cent redshift success out to $z = 1$; see Smith et al., 2016).

Several previous studies have focused on the classification of faint radio sources in the ELAIS-N1 deep field. Among these, Das et al. (2024, hereafter D24)[2], Best et al. (2023, hereafter B23), and Arnaudova et al. (2025, hereafter A25) are of particular relevance to this work. D24 used the state-of-the-art energy balance SED fitting code PROSPECTOR to model multiwavelength photometry and estimate key physical parameters. By combining these with LoTSS deep fields DR1 radio observations of the ELAIS-N1 field, they classified the source population as SFGs, RQ AGN, and high-/low-excitation radio galaxies (HERGs/LERGs). D24 follows from B23, who carried out similar source classifications in three of the LoTSS deep fields by deriving consensus galaxy parameters through fitting multiwavelength photometry using four independent SED fitting codes – MAGPHYS (da Cunha et al., 2008), BAGPIPES (Carnall et al., 2018), CIGALE (Noll et al., 2009; Boquien et al., 2019), and AGNFITTER (Calistro Rivera et al., 2016) – and combining these consensus estimates with 150 MHz radio luminosities from LoTSS deep fields DR1. Unlike both B23 and D24 which are photometry-based studies, A25 used a sophisticated emission line modelling program to fit DESI spectra of sources in the ELAIS-N1 deep field, combining Baldwin-Phillips-Terlevich (BPT; Baldwin et al., 1981) and modified Mass-Excitation (MEx; Juneau et al., 2011, 2014) diagnostics with radio observations from LoTSS deep fields DR1 to classify the sources as SFGs, RQ AGN, LERGs, and HERGs.

In this chapter, we present a new classification approach that combines the strengths of spectroscopic, UV–far-IR photometric, and radio classification methods. We build upon the work of D24 and use the SED fitting code PROSPECTOR, leveraging its ability to self-consistently model photometry and spectroscopy within a fully Bayesian framework. This chapter is structured as follows: in Section 3.1, we describe the datasets used in this work. In Section 3.2, we outline the process of modelling spectrophotometric data using PROSPECTOR. In Section 3.3, we describe our classification scheme. We discuss our results in Section 3.4, followed by the conclusions in Section 3.5.

[2] D24 forms Chapter 2 of this thesis.

3.1 Data

In this chapter, we focus on the ELAIS-N1 field (centred at $16^{h}\ 11^{m}\ 00^{s}$, +55 deg 00′00″), which not only has the most sensitive radio data among the LoTSS deep fields DR1, but is also covered by several multiwavelength surveys and benefits from both photometry- and spectroscopy-based classifications, as previously mentioned. This makes it an ideal reference field for extensively comparing and testing classifications derived from joint photometry + spectroscopy fitting.

3.1.1 Radio observations

As part of the LoTSS deep fields DR1, the ELAIS-N1 field was observed using the LOFAR High Band Antenna (HBA; central observing frequency ≈150 MHz) over multiple 8-hour observing blocks, yielding a total effective on-source integration time of 164 hours. LoTSS deep fields DR1 includes observations only from the Dutch LOFAR stations, with a spatial resolution of 6 arcsec and an RMS of ≤ 30 μJy beam^{-1} in the central regions, reaching ≤ 20μJy beam^{-1} away from bright sources. Sabater et al. (2021) performed calibration and continuum imaging, generating a catalogue of sources extracted within the 30 per cent power point of the primary beam using the Python Blob Detector and Source Finder (`PyBDSF`; Mohan and Rafferty, 2015) tool. Sources were identified by detecting islands and peaks with 3σ and 5σ thresholds, respectively (see Sabater et al., 2021; Kondapally et al., 2021, for details).

3.1.2 Multiwavelength photometry

Kondapally et al. (2021) compiled a 26-band photometric catalogue by combining galactic extinction-corrected UV to mid-IR fluxes with far-IR photometry. The far-IR photometry was measured using the XID+ tool (see Hurley et al., 2017; McCheyne et al., 2022, for details). The following survey datasets were used to construct the multiwavelength catalogue:

- *Spitzer* Adaptation of the Red-sequence Cluster Survey (SpARCS) u-band (Wilson et al., 2009; Muzzin et al., 2009),
- Panoramic Survey Telescope and Rapid Response System (PanSTARRS) g, r, i, z, y bands (Kaiser et al., 2010; Chambers et al., 2016),

- g, r, i, z, y, and the narrow-band NB921 data from Hyper-Suprime-Cam (HSC; Miyazaki et al., 2012, 2018) Subaru Strategic Program (HSC-SSP) public DR1 (Aihara et al., 2018),
- J- and K-band data from the UK Infrared Deep Sky Survey (UKIDSS) Deep Extragalactic Survey (DXS) DR10 (Lawrence et al., 2007),
- Infrared Array Camera (IRAC) 3.6–8μm data from the *Spitzer* Wide-Area Infrared Extragalactic Survey (SWIRE; Lonsdale et al., 2003),
- 3.6–4.5μm data from the *Spitzer* Extragalactic Representative Volume Survey (SERVS; Mauduit et al., 2012),
- 24 μm data from the Multiband Imaging Photometer for *Spitzer* (MIPS; Rieke et al., 2004) instrument on *Spitzer*,
- 100 and 160 μm data from Photodetector Array Camera and Spectrometer (PACS; Poglitsch et al., 2010), and,
- 250, 350 and 500 μm data from the Spectral and Photometric Imaging Receiver (SPIRE; Griffin et al., 2010) instrument.

The resulting multi-wavelength catalogue contains over 2.1 million sources, of which 31,610 have been cross-matched with $> 5\sigma$ 150 MHz source detections catalogued by Sabater et al. (2021). Duncan et al. (2021) used a combination of template fitting and machine learning techniques to measure photometric redshifts for these sources, complementing the spectroscopic redshifts that were available for only 0.2 per cent of the total 2.1 million deep-field sources (and approximately 5 per cent of the $> 5\sigma$ 150 MHz detections; see B23 and D24) at the time the catalogue was created. Duncan et al. (2021) also flagged sources as AGN based on prior identifications through optical spectroscopy, X-ray properties, and/or mid-IR colour cuts.

3.1.3 Spectroscopic data

Historically, the ELAIS-N1 field had very limited spectroscopic coverage, with only 4.3 per cent of its radio-detected sources having spectroscopic data (see B23 and D24). While this will be remedied when data from the WEAVE-LOFAR survey becomes available, the current situation has improved with DESI EDR providing spectra for $\sim$ 27 per cent of the radio-detected sources in the ELAIS-N1 deep field. These spectra were taken in the wavelength range of

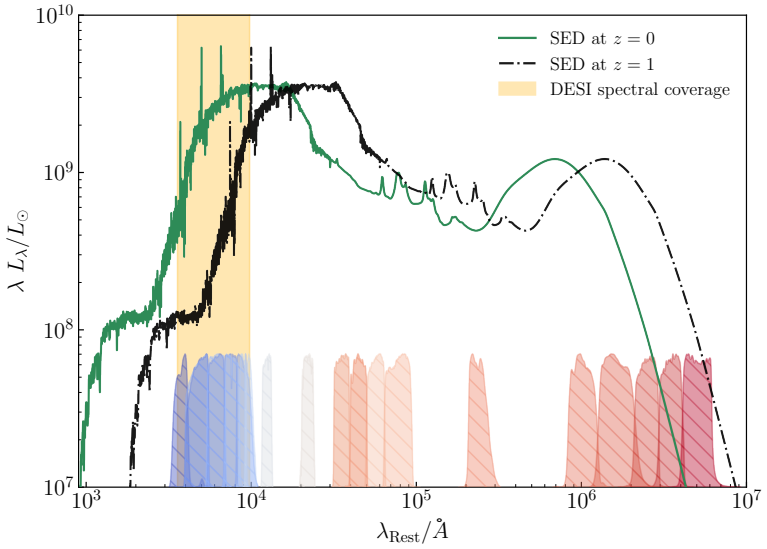

FIGURE 3.1: Transmission curves of the LoTSS UV–far-IR filters used in this work are shown, with a sample galaxy SED redshifted to $z = 0$ and $z = 1$ overplotted to illustrate the photometric coverage of typical galaxy spectral features. The galaxy was selected at random from the 6,038 galaxies in our sample. The yellow-shaded region indicates the approximate range of wavelengths sampled by the DESI EDR spectroscopy used in this work.

3600 – 9824 Å at a resolving power of $\lambda/\Delta\lambda \sim 2000 - 5500$ (Guy et al., 2023). DESI EDR consists of three survey validation stages, namely "sv1", "sv2", and "sv3", each with a different targeting algorithm. These stages were further divided into programmes based on observing conditions: "bright" targeted sources for the Bright Galaxy Survey and the Milky Way Survey, "dark" focused on fainter objects such as luminous red galaxies (LRGs), emission-line galaxies (ELGs), and QSOs, the "backup" programme was run under poor observing conditions, and the "other" programme was dedicated to secondary targets (see Myers et al., 2023, for further details).

3.1.4 Sample selection

In this work, we focus exclusively on the "sv3" programme, which has an effective exposure time (which is defined as the time that would have been required to achieve the same signal-to-noise ratio had the observations been taken under nominal dark-sky conditions and standard survey speeds; refer to the DESI documentations[3]) of 102.2 hours for the whole programme and covers ≈197 deg^2 (which is approximately 1 per cent of the area expected to be covered by the primary DESI science survey; DESI Collaboration et al., 2024). The target selection adopted in the "sv3" programme is very similar to that in the primary science survey. "sv3" consists of

[3] https://data.desi.lbl.gov/doc/glossary/#effective-exposure-time

a total of 858,364 unique extragalactic sources with a spectral classification flag (SPECTYPE) of GALAXY or QSO. As recommended in DESI Collaboration et al. (2024), we exclude sources with known problems in redshift estimation (i.e. those with non-zero ZWARN values), leaving us with 780,181 galaxies and QSOs that have reliable redshift measurements. We match the RA and DEC coordinates of these sources to the optical positions of the 31,610 radio detected sources in the ELAIS-N1 deep field using a nearest-neighbour algorithm with a maximum separation of 1 arcsec, identifying 6,576 common objects. Lastly, we remove sources that do not meet the flag cuts recommended in Kondapally et al. (2021), ensuring that our sample lies within the overlapping coverage of the PanSTARRS i-band, UKIDSS-DXS K-band, and *Spitzer*-SWIRE 4.5μm channel, while also excluding regions around bright stars as masked in the *Spitzer* data. This results in a sample of 6,038 sources. In Fig. 3.1, the photometric filter transmission curves and the wavelength coverage of DESI are overlaid on the SED of a representative galaxy from our sample, shown at both $z = 0$ and $z = 1$. It is evident that the combination of photometric filters and spectroscopy provides comprehensive coverage of key spectral features across the full rest-frame wavelength range.

3.2 SED modelling

3.2.1 Model construction

In this work, we use the PYTHON-based SED modelling code PROSPECTOR (Leja et al., 2017; Johnson et al., 2021) to simultaneously fit LoTSS photometry and DESI EDR spectra. We build upon the model adopted by D24 and summarise the key features here. The Kroupa (2001) initial mass function (IMF) is adopted throughout. Source redshifts are fixed to the values provided in the DESI value-added catalogue[4]. Stellar populations are modelled using the Flexible Stellar Populations Synthesis (FSPS; Conroy et al., 2009; Johnson et al., 2023) code, incorporating the Padova isochrones (Bertelli et al., 1994; Girardi et al., 2000; Marigo et al., 2008), and the MILES (Sánchez-Blázquez et al., 2006) and the C3K (Choi et al., 2016; Byrne and Stanway, 2023) spectral libraries. The metallicity of all the stars in a source (Z) is represented by a single value, $\log_{10}(Z/Z_\odot)$, where the solar metallicity is set to $Z_\odot = 0.019$[5]. $\log_{10}(Z/Z_\odot)$ is treated as a free parameter and a uniform prior is adopted over the range $-2.0 < \log_{10}(Z/Z_\odot) < 0.5$, motivated by the coverage of the Padova isochrones (Marigo et al., 2008; Leja et al., 2017). We

[4] https://data.desi.lbl.gov/doc/releases/edr/
[5] https://github.com/cconroy20/fsps

	Parameter	Description	Prior/Value
Stellar metallicity	$\log_{10}(Z_\star/Z_\odot)$	Stellar metallicity	Uniform; between −2.0 to 0.5
Stellar Mass	$\log_{10}(M_\star/M_\odot)$	Total stellar mass formed †	Uniform; between 6.5 to 13.5
Dust attenuation	$\tau_{\lambda,2}$	Diffuse dust V-band optical depth	Uniform; between −1 and 4
	n	Diffuse dust attenuation index	Uniform; between −2 and 0.5
	$\tau_{\lambda,1}/\tau_{\lambda,2}$	The ratio of the optical depth of the birth cloud to the diffuse dust screen optical depth	Clipped normal; mean = 1, variance = 0.3, between 0 and 2
Dust emission	$U_{\rm min}$	The minimum intensity of starlight which heats up the diffuse dust and ISM	Uniform; between 0.1 and 25
	γ_e	Fraction of total dust mass affected by $U_{\rm min}$	Log uniform; between 0.001 and 0.15
	$Q_{\rm PAH}$	The fraction of total dust mass coming from polycyclic aromatic hydrocarbons (PAHs)	Uniform; between 0.1 and 10
AGN	$f_{\rm AGN}$	Total luminosity of the AGN defined as a fraction of total mid-IR ($4-20\mu$m) luminosity	Log uniform; between 10^{-5} and 3
	$\tau_{\rm AGN}$	Optical depth of the AGN torus	Log uniform; between 5 and 150
Nebular emission	$\log_{10}(U_{\rm gas})$	Gas-phase ionisation parameter	Uniform; between −4 and −1
	$\log_{10}(Z_{\rm gas}/Z_\odot)$	Gas-phase metallicity	Uniform; between −2.0 and 0.5
Spectral smoothing	$\sigma_{\rm smooth}$	Width of Gaussian line spread function	Uniform; between 50.0 and 300.0
Nebular marginalisation	$\sigma_{\rm eline}$	Width of normalised Gaussian profiles	Uniform; between 30.0 and 300.0
Spectral noise	$K_{\rm jitter}$	Jitter parameter	Uniform; between 1 and 3
	$f_{\rm outlier}$	Fraction of outlier pixels	Uniform; between 10^{-5} and 0.1
Fixed Parameters	IMF	Initial mass function	Kroupa (2001)
	z	Redshift	Fixed at DESI redshift measurement.
	$\tau_{\lambda,1}$	Additional optical depth attenuating the light from young stars	Function of $\tau_{\lambda,1}/\tau_{\lambda,2}$
	$k'(\lambda)$	Dust attenuation	Kriek and Conroy (2013) attenuation curve
	$t_{\rm bins}$	Discrete time binning scheme	Fixed, defined in Section 2.3
	$N_{\rm poly}$	Order of polynomial fitted to continuum	Equal to 12

TABLE 3.1: Description of the PROSPECTOR parameters used in the final model. Similar to Chapter 2, † denotes the total stellar mass formed in a source which is used as a free parameter, and is larger than the currently surviving stellar mass.

adopt the non-parametric "continuity" SFH prior. The lifetime of each source is divided into N discrete time bins. The first two and last time bins are fixed for all sources, covering $0 < t_l < 10$ Myrs, $10 < t_l < 100$ Myrs, and $0.85t_z < t_l < t_z$, where t_z is the age of the Universe at the object redshift and t_l is the lookback time. N ranges from nine for the lowest-redshift sources to seven for the highest. Dust attenuation is modelled using the two-component Charlot and Fall (2000) prescription combined with the Kriek and Conroy (2013) attenuation curve. Dust emission is incorporated using the Draine and Li (2007) templates. Energy balance is assumed between dust attenuation and emission. The contribution of the AGN torus to the MIR SED is modelled using the two-component CLUMPY models (Nenkova et al., 2008a,b).

Nebular line and continuum emission are computed using the `CLOUDY` photoionisation code (Ferland et al., 2013), where the ionising spectrum is provided by the `FSPS`-generated stellar populations (see Byler et al., 2017). This is parametrised by two free parameters: (i) the intensity of the ionising spectrum which is denoted by a dimensionless ionization parameter $U_{\rm gas}$, and (ii) the gas-phase metallicity $Z_{\rm gas}$. The emission line models are attenuated by the IGM following the Madau (1995) formulation and subsequently corrected for line-of-sight variations. The inference of physical parameters, such as stellar mass, depends on the shape of the continuum (e.g., Koleva et al., 2009). To mitigate the impact of spectrum normalisation errors (such as those from aperture correction issues) on galaxy parameter estimates, we normalise the spectrum by the continuum. Following Johnson et al. (2021), we divide the spectrum by a $12^{\rm th}$-order polynomial fitted to wavelength ranges that do not contain strong absorption and emission lines. The normalised, observed-frame spectrum is then smoothed in the rest-frame line-of-sight velocity space using a fast Fourier transform (FFT) in `PROSPECTOR`, assuming a Gaussian line spread function (LSF). The width of this Gaussian LSF is treated as a free parameter with a uniform prior of $50 < \sigma_{\rm smooth} < 300$ km s^{-1}. The standard `CLOUDY` formulation assumes that emission lines are powered solely by star formation; however, this is often insufficient to model lines arising from non-stellar emission mechanisms (such as shocks and AGN), making it necessary to adopt a non-physical model in which the line normalisation is decoupled from `FSPS` (see Johnson et al., 2021, Appendix E). This is implemented by marginalising over the emission lines included in the `CLOUDY` models, using normalised Gaussian profiles centred at the `CLOUDY` model wavelengths. Their widths ($\sigma_{\rm eline}$) are treated as free parameters, with a uniform prior between 30 and 300 km s^{-1}. A free parameter, $K_{\rm jitter}$, is included in the model to scale the covariant spectroscopic uncertainties for an optimal fit (see Johnson et al., 2021; Suess et al., 2022), with a uniform prior between 1 and 3. Additionally, we introduce the free parameter

$f_{\rm outlier}$ (with a uniform prior between 10^{-5} and 0.1) to account for the fraction of spectral pixels that deviate significantly from the model relative to the noise (due to, e.g., cosmic rays or unmasked sky subtraction residuals; see Johnson et al., 2021). The complete spectrophotometric model parameters can be found in Table 3.1.

The dynamic nested sampling tool DYNESTY (Speagle, 2020) is used to estimate the Bayesian posteriors and evidences. DYNESTY uses so-called "live points" to sample the posterior distribution. Live points are a set of samples that are drawn from the prior volume and are iteratively replaced such that, at each step, the remaining live points occupy a progressively smaller prior volume bounded by increasing likelihood thresholds. Using the logarithmic ratio between the Bayesian evidence estimated in the $i^{\rm th}$ iteration ($\mathcal{Z}_i$) and the remaining evidence ($\Delta\mathcal{Z}_i$, approximated as the product of the prior volume at the $i^{\rm th}$ iteration and the maximum-likelihood live point within that volume), the quantity $\Delta\ln\mathcal{Z}_i$ can be defined as:

$$\Delta\ln\mathcal{Z}_i = \ln\left(1+\frac{\Delta\mathcal{Z}_i}{\mathcal{Z}_i}\right). \tag{3.1}$$

$\Delta\ln\mathcal{Z}_i$ is commonly used as a stopping criterion[6] in DYNESTY. We terminate the sampling process at $\Delta\ln\mathcal{Z}_i \leq 0.1$. This corresponds to $\Delta\mathcal{Z}_i/\mathcal{Z}_i \approx 0.11$, and we find that sampling beyond this threshold does not significantly affect the results.

3.2.2 Estimating parameters from the posterior distribution

To estimate key parameters such as the stellar masses, SFRs, and emission line fluxes, we construct marginalised PDFs from the DYNESTY sample chain after convergence. Nested sampling proceeds by iteratively removing the live point with the lowest likelihood and replacing it with a new point drawn from the prior, subject to the constraint that its likelihood exceeds that of the discarded point (Skilling, 2006; Higson et al., 2019). The median-likelihood estimates and their uncertainties, calculated as the differences between the 84$^{\rm th}$ percentile of the PDF and the median, and between the median and the 16$^{\rm th}$ percentile, are computed for physical parameters such as stellar mass, SFR averaged over 10 and 100 Myrs, specific SFR, AGN fraction parameter ($f_{\rm AGN}$, defined as the fractional contribution of the AGN torus to the total $4-20\mu$m luminosity), and emission line fluxes for the 166 lines included in FSPS.

[6] https://dynesty.readthedocs.io/en/stable/overview.html#stopping-criteria

The goodness of fit is calculated separately for photometry and spectroscopy. For photometry, we compute the χ^2 values between the observed fluxes (and their uncertainties) and those derived from the highest log-likelihood DYNESTY chain. A fit for a source is deemed acceptable if its χ^2 value falls below the 99 per cent confidence interval of the Smith et al. (2012) χ^2 PDF corresponding to the number of photometric bands. Although the Smith et al. (2012) χ^2 function was originally developed for MAGPHYS results, it was shown to produce reasonable results in D24 (see Section 2.2.2).

Before deriving the spectroscopic goodness-of-fit criterion, we correct for systematic offsets in the flux estimates and their associated uncertainties, which likely arise from internal processes within FSPS and PROSPECTOR. Although such offsets are present in all 166 emission lines fitted by PROSPECTOR and FSPS, we focus only on the four BPT emission lines, as these are the ones used in this Chapter for source classification. We begin by comparing the median-likelihood fluxes to those obtained from the FASTSPECFIT Spectral Synthesis and Emission-Line Catalogue, one of the value-added catalogues (VACs) published as part of DESI-EDR (hereafter referred to as the FASTSPECFIT catalogue; Moustakas et al., 2023, Moustakas et al., *in prep.*), as well as to the fluxes measured by A25. While we find good agreement in the median likelihood fluxes, a comparison of our flux uncertainties with those reported in the FASTSPECFIT catalogue and by A25 shows that our uncertainties are systematically offset relative to both. As shown in Fig. 3.2, the relationship between the uncertainties estimated in this work (σ_{F_λ}) and those from FASTSPECFIT catalogue ($\sigma_{F_\lambda,\mathrm{FastSpecFit}}$) is well described by the following parameterisation:

$$\log_{10}(\sigma_{F_\lambda}/\sigma_{F_\lambda,\mathrm{FastSpecFit}}) = M\log_{10}(F_\lambda) + C. \tag{3.2}$$

The coefficients M and C for the four BPT emission lines are calculated as follows:

(i) Hβ : $M = 0.593$, $C = -0.930$,

(ii) [OIII] : $M = 0.696$, $C = -0.150$,

(iii) Hα : $M = 0.601$, $C = -0.823$, and,

(iv) [NII] : $M = 0.560$, $C = -0.821$.

These corrections are then applied to our measurements of the four BPT emission line fluxes and their uncertainties.

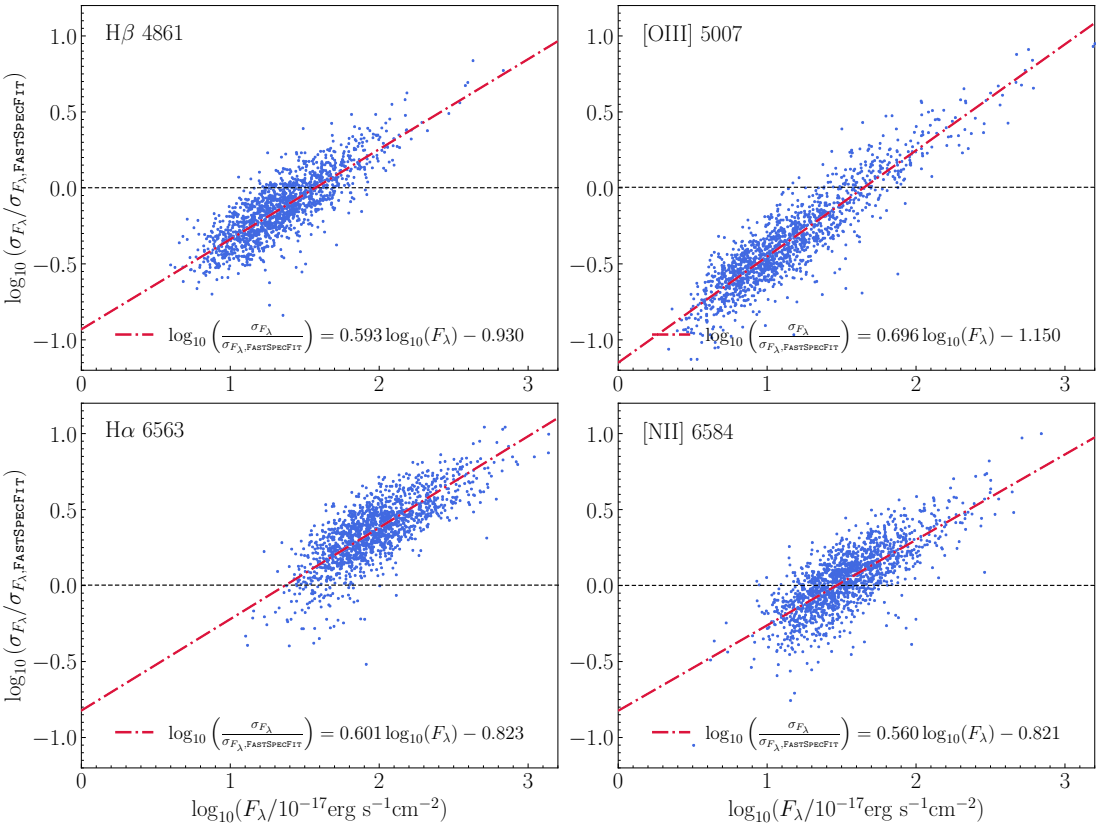

FIGURE 3.2: The logarithm of the ratio of uncertainties obtained from PROSPECTOR posterior PDFs to those obtained from the FASTSPECFIT catalogue is plotted as a function of the median likelihood fluxes estimated in this work. The panels show (top-left) Hβ, (top-right) [OIII], (bottom-left) Hα, and (bottom-right) [NII]. There is a clear indication of a flux-dependent systematic bias in the uncertainties estimated from the PROSPECTOR PDFs. The best-fit straight line, which is used to correct for this bias, is shown as a dot-dashed red line in each plot.

The criteria for the acceptability of the four BPT emission lines are defined in pairs – Hβ + [OIII] and Hα + [NII] – because the members of each pair are closely spaced in wavelength and can be partially blended. Defining acceptability criteria for the individual lines in isolation therefore risks contamination from the other member of the pair. We calculate the reduced chi-squared statistic ($\overline{\chi}^2$) for the Hβ + [OIII] and the Hα + [NII] line pairs by dividing the χ^2 value by the number of data points within the wavelength ranges 4855 – 5015 Å and 6535 – 6600 Å, respectively. As shown in Fig. 3.3, the distributions of $\overline{\chi}^2$ for the two line pairs are well described by the standardised form of the reduced chi-squared PDF (e.g. Andrae et al., 2010):

$$P(\overline{\chi}^2_\nu, N_{\mathrm{dof}}) = \frac{1}{\sigma}\frac{1}{2^{(N_{\mathrm{dof}}/2)}\Gamma(N_{\mathrm{dof}})}(\overline{\chi}^2_\nu)^{(N_{\mathrm{dof}}/2)-1}\exp^{-(\overline{\chi}^2_\nu/2)} \tag{3.3}$$

where $\overline{\chi}^2_\nu = (\chi^2_\nu - \mu)/\sigma$; N_{dof} is the number of degrees of freedom, μ is the location, and σ is the scale parameter. Using a non-linear least-squares fitting method, we calculate the following

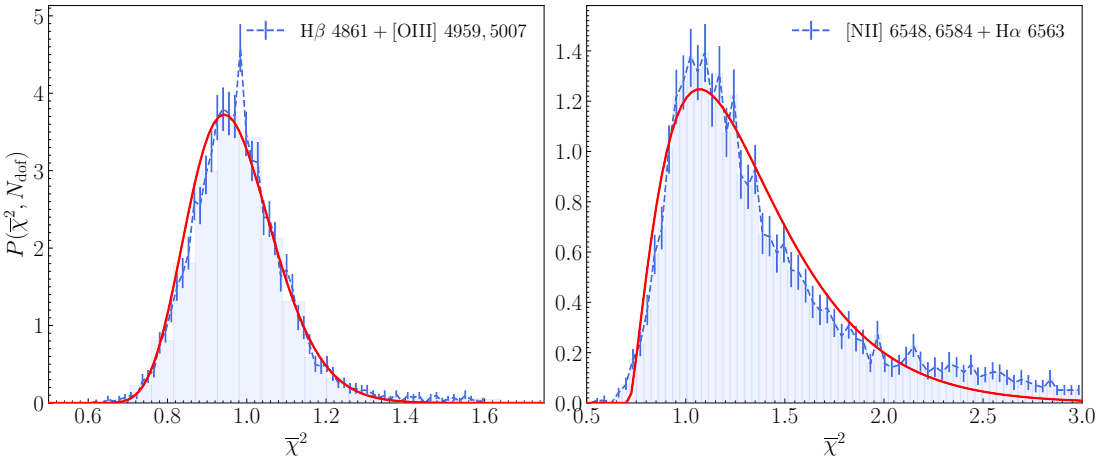

FIGURE 3.3: The blue-shaded histograms show the distribution of reduced chi-squares ($\overline{\chi}^2$) calculated for the two BPT emission line pairs: (left-hand panel) Hβ + [OIII], and (right-hand panel) Hα + [NII]. The uncertainties in the distribution, estimated using bootstrapping, are represented by the blue bars. The solid red curves depict the best-fit standardised reduced chi-squared PDFs for each line-pair.

best-fit values for the line-pairs:

(i) Hβ + [OIII] : $N_{\rm dof} = 30.71,\ \mu = 0.54,\ \sigma = 0.01$, and,

(ii) Hα + [NII] : $N_{\rm dof} = 4.75,\ \mu = 0.72,\ \sigma = 0.13$.

Uncertainties on the occupancy in each bin were calculated using bootstrap resampling to generate 3,000 realisations of the $\overline{\chi}^2$ distribution. The 99$^{\rm th}$ percentile bounds for the PDFs of these line pairs ($\overline{\chi}^2_{\nu,99}$) are calculated to be 1.25 and 2.58 for Hβ + [OIII], Hα + [NII], respectively. A fit to an emission line pair is considered acceptable if $\overline{\chi}^2 < \overline{\chi}^2_{\nu,99}$ for that line-pair.

In Fig. 3.4, we compare the key physical parameters – stellar mass, SFRs averaged over 10 and 100 Myrs, sSFR averaged over 100 Myrs, and the AGN fraction parameter – derived from the spectrophotometric fits presented in this Chapter to those obtained by D24 using photometry-only fits. We find general agreement between the two sets of estimates after accounting for uncertainties. This consistency is expected, as the estimates are largely determined by the shape of the UV–FIR continuum, which is itself constrained by the aperture-matched photometry. The increased scatter in the median-likelihood comparison for galaxies with low star formation activity (SFR $\lesssim 1\ M_\odot\ {\rm yr}^{-1}$ and sSFR $\lesssim 10^{-11}{\rm yr}^{-1}$) can be attributed to stochastic effects in the quiescent regime, where low-SNR photometry, coupled with degeneracies in the underlying models, leads to greater uncertainty and variability in the inferred parameters. In Fig. 3.5, we compare the offset-corrected emission line flux estimates derived from PROSPECTOR fits

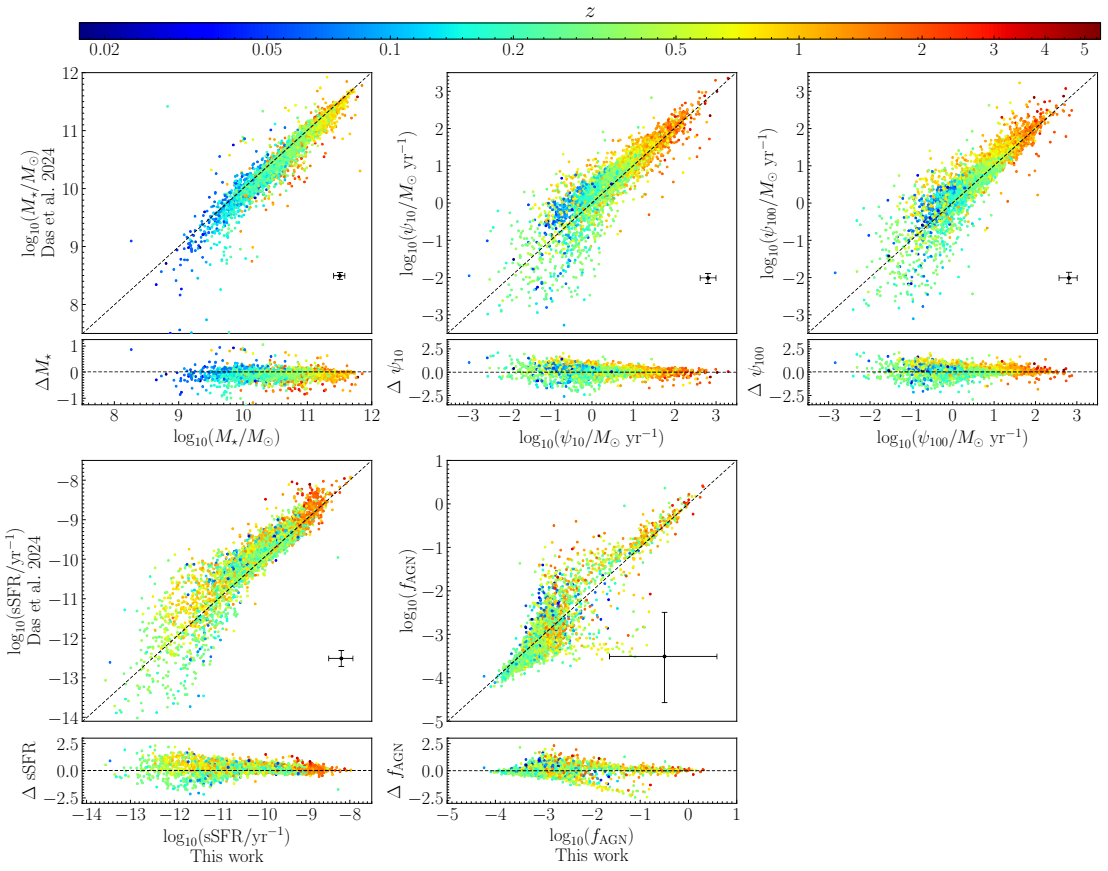

FIGURE 3.4: Comparison of the median-likelihood parameter estimates (clockwise from the top-left panel: current stellar mass, SFR averaged over 10 Myrs, SFR averaged over 100 Myrs, AGN fraction parameter, and the specific SFR averaged over 100 Myrs) obtained from the spectrophotometric PROSPECTOR fits used in this work (along the x-axis) with those from the PROSPECTOR photometry-only fits by D24 (along the y-axis). Typical uncertainties are indicated by the error bar in the lower right of each panel. The plots are colour-coded by redshift, as shown by the colourbar at the top.

deemed acceptable based on our goodness-of-fit criteria with those from the FASTSPECFIT catalogue.

3.3 Probabilistic source classification

In the previous sections, we produced spectrophotometric fits for the radio-detected sources in the ELAIS-N1 field and demonstrated that both the physical parameters and emission line fluxes are reliably estimated. Using these results, we compute the probability of each source belonging to SFGs and to different classes of AGN. Probabilistic classification approaches, such as Richards et al. (2012), de Souza et al. (2017), Tranin et al. (2022), Drake et al. (2024), and A25,

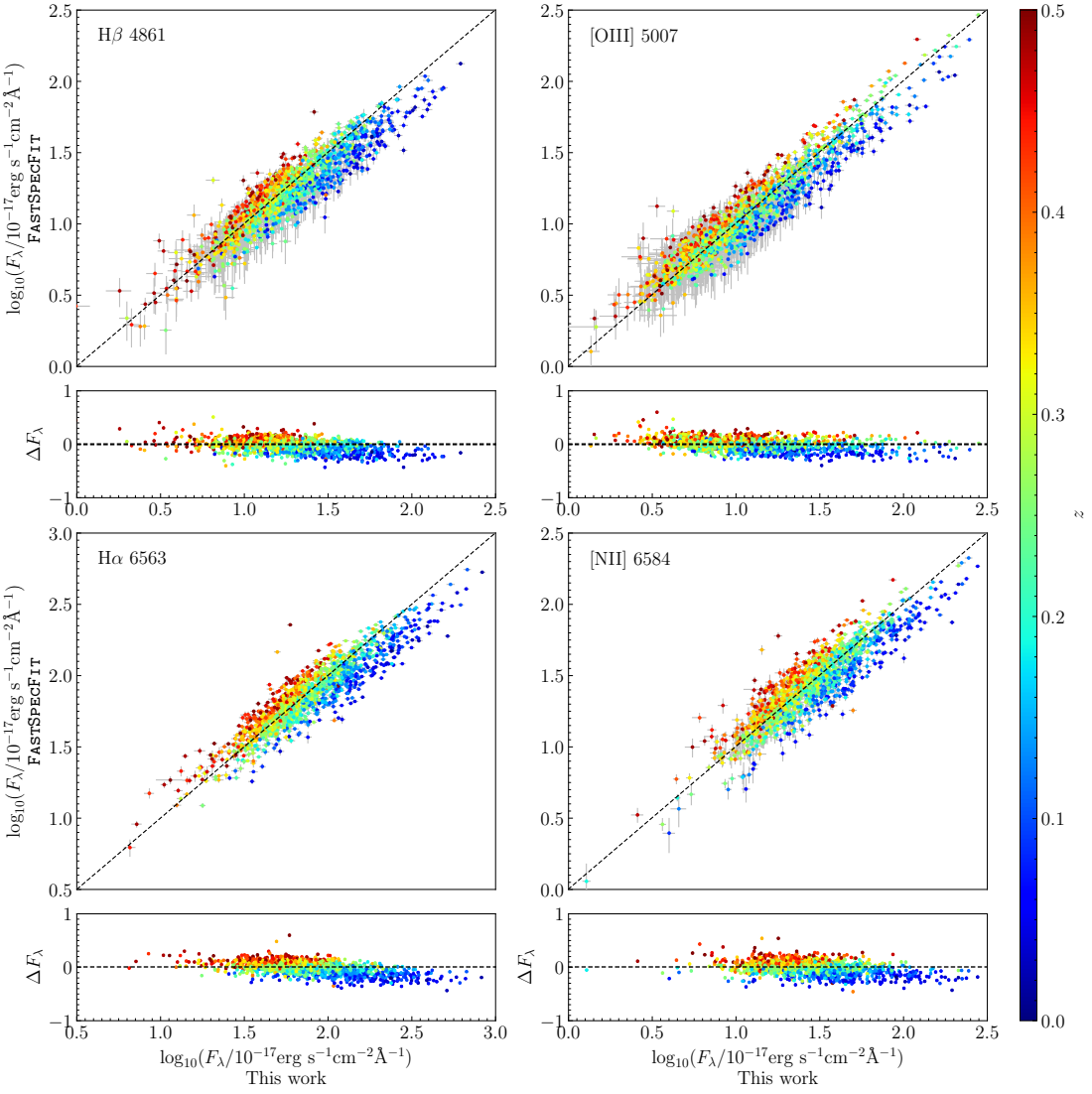

FIGURE 3.5: Comparison of the median-likelihood flux estimates for the four BPT emission lines: (top-left) Hβ, (top-right) [OIII], (bottom-left) Hα, and (bottom-right) [NII]. Fluxes calculated using PROSPECTOR, after applying corrections, are plotted on the x-axis, while those reported in the FASTSPECFIT catalogue are on the y-axis. The plots are colour-coded by redshift, with error bars shown as gray lines. Only sources with a 3σ detection in each line in both works are considered.

offer substantial advantages over deterministic/binary ("yes" or "no") classifications. They naturally fold in observational errors and underlying model uncertainties, making them better suited to handle low S/N data and cases with high degrees of ambiguity. They also allow for the principled combination of multiple differing classifications through the use of priors and weights, thus providing more flexibility and robustness compared to majority-driven schemes. Moreover, probabilistic classification techniques provide end-users the freedom to define samples of sources based on a desired degree of purity or completeness. By summing class probabilities rather than counting binary labels, they produce more reliable population-level statistics and

mitigate biases associated with faint and/or marginal sources. While spectroscopy-based probabilistic source classifications exist for LoTSS radio-detected sources (see Drake et al., 2024 and A25), in this work we adopt a fully Bayesian classification approach that leverages the full posterior PDFs produced by PROSPECTOR, enabling a more nuanced treatment of source classifications. We use three approaches to estimate the probability that a source hosts an AGN: (i) in Section 3.3.1, we use a method based on identifying sources with a mid-IR excess to determine the probability of the source containing an efficiently accreting radiative-mode AGN; (ii) in Section 3.3.2, we calculate the probability that the source is classified as an AGN host based on its relative emission line strengths; and (iii) in Section 3.3.3, we determine the probability that a source has a radio excess.

3.3.1 Identification of radiative-mode AGN based on mid-IR excess

SED fitting has been widely used to detect radiative-mode AGN due to its ability to simultaneously model various physical processes contributing to different parts of a galaxy's SED, including excess mid-IR radiation that cannot be attributed solely to stellar processes and is instead linked to the AGN torus. Studies such as Ciesla et al. (2015), Leja et al. (2018), Whittam et al. (2022), Thorne et al. (2022b), B23, and D24 have demonstrated that radiative-mode AGN can be identified by incorporating AGN templates into SED fitting, even in the absence of spectroscopic data (e.g., Baldwin et al., 1981; Veilleux and Osterbrock, 1987; Kauffmann et al., 2003; Best and Heckman, 2012; Drake et al., 2024). The AGN fraction parameter ($f_{\rm AGN}$) in PROSPECTOR (defined in Section 3.2.1) measures the fractional contribution of AGN to the total mid-IR ($4-20\mu$m) luminosity (e.g., Leja et al., 2018). However, as discussed in B23 and D24, the AGN fraction parameter is often poorly constrained by mid-IR photometry, resulting in large associated uncertainties. To mitigate this issue and produce classifications with a high degree of confidence, these studies adopted the more conservative 16$^{\rm th}$ percentile values rather than the commonly used median likelihood estimates.

While this 16$^{\rm th}$ percentile-based approach improves reliability, a more robust alternative is to adopt probabilistic classification schemes. We use a Bayesian scheme and compute the probability of a source hosting a radiative-mode AGN based on mid-IR excess in the SED ($\mathcal{P}_{\rm AGN,MIR}$). A first estimate is obtained by integrating the marginalised $f_{\rm AGN}$ PDF over $\log_{10}(f_{\rm AGN}) \geq -3$. This threshold is consistent with that adopted by D24 to classify sources as radiative-mode AGN

hosts, based on the 16$^{\text{th}}$ percentile f_{AGN} distribution for the radio-detected sources in the ELAIS-N1 field. This is referred to as the "no prior" probability estimate, as all DYNESTY sample chains post-convergence are used to construct the f_{AGN} PDF, without any additional weighting or selection criteria. (Fig. 3.6, top panels). For the majority of sources, the distribution of $\mathcal{P}_{\text{AGN,MIR}}$ (Fig. 3.6, top-right panel) is concentrated around 0.5, instead of being clustered near 0 or 1, as one might expect in a scenario where the data strongly support or refute the presence of an AGN. The top-left panel of Fig. 3.6 does not show a redshift dependence, strongly indicating that this behaviour is not physically motivated (e.g., due to the cosmic evolution of AGN activity), and instead points to this being a product of model degeneracies. The MIR SED is primarily composed of stellar, dust, and AGN emission. Unless the source has a pronounced AGN-driven MIR excess (leading to $\mathcal{P}_{\text{AGN,MIR}} \approx 1$) or a clear absence of AGN features ($\mathcal{P}_{\text{AGN,MIR}} \approx 0$), the observed SED can be plausibly fit by several combinations of dust emission templates and AGN models (e.g., Salim et al., 2016, Leja et al., 2018, B23, and D24). Consequently, the posterior distribution spans a wide range of AGN fractions, and the resulting $\mathcal{P}_{\text{AGN,MIR}}$ becomes effectively non-discriminative. It is therefore essential to adopt an informed prior that can help break the model degeneracies and appropriately down-weight marginal AGN solutions that are not strongly supported by the data.

While MID IR SEDs can be fit both with and without AGN templates, it has been shown that the former leads to better fits (i.e., lower χ^2) for sources with substantial AGN contributions (see Leja et al., 2018, Thorne et al., 2022b, and D24, and references therein). We use this as the foundation for our efforts to construct a prior that encodes the relative confidence in the AGN model. To that end, we fit the photometry for each source twice, once including AGN templates in the model and once without (similar to the approach adopted by D24). Given our focus on MIR wavelengths, we restrict the analysis to photometric data only, as the available DESI spectra do not extend into this spectral regime. Moreover, in our present model, spectroscopy does not directly constrain the mid-IR SED, although we plan to revisit this in a future work. We define the Bayes factor $\mathcal{R}_{\mathcal{L}}$ as the ratio of the marginal likelihoods of the models with and without AGN templates fitting the data, assuming that one of these two competing models is true (see, for example, Kass and Raftery, 1995; Han and Carlin, 2001; Trotta, 2008, for details):

$$\mathcal{R}_{\mathcal{L}} = \frac{\exp(-\frac{1}{2}\chi^2_{\text{AGN}})}{\exp(-\frac{1}{2}\chi^2_{\text{No AGN}})}, \tag{3.4}$$

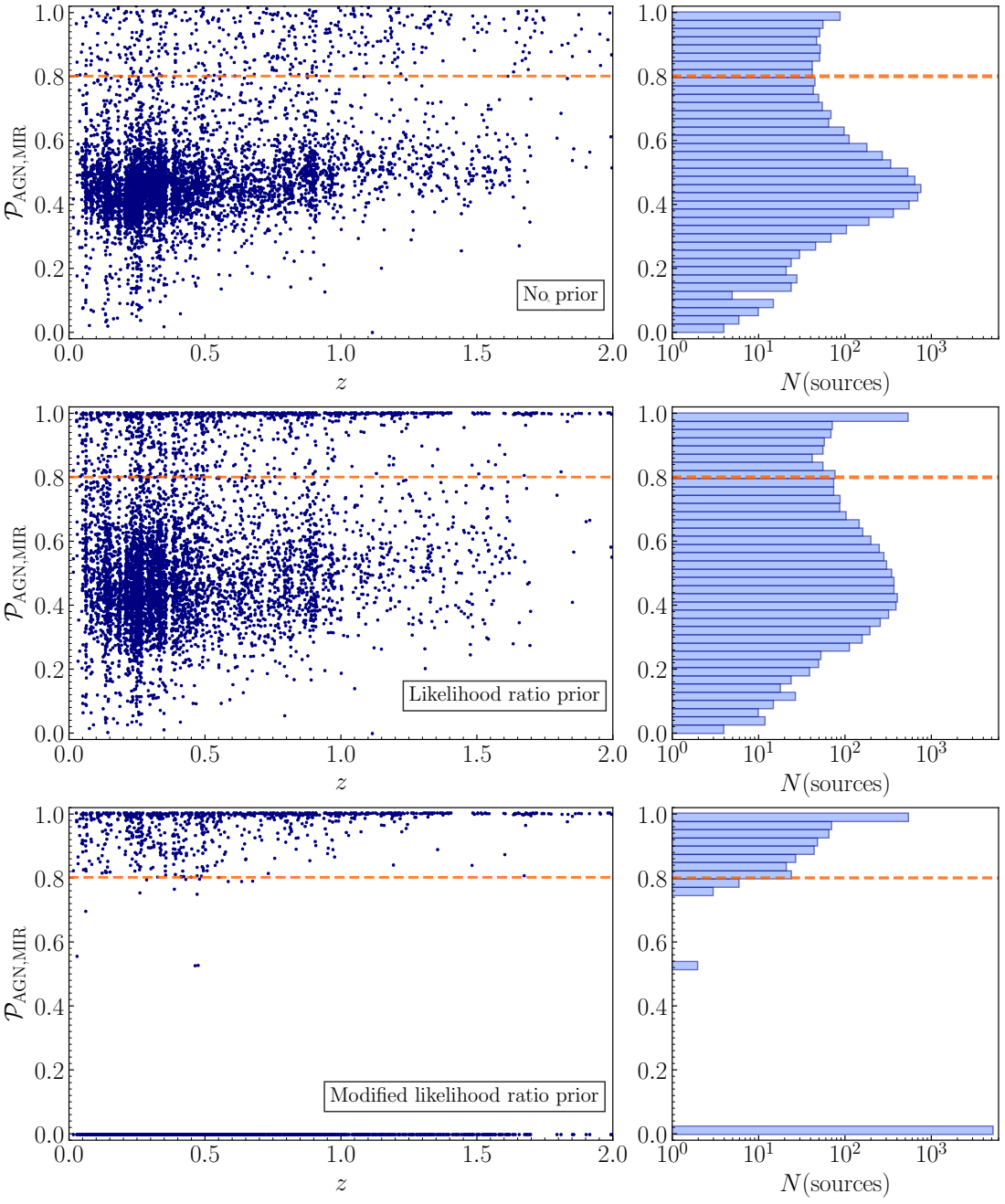

FIGURE 3.6: The distribution of the posterior probabilities of radio sources hosting radiative AGN ($\mathcal{P}_{\rm AGN,MIR}$) is shown without *a priori* restrictions (top panels), after applying a likelihood ratio prior (middle panels), and after applying the modified likelihood ratio prior (bottom panels). The left-hand columns show the distribution of the $\mathcal{P}_{\rm AGN,MIR}$ vs z plane. The lack of redshift evolution in $\mathcal{P}_{\rm AGN,MIR}$ supports the interpretation that the distributions are driven by model degeneracies rather than physical effects. The histograms in the right-hand columns demonstrate how the introduction of physically motivated priors enables more secure classification of sources hosting radiative-mode AGN.

where $\chi^2_{\rm AGN}$ and $\chi^2_{\rm No\ AGN}$ are the chi-squared statistic calculated for the best-fitting SEDs with and without the AGN template, respectively.[7]

The probability that the AGN model is preferred is given by:

$$\mathcal{P}_{\rm AGN\ Model} = \frac{\mathcal{R}_{\mathcal{L}}}{1+\mathcal{R}_{\mathcal{L}}}. \tag{3.5}$$

The probability that the model without AGN is favoured can then be written as $\mathcal{P}_{\rm No\ AGN\ Model} = 1-\mathcal{P}_{\rm AGN\ Model}$. The prior, which we refer to as the "likelihood ratio" (LR) prior, is defined as:

$$W_{f_{\rm AGN}} = \begin{cases} 1-\mathcal{P}_{\rm AGN\ Model}, & \text{if } f_{\rm AGN} < 10^{-3}, \\ \mathcal{P}_{\rm AGN\ Model}, & \text{if } f_{\rm AGN} \geq 10^{-3}. \end{cases} \tag{3.6}$$

When $\chi^2_{\rm AGN} << \chi^2_{\rm No\ AGN}$, this prior tends to unity, favouring the AGN model. Conversely, when the AGN model does not provide a substantial improvement, $\mathcal{P}_{\rm AGN\ Model}$ tends to zero, thereby penalising the AGN component. This approach has the advantage of being fully data-driven: it does not require external assumptions about AGN demographics, and instead relies solely on the relative model performance for a given source. As shown in the centre-right panel of Fig. 3.6, the application of this LR prior significantly suppresses the number of sources with intermediate AGN fractions, and results in more sources being conclusively identified as radiative-AGN hosts ($\mathcal{P}_{\rm AGN,MIR} > 0.9$). However, approximately 70 per cent of the sources are still clustered around $0.3 < \mathcal{P}_{\rm AGN,MIR} < 0.7$, arising from the cases where similar χ^2s are derived from fits with and without AGN templates ($0.9 < \chi^2_{\rm No\ AGN}/\chi^2_{\rm AGN} < 1.1$). To securely classify these sources, we set $\mathcal{P}_{\rm AGN\ Model} = 0$ whenever $\mathcal{P}_{\rm AGN\ Model} < 0.8$. This ensures that unless AGN templates significantly improve the SED fit, DYNESTY chains where AGN torus contributes more than 0.1 per cent of the mid-IR emission (i.e. $f_{\rm AGN} \geq 10^{-3}$) are not considered. We call this the "modified likelihood ratio" (MLR) prior. As shown in the bottom-right panel of Fig. 3.6, the MLR prior results in a much clearer separation between AGN and non-AGN sources, significantly reducing the number of systems with intermediate posterior probabilities. High AGN probabilities are now assigned only when (i) the SED exhibits a clear mid-IR excess, or (ii) the inclusion of AGN templates yields a substantial improvement in fit quality. Accordingly, the MLR $\mathcal{P}_{\rm AGN,MIR}$ is adopted as the probability that a source hosts a radiative-mode AGN.

[7] While this definition of the Bayes factor does not fully account for the width of the posterior distributions, we retain this approach for the sake of simplicity and adopt more physically motivated priors to obtain more realistic AGN probabilities in the subsequent analysis.

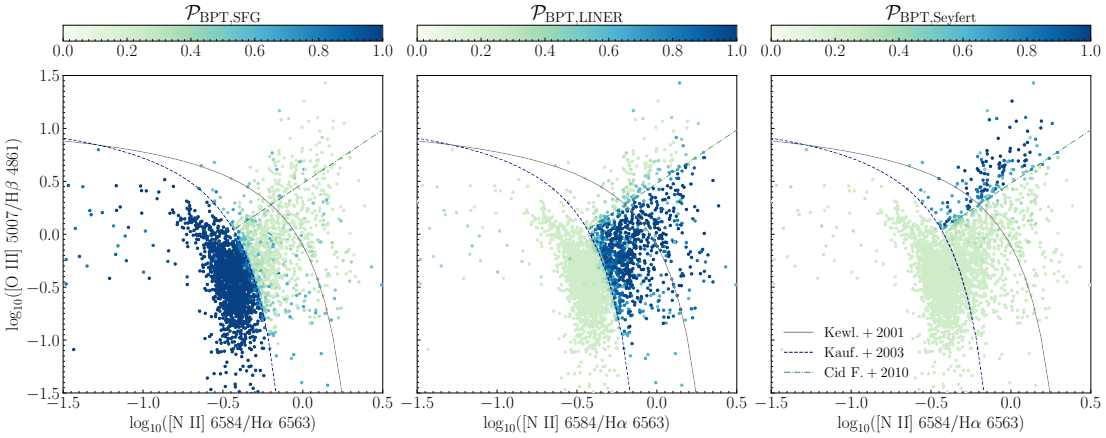

FIGURE 3.7: BPT diagram, colour-coded by the probabilities of sources belonging to the SFG ($\mathcal{P}_{\rm BPT,SFG}$), LINER ($\mathcal{P}_{\rm BPT,LINER}$), and Seyfert ($\mathcal{P}_{\rm BPT,Seyfert}$) classes, shown in the left-hand, centre, and right-hand panels, respectively. Overlaid are the Kewley et al. (2001), Kauffmann et al. (2003), and Cid Fernandes et al. (2010) demarcation lines.

3.3.2 Identification of radiative-mode AGN based on emission line rations

Since this work involves simultaneous fitting of photometry and spectroscopy, we can use the well-known BPT diagnostic to identify radiative-mode AGN. This method is based on the relative strengths of the [OIII]λ5007/Hβ and [NII]λ6584/Hα emission line pairs. Since the hot accretion disk is able to excite ions with higher ionisation energies than stellar radiation, the location of a source on the [OIII]/Hβ – [NII]/Hα plane can be used to classify galaxies. The precise conditions separating different galaxy classes have been a topic of active research, with various demarcation lines having been adopted depending on the science case (e.g., Kewley et al., 2001, 2006, 2019; Kauffmann et al., 2003; Best and Heckman, 2012; Cid Fernandes et al., 2010; Juneau et al., 2014). Works such as Drake et al. (2024) and A25 have used emission-line ratio diagnostics to identify radiative-mode AGN in the LoTSS radio source population. We follow both Drake et al. (2024) and A25 and use the empirically defined Kauffmann et al. (2003) line, which separates the SFGs from the radiative-mode AGN in the [OIII]/Hβ – [NII]/Hα plane. Additionally, following A25 we adopt the Cid Fernandes et al. (2010) line, which separates sources with hard ionising spectra (e.g., Seyferts) from those that lack high-ionisation lines, such as low-ionisation nuclear excitation regions (LINERS; see Best and Heckman, 2012; Drake et al., 2024). While Drake et al. (2024) used the LINER/Seyfert separation approach outlined by Kauffmann et al. (2003), A25 found the Cid Fernandes et al. (2010) line to be better aligned with the SFG – AGN divide in the BPT plane for deep radio sources in the ELAIS-N1 field (see A25 and references therein). BPT-based classification is performed only for sources

that had acceptable fits for the four emission lines following the reduced-χ^2 criterion defined in Section 3.2.2.

Drake et al. (2024) and A25 used Monte Carlo realisations to calculate the probability that a source belongs to one of the three BPT classes – SFG, LINER, or Seyfert. In contrast, since we have access to the full posterior probabilities from PROSPECTOR fits, we adopt a Bayesian approach. Specifically, we use the DYNESTY posterior chain after it has reached convergence (see Section 3.2.2 for the definition of convergence). For each sample in the DYNESTY posterior chain, we compute the line flux ratios [OIII]/$H\beta$ and [NII]/$H\alpha$, and determine the corresponding BPT classification based on demarcations discussed above. The probability of the source belonging to a given class is then calculated as:

$$\mathcal{P}_{\mathrm{BPT,C}} = \frac{N_C}{N_{\mathrm{total}}}, \quad C \in \{\mathrm{SFG}, \mathrm{LINER}, \mathrm{Seyfert}\} \tag{3.7}$$

where N_C is the number of posterior samples classified into the corresponding BPT class (SFG, LINER, or Seyfert), and N_{total} is the total number of samples in the converged DYNESTY posterior chain.

3.3.3 Identification of radio-excess AGN

Radio emission in galaxies is a combination of thermal free-free emission and non-thermal synchrotron radiation (for a review, see Condon, 1992). The synchrotron radiation is powered by two distinct mechanisms: the shock-acceleration of cosmic rays by supernova remnants of short-lived massive stars (Blumenthal and Gould, 1970; Condon, 1992; Condon and Ransom, 2016), and through the jets and lobes produced by accretion on to the central supermassive black hole (SMBH; see reviews by Bridle and Perley, 1984; Padovani et al., 2017; Hardcastle and Croston, 2020). Therefore, in galaxies lacking AGN activity, the non-thermal synchrotron radiation serves as an excellent probe of star formation activity. This has been demonstrated by the presence of the far-infrared radio correlation (FIRC) in SFGs, which has been observed to be linear over several orders of magnitude in luminosity (e.g., van der Kruit, 1971; de Jong et al., 1985; Jarvis et al., 2010; Bourne et al., 2011; Smith et al., 2014; Magnelli et al., 2015; Delhaize et al., 2017; Delvecchio et al., 2021). Low-frequency radio observations are particularly useful in this regard, as free-free emission – a significant contributor to the radio continuum at GHz frequencies and above (Condon, 1992; Murphy et al., 2011) – is practically absent at low frequencies.

Radio surveys at low frequencies, such as LoTSS, are therefore ideal for studying the relationship between radio luminosity and star formation activity. In this section, we use the relationship between the 150 MHz luminosity (L_{150}) and star formation activity indicators to identify radio excess AGN. We focus on two measures of star formation activity: the SFR calculated from the SED fit, and the Balmer-corrected Hα line luminosity. We then establish methods to compute the probability of a source being a radio excess AGN based on each of them, before combining them into a single estimate of the probability that its radio emission exceeds what is expected from star formation alone.

3.3.3.1 Radio-excess AGN identification through the SFR–150 MHz relation

In SFGs, L_{150} has been observed to have a linear relationship with SFR over several orders of magnitude, known as the "SFR–L_{150} relation" (Brown et al., 2017; Calistro Rivera et al., 2017; Gürkan et al., 2018; Read et al., 2018; Wang et al., 2019; Smith et al., 2021; Heesen et al., 2022). Deviations from this linearity are often used to identify AGN-hosting sources (Hardcastle et al., 2016; Williams et al., 2018; Hardcastle et al., 2019; Smolčić et al., 2017a; Calistro Rivera et al., 2017; Best et al., 2023). D24 (see Chapter 2, Section 2.4.2) used a 3.6 μm-selected sample of 130,000 galaxies from the ELAIS-N1 deep fields to derive the best-fit relation $\log_{10} L_{150} = (22.024 \pm 0.006) + (1.019 \pm 0.009) \log_{10}(\psi / M_{\odot}\ \mathrm{yr}^{-1})$. They classified sources as AGN candidates if their L_{150} exceeded the predicted value for star-forming galaxies by 0.867 dex. However, this approach comes with several important caveats. Firstly, deriving reliable estimates of the SFR–L_{150} relation ideally necessitates a large, statistically robust, and unbiased sample that spans a wide range of radio luminosities. And secondly, relying on a binary classification scheme can also be problematic, as it may lead to the misclassification of sources that lie near the boundary between categories, and therefore risks introducing systematic biases.

The distribution $\Phi_{\mathrm{TOTAL}} = \log_{10}(L_{150}) - \log_{10}(\psi)$ can be interpreted as a mixture of SFGs and AGN hosts ($\Phi_{\mathrm{TOTAL}} = \Phi_{\mathrm{SFGs}} + \Phi_{\mathrm{AGN}}$). Based on D24, it is reasonable to believe that the left-hand side of the distribution is predominantly composed of SFGs, and that the SFGs are distributed symmetrically around the peak of the total distribution. Under this assumption, we flip the left-hand side of the distribution to get a symmetric distribution of SFGs (Φ_{SFGs}). The distribution of AGN hosts is then given by: $\Phi_{\mathrm{AGN}} = \Phi_{\mathrm{TOTAL}} - \Phi_{\mathrm{SFGs}}$. We define the probability of a

source at any point along $x \equiv \log_{10}(L_{150}) - \log_{10}(\psi)$ being a radio-excess AGN, $\mathcal{P}_{\mathrm{REX},\psi}(x)$, as:

$$\mathcal{P}_{\mathrm{REX},\psi}(x) = \Phi_{\mathrm{AGN}}(x)/\Phi_{\mathrm{TOTAL}}(x). \tag{3.8}$$

Uncertainties on $\mathcal{P}_{\mathrm{REX},\psi}(x)$ are computed through 100 iterations of bootstrap resampling. As seen in the upper panels of Fig. 3.8, $\mathcal{P}_{\mathrm{REX},\psi}(x)$ is reasonably well described (reduced $\chi^2 = 0.98$) by a Gamma cumulative distribution function (Γ-CDF):

$$F(x) = \frac{1}{\Gamma(\alpha)}\,\gamma\left(\alpha, \frac{x-\mu}{\theta}\right) \tag{3.9}$$

with a location parameter (μ) = 22.251, shape parameter (α) = 1.486, and scale parameter (θ) = 0.264. For each source, we calculate the difference $x_i = \log_{10}(L_{150,i}) - \log 10(\psi_i)$, where ψ_i is derived from the i^{th} sample in the DYNESTY posterior chain after convergence, and $L_{150,i}$ is taken from a normal distribution centred on the L_{150} value calculated from the observed 150 MHz flux density, with a standard deviation equal to the uncertainty on L_{150}. Since PROSPECTOR presently does not support the modelling of radio data, the L_{150} DYNESTY chains are not available, and we therefore cannot use the posterior-based approach adopted elsewhere in this chapter. The expectation value

$$P_{\mathrm{REX},\psi} = \sum_i x_i \mathcal{P}_{\mathrm{REX},\psi}(x_i) \tag{3.10}$$

then represents the probability of the source in question being a radio-excess AGN.

3.3.3.2 Using the Hα line luminosity–150 MHz radio luminosity relation

Ionising photons produced by young, massive, and short-lived O- and B-type stars photoionise the surrounding gas, transforming neutral hydrogen into its ionised form (HII). Recombination of the ionised HII regions leads to line emission – most notably the Balmer recombination lines Hα (6563 Å) and Hβ (4861 Å) – which have traditionally been used as SFR indicators (see reviews by Kennicutt, 1998a; Calzetti, 2013). The Hα line, in particular, is one of the brightest and lies in the optical wavelength range in the low-redshift Universe. The dust attenuation-corrected Hα line luminosity ($L_{\mathrm{H}\alpha}$) is one of the most commonly used empirical tracer of SFR, sensitive to timescales of approximately 10 Myrs (e.g., Brinchmann et al., 2004; Kennicutt and Evans, 2012). The dust attenuation correction for Hα is derived by calculating the extinction factor A_V from the Balmer decrement, assuming case-B recombination (Osterbrock and Ferland,

2006), and adopting the Calzetti et al. (2000) attenuation curve with $R_V = 4.05$ (see Domínguez et al., 2013; Drake et al., 2024):

$$E(B-V) = 1.97 \log_{10}\left[\frac{(\mathrm{H}\alpha/\mathrm{H}\beta)_{\mathrm{obs}}}{2.86}\right] \tag{3.11}$$

$$A_{\mathrm{H}\alpha} = 3.33 \times E(B-V) \tag{3.12}$$

The relative location of sources on the $\log_{10}(L_{\mathrm{H}\alpha})$ vs $\log_{10}(L_{150})$ plane has been used to differentiate between SFGs/RQ AGN and radio-excess sources. For example, Sabater et al. (2019) used a pair of demarcation lines derived from LoTSS deep fields DR1 radio fluxes and spectroscopic data from Sloan Digital Sky Survey (SDSS; York et al., 2000) DR7. Meanwhile, Drake et al. (2024) and A25 calculated thresholds based on the distribution of $\log_{10}(L_{150}) - \log_{10}(L_{\mathrm{H}\alpha})$. Drake et al. (2024) used radio data from LoTSS DR2 and spectra from SDSS DR8 and BOSS DR12, while A25 used LoTSS DR1 radio observations and DESI EDR spectra.

Following the method adopted for the SFR–L_{150} based classifications (Section 3.3.3.1), we decompose the distribution of $\Omega_{\mathrm{TOTAL}} = \log_{10}(L_{150}) - \log_{10}(L_{\mathrm{H}\alpha})$ into a symmetric SFG and residual AGN components, and subsequently define the probability at any point along $x' \equiv \log_{10}(L_{150}) - \log_{10}(L_{\mathrm{H}\alpha})$ as:

$$\mathcal{P}_{\mathrm{REX,H}\alpha}(x') = \Omega_{\mathrm{AGN}}(x')/\Omega_{\mathrm{TOTAL}}(x'). \tag{3.13}$$

$\mathcal{P}_{\mathrm{REX,H}\alpha}(x')$ is well described (reduced $\chi^2 = 1.11$) by a Γ-CDF with $X = 13.162, \alpha = 47.911$, and $\theta = 0.048$ (Fig. 3.8, lower panels). We then use the Balmer-corrected Hα luminosities for each sample in the converged DYNESTY posterior to compute the expectation value $P_{\mathrm{REX,H}\alpha} = \sum_i x'_i \mathcal{P}_{\mathrm{REX,H}\alpha}(x'_i)$, which gives the probability of an individual source hosting a radio-excess AGN on the basis of the Hα emission.

At present, this approach can only classify sources up to $z < 0.49$, where the observed-frame Hα and Hβ wavelengths fall within the wavelength range observed by DESI, in addition to the conditions already discussed in Section 3.1. We intend to implement the new workflow under development in A25 imminently, which will allow us to extend this classification approach out to $z \approx 1$.

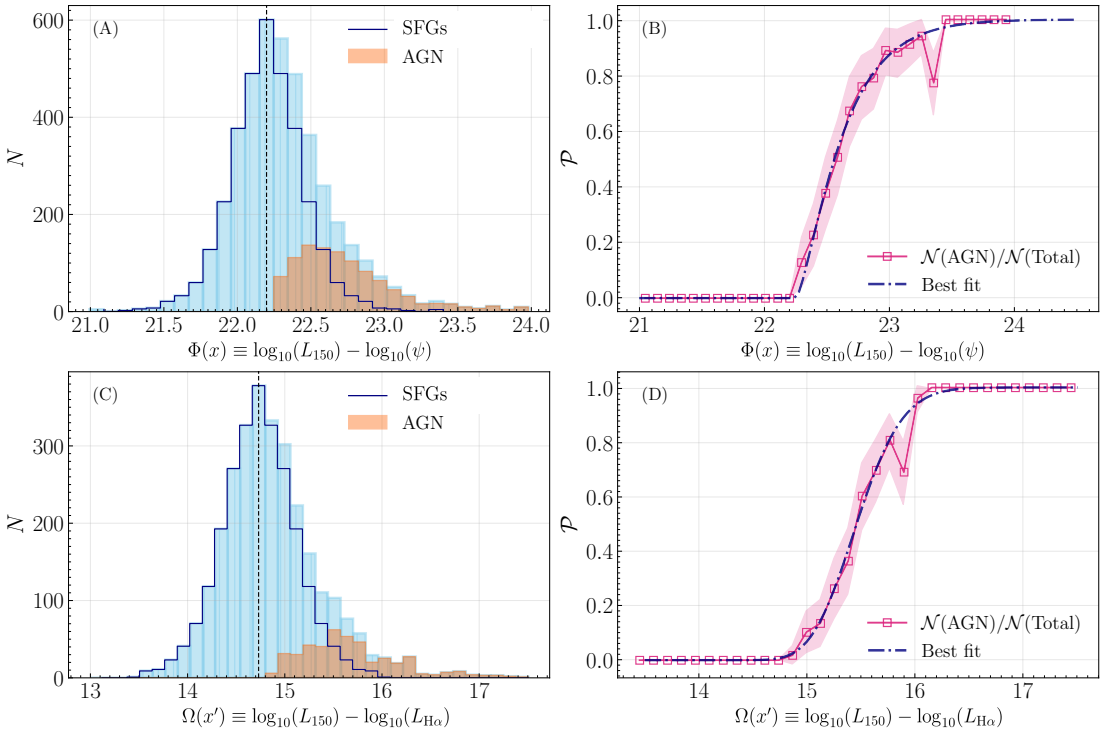

FIGURE 3.8: Distribution of $\log_{10}(L_{150}) - \log_{10}(\psi)$ (top-left panel) and $\log_{10}(L_{150}) - \log_{10}(L_{H\alpha})$ (bottom-left panel). The blue-shaded histogram in each panel represents the full source population, the navy-outlined histogram denotes the SFG population – obtained by reflecting the left-hand side of the full distribution about its peak, and the orange histogram shows the residual population, which is predominantly composed of radio-excess AGN. The right-hand panels show the Gamma cumulative distribution function (Γ-CDF) fits to the probability functions defined by Eqn. 3.8 (top) and Eqn. 3.13 (bottom). The uncertainties, represented by the shaded pink regions, are computed through bootstrapping.

3.3.3.3 Combining SFR- and Balmer-line -based radio-excess classification methods

In the previous sections, we defined the probability of a source being a radio-excess AGN based on the deviation of its 150 MHz radio luminosity from the SFR calculated directly from the SED fits ($P_{\mathrm{REX},\psi}$) and from the empirical SFR indicator, the Hα line luminosity ($P_{\mathrm{REX,H}\alpha}$). The probability of the source being a radio-excess AGN can be estimated by the weighted average of these two probabilities:

$$\mathcal{P}_{\mathrm{REX}} = \frac{w_\psi P_{\mathrm{REX},\psi} + w_{\mathrm{H}\alpha} P_{\mathrm{REX,H}\alpha}}{w_\psi + w_{\mathrm{H}\alpha}} \tag{3.14}$$

The weights w_ψ and $w_{\mathrm{H}\alpha}$ are defined as the inverse of the variances of the probabilities $\mathcal{P}_{\mathrm{REX},\psi}$ (see Eqn. 3.8) and $\mathcal{P}_{\mathrm{REX,H}\alpha}$ (see Eqn. 3.13), respectively. These variances are estimated for every source with both Hα and SFR estimates using the standard deviations calculated from the 16$^{\mathrm{th}}$

and 84$^{\text{th}}$ percentiles of the PDFs of the respective probabilities:

$$w_{\psi} = \frac{1}{\sigma^2_{\text{REX},\psi}}, \text{ and, } w_{\text{H}\alpha} = \frac{1}{\sigma^2_{\text{REX,H}\alpha}}. \tag{3.15}$$

In cases where one of the probabilities is unavailable (e.g., due to the source being outside the redshift range where the Balmer-line -based classification can be applied), the corresponding weight is set to 0. This definition accounts for the relative confidence in each diagnostic, and we believe it will provide a robust measure of the probability of a source being a radio-excess AGN.

3.3.4 Combined spectrophotometric classification of radio sources in the LoTSS deep field EN1

In this section, we combine the three sets of probabilities: (i) the probability of a source hosting a radiative-mode AGN based on mid-IR excess ($\mathcal{P}_{\text{AGN,MIR}}$), (ii) the probabilities of the source being in one of the three BPT classes ($\mathcal{P}_{\text{BPT,SFG}}$, $\mathcal{P}_{\text{BPT,LIN}}$, and $\mathcal{P}_{\text{BPT,SEY}}$), and (iii) the probability of it being a radio-excess AGN ($\mathcal{P}_{\text{REX}}$). We calculate the probabilities of the source belonging to the four galaxy classes: SFG ($\mathcal{P}_{\text{SFG}}$), RQ AGN ($\mathcal{P}_{\text{RQAGN}}$), LERG ($\mathcal{P}_{\text{LERG}}$), and HERG ($\mathcal{P}_{\text{HERG}}$). Sources are considered classifiable if they have a valid $\mathcal{P}_{\text{REX}}$, along with either a valid $\mathcal{P}_{\text{AGN,MIR}}$ value and/or valid BPT classification probabilities. Depending on the availabilities of these values, the classification approach can be divided into four cases:

1. For sources with acceptable PROSPECTOR photometric χ^2 values (see Section 3.2.2), $\mathcal{P}_{\text{AGN,MIR}}$ and $\mathcal{P}_{\text{REX}}$ values, but lacking emission-line -based classification probabilities (e.g., not meeting the criteria in Section 3.1 or lying outside the redshift range suitable for Balmer-line-based classification), the classification probabilities are defined as follows:

$$\begin{aligned}
\mathcal{P}_{\text{SFG}} &= (1-\mathcal{P}_{\text{REX}})\cdot(1-\mathcal{P}_{\text{AGN,MIR}}) \\
\mathcal{P}_{\text{RQAGN}} &= (1-\mathcal{P}_{\text{REX}})\cdot\mathcal{P}_{\text{AGN,MIR}} \\
\mathcal{P}_{\text{LERG}} &= \mathcal{P}_{\text{REX}}\cdot(1-\mathcal{P}_{\text{AGN,MIR}}) \\
\mathcal{P}_{\text{HERG}} &= \mathcal{P}_{\text{REX}}\cdot\mathcal{P}_{\text{AGN,MIR}}
\end{aligned} \tag{3.16}$$

2. When all four BPT emission lines have acceptable reduced-χ^2 values (see Section 3.2.2), and both BPT probabilities and valid $\mathcal{P}_{\rm REX}$ values are available, but $\mathcal{P}_{\rm AGN,MIR}$ is lacking, the classification probabilities are calculated as:

$$\begin{aligned}
\mathcal{P}_{\rm SFG} &= (1-\mathcal{P}_{\rm REX})\cdot\mathcal{P}_{\rm BPT,SFG} \\
\mathcal{P}_{\rm RQAGN} &= (1-\mathcal{P}_{\rm REX})\cdot(1-\mathcal{P}_{\rm BPT,SFG}) \\
\mathcal{P}_{\rm LERG} &= \mathcal{P}_{\rm REX}\cdot(1-\mathcal{P}_{\rm BPT,SEY}) \\
\mathcal{P}_{\rm HERG} &= \mathcal{P}_{\rm REX}\cdot\mathcal{P}_{\rm BPT,SEY}
\end{aligned} \tag{3.17}$$

3. Lastly, when both the photometric χ^2 and the four BPT emission-line reduced-χ^2 values are acceptable, and all the aforementioned probabilities are available, the classification probabilities are given by:

$$\begin{aligned}
\mathcal{P}_{\rm SFG} &= (1-\mathcal{P}_{\rm REX})\cdot(1-\mathcal{P}_{\rm AGN,MIR})\cdot\mathcal{P}_{\rm BPT,SFG} \\
\mathcal{P}_{\rm RQAGN} &= (1-\mathcal{P}_{\rm REX})\cdot[\mathcal{P}_{\rm AGN,MIR}+(1-\mathcal{P}_{\rm BPT,SFG})-\mathcal{P}_{\rm AGN,MIR}\cdot(1-\mathcal{P}_{\rm BPT,SFG})] \\
\mathcal{P}_{\rm LERG} &= \mathcal{P}_{\rm REX}\cdot(1-\mathcal{P}_{\rm AGN,MIR})\cdot(1-\mathcal{P}_{\rm BPT,SEY}) \\
\mathcal{P}_{\rm HERG} &= \mathcal{P}_{\rm REX}\cdot(\mathcal{P}_{\rm AGN,MIR}+\mathcal{P}_{\rm BPT,SEY}-\mathcal{P}_{\rm AGN,MIR}\cdot\mathcal{P}_{\rm BPT,SEY})
\end{aligned} \tag{3.18}$$

4. $\mathcal{P}_{\rm SFG}$, $\mathcal{P}_{\rm RQAGN}$, $\mathcal{P}_{\rm LERG}$ and $\mathcal{P}_{\rm HERG}$ cannot be calculated for sources that do not satisfy any of these three cases.

As discussed in Drake et al. (2024) and A25, a probabilistic approach supports classifications that can prioritise either purity – i.e., selecting sources that satisfy a given probability threshold (e.g., 90 per cent purity classifications, referred to as the "P_{90}" classifications in this chapter) – or completeness – i.e., assigning sources to the class with the highest probability (a.k.a., maximum-likelihood, or "ML" classifications). The number of sources classified into each class using both of these approaches is provided in Table 3.2. It is clear that using ML classifications allows for more sources to be classified ($\approx$ 90 per cent of the source sample). On the other hand, the 50 per cent of our sample classified using a strict >90 per cent probability threshold will, by definition, be more reliable than the ML classifications. It is therefore the responsibility of the end user to select the most appropriate approach based on their scientific goals.

In Fig. 3.9, we show the typical SEDs of the P_{90}-classified sources. The solid orange line in each panel represents the median unattenuated stellar SED, the solid green line shows the median

	SFGs	RQ AGN	LERGs	HERGs	Unc.
This work (P_{90})	$1,852 \pm 43$	522 ± 22	514 ± 22	69 ± 8	$2,444 \pm 49$
	34.3 (62.6) %	9.7 (17.7) %	9.5 (17.4) %	1.3 (2.3) %	45.3 %
This work (ML)	$2,892 \pm 53$	$1,168 \pm 34$	$1,105 \pm 33$	236 ± 15	0
	53.5 (53.5) %	21.6 (21.6) %	20.5 (20.5) %	4.4 (4.4) %	0.0 %
D24	$4,199 \pm 64$	373 ± 19	665 ± 25	68 ± 8	96 ± 9
	77.7 (79.2) %	6.9 (7.0) %	12.3 (12.5) %	1.3 (1.3) %	1.8 %

TABLE 3.2: The number of star forming galaxies, radio-quiet AGN, low/high-excitation galaxies, identified after setting a 90 per cent purity threshold (P_{90}), and using maximum-likelihood (ML) classification approach, out of a total of 5,401 sources that could be classified by either method. Poisson uncertainties are reported. The percentages of the 5,401 sources that fall into each class are quoted below, with the accompanying parentheses giving the percentages relative to the number of sources that could be classified using that method (i.e. excluding unclassified sources). For comparison, D24 classifications are also presented. While the ML classification allows for the classification of approximately twice as many sources as the P_{90} classification, the latter is more reliable.

AGN model, and the solid blue line indicates the median full UV–FIR SED. The shaded regions denote the scatter between the 16^{th} and 84^{th} percentile SEDs as a function of the wavelength. SFGs and RQ AGN exhibit similar full and unattenuated stellar SEDs. The key distinguishing feature is the AGN model component, which is more prominent in RQ AGN, as expected. LERGs display red UV–optical stellar slopes, indicative of older stellar populations. HERGs show the clearest evidence of AGN-driven MIR excess. They exhibit the bluest UV–optical SEDs among all classes, which is associated with emission from a young stellar population or with strong, radiatively efficient accretion-disk emission, typical of Seyferts and luminous quasars (e.g. Wilkes, 1999; Muñoz Marín et al., 2009; Tadhunter, 2016). The AGN model component shows considerable scatter, reflecting the typically broad f_{AGN} posteriors discussed in Section 3.3.1. The SEDs of unclassified sources broadly resemble those of SFGs and RQ AGN – the numerically dominant classes in Table 3.2.

3.4 Discussion

In this section, we investigate the reliability of our spectrophotometric classifications by looking at their distributions in different diagnostic planes. We use the P_{90} classifications throughout, unless specified otherwise. In Fig. 3.10, we plot the median likelihood SFRs of these sources relative to the so-called "main sequence" relation from Schreiber et al. (2015), parametrised by stellar mass and redshift (see Eqn. 3.19), after converting the latter to a Kroupa (2001) IMF

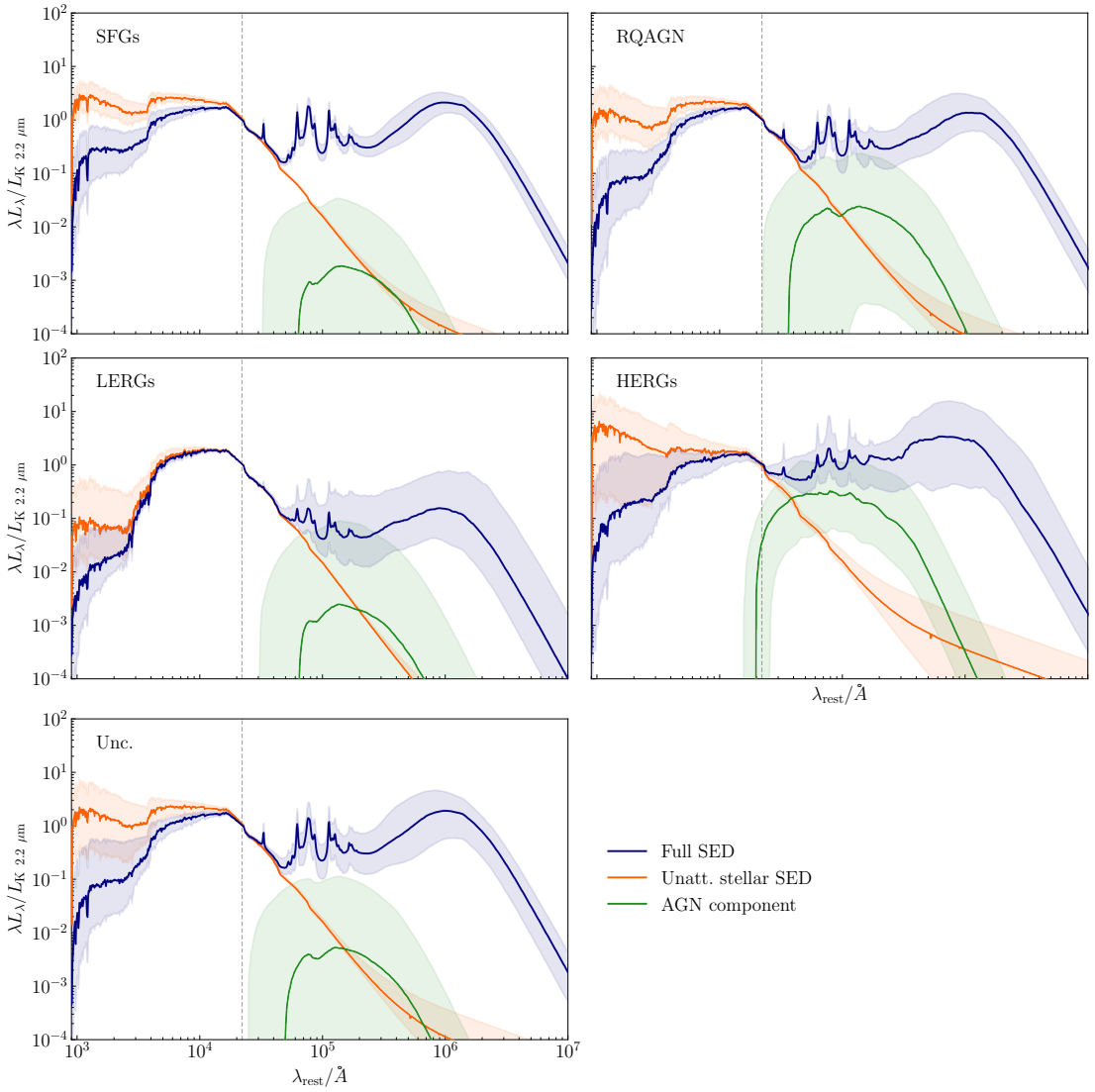

FIGURE 3.9: The typical SEDs of the P_{90}-classified sources in the (top-left panel) SFG, (top-right panel) RQ AGN, (centre-left) LERG, and (centre-right) HERG classes. Unclassified sources are in the bottom panel. The solid orange line in each panel represents the median unattenuated stellar SED, the solid green line shows the median AGN model, and the solid blue line indicates the median full UV–FIR SED. The shaded regions denote the scatter between the 16^{th} and 84^{th} percentile SEDs.

using the Madau and Dickinson (2014) conversion factor.

$$\log_{10}(\mathrm{SFR_{MS}}/\mathrm{M_\odot\ yr^{-1}}) = m - m_0 + a_0 r - a_1\left[\max(0, m - m_1 - a_2 r)\right]^2, \tag{3.19}$$

where $r \equiv \log_{10}(1+z)$ and $m \equiv \log_{10}(M_\star/10^9 M_\odot)$. The left-hand panel shows the stellar masses and SFRs estimated by D24, colour-coded according to their classifications. The right-hand panel shows the stellar masses and SFRs estimated from this chapter's spectrophotometric fitting, colour-coded according to the P_{90} classifications.

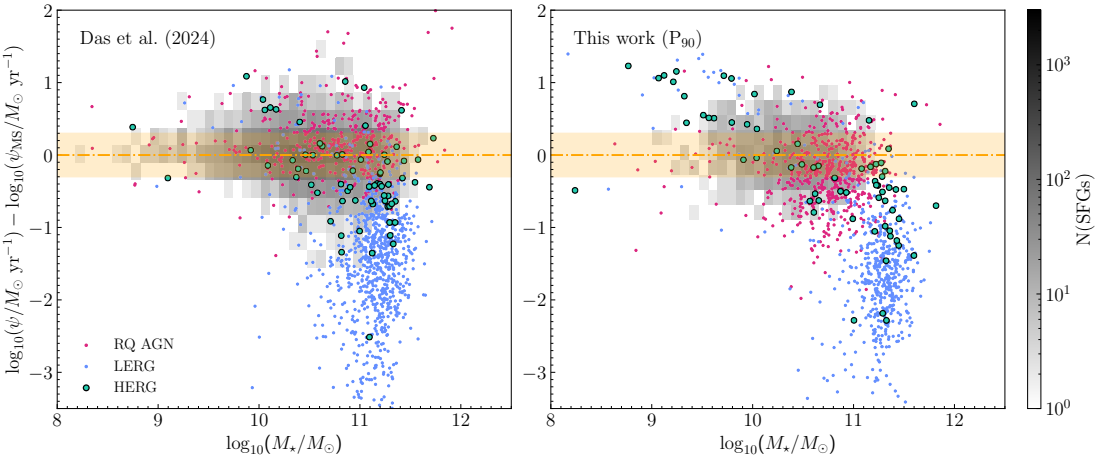

FIGURE 3.10: Sources in the four galaxy classes: SFGs (shaded gray histogram), RQ AGN (magenta points), LERGs (blue points), and HERGs (green points with black outlines), shown relative to the main sequence of star forming galaxies, with the stellar mass – SFR plane. The solid orange line and the shaded orange region depict the Schreiber et al. (2015) parametrisation of the main sequence, converted Kroupa (2001) IMF, with the typical 0.3 dex scatter. The left-hand panel displays stellar masses and SFRs from D24, colour-coded by their classifications, while the right-hand panel presents results from this chapter's spectrophotometric fitting, colour-coded according to the P_{90} classifications.

The SFRs of RQ AGN are similar to those of the SFGs; however, they are predominantly associated with massive sources (≈ 80 per cent of the RQ AGN have $\log_{10}(M_\star/M_\odot) > 10.5$, compared to only ≈ 42 per cent among SFGs). This is expected, as AGN are often found to reside in massive hosts, e.g., Gürkan et al. (2018) and Kondapally et al. (2022). The majority of LERGs are hosted by massive, quiescent galaxies, in agreement with the prevalent view that LERGs are found in massive red galaxies with old stellar populations (e.g. Tasse et al., 2008; Smolčić, 2009; Best and Heckman, 2012; Mingo et al., 2014). Only ~ 6 per cent of LERGs lie on or above the main sequence (with a ± 2 dex scatter, used here for consistency with Kondapally et al., 2025) at $0.3 < z < 1.5$, which is lower than the 18 per cent of star-forming LERGs (out of $\approx 3,500$ total) reported by Kondapally et al. (2025) in the same redshift range using a photometric classification scheme in the LoTSS deep fields (similar trends are also evident in Fig. 3.10). We interpret this difference as a consequence of the restrictive probability thresholds imposed in the P_{90} classification scheme. Indeed, when using the ML classifications, we find that 20 per cent of LERGs lie above the -0.2 dex scatter from the main sequence. The sensitivity of the LERG fraction to the probability threshold is noteworthy, and highlights the need for careful consideration of the trade-off between purity and completeness in classification catalogues when interpreting study results.

In Fig. 3.11 we look at the distribution of the P_{90} classified sources as a function of z and

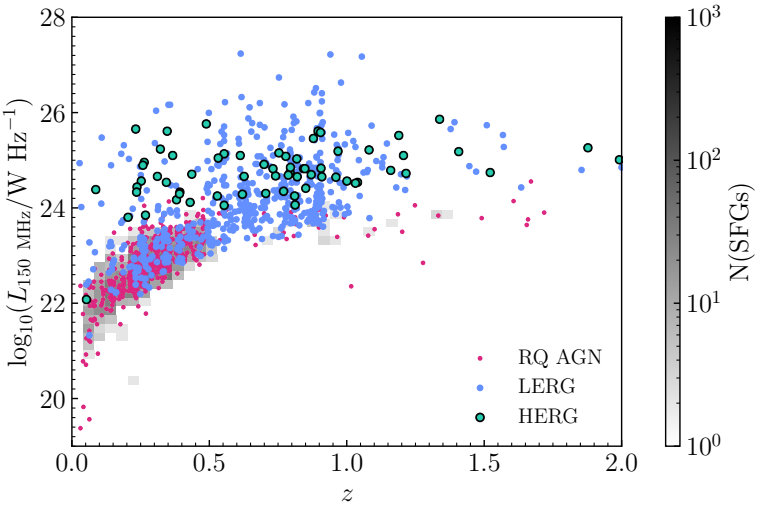

FIGURE 3.11: Distributions of the SFGs (shaded gray histogram), RQ AGN (magenta points), LERGs (blue points), and HERGs (green points with black outlines) in the redshift-150 MHz radio luminosity plane. The colourbar to the right denotes the number of SFGs.

L_{150}. The SFG and RQ AGN populations occupy similar parameter spaces, and are prevalent at lower redshifts and lower radio luminosities ($\log_{10} L_{150} < 24$). LERGs become more abundant at higher redshifts. We find HERGs only at $\log_{10} L_{150} > 24$ and at all redshifts. However, we do not find a clear $\log_{10} L_{150}$ threshold that separates radio-excess sources from SFGs and RQ AGN. The distribution of sources follows expected trends from the literature (for e.g., see Hardcastle et al., 2019, and references therein), and further establishes confidence in our method.

In Fig. 3.12, we examine the location of the P_{90}-classified sources in the BPT plane. We show only sources that have 3σ detections in all four BPT lines and acceptable PROSPECTOR fits. For the majority of sources, the trends follow expectations: SFGs occupy the star-forming region of the plane, while the vast majority of AGN (RQ AGN, LERGs, and HERGs) populate the Seyfert and LINER regions. 64 of the 1,614 sources with $> 3\sigma$ detections in all four BPT lines and $\mathcal{P}_{\mathrm{BPT,SFG}} > 0.9$ had $\mathcal{P}_{\mathrm{AGN,MIR}} > 0.9$, indicating an obscured AGN population. Of these, 36 sources are classified as RQ AGN in the P_{90} scheme (Fig. 3.12), with 90 per cent also classified as RQ AGN in the ML scheme. While the number of such sources is relatively small, they highlight the value of joint spectrophotometric classification approaches.

3.4.1 Comparison with photometric classification

To understand the impact of incorporating both photometric and spectroscopic information in the classification of radio sources, we compare our P_{90} classifications with the photometry-only

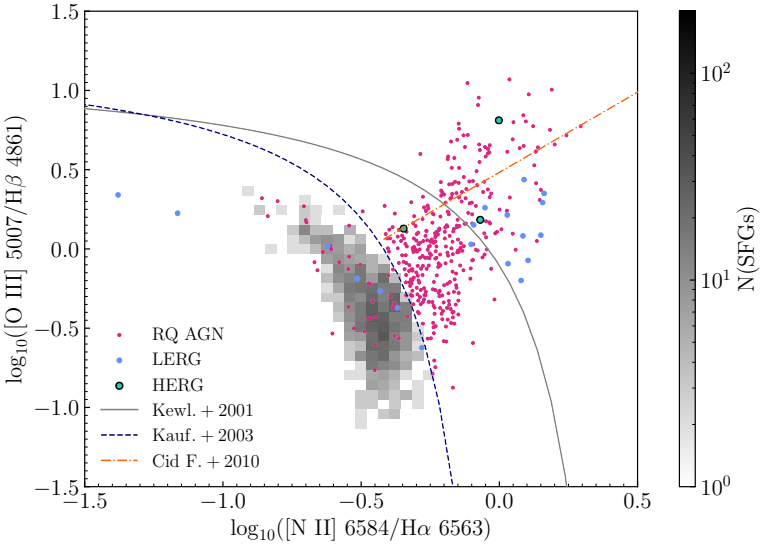

FIGURE 3.12: Distribution of the different AGN classes in the BPT plane. SFGs are denoted by the shaded gray histogram (with the colourbar to the right-hand side denoting the number of SFGs). The RQ AGN, LERGs, and HERGs are represented by the magenta, blue, and green points with black outlines, respectively. The BPT plane includes the Kewley et al. (2001), Kauffmann et al. (2003), and Cid Fernandes et al. (2010) demarcation lines. Only sources with 3σ detections are shown in this figure.

classifications from D24. The number of sources classified in both works is given in Table 3.2. The top rows of Fig. 3.13 show confusion matrices comparing our P_{90} classifications with those from D24, while the bottom rows of Fig. 3.13 compare our maximum-likelihood (ML) classifications to those of D24. In each case, the left-hand matrix indicates the number of sources assigned to a given class by our spectrophotometric classification (along the columns) that were classified into the corresponding D24 class (along the rows). Cells along the main diagonal quantify the level of agreement between the two classification methods, while off-diagonal cells indicate disagreements. The right-hand matrices present the same information in percentage form, with each cell reporting the percentage of sources in the P_{90} or ML class that were classified into the corresponding D24 class. The left-hand matrices are colour-coded by the percentage of the total number of sources classified, while the right-hand matrices are colour-coded by the percentage agreement between the two classifications. The percentage agreements are first reported considering all sources, followed by values in parentheses that exclude sources unclassified in either of the two classification schemes being compared. We follow this convention while discussing the results in this section as well as in Section 3.4.2. Additionally, Fig. 3.14 presents the unattenuated stellar SEDs (orange), AGN emission components (green), and total SEDs (blue) for the sources corresponding to each cell of the confusion matrices. All SEDs are normalised by the source K-band (2.2μm) luminosities. The thicker dashed lines in each colour indicate the

median SED for that component. We compare the results for the 5,401 sources with acceptable photometric fits in both works. The classifications compared in this section are from the P_{90} scheme unless specified otherwise.

Due to the increased complexity of the classification process and the probability cuts imposed to ensure a high degree of purity, P_{90} classification scheme leads to significantly more unclassified sources (2,444) compared to 96 in D24. 98.5 (99.2) per cent of the P_{90} SFGs classifications are concurrent with D24. Only 20.7 (21.0) per cent agreement is seen for the RQ AGN class. 72.4 (73.5) per cent of the P_{90} RQ AGN were classified as SFGs by D24. As shown in Fig. 3.9, the full SEDs of RQ AGN and SFGs are very similar; a key distinguishing feature is the contribution from the AGN component to the MIR portion of the SED. The large discrepancy noted here arises because the AGN fraction posterior does not provide a secure classification (~ 90 per cent of these sources have $\mathcal{P}_{\rm AGN,MIR} \approx 0$ after applying the MLR priors). Nevertheless, > 80 per cent of these sources were classified as Seyferts or LINERs based on emission-line diagnostics, thus placing them in the RQ AGN category. We find 83.7 (86.4) per cent agreement between the LERG classifications. Notably, 12.8 (13.3) per cent of the P_{90} LERGs were classified as SFGs by D24, primarily due to the differences in the precise definition of the SFR-based radio-excess threshold arising out of the differences between the median SFRs estimated by the two works. While these SFR differences are not statistically significant (i.e., are within the bounds of uncertainties), the resulting discrepancies in classification highlight the limitations of non-probabilistic schemes, where marginal changes can lead to shifts in class assignments. 20.3 per cent of the P_{90} HERGs were left unclassified by D24 owing to the lack of acceptable SED fits. Nonetheless, 39.1 (49.1) per cent agreement was seen in the HERG classifications. 18.8 (23.6) per cent of the P_{90} HERGs were classified as RQ AGN by D24, due to similar discrepancies in SFR estimates as seen in LERG-SFG case. 8.7 (10.9) per cent of the P_{90} HERGs were classified as LERGs by D24, as their fits indicated a lack of MIR AGN contribution ($f_{\rm AGN,16\ percentile} < 10^{-3}$). This, combined with the lack of acceptable D24 fits to a large fraction of P_{90} HERGs, indicates that the current spectrophotometric fitting approach where the latter is better capable of modelling the AGN contribution to the MIR SED. We believe this improvement is due to nebular line marginalisation adopted in this work, which, as noted by Johnson et al. (2021), allows for extrapolation of the `CLOUDY` models outside of the standard grid, thus being able to model emission lines that are powered by old stellar populations, AGN, and shocks. We intend to investigate this further in future works. Broadly similar trends are seen in the comparison of ML classifications to D24 with a couple of notable deviations: (i) there are more ML LERGs

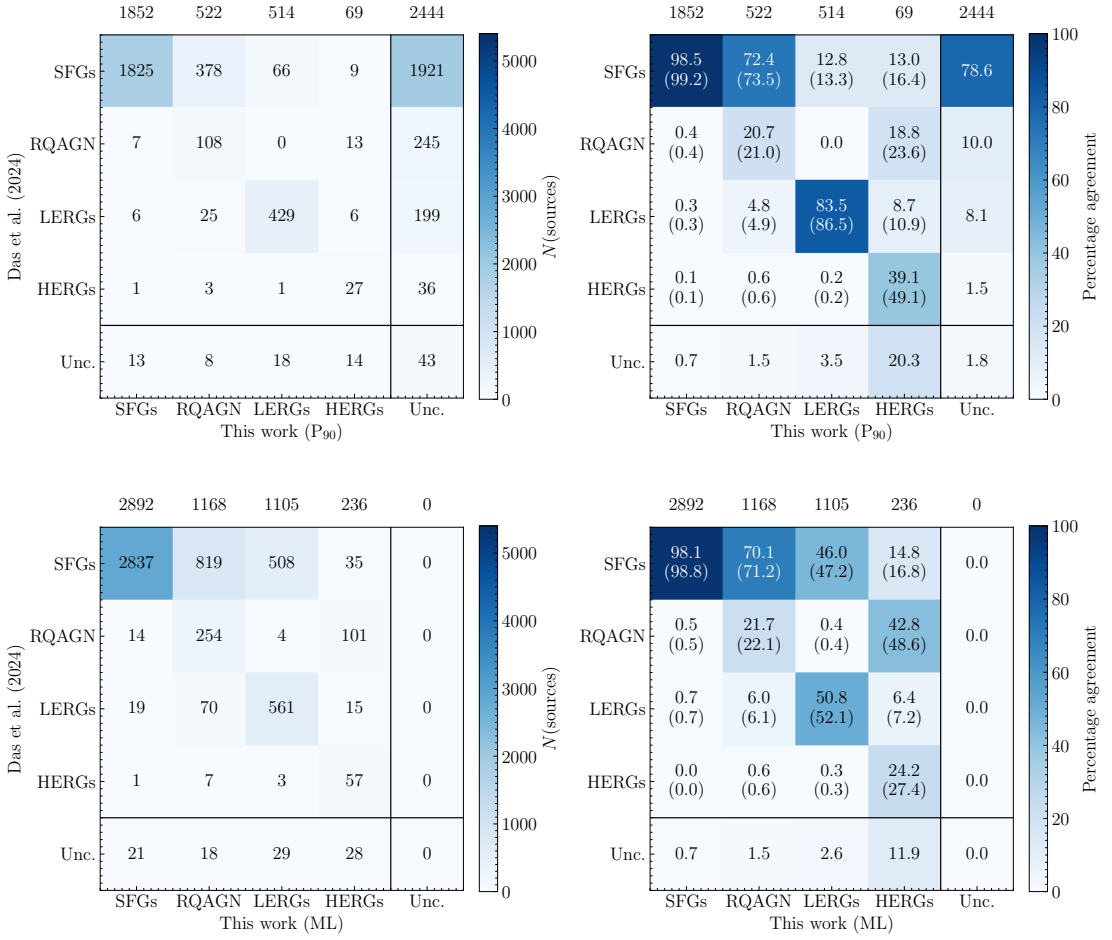

FIGURE 3.13: Confusion matrices comparing the probabilistic classifications from this work with the photometry-only classifications from D24. The comparison between our P_{90} and ML classifications and the D24 classifications is shown in the top and bottom rows, respectively. In each case, the left-hand panel shows the number of sources, while the right-hand panel shows the percentage agreement between the two classification schemes. In each cell of the right-hand panel, the top value includes unclassified sources, while the parenthesis-enclosed value below excludes them. The total number of sources in each class (from this work) is indicated at the top of each row.

classified as D24 SFGs – 46.0 (47.2) per cent compared to 12.8 (13.3) per cent, and (ii) there are more ML HERGs classified as D24 RQ AGN as compared to P_{90}. These can be attributed to the amplification of marginal effects, e.g., more sources with offsets in SFRs leading to differing radio excess thresholds.

3.4.2 Comparison with probabilistic spectroscopic classification

We further investigate the reliability of spectrophotometric classifications by comparing them with the probabilistic spectroscopic classifications performed by A25. We examine 3,402 sources

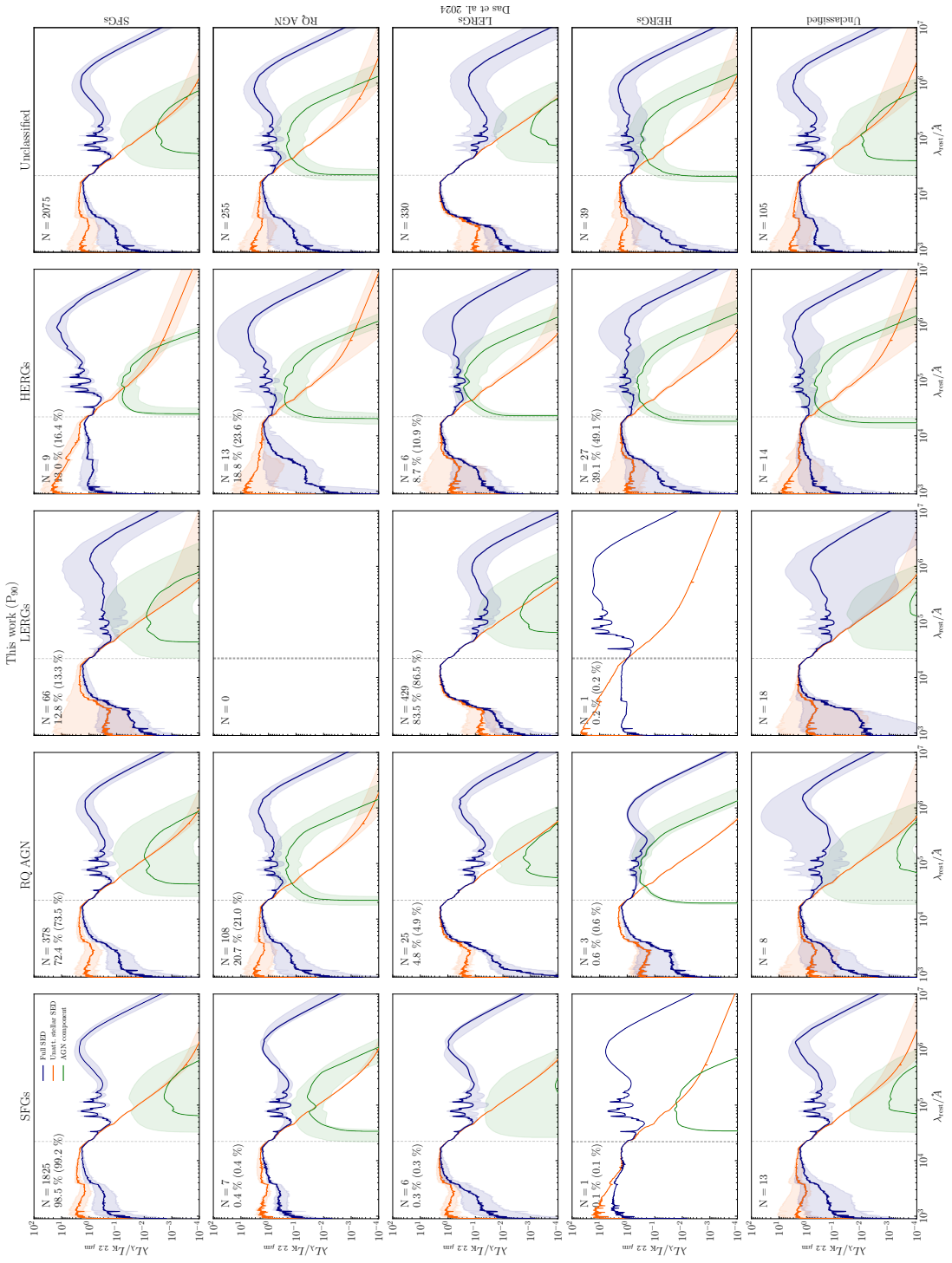

FIGURE 3.14: The K-band (2.2μm) normalised full UV-FIR SEDs (blue), unattenuated stellar SEDs (orange), and AGN models (green), for sources corresponding to the confusion matrix in top rows of Fig. 3.13. The thicker dashed lines denote the median SEDs and their respective components.

common to both studies, as the classifications by A25 are limited by redshift (A25 classifications were available up to $z \approx 0.45$ at the time of conducting this study). We compare our P_{90} results with the >90 per cent purity classification obtained from their catalogue. Similar to the classification results presented in Section 3.4.1, we present the number of sources in the different classes in Table 3.3, show the confusion matrices with the absolute numbers and percentage agreements in Fig. 3.15, and display the corresponding SEDs in Fig. 3.16. The main diagonal in the right-hand panel of Fig. 3.15 demonstrates overall good agreement between the two sets of classifications for sources that had valid classifications in both, i.e., those meeting the necessary criteria (e.g., appropriate redshift range, SNR thresholds) and not marked as "unclassified" for falling outside the four source classes : 83.6 (98.7), 57.3 (87.8), and 50.0 (95.9) agreement for the SFG, RQ AGN, and LERG classes, respectively. A total of 8.0 (12.2) per cent of the P_{90} classified RQ AGN were classified as SFGs by A25. Although the full SEDs of these source classes appear similar (see Fig. 3.16), PROSPECTOR attributes a substantial fraction of the MIR SED to the AGN torus, as indicated by the distribution of AGN models shown in green. This is supported by $\mathcal{P}_{\rm AGN,MIR} > 0.9$ values computed for all these sources. However, all of these sources exhibit emission line ratios corresponding to SFGs in the BPT diagnostic derived from the PROSPECTOR flux estimates, which explains the classification discrepancy. We believe these sources to be obscured AGN, which cannot be securely classified on the basis of spectroscopy alone. Joint spectrophotometric classification approach is highly desirable for dealing with these sources. 1.1 (1.3) per cent of the P_{90}-classified SFGs are identified as RQ AGN by A25. These sources exhibit highly scattered AGN model components, preventing a secure classification based on the AGN fraction posterior. P_{90} classifies more HERGs (16) compared to A25, who classify only 6 sources as HERGs. Notably, 56.2 per cent of the P_{90}-classified HERGs are left unclassified by A25. The agreement in HERG classifications is 18.8 (42.9) per cent. However, given the small sample sizes, we defer a detailed comparison until updated classifications from A25 become available, which are expected to include significantly more HERGs (*private communication*). Both our method and that of A25 produce unclassified sources. Full SED coverage in our approach allows us to classify sources for which A25 could not obtain acceptable spectroscopic fits (e.g., due to low S/N ratios). Conversely, some sources remain unclassified in our scheme because their spectra could not be reliably fit by PROSPECTOR, or whose SED posteriors did not yield conclusive classifications (e.g. due to broad or ambiguous AGN fraction posteriors). In several such cases, A25's more sophisticated spectroscopic fitting was able to model complex emission-line profiles and provide conclusive classifications. These sources are thus unclassified by us but not by A25. This mutual incompleteness underscores the need for

	SFGs	RQ AGN	LERGs	HERGs	Unc.
This work (P_{90})	$1,490 \pm 38$	363 ± 19	232 ± 15	16 ± 4	$1,603 \pm 40$
	40.2 (70.9) %	9.8 (17.3) %	6.3 (11.0) %	0.4 (0.8) %	43.3 %
A25	$1,650 \pm 40$	483 ± 21	190 ± 13	6 ± 2	$1,375 \pm 37$
	44.5 (70.8) %	13.0 (20.7) %	5.1 (8.2) %	0.2 (0.3) %	37.1 %

TABLE 3.3: Number of sources in each class from this work and the spectroscopic classifications of A25, both limited to a >90 per cent probability threshold. The values correspond to a total of 3,704 sources common to both datasets for which the necessary conditions for classification were met. As in Table 3.2, Poisson uncertainties are reported, and the number of sources in each class is given both as a percentage of the total 3,704 sources compared here and as a percentage of the sources classified as SFG, RQ AGN, LERG, or HERG (i.e., excluding unclassified sources).

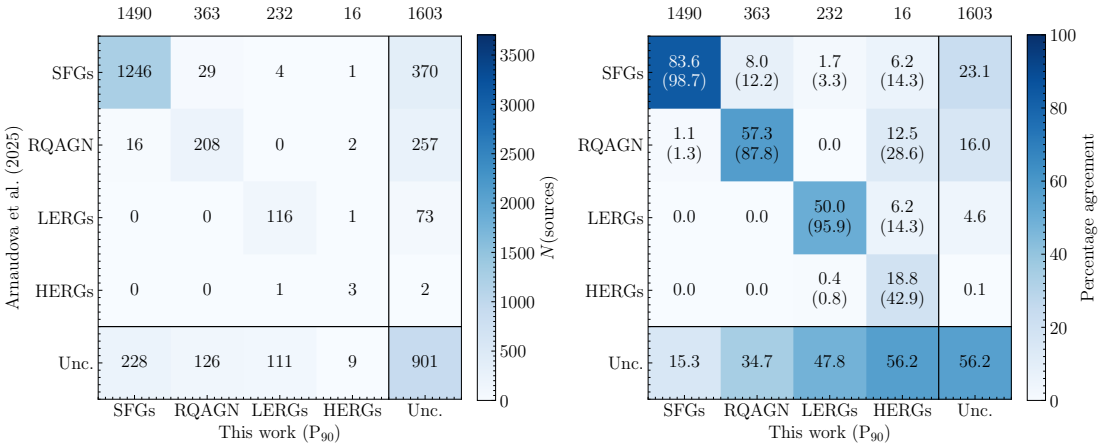

FIGURE 3.15: Confusion matrices comparing the spectrophotometric classifications from this work with the spectroscopy-only classifications from A25. Both classifications are >90 per cent purity limited. The left panel shows source counts; the right shows percentage agreement between classifications. In each right-hand cell, the top value includes unclassified sources, while the value in parentheses excludes them. The total number of sources in each class (from this work) is shown at the top.

further improvements in joint spectrophotometric classification approaches, which will benefit from the large volumes of data expected from upcoming surveys such as WEAVE-LOFAR.

3.5 Conclusion

In this work, we use PROSPECTOR (Leja et al., 2017; Johnson et al., 2021) – one of the new-generation spectral energy distribution (SED) fitting codes – to simultaneously model the UV – far-IR photometry and DESI spectroscopy for 6,038 radio-detected galaxies in the ELAIS-N1 field, one of the LoTSS deep fields. We present a novel Bayesian classification approach that incorporates both photometry and spectroscopy, complementing deep radio observations

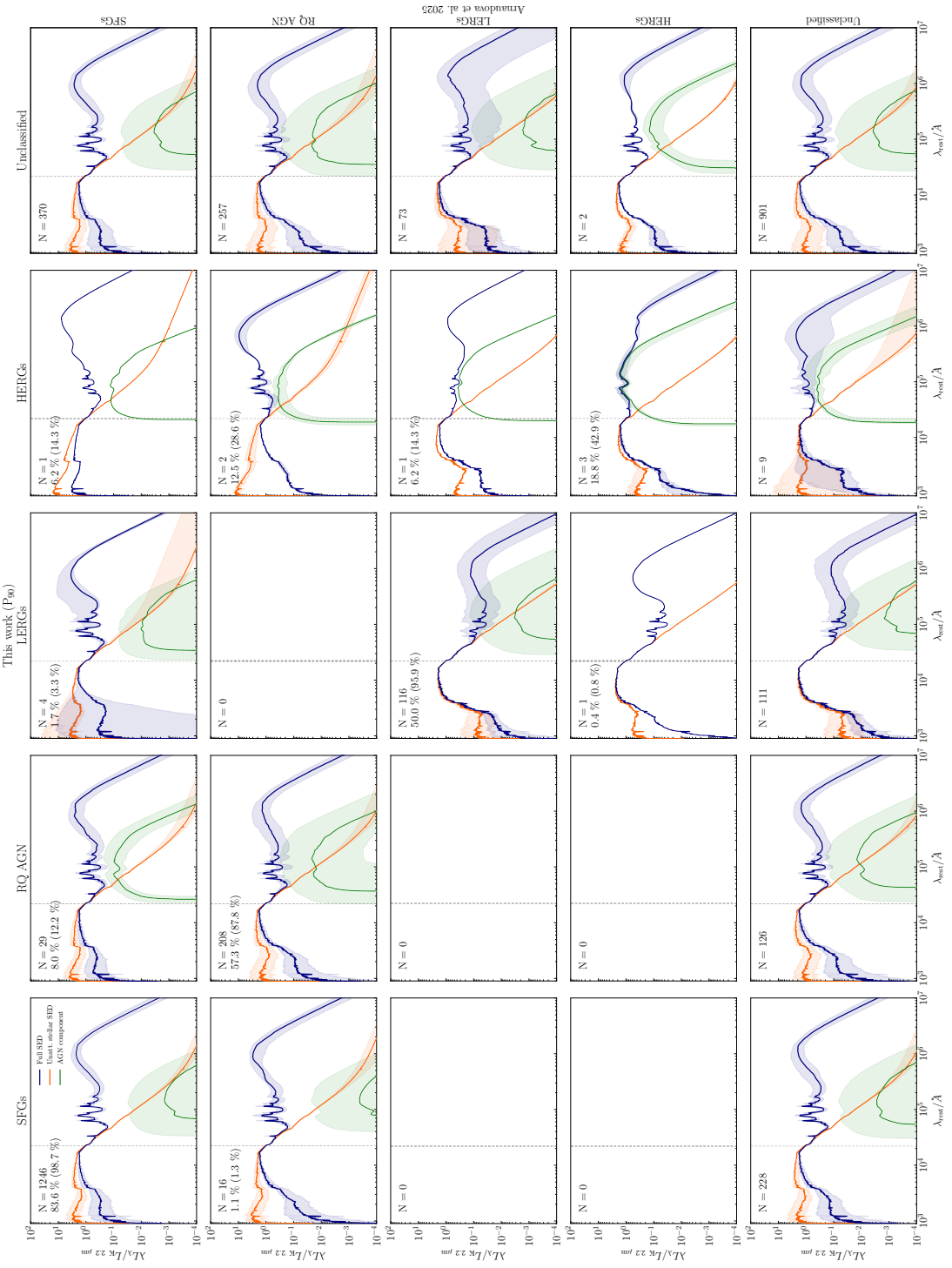

FIGURE 3.16: The K-band (2.2μm) normalised full UV–FIR SEDs (blue), unattenuated stellar SEDs (orange), and AGN models (green) for sources corresponding to the confusion matrix in Fig. 3.15. The thicker dashed lines represent the median SEDs and their respective components.

from LoTSS deep fields data release 1 (DR1; Tasse et al., 2021; Sabater et al., 2021; Kondapally et al., 2021; Duncan et al., 2021; Best et al., 2023), to compute the probability of the faint radio source population in ELAIS-N1 (EN1) falling into star-forming galaxy (SFG), radio-quiet AGN (RQ AGN), low-excitation radio galaxy (LERG), and high-excitation radio galaxy (HERG) classes. PROSPECTOR is capable of simultaneously fitting photometry and spectroscopy, using a flexible non-parametric SFH, physically motivated dust and AGN torus models, and nebular emission. We derived key galaxy properties such as stellar masses, SFRs, emission line fluxes, and AGN mid-IR fractions ($f_{\rm AGN}$), along with robust uncertainties from the posterior distributions. This information was used to compute three independent probabilities for each source: the probability of hosting an efficiently accreting radiative-mode AGN (from mid-IR excess), the probability of containing emission lines powered by nuclear activity (via BPT diagnostics), and the probability of exhibiting excess radio emission relative to SFR (based on the 150 MHz radio luminosity – SFR relation, and on the relation between 150 MHz radio luminosity – Balmer corrected Hα line luminosity). These were then combined into a probabilistic classification scheme, identifying sources as SFGs, RQ AGN, LERGs, or HERGs. The main conclusions of this work are as follows:

(i) Probabilistic classifications have been produced for 90 per cent of the radio sources in the ELAIS N1 deep field with spectra from the early data release of the Dark Energy Spectroscopic Instrument (DESI EDR; DESI Collaboration et al., 2016a, 2022). The end user has the freedom to choose between completeness and purity. Upon setting a >90 per cent confidence threshold, we identify 1,852 SFGs, 522 RQ AGN, 514 LERGs, and 69 HERGs.

(ii) Joint spectrophotometric classification is more effective at breaking degeneracies in the underlying emission mechanisms and, therefore, more successful in identifying AGN populations, when compared to photometry-only and spectroscopy-only classification efforts.

(iii) Joint spectrophotometric classification can identify populations of obscured AGN through their mid-IR excess in cases where classification using only spectroscopy is not possible.

This work showcases the potentially superior classifications that can be produced by leveraging both photometry and spectroscopy. Such an approach will be crucial in dealing with the large volumes of data that will be produced by ongoing and upcoming massively multiplexed surveys, such as the WEAVE-LOFAR survey (Smith et al., 2016), Optical, Radio Continuum and

HI Deep Spectroscopic Survey (ORCHIDSS; Duncan et al., 2023), and part of the Wide-Area VISTA Extragalactic Survey (WAVES; Driver et al., 2019). However, before such an approach can be widely adopted, several limitations will need to be overcome. Firstly, improvements will need to be made to the simplistic single-component model that is used to fit emission lines, such as introduction of dynamic, more physical modelling of the emission line profiles. Secondly, spectrophotometric fitting is computationally expensive. Improvements will need to be made to reduce the runtimes of PROSPECTOR, such as by dynamically scaling the wavelength resolution of the models, or by complementing PROSPECTOR with methods such as simulation-based inference (SBI; Cranmer et al., 2020) and neural posterior estimation (NPE; Greenberg et al., 2019; Khullar et al., 2022). Successfully addressing these challenges, and integrating photometry and spectroscopy to analyse vast incoming datasets, will be pivotal for advancing the next generation of galaxy evolution research.

Chapter 4

Measuring the recent histories of high-redshift galaxies using *HST* and *JWST* photometry with Prospector SED fitting

"The story so far: In the beginning the Universe was created. This has made a lot of people very angry and been widely regarded as a bad move."
–Douglas Adams (The Restaurant at the End of the Universe)

Early galaxies, which formed within the first few hundred million years after the Big Bang, are widely regarded as some of the key drivers of the transition of the Universe from a largely homogeneous and isotropic phase to the highly structured form that we observe today (see reviews by Bromm and Yoshida, 2011; Robertson, 2022; Stark et al., 2025). The influx of large volumes of data from the first two years of the James Webb Space Telescope (*JWST*; Gardner et al., 2006, 2023) has been pivotal in studying the rate at which mass is assembled onto these early galaxies (i.e., their star formation histories, a.k.a., SFHs). Early galaxies tend to exhibit highly stochastic (or "bursty") SFHs, with a significant fraction of the total stellar mass forming in brief, intense bursts followed by rapid quenching events (e.g., Strait et al., 2023; Endsley et al., 2023, 2024; Glazebrook et al., 2023, 2024; Alberts et al., 2024; Asada et al., 2024; Clarke et al., 2024; Dressler et al., 2024; Nanayakkara et al., 2024; Park et al., 2024). This is in sharp contrast to the continuous and steady star formation activity typically seen in the low redshift universe

(e.g., Guo et al., 2016; Sklias et al., 2017; Smith and Hayward, 2018), and instead more closely resembles the SFHs of dwarf galaxies at low redshifts (e.g. Domínguez et al., 2015; Emami et al., 2019). Cosmological zoom-in simulations, such as those by Sparre and Springel (2016); Sparre et al. (2017); Ma et al. (2018); Furlanetto and Mirocha (2022); Hopkins et al. (2023) and Gurvich et al. (2023), have shown that the transition from bursty to steady SFHs in Milky-Way mass galaxies happens very rapidly (on timescales of 100 Myrs to 1 Gyr), and is accompanied by an increase in galaxy mass and the formation of a stable gaseous disk. While *JWST* observations have identified a recently quenched/temporarily-quenched ("temp-quenched") galaxy at $z \sim 7.3$ (JADES-GS-z7-01-QU; Looser et al., 2023, 2024b) – the precise combination of physics regulating star formation activity in the early Universe (such as, feedback from supernovae and active galactic nuclei, virial shock heating, and mergers; Davé et al., 2012; Cortese et al., 2021; Davé et al., 2012; Alberts et al., 2024) remains unclear.

Energy balance spectral energy distribution (SED) fitting represents the state-of-the-art for measuring physical parameters of galaxies, and has been demonstrated to be effective even at high redshifts (see Haskell et al., 2023, 2024). However, the results from SED fitting are prone to errors due to variations in–/mischaracterization of- the SFH. For example, Haskell et al. (2024) reported that the star formation rates (SFRs) estimated using SED fitting could be off by up to 1 dex from the ground truth, depending on the adopted SFH model and the treatment of star bursts. Assuming a constant SFH during SED modelling can also potentially underestimate the stellar masses of galaxies with bursty SFH by up to 1 dex (e.g. Clarke et al., 2024; Endsley et al., 2024; Wang et al., 2024) – this issue can be further exacerbated by light from the recently formed stellar populations dominating the galaxy's SED, outshining the light from older, less luminous populations (e.g. Papovich et al., 2001; Maraston et al., 2010; Sorba and Sawicki, 2015; Papovich et al., 2023; Narayanan et al., 2024). Characterizing the "burstiness" of SFHs is therefore critical to accurately inferring the physical properties of galaxies. Burstiness is typically quantified by comparing SFR indicators that are sensitive to different time-scales (e.g., Guo et al., 2016; Broussard et al., 2019; Faisst et al., 2019; Flores Velázquez et al., 2021; Mehta et al., 2023). One of the commonly-used metrics is the burst indicator η, defined by Broussard et al. (2019) as:

$$\eta = \log_{10}(\psi_{10}/\psi_{100}), \tag{4.1}$$

where ψ_{10} and ψ_{100} denote the average SFR in the most recent 10 and 100 Myrs of the galaxy

lifetime. When $\eta > 0$, it indicates that, on average, more star formation activity has occurred in the past 10 Myrs of the galaxy's lifetime than in the past 100 Myrs, thereby representing a bursty SFH. Similarly, $\eta < 0$ denotes a temp-quenched SFH, and $\eta = 0$ corresponds to the SFH being constant over 100 Myrs.

High redshift galaxy SFHs typically exhibit variability on very short timescales ($\sim 20 - 40$ Myrs), which makes spectroscopic SFR indicators ideal for measuring burstiness (Dome et al., 2024; Alberts et al., 2024). However, spectroscopic studies of burstiness are often not feasible due to limited availability of high signal-to-noise spectra, as well as constraints on sky coverage, redshift, and surface brightness. Hence, modelling SEDs using photometric data is often the only viable approach for large statistical studies. There are several challenges to this approach: first, photometric data are not particularly sensitive to SFRs on time scales of $\sim$ 10 Myrs (e.g. Kennicutt and Evans, 2012). Secondly, the limited spectral resolution of photometry means that different sets of physical conditions and emission mechanisms (e.g. combinations of varying stellar populations, dust, metallicities, nebular emission, and Active Galactic Nuclei; AGN) can produce similar colours (e.g. Carter et al., 2009; McKinney et al., 2023). Additionally, the results of SED modelling are potentially strongly dependent on the assumed priors (e.g. Leja et al., 2017; Carnall et al., 2019). Given these challenges, it is crucial to assess the reliability of photometry-based SED modelling in measuring the burstiness of star formation histories.

Our work follows the approach outlined in studies such as Hayward and Smith (2015), Smith and Hayward (2015), Smith and Hayward (2018), and Haskell et al. (2023), where synthetic observations from simulations are modelled using SED fitting codes under idealised conditions, and the results from the fits are compared to the known ground truth properties. Here, we work with simulated galaxies in the redshift range $4.64 < z \leq 10$ from the Version 1 of SPHINX Public Data Release (SPDRv1; Katz et al., 2023). SPHINX is a state-of-the-art cosmological radiation-hydrodynamic simulation suite, which is designed to model large populations of galaxies in a full cosmological volume with radiative hydrodynamics, while retaining the ability to resolve the multiphase ISM by reaching resolutions of $\sim$10 physical pc. We use the SED fitting code PROSPECTOR (Leja et al., 2017; Johnson et al., 2021) to derive the physical parameters for these galaxies. This chapter is structured as follows: in Section 4.1, we describe the datasets used in this chapter, and detail the SED fitting process in Section 4.2. In Section 4.3 we estimate several key physical parameters, and then look at the recovery of burstiness. Finally, we present some concluding remarks in Section 4.4. This chapter is the first in a series of studies exploring the recovery of η. Here, we examine the dependence of η on the SFH prior, redshift,

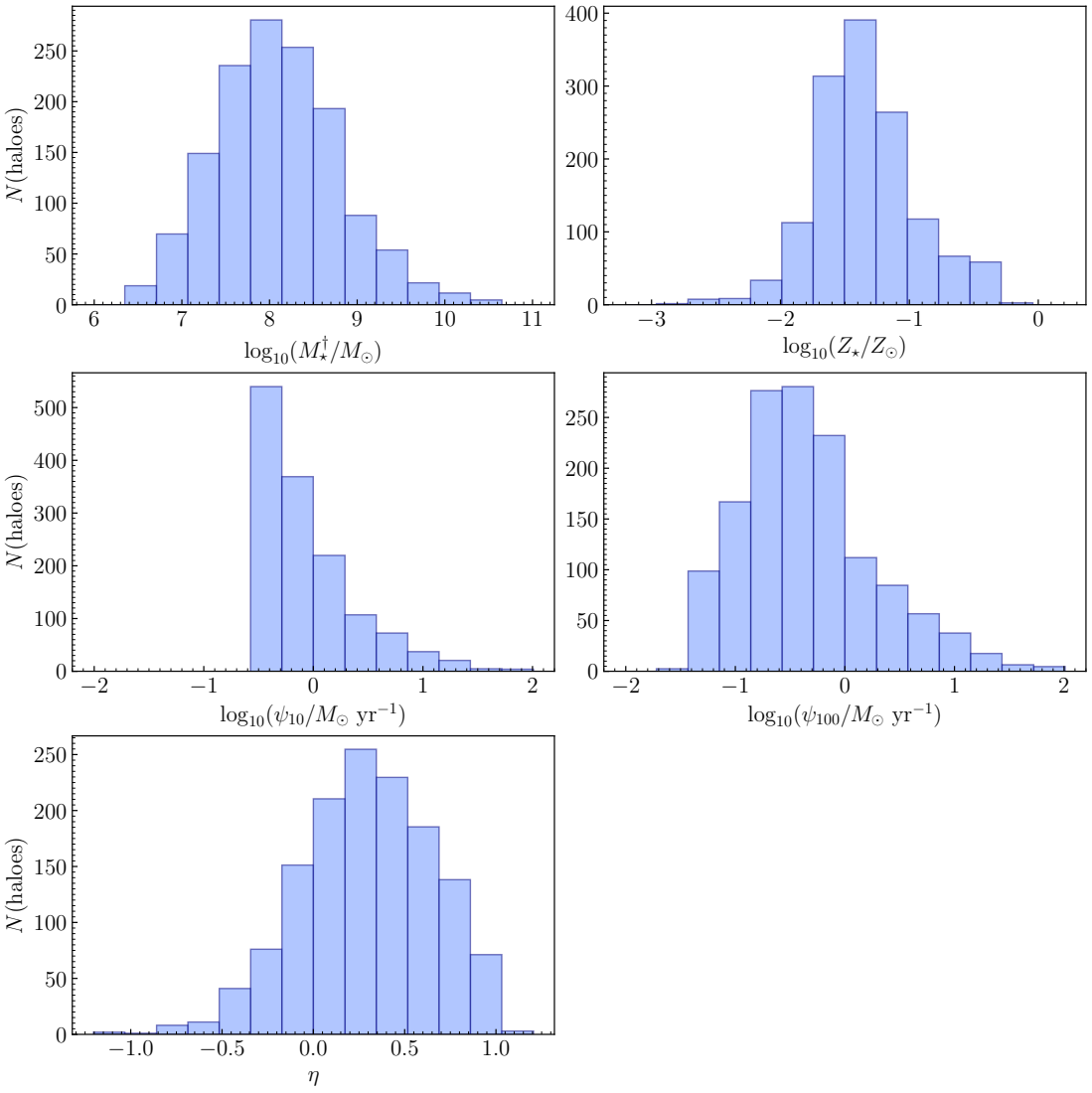

FIGURE 4.1: Histograms showing the distributions of the true physical parameters covered in the SPHINX Public Data Release Version 1 (SPDRv1) sample. The panels show the total stellar mass formed, the stellar metallicity in the units of solar metallicity, the star formation rate averaged over 10 and 100 Myrs, and the burstiness parameter η.

and wavelength coverage using only photometric data, with future work set to demonstrate the improvement achievable when spectra are incorporated.

4.1 Data

In this chapter, we use a sample of 1,380 simulated galaxy haloes from SPHINX Public Data Release Version 1 (SPDRv1). The sample consists of predominantly star-forming galaxies from SPHINX^{20} (which is the largest volume simulation in SPHINX with a volume of 20^3 comoving Mpc) at discrete redshifts of $z = 4.64, 5, 6, 7, 8, 9$ and 10. SPHINX^{20} used the RAMSES mesh

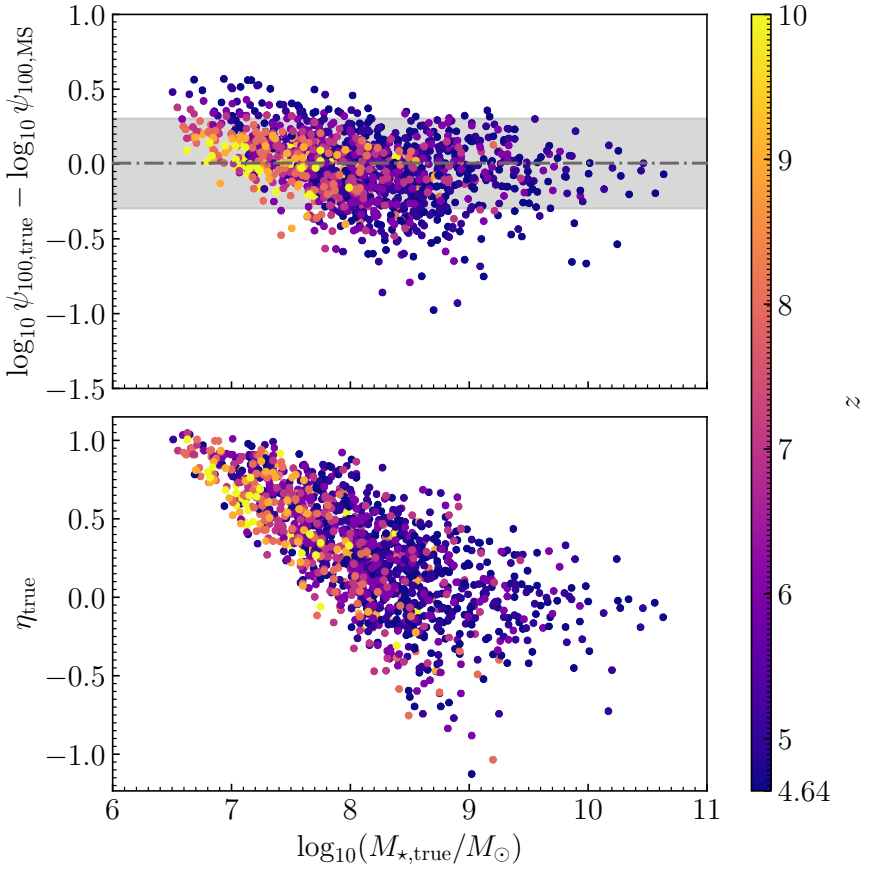

FIGURE 4.2: (Top) Location of the SPHINX^{20} galaxies relative to the galaxy star formation rate–stellar mass relation, shown as the difference between the true 100 Myr averaged SFR and the SFR expected for a source with the same stellar mass and redshift using the Schreiber et al. (2015) parametrisation (converted to our adopted Kroupa, 2001 IMF) as a function of the true stellar mass. The grey shaded region indicates the canonical ±0.3 dex width of the so-called 'main-sequence'. (Bottom) Burstiness parameter η vs total stellar mass, demonstrating the stochasticity of SFHs of SPHINX^{20} galaxies. In both panels the points are colour coded by redshift relative to the colour bar located to the right.

refinement code (Teyssier, 2002). Initial conditions were set up to produce a typical patch of the sky without notable over–/under– dense regions and designed to produce galaxies comparable to those observed using *JWST* at these redshift ranges (see Katz et al., 2023; Cochrane et al., 2024). SPHINX^{20} uses a Kroupa (2001)-like IMF. Fig. 4.1 shows the true physical parameters (total stellar mass formed[1], stellar metallicity[2], ψ_{10}, ψ_{100}, and the burstiness parameter η) covered by this sample. SPHINX^{20} galaxies span a wide range of stellar masses and successfully reproduce the distribution of stellar masses at different redshifts, as observed in recent *JWST* studies, such as Santini et al. (2023). At high redshifts ($z > 7$), the sources are typically compact and have

[1]The total stellar mass formed differs from the surviving stellar mass, as the latter accounts for losses due to evolution (e.g. due to AGB winds, supernovae).

[2]We consider the mass-weighted stellar metallicity provided in the SPDRv1 catalogue to be the true stellar metallicity for a given source.

lower stellar masses ($7 \leq \log_{10}(M_\star/M_\odot) \leq 9$), while more massive galaxies ($\log_{10}(M_\star/M_\odot) > 10$) are observed at $z = 4.64$. Katz et al. (2023) also set a limit of $\psi_{10} > 0.3$ M$_\odot$ yr^{-1}, consistent with the SFRs of high-redshift galaxies in early *JWST* observations (e.g., Leethochawalit et al., 2023; Fujimoto et al., 2023; Shapley et al., 2023).

The distribution of SPHINX^{20} galaxies in the stellar mass-SFR plane relative to the well-known galaxy "main sequence" (Brinchmann et al., 2004; Daddi et al., 2007; Noeske et al., 2007) is illustrated in the top panel of Fig. 4.2, using the main sequence parametrisation from Schreiber et al. (2015), converted to our adopted Kroupa (2001) IMF. The majority of sources lie within the typical ±0.3 dex scatter about the main sequence, meaning that the SPHINX^{20} sample is dominated by normal star-forming galaxies. As discussed previously, SFHs at high redshifts tend to be highly stochastic, and this can be seen in the bottom panel of Fig. 4.2; around half of the SPHINX^{20} galaxies have a bursty SFH ($\eta > 0.3$). It is also apparent that the degree of burstiness increases with higher redshift (indicated by the colour bar to the right of Fig. 4.2) and decreasing stellar mass.

To generate the emergent SPHINX^{20} spectra, the integrated stellar continuum emission was generated by interpolating the SEDs from BPASS v2.2.1 (Stanway and Eldridge, 2018), while emission line luminosities and nebular continuum were computed using the CLOUDY v17.03 models (Ferland et al., 2017). AGN activity is not included. All continuum and line emission is subject to dust absorption and scattering, modelled using the Monte-Carlo radiative transfer code RASCAS (Michel-Dansac et al., 2020). SPDRv1 provides observed-frame, dust-attenuated spectra covering the wavelength range from 0.56 to 10.89 μm, along ten fixed lines of sight. We generated synthetic photometry by convolving the dust-attenuated spectra with the filter response curves provided by SEDPY[3] (Johnson, 2019) for the 25 bands listed in Table 4.1.

Since the SPDRv1 spectra are noiseless, in order to fit the emergent synthetic photometry with PROSPECTOR we follow Smith and Hayward (2018) and Haskell et al. (2023) in assuming a signal-to-noise ratio of 5 in each band. However to avoid giving undue weight to the photometry blue-ward of the Lyman break in our fitting, we add an additional 10 per cent of the median flux (across all bands, measured in Jy) to the uncertainty in quadrature. Although the SNR typically varies significantly across filters in real observations, our adopted photometry enables us to perform this study under idealised conditions. The bandpasses that we consider come from the following instruments: Hubble Space Telescope (*HST*; Williams et al., 1996) Advanced

[3] https://github.com/bd-j/sedpy

Camera for Surveys (ACS) Wide Field Channel (WFC), *HST* Wide Field Camera 3 (WFC3) IR, *JWST* Near Infrared Camera (NIRCam; Rieke et al., 2005), and *JWST* Mid-Infrared Instrument (MIRI). This list was compiled to include the filters from three key *JWST* Early Release Science (ERS) programs and surveys: Cosmic Evolution Early Release Science (CEERS; Finkelstein et al., 2017, 2024), *JWST* Advanced Deep Extragalactic Survey (JADES; Eisenstein et al., 2023), and the GLASS-*JWST* ERS program (Treu et al., 2022), along with a few other filters that have been widely used in the literature. This choice of filters, therefore, forms a superset of these surveys, providing us with an idealised dataset with which to test our ability to recover η using photometric data.

Fig. 4.3 shows example SPHINX^{20} observed-frame spectra of galaxies at $z = 4.64, 5, 6, 7, 8, 9,$ and 10, relative to the assembled set of *HST* and *JWST* filter curves. Fig. 4.4 presents a zoomed-in view of the same spectra, highlighting the continuum features. Both figures show that it is not possible to use the longest wavelength MIRI filters for the lowest redshift galaxies in the SPHINX^{20} sample (at $z \leq 5$) since the synthetic spectra do not include long enough wavelengths, and we bear this in mind in what follows since different photometric coverage at different redshifts could mean that we are not comparing like with like. However, we also note the other side of this, which is that we use filters sampling a consistent rest wavelength range at all redshifts.

4.2 SED Modelling

We use the SED fitting code PROSPECTOR (Leja et al., 2017; Johnson et al., 2021) to model the photometry generated in Section 4.1. PROSPECTOR infers the properties of the stellar population using Flexible Stellar Populations Synthesis framework (FSPS; Conroy et al., 2009; Johnson et al., 2023). To ensure consistency with the input SPHINX^{20} simulations, we used the BPASS v2.2 stellar population models included with FSPS, along with an initial mass function (IMF) from Kroupa (2001). Additionally, since photometry alone provides only weak constraints on metallicities (e.g. Smith and Hayward, 2018), we fix the source stellar metallicity equal to the true mass-weighted stellar metallicity at the source redshift, with the intention of revisiting this assumption in a future work.

The two-component Charlot and Fall (2000) dust attenuation model is used to compute the attenuation of light from younger and older stellar populations. We use the Kriek and Conroy

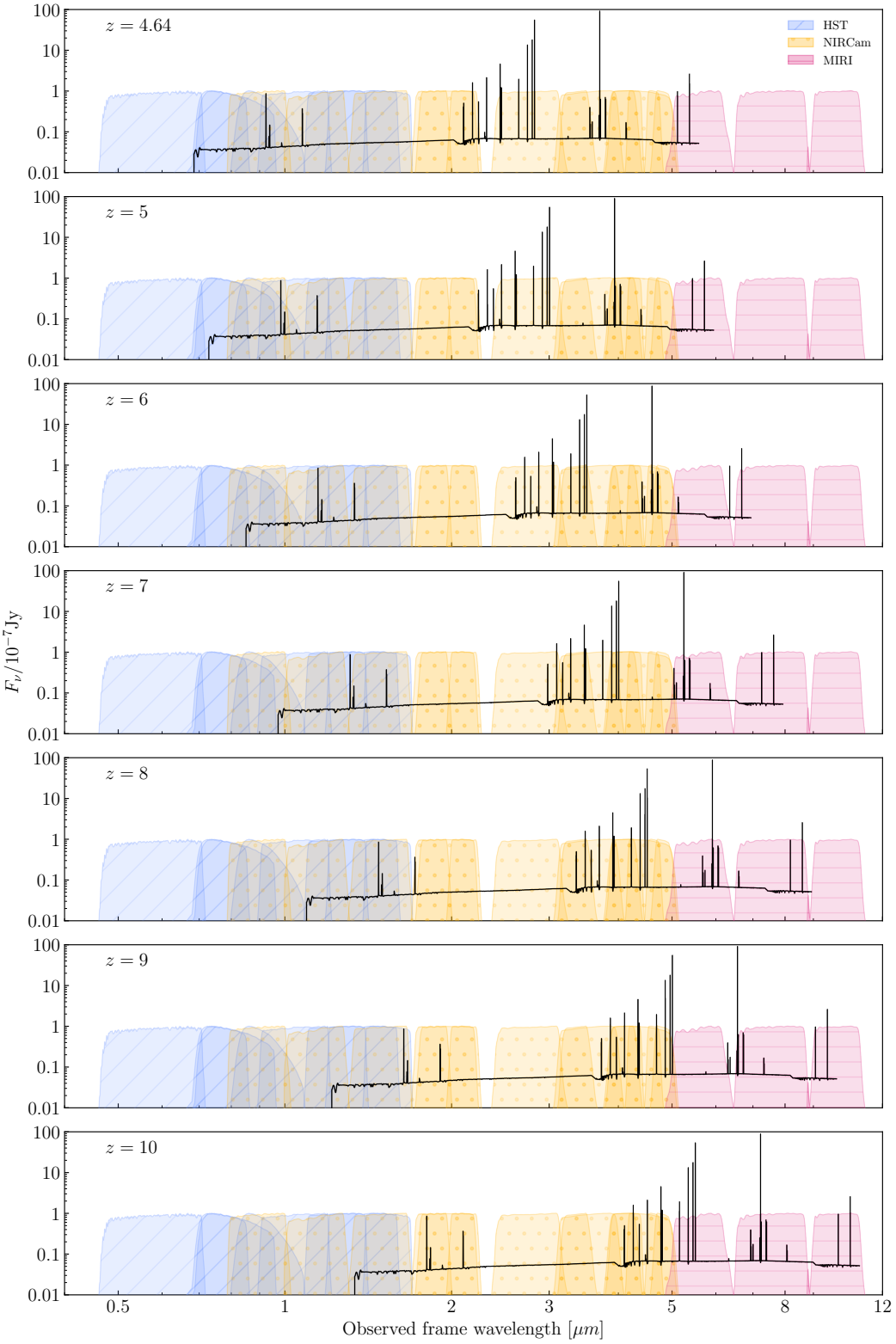

FIGURE 4.3: SED of a sample SPHINX^{20} galaxy, selected at random, and redshifted to $z = 4.64, 5, 6, 7, 8, 9$, and 10 (from topmost panel to bottom). Transmission curves of the *HST*, *JWST* NIRCam, and *JWST* MIRI filters, listed in Table 4.1, are shown as blue, yellow, and pink shaded regions, respectively, to demonstrate the coverage they provide to the SEDs (and the accompanying spectral features) at each redshift.

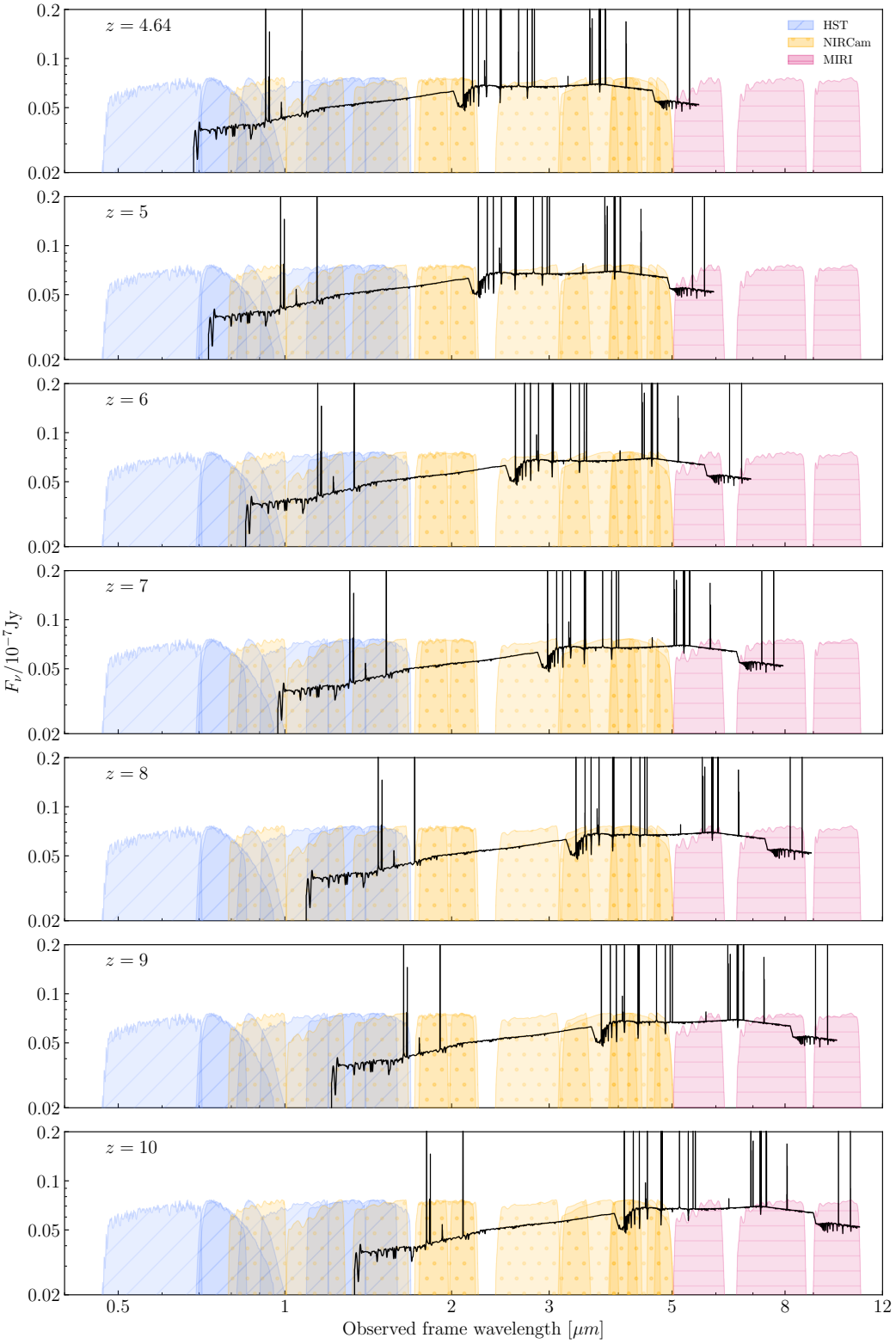

FIGURE 4.4: SED of the same SPHINX^{20} galaxy as in Fig. 4.3 at $z = 4.64, 5, 6, 7, 8, 9$, and 10, with the y-axis range adjusted to highlight the continuum features. Transmission curves of the *HST*, *JWST* NIRCam, and *JWST* MIRI filters are shown as blue, yellow, and pink shaded regions, respectively.

TABLE 4.1: *HST*, *JWST* NIRCam, and *JWST* MIRI photometric filters used in this work. Check marks indicate whether that filter was used in that programme.

Instrument	Filters	CEERS	JADES	GLASS
HST ACS/WFC	F606W	✓	✓	
	F775W		✓	
	F814W	✓	✓	
	F850LP		✓	
HST WFC3/IR	F105W	✓	✓	
	F125W	✓	✓	
	F140W	✓	✓	
	F160W	✓	✓	
JWST NIRCam	F090W		✓	✓
	F115W	✓	✓	✓
	F150W	✓		✓
	F182M			
	F200W	✓	✓	✓
	F210M			
	F277W	✓	✓	✓
	F335M		✓	
	F356W	✓	✓	✓
	F410M	✓	✓	
	F430M			
	F444W	✓	✓	✓
	F460M			
	F480M			
JWST MIRI	F560W	✓		
	F770W	✓		
	F1000W	✓		

(2013) attenuation curve, which is characterised by three parameters: the diffuse dust V-band optical depth, the diffuse dust attenuation index, and the ratio of the birth cloud optical depth to the diffuse dust screen optical depth. Since the SPHINX^{20} simulations do not include dust emission or AGN feedback, we do not include these components in our model. PROSPECTOR uses the CLOUDY photoionization code to model nebular lines and continuum emission, with ionizing sources represented by stellar populations generated using FSPS (Byler et al., 2017). The model is parametrised by the intensity of the ionizing spectrum, denoted by the dimensionless ionization parameter (kept as a free parameter), and the gas-phase metallicity, which is fixed equal to the stellar metallicity.

In this work, we use non-parametric priors to model galaxy SFHs, as these have been shown to better handle complex SFH features, including episodes of starburst activity, sudden quenching, and rejuvenation (see Simha et al., 2014; Carnall et al., 2019; Leja et al., 2019; Haskell et al., 2024; Das et al., 2024). We use two non-parametric SFH priors: the "continuity" SFH prior (hereafter CSFH; Leja et al., 2019) and the "bursty-continuity" SFH prior (or, "bursty",

hereafter BSFH; Tacchella et al., 2022b). In both of these priors, the lifetime of the galaxy is divided into $N = 4$ discrete time bins: $0-10$ Myrs, $10-100$ Myrs, 100 Myrs $-0.85t_z$, and $0.85t_z - t_z$, where t_z represents the age of the Universe at the object's redshift. The prior on $x = \log(\mathrm{SFR}_n/\mathrm{SFR}_{n+1})$, with $n \,\epsilon\, [1, N-1]$, is given by a Student's-t distribution:

$$\mathrm{PDF}(x, \nu) = \frac{\Gamma\left(\frac{\nu+1}{2}\right)}{\sqrt{\nu\pi}\,\Gamma\left(\frac{\nu}{2}\right)} \left(1 + \frac{(x/\sigma)^2}{\nu}\right)^{-\frac{\nu+1}{2}}. \tag{4.2}$$

Here, Γ denotes the Gamma function, σ is a scale factor, and ν represents the degrees of freedom. The parameter σ controls the width of the distribution, whereas ν determines the probability in the tails. For CSFH, we set $\sigma = 0.3$ and $\nu = 2$, and for BSFH we set $\sigma = 1$ and $\nu = 2$, following Leja et al. (2019) and Tacchella et al. (2022b), respectively.

The dynamic nested sampling tool DYNESTY (Speagle, 2020) is used by PROSPECTOR to estimate Bayesian posteriors and evidences. We use DYNESTY's evidence-based stopping criterion (detailed discussion in Section 3.2.1) and terminate the run at $\Delta \ln \mathcal{Z}_i \leq 0.1$, where $\Delta \ln \mathcal{Z}_i$ is the logarithmic ratio between the evidence estimated in the i^{th} iteration ($\mathcal{Z}_i$) and the remaining evidence ($\Delta\mathcal{Z}_i$). This corresponds to $\Delta\mathcal{Z}_i/\mathcal{Z}_i \approx 0.11$, and we find that sampling beyond this threshold does not significantly affect the final results. We follow Smith et al. (2012) and consider an SED fit to be acceptable if the best-fit χ^2 is below the 99 per cent confidence threshold for the given number of photometric bands. This criterion has been demonstrated to provide a reasonable quality cut for PROSPECTOR SED fits (see Haskell et al., 2023, 2024; Das et al., 2024). Table 4.2 contains the final set of model parameters used in this work. In Fig. 4.5 we show example PROSPECTOR SED fits to the synthetic photometry, along with reconstructed SFHs of randomly selected SPHINX^{20} galaxies at $z = 4.64$ (top two rows) and $z = 8$ (bottom two rows) with temp-quenched, constant, and bursty SFHs (left-, middle- and right-hand columns, respectively). The true SPHINX^{20} spectrum and SFH are shown in grey, overlaid with the PROSPECTOR BSFH (in dot-dashed magenta) and CSFH (in dashed blue) recovered values, with the shading of the same colour indicating the uncertainties of the posterior derived by taking the 16^{th} and 84^{th} percentiles of the converged DYNESTY chains (see Section 3.2.2). The synthetic photometry is shown as the grey squares with associated error bars.

TABLE 4.2: Details of the PROSPECTOR parameters used in our SED model, including the choice of prior.

	Parameter	Description	Prior/Value
Stellar Mass	$\log_{10}(M_\star/M_\odot)$	Total stellar mass formed	Uniform; between 6.5 to 13.5
Dust attenuation	$\tau_{\lambda,2}$	Diffuse dust V-band optical depth	Uniform; between -1 and 4
	n	Diffuse dust attenuation index	Uniform; between -2 and 0.5
	$\tau_{\lambda,1}/\tau_{\lambda,2}$	The ratio of the optical depth of the birth cloud to the diffuse dust screen optical depth	Clipped normal; mean = 1, variance = 0.3, between 0 and 2
Nebular Emission	$\log_{10}(U_{\rm gas})$	Gas-phase ionisation parameter	Uniform; between -4 and -1
Fixed Parameters	IMF	Initial mass function	Kroupa (2001)
	z	Redshift	Fixed at the value provided in the SPDRv1 catalogue
	$\log_{10}(Z/Z_\odot)$	Stellar metallicity	Fixed at the median stellar metallicity of sources at that redshift.
	$\tau_{\lambda,1}$	Additional optical depth attenuating the light from young stars	Function of $\tau_{\lambda,1}/\tau_{\lambda,2}$
	$k'(\lambda)$	Dust attenuation	Kriek and Conroy (2013) curve
	$t_{\rm bins}$	Discrete time binning scheme	Fixed, defined in Section 4.2
	$\log_{10}(Z_{\rm gas}/Z_\odot)$	Gas-phase metallicity	Equal to $\log_{10}(Z/Z_\odot)$

4.3 Results and discussion

In this section, we compare the total stellar mass and SFRs estimated using both the BSFH and CSFH priors with the true values provided in the SPDRv1 catalogue. We examine how well the burstiness parameter (η) is recovered, including the impact of varying run conditions on η-recovery.

4.3.1 Estimation of physical parameters

Fig. 4.6 contrasts the median likelihood stellar mass, ψ_{10}, and ψ_{100} (estimated using BSFH and CSFH priors in the top and bottom rows, respectively) with the true values from the SPDRv1 catalogue. In each panel, the galaxies are colour-coded by their redshift, relative to the colour bar to the right. The deviation between the PROSPECTOR estimates and the true values is quantified as $\Delta\ \log_{10} M_\star = \log_{10}(M_\star, \text{PROSPECTOR}) - \log_{10}(M_\star, \text{true})$, and it is clear that for the SPHINX^{20} sample, stellar masses estimated using the BSFH prior are in better agreement with the true values than those estimated using the CSFH prior. For the full sample, $\Delta \log_{10} M_\star$ has a median of 0.09 dex and a standard deviation of 0.14 dex for BSFH, while CSFH yields 0.22 dex and 0.13 dex, respectively. The typical uncertainties on stellar mass estimates from both priors are ~ 0.1 dex. While the averages tell part of the story, there is a systematic trend visible in the CSFH stellar mass recovery, in that the masses are increasingly overestimated

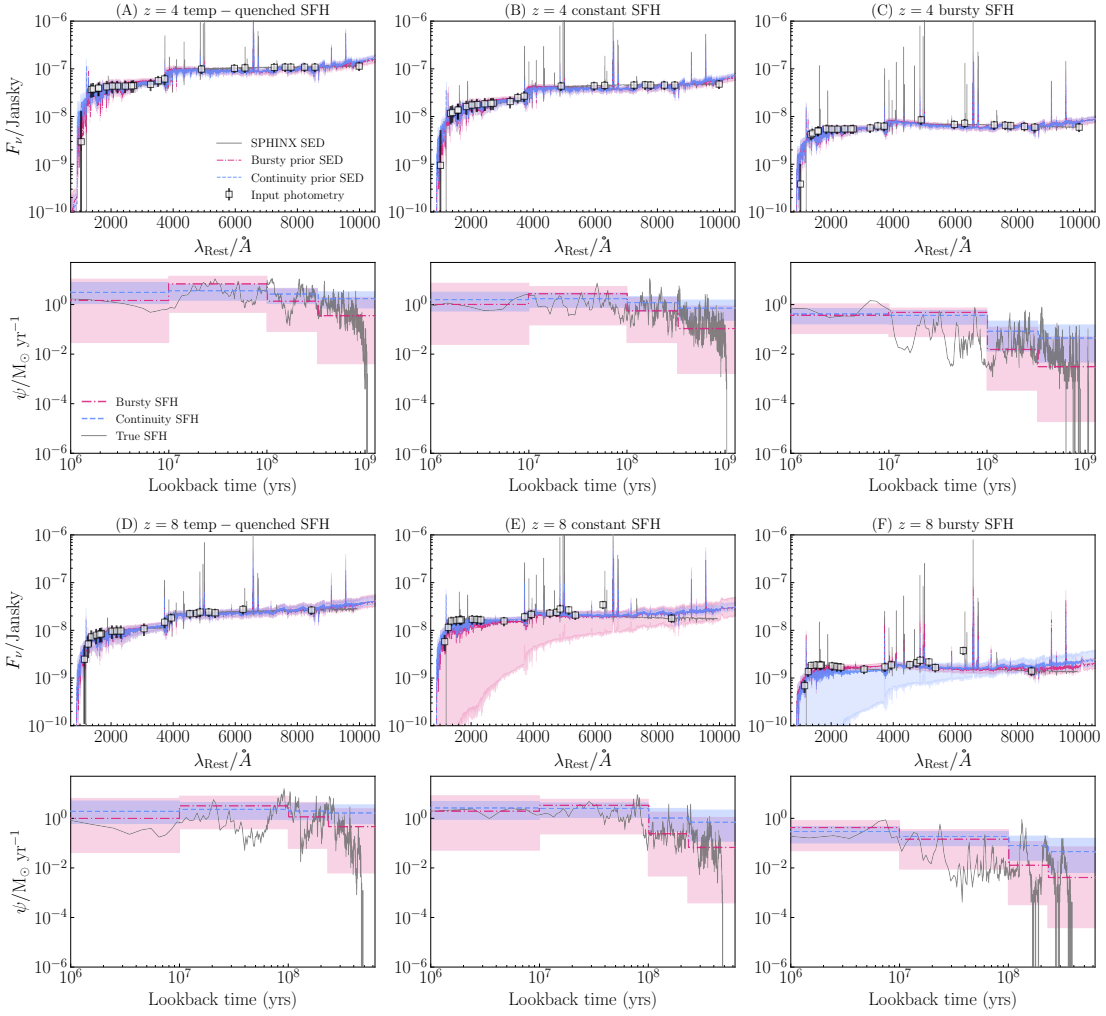

FIGURE 4.5: SED fits and recovered SFHs for sources randomly selected at $z = 4.64$ and $z = 8$, with varying degrees of burstiness. The plots for each source are presented in two panels: the top panel shows the SED fits, and the bottom panel shows the SFH. The top two rows show sources at $z = 4.64$ with temp-quenched, constant, and bursty SFHs (in the left-, middle- and right-hand columns, respectively) while the third and fourth rows show sources at $z = 8$. Median likelihood SEDs and SFHs from the CSFH fitting are denoted by dashed blue lines, while those assuming a BSFH prior are denoted by dot-dashed magenta lines, with associated uncertainties indicated by the shaded area. The input photometry is shown with black outlined squares and error bars, overlaid on the true SPHINX^{20} spectra (in grey).

at the lower end of the range ($\log_{10} M_\star$,true < 8), which are typically associated with higher redshifts and bursty SFHs (Fig. 4.2). This behaviour is consistent with the stellar mass recovery observed by Cochrane et al. (2024) – who used the BAGPIPES code – though we observe it only using the CSFH prior (i.e. not when using the BSFH prior). Additionally, our redshift-binned median $\Delta \log_{10} M_\star$ and standard deviation values for both priors are lower than those in Cochrane et al. (2024, Table 1). While their median values peak at 0.37 dex for CSFH and 0.27 dex for BSFH, the peak median values for this work are 0.29 dex and 0.17 dex, respectively. This difference primarily arises due to the different choice of filters used in this work; if we

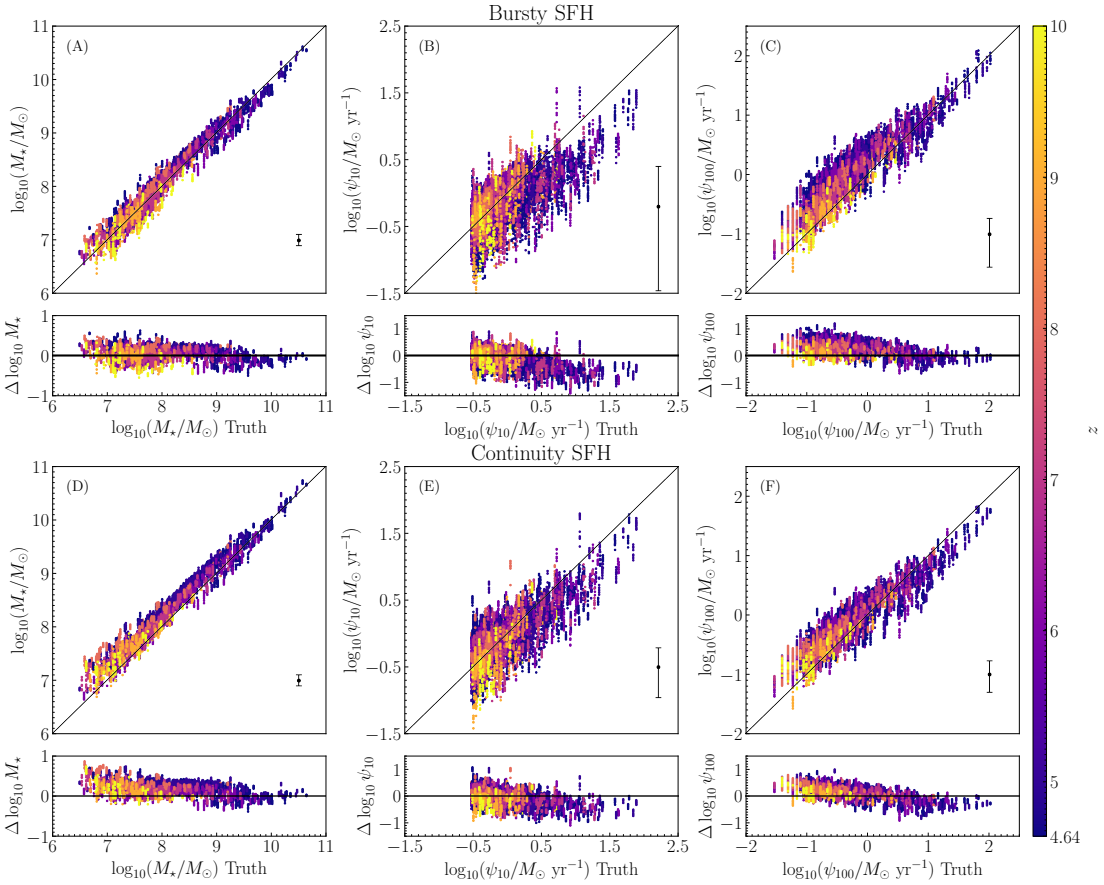

FIGURE 4.6: Comparison of median likelihood estimates from PROSPECTOR (plotted along the y-axis) – total stellar mass (left-hand panels), SFR averaged over 10 Myrs (middle panels), and the SFR averaged over 100 Myrs (right-hand panels) versus the true values (along the x-axis), along with the typical uncertainties which are indicated by the error bar to the lower right in each panel. The top panels (A to C) show estimates using the bursty prior, while the bottom panels (D to F) show results with the continuity SFH prior. Plots are coloured according to their redshift, relative to the colour-bar at the right.

repeat the experiment neglecting the MIRI bands we see the same upturn in stellar mass at the low-mass end. As in Cochrane et al. (2024), we find no significant evidence that outshining affects stellar mass recovery.

Median-likelihood SFRs (averaged over 10 and 100 Myr) estimated using both SFH priors show some degree of proportionality, albeit with significant systematic offsets and large scatter (especially for ψ_{10}). Using the BSFH prior, the median and standard deviation of $\Delta \log_{10}\psi_{10}$ are -0.06 dex and 0.33 dex, respectively, with a typical uncertainty on $\log_{10}\psi_{10}$ of 0.86 dex. For CSFH, these values are -0.02 dex, 0.27 dex, and 0.39 dex, respectively. Similarly, for $\Delta \log_{10}\psi_{100}$, the median and standard deviation are 0.30 dex and 0.25 dex for BSFH, and 0.18 dex and 0.23 dex for CSFH. The typical uncertainties in $\log_{10}\psi_{100}$ are 0.36 dex for BSFH and 0.26 dex for CSFH. Median likelihood ψ_{10} appears to be systematically underestimated at higher

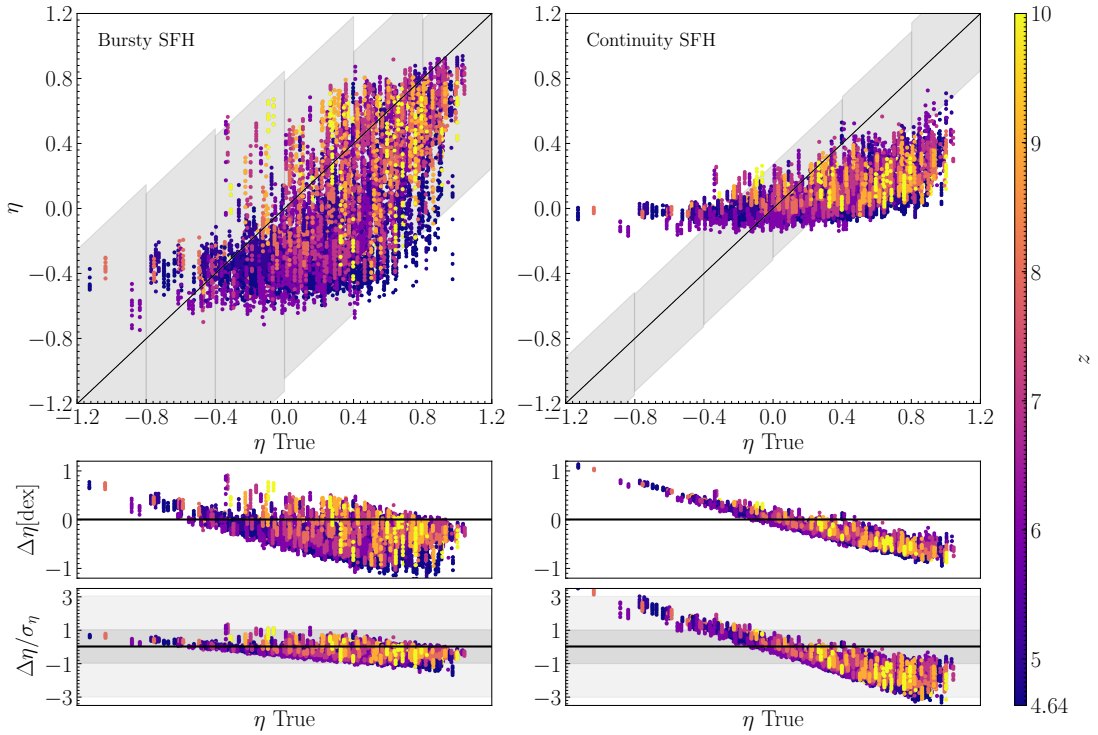

FIGURE 4.7: Burstiness parameter (η) recovered using the bursty SFH prior (left) and continuity SFH prior (right), colour-coded by redshift relative to the colour-bar to the right. For each prior, the top panel shows the median-likelihood η estimates vs the true values, overlaid with a 1:1 line surrounded by shading indicating the typical η uncertainty estimated as a function of true η. The middle and bottom panels display $\Delta\eta$ (i.e. the difference between the median likelihood estimate and the truth) as a function of true η in the units of dex and the actual uncertainty (σ_η), respectively.

values of the true ψ_{10}, which appear to correspond to sources predominantly at low redshifts. This is likely due to inherent degeneracies in the exact combination of photometric bands used at this redshift, which we discuss in Section 4.3.2.1.

4.3.2 Recovery of the burstiness parameter

Fig. 4.7 shows the median likelihood burstiness parameter (η) estimated using the PROSPECTOR BSFH and CSFH priors, colour-coded by redshift relative to the bar at the right, and with the 1:1 line overlaid in black, plus grey shading to indicate the typical uncertainty on recovered η as a function of the ground truth η. The left side (showing the results using the BSFH prior) shows a roughly positive correlation between BSFH η estimates and true values, although there is very large scatter, and the median-likelihood η are generally underestimated. Over 96 per cent of BSFH η estimates fall within 1σ of the true values, but the large uncertainty ($\sigma \approx 1$ dex) stems from the difficulty of measuring short timescale SFHs using photometric data. Fig. 4.8

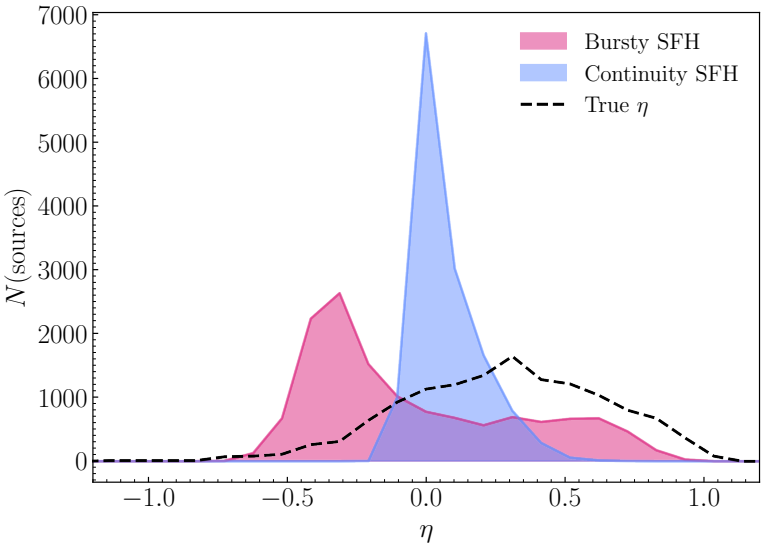

FIGURE 4.8: The true (black dashed line) and recovered (magenta and blue shading, showing the BSFH and CSFH values, respectively) distribution of burstiness parameter, η.

shows that the recovered distribution of BSFH η (magenta shading) covers a similar range of values to the ground truth (black dashed line), however the peak is in the wrong place, favouring temp-quenched $\eta \approx -0.3$.

The right-hand panels of Fig. 4.7 highlight that CSFH (which weighs out abrupt variations in the SFH, unlike the more flexible BSFH; see Tacchella et al., 2022b) generally favours fits with constant SFHs. This is reflected in Fig. 4.8, in which the recovered CSFH η (shaded blue) are centrally distributed, peaking at $\eta = 0$ with a standard deviation of 0.12 dex. This contrasts with the true η distribution, which peaks at $\eta \approx 0.3$ with a much larger standard deviation of 0.35 dex. The typical uncertainty in CSFH η is $\sigma \approx 0.3$ dex, and the CSFH-estimated median-likelihood η values fall within 1σ of the true values for 52 per cent of sources.

It is clear that using photometric data alone, the choice of SFH prior has a large influence on the recovered η values. The CSFH prior is unable to sample the full range of η, and underestimates the uncertainty on η; it is therefore – unsurprisingly – not suitable for dealing with bursty or temp-quenched galaxies. On the other hand, the BSFH prior allows much greater freedom, but systematically underestimates the median likelihood photometric η and has very large associated uncertainties.

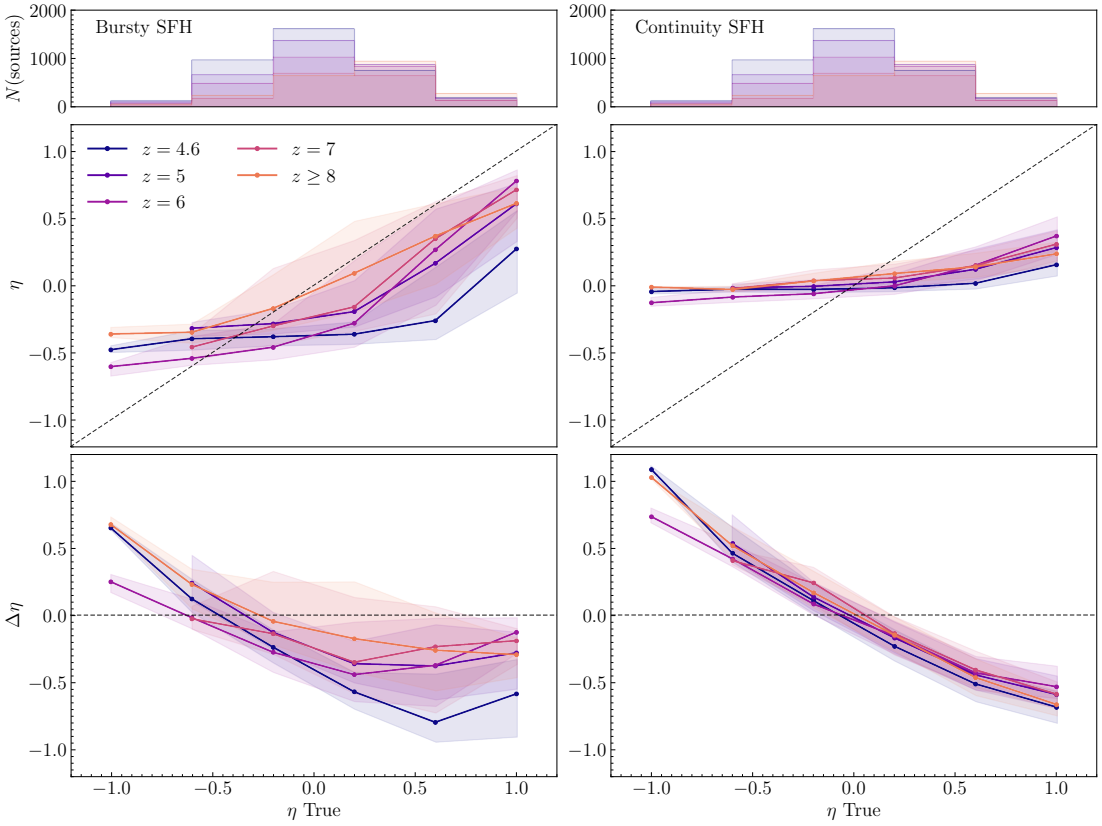

FIGURE 4.9: The average recovered η as a function of true η, at redshifts of $z = 4.64, 5, 6, 7$, and $z \geq 8$ (as indicated in the legend). The left-hand panels show the recovery of η using the BSFH prior, while the right-hand panels use the CSFH prior. The solid lines show the median values at each redshift, with shaded regions representing the scatter within each bin. Each panel includes a one-to-one line, plotted as a dashed gray line. η from the bursty SFH prior shows a weak correlation with the true values, while those from the continuity prior are generally consistent with 0 ± 0.2 dex, irrespective of the true values. The coloured histograms on the top of the plot shows the source count in each η bin at each redshift. The bottom panel shows $\Delta\eta = \eta_{\text{recovered}} - \eta_{\text{true}}$ in each redshift bin.

4.3.2.1 Dependence on redshift

In the previous section we investigated the recovery of η using photometric data and the BSFH and CSFH priors. We now investigate the η recovery further by comparing the median-likelihood estimates to the ground truth at the different redshifts produced by SPHINX^{20}; $z = 4.64, 5, 6, 7$, and $z \geq 8$ for both SFH priors. At each redshift we split the sample into 8 equally spaced bins of true η between $-1 < \eta < 1$, and calculate the median recovered η distributon in each. In Fig. 4.10 the median values are shown as the solid line (coloured according to the redshift as in the legend), and surrounded by shading according the to area enclosed by the 16$^{\text{th}}$ and 84$^{\text{th}}$ percentiles of the distribution. We disregard bins with an occupancy of fewer than 15 sources to limit the impact of small-number statistics.

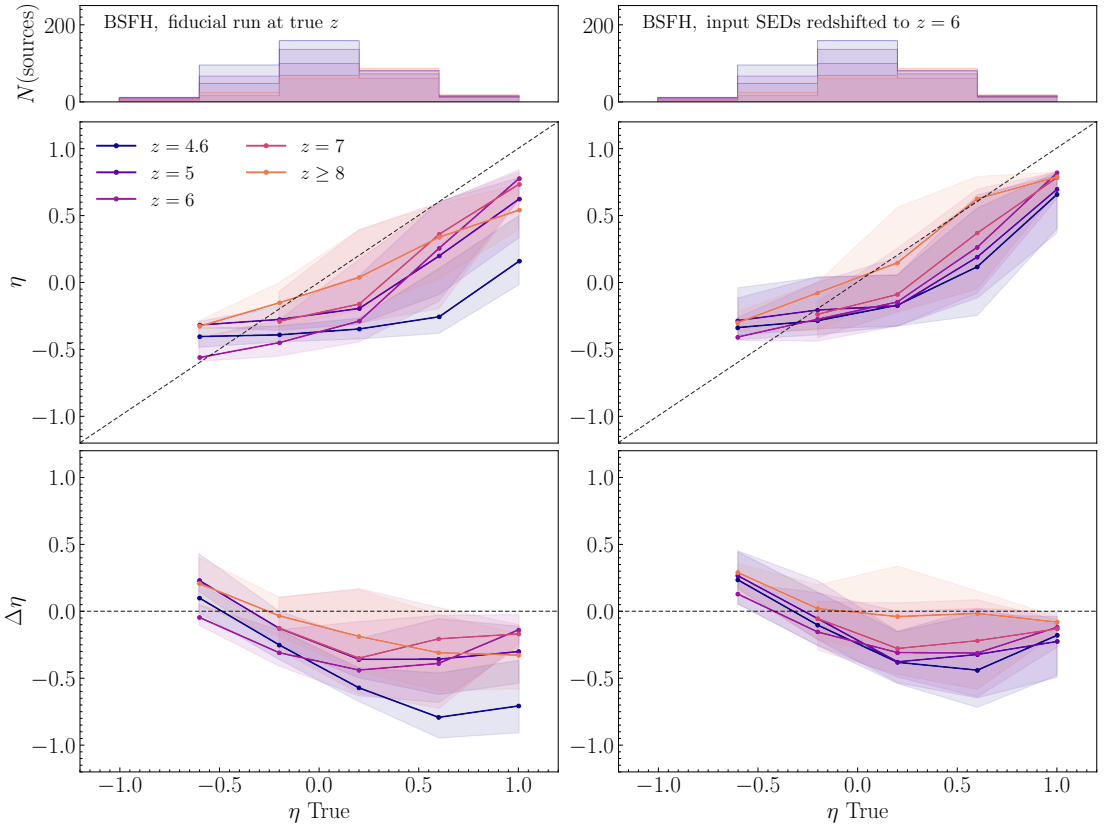

FIGURE 4.10: Similar to Fig. 4.9, but showing the median η recovery (using the BSFH prior) when all galaxies are artificially shifted to $z = 6$ to force the same photometric coverage in each band (right-hand panels). The left-hand panels show the sources from the fiducial run with BSFH for comparison. Only one randomly selected direction from all the SPHINX^{20} haloes is used to make these plots.

For BSFH estimates at $z \geq 5$, we find a reasonable correlation between the average recovered η and its true values. The slope of the recovered vs. true η is consistent with unity, with deviations of up to -0.5 dex in bins where $\eta_{\rm true} > 0$ (Fig. 4.10, left-hand panels). Thus, for sources with constant and bursty SFHs, BSFH measures burstiness with a constant degree of underestimation. On average, however, at $\eta_{\rm true} < 0$, the slopes of these curves flatten and tend to zero as $\eta_{\rm true}$ gets smaller. Overall, this suggests that the SEDs of bursty galaxies weakly influence the recovery of burstiness; whereas the SEDs of temp-quenched galaxies provide no such constraints, which leads median likelihood estimates from BSFH to default to $\eta \approx -0.5$. At $z = 4.64$, however, we find the recovered η to be consistently around -0.5 up to $\eta_{\rm true} < 0.6$ (which corresponds to 85 per cent of the sources in this redshift bin). This suggests that the photometric data at this redshift are unable to constrain burstiness altogether. The η values recovered using CSFH across all redshift bins fail to show a correlation with the true values as well, and are generally consistent with $\eta \approx 0 \pm 0.2$ dex.

To investigate the potential redshift bias in the recovery of η, we randomly select one direction from all the SPHINX^{20} haloes and generate photometry as before, after shifting the rest-frame dust-attenuated SEDs to $z = 6$. We will refer to this catalogue as the $z = 6$ catalogue hereafter. We then fit this catalogue using only the BSFH prior with all other details unchanged. In Fig. 4.10, we show the median recovered η in redshift bins of $z = 4.64, 5, 6, 7$, and $z \geq 8$ versus the true η. The left-hand panel presents the trends in the fiducial BSFH catalogue, while the right-hand panel shows the results for the $z = 6$ catalogue. In both panels, only one direction is shown per SPHINX^{20} halo, as discussed above. The recovery of η in the $z = 5$ and $z = 7$ bins is similar in both catalogues, which is expected since these redshifts are closest to the forced redshift $z = 6$. In contrast, the $z = 4.64$ and $z \geq 8$ bins show significant improvement. For $z = 4.64$ sources, the offsets in the median likelihood η estimates relative to the true values are reduced by $0.2 - 0.5$ dex, while for $z \geq 8$ sources the reduction is $0.1 - 0.3$ dex, after their rest-frame SEDs are shifted to $z = 6$ (Fig. 4.9).

While redshift-induced biases in the recovery of η are evident, their precise origin remains uncertain. One possible explanation is that they arise from the interplay between redshift and photometric band coverage, which governs how emission lines and continuum features are sampled in the observed frame (see Fig. 4.3 and Fig. 4.4). To test this, we examine the distribution of χ values $\left(= \frac{F_{\nu,\text{PROSPECTOR best fit}} - F_{\nu,\text{obs}}}{\sigma_{F_{\nu,\text{obs}}}}\right)$ as a function of observed-frame wavelength across different redshift bins (Fig. 4.11). The bottom panel shows χ when all SEDs are artificially redshifted to $z = 6$, colour-coded by their true redshifts, revealing broadly consistent behaviour across all bins. The top panel presents the χ values from the fiducial BSFH run, again as a function of observed-frame wavelength. Only one direction is shown per halo, similar to Fig. 4.10. While we see variations in χ, the bottom panel makes it clear that they are linked to the rest-frame wavelengths. This indicates that certain spectral features are being fitted with varying degrees of accuracy. However, this is a general limitation of using photometric data, rather than a consequence of the particular photometric filters used here. Crucially, no distinct redshift-dependent features emerge that could explain the biases in the recovery of ψ_{10} and η. Thus, there appears to be a degeneracy that we are not presently able to identify. We intend to revisit this in a future work after incorporating spectroscopy.

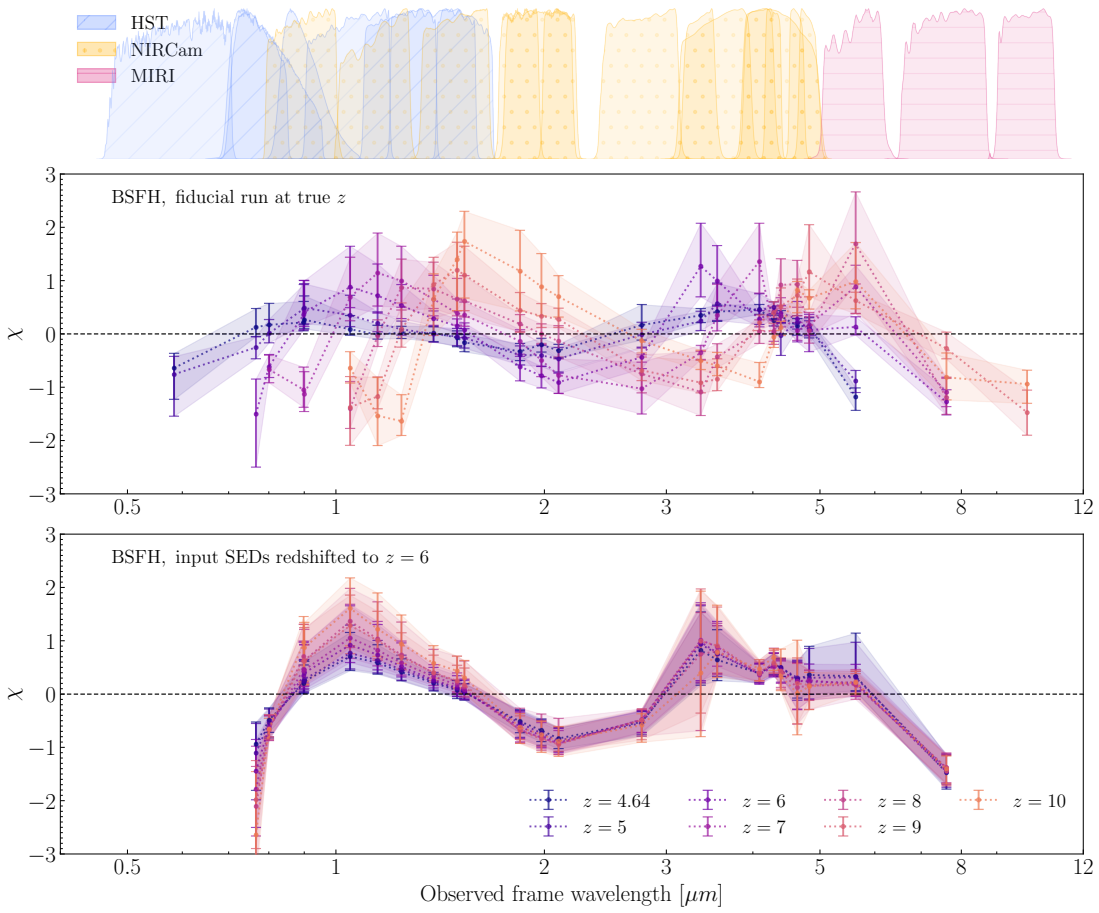

FIGURE 4.11: We show $\chi = \left(\frac{F_{\nu,\text{PROSPECTOR best fit}} - F_{\nu,\text{obs}}}{\sigma_{F_{\nu,\text{obs}}}}\right)$, computed between input and PROSPECTOR best-fit photometry, as a function of observed-frame wavelength across different redshift bins. The top panel shows the sources from the fiducial BSFH run, while the bottom panel shows the results where the input SEDs were redshifted to $z = 6$ prior to fitting. The solid lines denote the median χ value, while the shaded regions denote the spread between 16^{th} and 84^{th} percentile bounds within a wavelength range. Only one direction is shown per halo. We find that there is a consistent trend in χ across all redshift ranges as a function of rest-frame wavelength, which indicates that certain spectral features are fit better than others – a limitation of photometry-only fitting process. However, we do not find a clear dependence of χ on redshift, that could explain the observed redshift-biases in η recovery.

4.3.3 Influence of different multi-wavelength coverage

The selection of filters used in this work is designed to investigate the recovery of burstiness under ideal conditions and is a superset of the filters used in multiple surveys (see Section 2.2). In this section, we examine how the recovery of η is affected when only small subsets of filters are used. We focus on two subsets: one containing only the NIRCam filters and the other comprising of NIRCam and MIRI filters. As in Section 4.3.2.1, we randomly select one direction for each SPHINX^{20} halo and convolve the dust-attenuated SEDs with these two filter

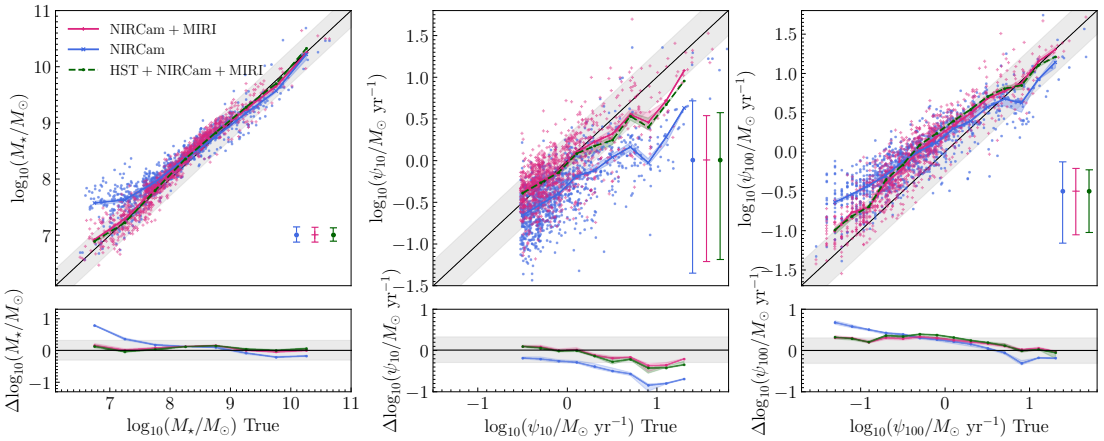

FIGURE 4.12: Comparison of median likelihood estimates from the BSFH prior (plotted along the y-axis) – total stellar mass (left-hand panels), SFR averaged over 10 Myrs (middle panels), and the SFR averaged over 100 Myrs (right-hand panels) versus the true values (along the x-axis), along with the typical uncertainties which are shown as error bars to the lower-right, for the three sets of fits: NIRCam-only (blue), NIRCam + MIRI (magenta), and *HST* + NIRCam + MIRI (green). Scatter plots for NIRCam only and NIRCam + MIRI fits are shown here, those for the fiducial fits can be found in Fig. 4.6. The solid lines with the shaded regions show the median likelihood estimate and the uncertainties calculated using bootstrap resampling.

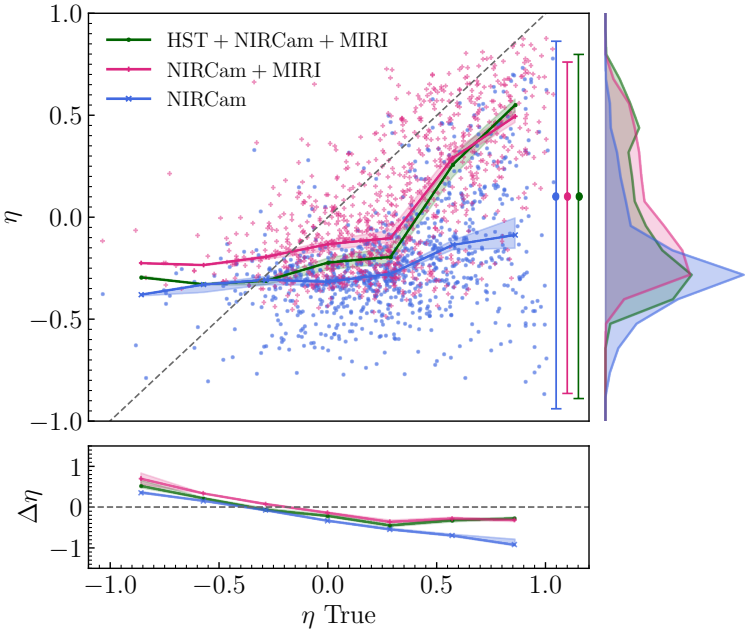

FIGURE 4.13: The median likelihood η was estimated with the bursty prior using the NIRCam-only (blue), NIRCam + MIRI (magenta), and *HST* + NIRCam + MIRI (green) filter configurations. The solid lines with shaded regions denote the median η with uncertainties estimated through bootstrapping. The scattered blue and magenta points also show the spread of the corresponding η values vs the true values. The scatter for *HST* + NIRCam + MIRI is not included, it can be seen instead in Fig. 4.7. Typical uncertainties are also shown in the corresponding colours. The lower panel shows $\Delta\eta$ (= median likelihood estimate − true) as a function of the true η for the different sets of fits. The histogram to the right of the top panel shows the distributions of median likelihood η values from the three sets of fits.

subsets to generate two photometric catalogues. We also compare these results to those obtained using our fiducial catalogue (which includes *HST*, NIRCam, and MIRI filters).

In Fig. 4.12, we compare the median likelihood estimates of total stellar mass, ψ_{10}, and ψ_{100}, derived using the BSFH prior for the three catalogues to the true values. The associated statistics are presented in Table 4.3. We find that the properties derived using NIRCam and MIRI bands are consistent with those from our fiducial catalogue. However, median likelihood estimates of total stellar masses drawn from the NIRCam only catalogue show an overestimation of stellar masses of low mass galaxies ($\log_{10} M_\star/M_\odot < 8$) by up to 1 dex. The systematic deviation of NIRCam only total stellar masses from the true values is similar to the findings of Cochrane et al. (2024)[4], who used a similar filter configuration. They attribute this trend to the inability of their SED fitting code to fit strong emission lines with high equivalent widths. This could be driving the overestimation that we observe when using NIRCam bands only. Inclusion of MIRI bands adds additional wavelength coverage along the redder part of the spectrum, which then is able to accurately constrain the total stellar masses of these low-mass sources. As a result, we do not see the 0.5 dex underestimation of total stellar masses reported by Cochrane et al. (2024) in the high-mass sources. We find that the underestimation of ψ_{10} from NIRCam-only fits is about 0.3 dex greater than what is observed from NIRCam + MIRI and the fiducial fits (Section 4.3.1). This difference is primarily due to the absence of MIR data. Lastly, the median ψ_{100} estimated using NIRCam-only data exhibit marginally more overestimation than the other two sets of fits at the lower bounds of the true ψ_{100} (≈ 0.2 dex at $\log_{10}\psi_{100} \approx -1$), which again can be attributed to the lack of MIR data leading to weaker constraints on the stellar continuum.

Fig. 4.13 compares the median likelihood η estimates from the three catalogues. The recovery of the burstiness parameter η from NIRCam + MIRI data is comparable to that from the *HST* + NIRCam + MIRI fits, with median η estimates from NIRCam + MIRI being marginally higher (up to 0.1 dex, much smaller than the typical uncertainties) than those from the *HST* + NIRCam + MIRI fits. This discrepancy is mainly observed at $z = 4.64$ and $z = 5$, where part of the UV spectrum (including Lyman-α at 1216 Å) falls beyond the coverage of the NIRCam filters we use and is covered by the *HST* filters in one set of fits, but not in the other. However, this is ultimately of little consequence, as the difference is much smaller than the uncertainties. In contrast, η recovered using only the NIRCam filters displays the greatest deviation from the true values and the highest degree of scatter compared to the other configurations. Specifically, the

[4]Cochrane et al. (2024) only consider sources at $z \geq 5$. When limiting our sample to this redshift range, we find a comparable 0.54 dex total stellar mass overestimation at $\log_{10}(M_\star/M_\odot) \approx 7$.

TABLE 4.3: Goodness of physical parameter (= recovered − true) recovery using PROSPECTOR BSFH prior using different sets of photometric filters, quantified by the median $\Delta \log_{10}$ parameter, its standard deviation, and typical uncertainty on $\log_{10}$ parameter.

Filter configuration	Parameter	μ	σ	Typical uncertainty
NIRCam	$M_\star$	0.13	0.19	0.13
	ψ_{10}	−0.29	0.30	0.93
	ψ_{100}	0.31	0.27	0.49
NIRCam+MIRI	$M_\star$	0.11	0.16	0.13
	ψ_{10}	0.01	0.27	0.87
	ψ_{100}	0.25	0.21	0.36
HST+NIRCam+MIRI	$M_\star$	0.09	0.14	0.11
	ψ_{10}	−0.06	0.33	0.86
	ψ_{100}	0.30	0.25	0.36

median likelihood value in all η bins consistently falls between −0.3 and −0.2, pointing to a general lack of observational constraints on burstiness. The marginalized histogram (Fig. 4.13, right-hand panel) shows that the distribution of median likelihood η using only NIRCam filters is more concentrated around the peak than that of the other filter sets. Thus, η-recovery using photometry is highly reliant on MIRI data, particularly at high redshifts where a significant part of the SED is out of range of NIRCam filters.

4.4 Conclusions

In this work, we investigate our ability to recover the burstiness of galaxies using UV to mid-IR photometry using an idealised data set comprising filters available on the *HST* as well as the *JWST* (both NIRCAM and MIRI). To do this, we generated synthetic photometry from the dust-attenuated SEDs of 1,380 haloes from the first data release of SPHINX^{20} cosmological radiation-hydrodynamic simulation suite, spanning $4.64 < z < 10$. By modelling the photometric data with the SED fitting code PROSPECTOR, we measured key physical parameters, such as the total stellar mass and the star formation rates (averaged over 10 and 100 Myrs), and estimated the burstiness parameter η, defined as the log of the ratio of the SFR averaged over the last 10 Myr to that averaged over the last 100 Myr. We make use of two non-parametric star formation history (SFH) priors: the continuity and the bursty-continuity priors. The main conclusions of this work are as follows:

1. The photometric recovery of burstiness, η, is strongly impacted by the choice of the choice of the SFH prior. Unsurprisingly, the continuity SFH prior, which weighs against abrupt changes in the SFH, favours SED fits with constant SFHs. As a result, recovered η is consistent with 0 for the majority of sources. We find the continuity SFH prior leads to incorrect η for sources with stochastic SFHs, which are thought to be prevalent at high redshifts.

2. When using the more flexible bursty SFH prior, we find that the recovered η correlates with the ground truth for sources with both constant and stochastic SFHs; however, the scatter is very large, and the typical uncertainties on η are around 1 dex in magnitude making the estimates very hard to believe for individual galaxies.

3. While uncertainties on individual estimates are large, we show that at $z \geq 5$ the recovered η using the bursty SFH prior averaged over multiple samples correlate well with the true values, albeit with an underestimate of $\sim$0.5 dex for $\eta_{\rm True} > 0$.

4. Even averaging over samples of galaxies, photometric inference of η using the bursty SFH prior depends on the precise combination of source redshift and photometric band selection.

This work has focused on studying the shortcomings and identifying the systematic biases that arise when using only photometric data to constrain the burstiness of galaxies at high redshifts under best-case scenarios. Based on our results, we urge caution when using real photometric data, such as from the *JWST*, to study the stochasticity of galaxy SFHs. This work therefore provides an important baseline against which improvements can be judged when additional data (e.g. spectroscopy) are incorporated. We intend to build on this in a companion paper, where we will revisit these results using *JWST* spectroscopy.

Chapter 5

Conclusions and Future Work

"Final is the most misused word in science."
–Prof. Daniel J. B. Smith (*private communication*)

In this thesis, we have studied the nature of the faint radio source population in the ELAIS-N1 field, one of the LOFAR Two-Metre Sky Survey (LoTSS; Shimwell et al., 2017, 2019, 2022) data release 1 (DR1; Tasse et al., 2021; Sabater et al., 2021; Kondapally et al., 2021; Duncan et al., 2021; Best et al., 2023) deep fields. In Chapter 2, we demonstrated the ability of energy balance SED fitting to obtain estimates of radio source properties, such as stellar masses, star formation rates (SFR), and contribution of the AGN torus emission to the mid-IR SED ($f_{\rm AGN}$), by modelling UV – far-IR photometry. We combined these estimates with the 150 MHz observations of 31,610 radio sources from the LoTSS deep fields DR1 and classified 92 per cent of them into one of four classes: star forming galaxies (SFGs), radio quiet AGN (RQ AGN), low-excitation radio galaxies (LERGs), or high-excitation radio galaxies (HERGs). We also studied the source demographics as a function of the 150 MHz flux density, luminosity, SFR, stellar mass, redshift, and apparent r-band magnitude. Additionally, we modelled the SEDs of ~133,000 3.6 μm-selected $z < 1$ sources in the ELAIS-N1 deep field, and used them to revisit the well-known SFR–150 MHz luminosity (SFR–L_{150}) relation. We found the stellar mass dependence in the SFR–L_{150} relation to be significantly weaker than previously reported, and that it may disappear altogether at $\log_{10}(\mathrm{SFR}/M_{\odot}\,\mathrm{yr}^{-1}) > 0.5$.

However, using parameter estimates from SED modelling in conjunction with radio observations to classify sources is not new in the context of LoTSS deep fields DR1. In particular, Best et al. (2023) combined results from four different SED fitting codes to derive consensus physical

parameters and performed a similar classification. The strength of our work lies in the use of a single code – the new-generation SED fitting program PROSPECTOR (Leja et al., 2017; Johnson et al., 2021) – thereby reducing the complexity involved in learning and setting up multiple codes and streamlining the process. PROSPECTOR has several features that make it valuable for our science goals. It uses the CLUMPY models (Nenkova et al., 2008a,b) to account for the contribution of the AGN torus emission to the mid-IR SED, thus providing a clear avenue to identify radiatively efficient AGN (also known as radiative-mode AGN). It models star formation histories (SFHs) using highly flexible, non-parametric forms. It uses the DYNESTY (Speagle, 2020) dynamic nested sampling framework, which can handle complicated posterior distributions better than the commonly used Markov Chain Monte Carlo (MCMC) sampling. Crucially, PROSPECTOR is capable of modelling photometry and spectroscopy self-consistently, thereby facilitating the push towards joint spectrophotometric classification efforts.

Chapter 3 of this thesis presents a novel spectrophotometric approach for classifying faint radio source populations. Here, we simultaneously modelled the LoTSS deep fields DR1 photometry alongside spectroscopy from the early data release of the Dark Energy Spectroscopic Instrument (DESI EDR; DESI Collaboration et al., 2016a, 2022) for 6,038 radio sources. We built upon the works by Drake et al. (2024) and Arnaudova et al. (2025) and performed probabilistic source classifications. Drake et al. (2024) and Arnaudova et al. (2025) used spectroscopy from the Sloan Digital Sky Survey (SDSS; York et al., 2000) DR8 and BOSS DR12, and DESI, respectively, in combination with 150 MHz radio observations from LoTSS DR2 and LoTSS DR1, respectively, and used a Monte Carlo realisation-based approach to probabilistically classify radio sources. Our work, however, additionally incorporates UV–far-IR photometry and leverages the full posterior probability distributions from the PROSPECTOR sampling results to enable a fully Bayesian probabilistic classification framework. We apply an informative prior on the posterior probability distributions of $f_{\rm AGN}$ to compute the probability of the sources hosting radiative mode AGN on the basis of mid-IR excess. Through the posterior probabilities of the four Baldwin-Phillips-Terlevich (BPT; Baldwin et al., 1981) line fluxes, we compute the probabilities of the sources being classified as SFG, Seyfert, and low-ionisation nuclear excitation regions (LINERs). We then derive the probabilities of the sources hosting radio-excess AGN based on the SFR–L_{150} relation or $L_{\rm H\alpha}$ – L_{150} relation. By combining these probabilities, we compute the probability of each source falling into each of the SFG, RQ AGN, LERG, and HERG classes. A key advantage of probabilistic classification methods is the option to produce

classifications satisfying a particular confidence threshold, in addition to the maximum likelihood classifications. This gives the end user the freedom to choose an option that best suits their science goals, e.g., finding the right balance between reliability and confidence. Our 90 per cent reliability classifications (P_{90}) highlighted certain key advantages over purely photometric or spectroscopic ones. For example, 70 per cent of the sources classified as P_{90} RQ AGN had been classified as SFGs in Chapter 2 through photometric methods. This change in classification was driven by the inclusion of emission-line diagnostics, providing a complementary approach to identify radiative-mode AGN. Similarly, about 10 per cent of the sources spectroscopically classified as SFGs by Arnaudova et al. (2025) were identified as RQ AGN in our method, potentially pointing to a population of obscured AGN, which can be identified through MIR excess. This chapter demonstrated the advantages of a joint spectrophotometric classification approach over purely photometric or spectroscopic ones. We plan on extending this work once large volumes of spectroscopy from surveys such as the WEAVE-LOFAR survey (Smith et al., 2016) and ORCHIDSS (Duncan et al., 2023) become available.

This thesis also investigates the nature of high-redshift galaxies in cosmological hydrodynamic simulations, particularly in the context of studies with the James Webb Space Telescope (*JWST*; Gardner et al., 2006, 2023) reporting a large number of galaxies with apparently bursty SFHs (e.g., Strait et al., 2023; Endsley et al., 2023, 2024; Glazebrook et al., 2023, 2024; Alberts et al., 2024; Asada et al., 2024; Clarke et al., 2024; Dressler et al., 2024; Nanayakkara et al., 2024; Park et al., 2024). The aim of Chapter 4 is to investigate how well key parameters, such as the recent SFH (parameterised by η, defined as the logarithm of the ratio of the SFR averaged over the last 10 Myrs to that averaged over the last 100 Myrs), can be estimated using energy balance SED modelling of photometric data alone under idealised conditions (following an approach similar to Hayward and Smith, 2015; Smith and Hayward, 2015; Haskell et al., 2023). This chapter represents the first step in a series of studies aimed at recovering the burstiness of galaxies, providing a baseline against which future results incorporating spectroscopy can be evaluated to assess whether spectroscopy improves the fidelity of such estimates. We focus on 1,380 simulated haloes in the redshift range $4.64 \leq z \leq 10$ from the SPHINX^{20} Public Data Release Version 1 (SPDRv1; Katz et al., 2023). SPHINX^{20} is a state-of-the-art cosmological simulation suite designed to model large populations of galaxies in a full cosmological volume with radiative hydrodynamics, while retaining the ability to resolve the multiphase ISM by reaching resolutions of $\sim$10 physical pc. Synthetic photometry was generated from the dust-attenuated spectrum available as part of SPDRv1 using up to 25 *HST*, *JWST*/NIRCam and *JWST*/MIRI filters,

thereby representing the best-case space-based photometric coverage currently achievable. We again use the SED modelling code PROSPECTOR in this chapter. We use two non-parametric SFH priors: the continuity and the bursty-continuity priors. While the former favours relatively constant SFHs, the latter allows for more flexibility and therefore is believed to be better suited for modelling irregular SFHs, containing short-lived bursts and quenching events (e.g., Carnall et al., 2019; Leja et al., 2019). η recovery was strongly dependent on the SFH prior used. We found the recovered η to be consistent with zero (i.e. consistent with a constant SFH) when using the continuity prior, irrespective of the true value. With the bursty SFH prior, we found the recovered η, averaged over multiple samples, to be correlated with the true values – although the recovered η estimates for individual sources had large associated uncertainties. The recovery of average η and the 10 Myr averaged SFR was strongly biased with redshift, particularly in the lowest redshift bin ($z = 4.64$), where a degeneracy arose between the photometric filters and the observed-frame sampling of the SEDs. Although the precise cause of this degeneracy remains unclear, this chapter demonstrates that photometry-only approaches inevitably face limitations in recovering physical parameters accurately, even under idealised conditions. Incorporating spectroscopic information is therefore essential in future work to break such degeneracies and improve the robustness of SED-based inference. Together, these results highlight the constraints of photometry-only analyses, underscore the need for spectroscopy, and provide a benchmark for future studies assessing improvements in burstiness recovery.

5.1 Plans for the future

The landscape of modern extragalactic astronomy is being shaped by current and forthcoming large-scale facilities. On the radio side, these include the Square Kilometre Array (SKA; Rawlings et al., 2004; Dewdney et al., 2009) and its pathfinders, such as the APERture Tile In Focus (APERTIF; van Cappellen et al., 2022), the European VLBI Network (EVN; Zensus and Ros, 2015), the enhanced Multi Element Remotely Linked Interferometer Network (e-MERLIN; Garrington et al., 2004), and the LOw-Frequency ARray (LOFAR; van Haarlem et al., 2013). Complementing these efforts are wide and deep spectroscopic surveys, conducted with instruments like the William Herschel Telescope Enhanced Area Velocity Explorer (WEAVE; Dalton et al., 2012; Dalton, 2016; Jin et al., 2024), the 4-metre Multi-Object Spectroscopic Telescope

(4MOST; de Jong et al., 2012, 2019), and the Multi-Object Optical and Near-infrared Spectrograph (MOONS; Cirasuolo and MOONS Consortium, 2016). In parallel, space-based observatories such as the *James Webb Space Telescope* (*JWST*; Gardner et al., 2006, 2023) are providing exquisite photometric and spectroscopic data, pushing the observational frontier to increasingly higher redshifts. The influx of large volumes of data from these instruments will provide exciting opportunities to study diverse populations of objects in great detail, paving the way for further advances in our understanding of galaxy evolution. Against this backdrop, we outline some research directions that we aim to pursue in the near future in Section 5.1.1 and Section 5.1.2.

5.1.1 Future Directions for the current projects

5.1.1.1 Joint spectrophotometric studies of the faint radio source population

In the era of massively multiplexed spectroscopic surveys, such as WEAVE-LOFAR (Smith et al., 2016) and the Optical, Radio Continuum and HI Deep Spectroscopic Survey (ORCHIDSS; Duncan et al., 2023), designed to target radio sources from deep surveys and complement existing multiwavelength datasets, joint spectrophotometric classification approaches are emerging as the new gold standard for classifying the faint radio source population. Building on this context, we presented the preliminary results from a novel, fully Bayesian joint spectrophotometric classification scheme in Chapter 3. The plans for the immediate future include fixing the issues currently present in our method, e.g., identifying the origin of the offsets in flux and flux uncertainties measured by PROSPECTOR and correcting them, and subsequently continuing the development of this approach by working with spectroscopic data from the first data release of DESI (DESI DR1; DESI Collaboration et al., 2016a, 2025). Looking further ahead, WEAVE-LOFAR and ORCHIDSS are expected to deliver high-completeness ($\gtrsim$ 90 per cent) redshift coverage out to $z \sim 1$, enabling analyses across the "cosmic happy hour" epoch when star formation declines and AGN feedback becomes increasingly important. Accurately classifying sources from these survey datasets into the underlying SFG, RQ AGN, LERG, and HERG classes would allow us to provide deeper insights to the question of the nature of the faint radio source population. Some key highlights of this work are listed below:

- By using redshift-complete data up to $z = 1$, we will be able to perform detailed studies of the faint radio source demographics. Efforts in this direction have been ongoing for

some time, for example, Best et al. (2023) and Das et al. (2024) attempted such studies using photometric maximum-likelihood classifications, which inherently introduced large uncertainties. Drake et al. (2024), on the other hand, approached this spectroscopically, but their sample included only 4 per cent spectroscopic coverage of the entire LoTSS-wide sample. With the extensive spectroscopic data from WEAVE-LOFAR, our joint spectrophotometric classification approach can investigate radio source demographics as a function of parameters such as accretion mode and radio luminosity.

- Through joint spectrophotometric studies, we aim to quantify the cosmic energy budget of the underlying source populations and constrain the role of AGN in regulating galaxy evolution via both positive and negative feedback on star formation. Improved separation of SFGs and AGN will enable tighter constraints on the cosmic star formation rate density (CSFRD) and the radio luminosity function (RLF), providing more robust insights into galaxy growth and evolutionary pathways. This approach will also allow the identification and characterisation of low-luminosity and "hidden" AGN populations, which may be significantly more prevalent than previously recognised (e.g. Morabito et al., 2025). Furthermore, the data will facilitate detailed investigations of the fuelling processes and triggering mechanisms of AGN activity, including their dependence on host-galaxy properties and environment (e.g. Kondapally et al., 2022, 2025).

We also plan to continue improving our classification framework, incorporating additional diagnostics, such as brightness temperature.

5.1.1.2 Spectrophotometric study of burstiness in high-redshift galaxies

In Chapter 4, we investigated the ability of SED modelling using *HST*+*JWST* photometry to measure the burstiness parameter η, which characterises the shape of the recent SFHs of galaxies. We identified an unexplained degeneracy in the specific combination of source redshift and photometric band selection, which introduced biases in the recovery of recent SFRs (averaged over 10 Myrs) and the burstiness parameter η. The next step is to incorporate spectroscopy into this study. Using Chapter 4 as a baseline, we plan to examine whether these limitations persist when spectroscopy is included and to quantify any improvements. We also aim to determine the minimum spectral resolution required to reliably constrain the burstiness of galaxies, exploring different combinations of photometry and spectroscopic data (e.g. R100, R1000, or R2700 resolution spectra from *JWST*/NIRSpec). This line of investigation will help inform observational

studies of the SFHs of high-redshift galaxies by identifying potential biases and limitations in current methods. Such a study would benefit from the improvements we plan in the emission line fitting in PROSPECTOR (discussed in the next paragraph). The ability to include Balmer line fluxes to place constraints on the SFRs would be highly useful, as they are highly sensitive to the most recent 10 Myrs of a galaxy's lifetime (e.g. Calzetti, 2013).

5.1.2 Plans for improving the SED fitting framework

5.1.2.1 Reducing the time required for joint spectrophotometric fitting

Modern SED modelling codes that generate models on the fly and incorporate a wide range of emission physics (e.g. nebular emission lines and AGN tori) are highly desirable for dealing with the large volumes of data being produced/are expected to be produced by the current and forthcoming surveys. However, such codes are computationally expensive. For example, in Chapter 3, the spectrophotometric fitting with PROSPECTOR required approximately 35, 70, and 140 hours per source to reach the 50, 84, and 99 per cent completion rates, respectively. This presents a significant challenge when scaling to large samples, such as the $\sim 10^6$ spectra anticipated from the WEAVE-LOFAR survey. Therefore, a key focus of our future plans is to improve the SED fitting framework and reduce runtimes. First, we propose revising the way PROSPECTOR models galaxy SEDs at a fixed wavelength resolution. The MILES (Sánchez-Blázquez et al., 2006) library, commonly used in FSPS, has a resolution of ~2.5 Å FWHM between rest-frame wavelength 3,750 - 7,200 Å, with other FSPS libraries offering similar resolutions. While such high-resolution sampling is favourable at UV – NIR wavelengths, i.e., regimes that will have observed spectroscopy from these surveys, it is not necessary at FIR wavelengths, where observations are typically limited to a few photometric bands. To address this, we aim to implement a wavelength-dependent resolution scheme within PROSPECTOR. This would involve using high-resolution spectral libraries only in wavelength regimes where the observational data warrant it (e.g., where spectra are available), and lower-resolution libraries elsewhere. Such an approach is anticipated to reduce runtimes by an order of magnitude without significantly compromising modelling accuracy. In future iterations, this strategy could be generalised into a fully dynamic resolution-scaling scheme, where the model resolution adaptively matches that of the input observational data. Second, we aim to incorporate machine learning techniques to accelerate inference of galaxy physical properties. In particular, we are interested in the Simulation-Based Inference (SBI; Cranmer et al., 2020; Khullar et al., 2022), which use

neural density estimators trained on simulated datasets to infer posterior distributions of model parameters directly from observed data. By forgoing the full forward modelling of the SED at each sampling step, SBI techniques have been demonstrated to infer properties from simulated spectra 10^5 times faster than MCMC-based fits (e.g Khullar et al., 2022).

5.1.2.2 Improving emission line fitting

PROSPECTOR by default uses a physically motivated emission line model based on the CLOUDY photoionisation code (Ferland et al., 2013; Byler et al., 2017), which is included in FSPS. In this framework, emission lines are assumed to be powered exclusively by young stellar populations. This assumption carries a caveat, as it does not account for deviations caused by AGN, shocks, or other non-stellar ionising sources (see Appendix E of Johnson et al., 2021). To mitigate this, PROSPECTOR allows for marginalisation over emission lines, providing additional flexibility to model lines influenced by non-stellar ionising mechanisms. However, this treatment is not physically motivated and does not strictly adhere to emission-line physics. Therefore, it is highly desirable to use a physically motivated model that accounts for the effects of non-stellar physics on emission lines. We plan to update the PROSPECTOR models to include such a treatment of emission lines. Furthermore, we aim to implement more complex emission line profiles and establish a connection between the observed emission lines and the underlying galaxy properties.

5.2 Additional research not included in this thesis

Throughout the course of my PhD, I have made significant contributions the following two works that are not included in this thesis:

1. *WEAVE First Light Observations: Origin and Dynamics of the Shock Front in Stephan's Quintet* (second authorship, published as Arnaudova et al., 2024) – We used the first observations from WEAVE's panoramic optical integral field unit (LIFU) to study the large-scale shock front in the compact, interacting local galaxy group Stephan's Quintet (SQ). In this work, we introduced a new dynamic definition of the shock region using the line-of-sight velocity versus velocity dispersion diagram and provided new constraints on the shock properties and its role in SQ. I led the radio analysis, using the interferometric data reduction software packages AIPS and CASA to calibrate and image archival VLA 1.4

and 5 GHz observations. These were then combined with a new LOFAR 150 MHz image to create spectral index and curvature maps. From these maps, we derived the equipartition parameters, age estimates, and Mach number of the radio plasma. Additionally, we found that the 1.7 GHz flux density is boosted by a factor of ∼10, supporting our hypothesis that the relatively weak ($\mathcal{M} \approx 3.8$) shock cannot efficiently accelerate particles and instead adiabatically compresses the medium.

2. *Beware the recent past: a bias in spectral energy distribution modelling due to bursty star formation* (second authorship, published as Haskell et al., 2024) – We investigated how the recovery of galaxy SFRs using energy-balance SED fitting is potentially biased by their recent SFHs. I used PROSPECTOR to model photometry generated from the SEDs of 6,706 simulated galaxies at $1 < z < 8$ from the Feedback in Realistic Environments (FIRE; Hopkins et al., 2014, 2018) zoom-in cosmological radiative hydrodynamic suite. The results of my fits were contrasted against the fiducial MAGPHYS fits to these galaxies, revealing a previously unknown systematic error in the MAGPHYS results due to bursty star formation: the derived SFRs can differ from the ground truth by as much as 1 dex (with $> 5\sigma$ significance), depending on the details of their recent SFH. We attributed this to a combination of the precise details of the stochastic prior sampling and the burst implementation in the MAGPHYS libraries. This work highlights the critical importance of the assumed SFH in determining the estimated results and urges caution when using SED fitting with parametric SFHs or predefined libraries and templates to model high-redshift galaxies with JWST.

5.3 Concluding remarks

This thesis has demonstrated the power and flexibility of modern SED fitting codes in advancing our understanding of the faint radio source population in deep fields of low frequency radio surveys. In addition, it has underscored the challenges associated with studies of star formation histories at high redshifts using data with limited wavelength resolution. By incorporating both photometric and spectroscopic data within a Bayesian framework, we have shown how joint spectrophotometric analyses can improve classification accuracy and uncover hidden populations of AGN. The results highlight the promise and limitations of photometry-only approaches, especially at high redshifts, and motivate the inclusion of spectroscopy to break degeneracies in SED modelling. With the advent of massively multiplexed spectroscopic surveys, there is

a clear need for scalable, physically motivated, and computationally efficient inference frameworks. The groundwork laid in this thesis provides a foundation for future spectrophotometric investigations of galaxy evolution in the next decade of astrophysical surveys.

Appendix A

Assessment of Prospector derived SFRs

A.1 Comparison with spectroscopically measured SFRs

To determine the reliability of SFRs obtained using SED fitting, we compare PROSPECTOR (Johnson et al., 2021) SFR estimates with those obtained from Hα emission line measurements. The latter, which accounts for the possible presence of dust, is widely regarded as the gold standard tracer of SFR up to 10 Myrs (see Calzetti, 2013; Tacchella et al., 2022c). We use the SFRs measured from the dust extinction and aperture corrected Sloan Digital Sky Survey (SDSS DR8; Abazajian et al., 2009) line fluxes provided by the Max Planck Institute for Astrophysics and the Johns Hopkins University (MPA-JHU) group (see Brinchmann et al., 2004). We match the optical positions of sources in our SWIRE-selected sample with the MPA-JHU catalogue using a nearest-neighbour algorithm with a maximum 1 arcsec separation, finding 241 common sources. Our analysis is limited to 96 sources not flagged as stars by the Schlegel classification (Bolton et al., 2012), with significant ($> 3\sigma$) Hβ detection (allowing reliable dust corrections) and acceptable PROSPECTOR fits. For this test, we average PROSPECTOR SFRs over 10 Myrs to enable a like-for-like comparison given the expected timescale associated with the Balmer line emission (e.g. Kennicutt and Evans, 2012). Figure A.1 shows excellent consistency between the PROSPECTOR and Balmer-line SFRs. We obtain a best-fit relation of $\log_{10}(\psi_{\text{PROSPECTOR}}) = \log_{10}(\psi_{\text{H}\alpha}) - (0.03 \pm 0.03)$, as well as a reduced $\chi^2 \approx 1$ (where $\chi = \frac{\psi_{\text{PROSPECTOR}} - \psi_{\text{H}\alpha}}{\sigma_\psi}$; σ_ψ represents the PROSPECTOR and Hα SFR uncertainties added in quadrature).

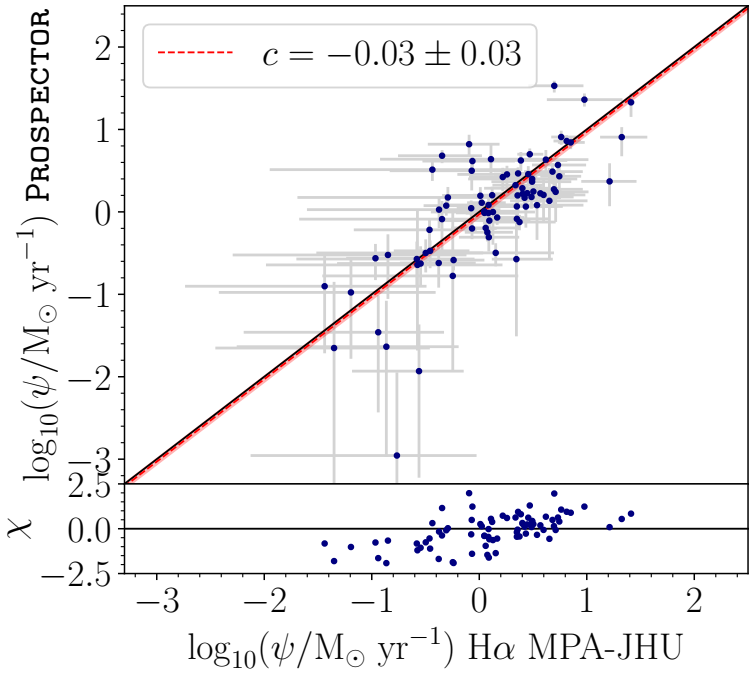

FIGURE A.1: Comparison of PROSPECTOR estimated median likelihood SFRs (averaged over 10 Myrs) with the Balmer corrected Hα SFRs. The solid black line denotes the ideal 1:1 relation. The red dashed line represents the best-fit deviation of the PROSPECTOR estimated SFRs from the Hα SFRs, while the bottom panel shows the difference of the PROSPECTOR SFR estimates of the individual sources from Hα SFRs, in units of the (propagated) uncertainties.

A.2 Star forming main sequence

To further assess the performance of PROSPECTOR, in Figure A.2 we show a comparison between the location of our SWIRE-selected sample in the stellar mass–SFR plane, derived using the PROSPECTOR (top) and MAGPHYS (bottom) SED fits. We focus on the 120,307 sources from the complete SWIRE-selected sample for which PROSPECTOR produced acceptable fits. To produce the PDFs, we follow an approach similar to the one used in Section 2.4.2, wherein we generate 100 samples from the stellar mass and SFR distributions for each source using 50 bins evenly spaced between $7 < \log_{10}(M_\star/M_\odot) < 12$, and $-3 < \log_{10}(\psi/M_\odot\,\mathrm{yr}^{-1}) < 3$, respectively. Sources with $\log_{10}(\psi/M_\odot\ \mathrm{yr}^{-1}) < -3$ were arbitrarily assigned to the lowest log SFR bins. The PDFs shown are derived by summing the individual stellar mass–SFR PDFs over the whole sample.

In both panels we have overlaid a shaded region enclosing the location of the "main sequence" (hereafter MS) expected for star forming galaxies at $0 < z < 1$ using the Schreiber et al. (2015) parameterisation, and converted to our adopted IMF. In each case, a distinct MS is evident, accompanied by a region of quiescent galaxies (i.e. those falling below the main sequence), in

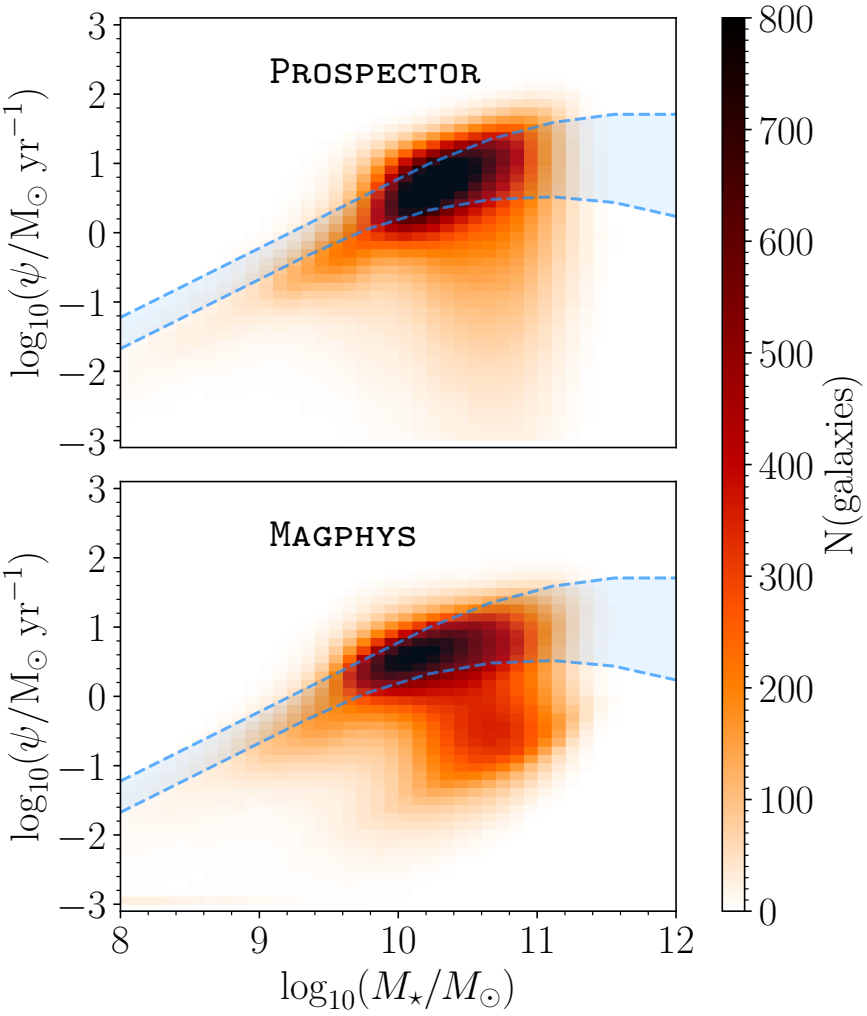

FIGURE A.2: Stellar mass vs SFR plots for ~120,000 SWIRE-selected sources using estimates obtained from PROSPECTOR (top panel) and MAGPHYS (bottom panel) SED fits. The blue shaded region represents the region enclosed by the Schreiber et al. (2015) parametrisation of the main sequence of star forming galaxies between $0 < z < 1$, converted to our adopted Kroupa (2001) IMF.

line with our expectations on the basis of recent literature (e.g. Brinchmann et al., 2004; Daddi et al., 2007; Elbaz et al., 2007; Whitaker et al., 2012). Together with the results in Appendix A.1, these results offer significant encouragement that our PROSPECTOR SED fitting is producing realistic results.

Bibliography

Abazajian, K.N., Adelman-McCarthy, J.K., Agüeros, M.A., et al., 2009. The Seventh Data Release of the Sloan Digital Sky Survey. *The Astrophysical Journal Supplement Series*, 182(2):543.

Abel, T., Bryan, G.L., and Norman, M.L., 2002. The Formation of the First Star in the Universe. *Science*, 295(5552):93.

Abramowicz, M.A., Calvani, M., and Nobili, L., 1980. Thick accretion disks with super-Eddington luminosities. *The Astrophysical Journal*, 242:772.

Aihara, H., Arimoto, N., Armstrong, R., et al., 2018. The Hyper Suprime-Cam SSP Survey: Overview and survey design. *Publications of the Astronomical Society of Japan*, 70:S4.

Alberts, S., Williams, C.C., Helton, J.M., et al., 2024. To High Redshift and Low Mass: Exploring the Emergence of Quenched Galaxies and Their Environments at 3 ¡ z ¡ 6 in the Ultra-deep JADES MIRI F770W Parallel. *The Astrophysical Journal*, 975(1):85.

Alexander, D.M., Bauer, F.E., Chapman, S.C., et al., 2005. The X-Ray Spectral Properties of SCUBA Galaxies. *The Astrophysical Journal*, 632(2):736.

Amaro-Seoane, P., Audley, H., Babak, S., et al., 2017. Laser Interferometer Space Antenna. *arXiv e-prints*, arXiv:1702.00786.

Amorín, R., Pérez-Montero, E., Contini, T., et al., 2015. Extreme emission-line galaxies out to z ~1 in zCOSMOS. I. Sample and characterization of global properties. *Astronomy and Astrophysics*, 578:A105.

Anders, P. and Fritze-v. Alvensleben, U., 2003. Spectral and photometric evolution of young stellar populations: The impact of gaseous emission at various metallicities. *Astronomy and Astrophysics*, 401:1063.

Andrae, R., Schulze-Hartung, T., and Melchior, P., 2010. Dos and don'ts of reduced chi-squared. *arXiv e-prints*, arXiv:1012.3754.

Antonucci, R., 1993. Unified models for active galactic nuclei and quasars. *Annual Review of Astronomy and Astrophysics*, 31:473.

Arnaud, K.A., Branduardi-Raymont, G., Culhane, J.L., et al., 1985. EXOSAT observations of a strong soft X-ray excess in MKN 841. *Monthly Notices of the Royal Astronomical Society*, 217:105.

Arnaudova, M.I., Das, S., Smith, D.J.B., et al., 2024. WEAVE First Light Observations: Origin and Dynamics of the Shock Front in Stephan's Quintet. *Monthly Notices of the Royal Astronomical Society*, 535(3):2269.

Arnaudova, M.I., Smith, D.J.B., Hardcastle, M.J., et al., 2025. The lofar two-metre sky survey deep fields: new probabilistic spectroscopic classifications and the accretion rates of radio galaxies. *Monthly Notices of the Royal Astronomical Society*, page staf1347.

Arnouts, S., Cristiani, S., Moscardini, L., et al., 1999. Measuring and modelling the redshift evolution of clustering: the hubble deep field north. *Monthly Notices of the RAS*, 310(2):540.

Asada, Y., Sawicki, M., Abraham, R., et al., 2024. Bursty star formation and galaxy-galaxy interactions in low-mass galaxies 1 Gyr after the Big Bang. *Monthly Notices of the Royal Astronomical Society*, 527(4):11372.

Asada, Y., Sawicki, M., Desprez, G., et al., 2023. JWST catches the assembly of a z 5 ultra-low-mass galaxy. *Monthly Notices of the Royal Astronomical Society*, 523(1):L40.

Assef, R.J., Stern, D., Noirot, G., et al., 2018. The WISE AGN Catalog. *The Astrophysical Journal Supplement Series*, 234(2):23.

Bañados, E., Venemans, B.P., Morganson, E., et al., 2014. Discovery of Eight z ~6 Quasars from Pan-STARRS1. *The Astronomical Journal*, 148(1):14.

Bacon, R., Maineiri, V., Randich, S., et al., 2024. WST – Widefield Spectroscopic Telescope: Motivation, science drivers and top-level requirements for a new dedicated facility. *arXiv e-prints*, arXiv:2405.12518.

Baldwin, J.A., Phillips, M.M., and Terlevich, R., 1981. Classification parameters for the emission-line spectra of extragalactic objects. *Publications of the Astronomical Society of the Pacific*, 93:5.

Barcons, X., Barret, D., Decourchelle, A., et al., 2012. Athena (Advanced Telescope for High ENergy Astrophysics) Assessment Study Report for ESA Cosmic Vision 2015-2025. *arXiv e-prints*, arXiv:1207.2745.

Barmby, P., Alonso-Herrero, A., Donley, J.L., et al., 2006. Mid-Infrared Properties of X-Ray Sources in the Extended Groth Strip. *The Astrophysical Journal*, 642(1):126.

Barret, D., Decourchelle, A., Fabian, A., et al., 2020. The Athena space X-ray observatory and the astrophysics of hot plasma†. *Astronomische Nachrichten*, 341(2):224.

Barvainis, R., 1987. Hot Dust and the Near-Infrared Bump in the Continuum Spectra of Quasars and Active Galactic Nuclei. *The Astrophysical Journal*, 320:537.

Bassini, L., Feldmann, R., Gensior, J., et al., 2023. The inefficiency of stellar feedback in driving galactic outflows in massive galaxies at high redshift. *Monthly Notices of the Royal Astronomical Society*, 525(4):5388.

Battisti, A.J., da Cunha, E., Grasha, K., et al., 2019. MAGPHYS+photo-z: Constraining the Physical Properties of Galaxies with Unknown Redshifts. *The Astrophysical Journal*, 882(1):61.

Baumann, D., 2009. TASI Lectures on Inflation. *arXiv e-prints*, arXiv:0907.5424.

Becker, R.H., Fan, X., White, R.L., et al., 2001. Evidence for Reionization at z~6: Detection of a Gunn-Peterson Trough in a z=6.28 Quasar. *The Astronomical Journal*, 122(6):2850.

Becker, R.H., White, R.L., and Helfand, D.J., 1994. The VLA's FIRST Survey. In D.R. Crabtree, R.J. Hanisch, and J. Barnes, editors, *Astronomical Data Analysis Software and Systems III*, volume 61 of *Astronomical Society of the Pacific Conference Series*, page 165.

Begelman, M.C. and Rees, M.J., 1978. The fate of dense stellar systems. *Monthly Notices of the Royal Astronomical Society*, 185:847.

Begelman, M.C., Volonteri, M., and Rees, M.J., 2006. Formation of supermassive black holes by direct collapse in pre-galactic haloes. *Monthly Notices of the Royal Astronomical Society*, 370(1):289.

Bell, E.F., 2003. Estimating Star Formation Rates from Infrared and Radio Luminosities: The Origin of the Radio-Infrared Correlation. *Astrophysical Journal*, 586(2):794.

Bell, E.F. and Kennicutt, Robert C., J., 2001. A Comparison of Ultraviolet Imaging Telescope Far-Ultraviolet and Hα Star Formation Rates. *The Astrophysical Journal*, 548(2):681.

Belli, S., Newman, A.B., and Ellis, R.S., 2015. Stellar Populations from Spectroscopy of a Large Sample of Quiescent Galaxies at Z ¿ 1: Measuring the Contribution of Progenitor Bias to Early Size Growth. *The Astrophysical Journal*, 799(2):206.

Bellstedt, S., Robotham, A.S.G., Driver, S.P., et al., 2020. Galaxy And Mass Assembly (GAMA): a forensic SED reconstruction of the cosmic star formation history and metallicity evolution by galaxy type. *Monthly Notices of the RAS*, 498(4):5581.

Bellstedt, S., Robotham, A.S.G., Driver, S.P., et al., 2021. Galaxy and mass assembly (GAMA): the inferred mass-metallicity relation from z = 0 to 3.5 via forensic SED fitting. *Monthly Notices of the RAS*, 503(3):3309.

Bennett, A.S., 1962. The revised 3C catalogue of radio sources. *Memoirs of the Royal Astronomical Society*, 68:163.

Benson, A.J., Bower, R.G., Frenk, C.S., et al., 2003. What Shapes the Luminosity Function of Galaxies? *The Astrophysical Journal*, 599(1):38.

Benson, A.J., Sugiyama, N., Nusser, A., et al., 2006. The epoch of reionization. *Monthly Notices of the Royal Astronomical Society*, 369(3):1055.

Bergström, L., 2000. Non-baryonic dark matter: observational evidence and detection methods. *Reports on Progress in Physics*, 63(5):793.

Berkhuijsen, E.M., Beck, R., and Tabatabaei, F.S., 2013. How cosmic ray electron propagation affects radio-far-infrared correlations in M 31 and M 33. *Monthly Notices of the RAS*, 435(2):1598.

Bertelli, G., Bressan, A., Chiosi, C., et al., 1994. Theoretical isochrones from models with new radiative opacities. *Astronomy and Astrophysics Supplement Series*, 106:275.

Best, P.N. and Heckman, T.M., 2012. On the fundamental dichotomy in the local radio-AGN population: accretion, evolution and host galaxy properties. *Monthly Notices of the Royal Astronomical Society*, 421(2):1569.

Best, P.N., Kauffmann, G., Heckman, T.M., et al., 2005. The host galaxies of radio-loud active galactic nuclei: mass dependences, gas cooling and active galactic nuclei feedback. *Monthly Notices of the Royal Astronomical Society*, 362(1):25.

Best, P.N., Ker, L.M., Simpson, C., et al., 2014. The cosmic evolution of radio-AGN feedback to z = 1. *Monthly Notices of the Royal Astronomical Society*, 445(1):955.

Best, P.N., Kondapally, R., Williams, W.L., et al., 2023. The LOFAR Two-metre Sky Survey Deep Fields Data Release 1: V. Survey description, source classifications and host galaxy properties. *arXiv e-prints*, 523(2):arXiv:2305.05782.

Best, P.N., Röttgering, H.J.A., and Lehnert, M.D., 1999. A 98 per cent spectroscopically complete sample of the most powerful equatorial radio sources at 408MHz. *Monthly Notices of the Royal Astronomical Society*, 310(1):223.

Blain, A.W., Smail, I., Ivison, R.J., et al., 2002. Submillimeter galaxies. *Physics Reports*, 369(2):111.

Blandford, R.D. and Payne, D.G., 1982. Hydromagnetic flows from accretion disks and the production of radio jets. *Monthly Notices of the Royal Astronomical Society*, 199:883.

Blandford, R.D. and Znajek, R.L., 1977. Electromagnetic extraction of energy from Kerr black holes. *Monthly Notices of the Royal Astronomical Society*, 179:433.

Blumenthal, G.R., Faber, S.M., Primack, J.R., et al., 1984. Formation of galaxies and large-scale structure with cold dark matter. *Nature*, 311:517.

Blumenthal, G.R. and Gould, R.J., 1970. Bremsstrahlung, Synchrotron Radiation, and Compton Scattering of High-Energy Electrons Traversing Dilute Gases. *Reviews of Modern Physics*, 42(2):237.

Bolton, A.S., Schlegel, D.J., Aubourg, É., et al., 2012. Spectral Classification and Redshift Measurement for the SDSS-III Baryon Oscillation Spectroscopic Survey. *The Astronomical Journal*, 144(5):144.

Bondi, M., Scaramella, R., Zamorani, G., et al., 2024. LOFAR HBA observations of the Euclid Deep Field North (EDFN). *Astronomy and Astrophysics*, 683:A179.

Bonzini, M., Padovani, P., Mainieri, V., et al., 2013. The sub-mJy radio sky in the Extended Chandra Deep Field-South: source population. *Monthly Notices of the Royal Astronomical Society*, 436(4):3759.

Boquien, M., Buat, V., Burgarella, D., et al., 2022. The ALPINE-ALMA [C II] survey. Dust attenuation curves at z = 4.4-5.5. *Astronomy and Astrophysics*, 663:A50.

Boquien, M., Burgarella, D., Roehlly, Y., et al., 2019. CIGALE: a python Code Investigating GALaxy Emission. *Astronomy and Astrophysics*, 622:A103.

Boselli, A. and Gavazzi, G., 2006. Environmental Effects on Late-Type Galaxies in Nearby Clusters. *Publications of the Astronomical Society of the Pacific*, 118(842):517.

Bourne, N., Dunne, L., Ivison, R.J., et al., 2011. Evolution of the far-infrared-radio correlation and infrared spectral energy distributions of massive galaxies over z= 0-2. *Monthly Notices of the Royal Astronomical Society*, 410(2):1155.

Bower, R.G., Benson, A.J., Malbon, R., et al., 2006. Breaking the hierarchy of galaxy formation. *Monthly Notices of the Royal Astronomical Society*, 370(2):645.

Boyett, K., Mascia, S., Pentericci, L., et al., 2022. Early Results from GLASS-JWST. VI. Extreme Rest-optical Equivalent Widths Detected in NIRISS Wide Field Slitless Spectroscopy. *The Astrophysical Journal*, 940(2):L52.

Bressan, A., Marigo, P., Girardi, L., et al., 2012. PARSEC: stellar tracks and isochrones with the PAdova and TRieste Stellar Evolution Code. *Monthly Notices of the Royal Astronomical Society*, 427(1):127.

Bridle, A.H. and Perley, R.A., 1984. Extragalactic Radio Jets. *Annual Review of Astronomy and Astrophysics*, 22:319.

Brinchmann, J., Charlot, S., White, S.D.M., et al., 2004. The physical properties of star-forming galaxies in the low-redshift Universe. *Monthly Notices of the Royal Astronomical Society*, 351(4):1151.

Bromm, V., Ferrara, A., Coppi, P.S., et al., 2001. The fragmentation of pre-enriched primordial objects. *Monthly Notices of the Royal Astronomical Society*, 328(3):969.

Bromm, V. and Larson, R.B., 2004. The First Stars. *Annual Review of Astronomy and Astrophysics*, 42(1):79.

Bromm, V. and Yoshida, N., 2011. The First Galaxies. *Annual Review of Astronomy and Astrophysics*, 49(1):373.

Bromm, V., Yoshida, N., Hernquist, L., et al., 2009. The formation of the first stars and galaxies. *Nature*, 459(7243):49.

Brookes, M.H., Best, P.N., Peacock, J.A., et al., 2008. A Combined EIS-NVSS Survey Of Radio Sources (CENSORS) - III. Spectroscopic observations. *Monthly Notices of the Royal Astronomical Society*, 385(3):1297.

Broussard, A., Gawiser, E., Iyer, K., et al., 2019. Star formation stochasticity measured from the distribution of burst indicators. *Astrophysical Journal*, 873(1):74.

Brown, M.J.I., Moustakas, J., Kennicutt, R.C., et al., 2017. Calibration of Ultraviolet, Mid-infrared, and Radio Star Formation Rate Indicators. *The Astrophysical Journal*, 847(2):136.

Brown, M.J.I., Moustakas, J., Smith, J.D.T., et al., 2014. An Atlas of Galaxy Spectral Energy Distributions from the Ultraviolet to the Mid-infrared. *The Astrophysical Journal Supplement Series*, 212(2):18.

Bruzual, G. and Charlot, S., 2003. Stellar population synthesis at the resolution of 2003. *Monthly Notices of the Royal Astronomical Society*, 344(4):1000.

Bruzual A., G., 1983. Spectral evolution of galaxies. I. Early-type systems. *The Astrophysical Journal*, 273:105.

Bruzual A., G. and Charlot, S., 1993. Spectral Evolution of Stellar Populations Using Isochrone Synthesis. *The Astrophysical Journal*, 405:538.

Buat, V., Boissier, S., Burgarella, D., et al., 2008. Star formation history of galaxies from z = 0 to z = 0.7. A backward approach to the evolution of star-forming galaxies. *Astronomy and Astrophysics*, 483(1):107.

Bull, P., Akrami, Y., Adamek, J., et al., 2016. Beyond Λ CDM: Problems, solutions, and the road ahead. *Physics of the Dark Universe*, 12:56.

Bullock, J.S. and Boylan-Kolchin, M., 2017. Small-Scale Challenges to the ΛCDM Paradigm. *Annual Review of Astronomy and Astrophysics*, 55(1):343.

Buttiglione, S., Capetti, A., Celotti, A., et al., 2009. An optical spectroscopic survey of the 3CR sample of radio galaxies with z ¡ 0.3. I. Presentation of the data. *Astronomy and Astrophysics*, 495(3):1033.

Byler, N., Dalcanton, J.J., Conroy, C., et al., 2017. Nebular Continuum and Line Emission in Stellar Population Synthesis Models. *The Astrophysical Journal*, 840(1):44.

Byrne, C.M. and Stanway, E.R., 2023. On the impact of spectral template uncertainties in synthetic stellar populations. *Monthly Notices of the Royal Astronomical Society*, 521(4):4995.

Calistro Rivera, G., Lusso, E., Hennawi, J.F., et al., 2016. AGNfitter: A Bayesian MCMC Approach to Fitting Spectral Energy Distributions of AGNs. *The Astrophysical Journal*, 833(1):98.

Calistro Rivera, G., Williams, W.L., Hardcastle, M.J., et al., 2017. The LOFAR window on star-forming galaxies and AGNs - curved radio SEDs and IR-radio correlation at 0¡z¡2.5. *Monthly Notices of the Royal Astronomical Society*, 469(3):3468.

Calzetti, D., 2001. The Dust Opacity of Star-forming Galaxies. *Publications of the Astronomical Society of the Pacific*, 113(790):1449.

Calzetti, D., 2013. Star Formation Rate Indicators. In J. Falcón-Barroso and J.H. Knapen, editors, *Secular Evolution of Galaxies*, page 419. Cambridge University Press.

Calzetti, D., Armus, L., Bohlin, R.C., et al., 2000. The dust content and opacity of actively star-forming galaxies. *Astrophysical Journal*, 533(2):682.

Cameron, A.J., Katz, H., Witten, C., et al., 2024. Nebular dominated galaxies: insights into the stellar initial mass function at high redshift. *Monthly Notices of the Royal Astronomical Society*, 534(1):523.

Cameron, E., 2011. On the Estimation of Confidence Intervals for Binomial Population Proportions in Astronomy: The Simplicity and Superiority of the Bayesian Approach. *Publications of the Astronomical Society of Australia*, 28(2):128.

Cano-Díaz, M., Ávila-Reese, V., Sánchez, S.F., et al., 2019. SDSS-IV MaNGA: effects of morphology in the global and local star formation main sequences. *Monthly Notices of the Royal Astronomical Society*, 488(3):3929.

Caputi, K.I., Deshmukh, S., Ashby, M.L.N., et al., 2017. Star Formation in Galaxies at z $\sim$ 4-5 from the SMUVS Survey: A Clear Starburst/Main-sequence Bimodality for Hα Emitters on the SFR-M* Plane. *The Astrophysical Journal*, 849(1):45.

Carnall, A.C., Leja, J., Johnson, B.D., et al., 2019. How to Measure Galaxy Star Formation Histories. I. Parametric Models. *The Astrophysical Journal*, 873(1):44.

Carnall, A.C., McLure, R.J., Dunlop, J.S., et al., 2018. Inferring the star formation histories of massive quiescent galaxies with BAGPIPES: evidence for multiple quenching mechanisms. *Monthly Notices of the Royal Astronomical Society*, 480(4):4379.

Carter, D., Smith, D.J.B., Percival, S.M., et al., 2009. Optical and near-infrared colours as a discriminant of the age and metallicity of stellar populations. *Monthly Notices of the RAS*, 397(2):695.

Casey, C.M., Chapman, S.C., Muxlow, T.W.B., et al., 2009. Constraining star formation and AGN in z ~2 massive galaxies using high-resolution MERLIN radio observations. *Monthly Notices of the Royal Astronomical Society*, 395(3):1249.

Cen, R. and Kimm, T., 2014. Infrared Properties of z = 7 Galaxies from Cosmological Simulations. *The Astrophysical Journal*, 782(1):32.

Ceverino, D. and Klypin, A., 2009. The Role of Stellar Feedback in the Formation of Galaxies. *The Astrophysical Journal*, 695(1):292.

Chabrier, G., 2003. Galactic Stellar and Substellar Initial Mass Function. *Publications of the Astronomical Society of the Pacific*, 115(809):763.

Chambers, K.C., Magnier, E.A., Metcalfe, N., et al., 2016. The Pan-STARRS1 Surveys. *arXiv e-prints*, 231:arXiv:1612.05560.

Chang, Y.Y., Le Floc'h, E., Juneau, S., et al., 2017. Infrared Selection of Obscured Active Galactic Nuclei in the COSMOS Field. *The Astrophysical Journal Supplement Series*, 233(2):19.

Charlot, S. and Bruzual A, G., 1991. Stellar Population Synthesis Revisited. *The Astrophysical Journal*, 367:126.

Charlot, S. and Fall, S.M., 2000. A Simple Model for the Absorption of Starlight by Dust in Galaxies. *The Astrophysical Journal*, 539(2):718.

Chary, R. and Elbaz, D., 2001. Interpreting the Cosmic Infrared Background: Constraints on the Evolution of the Dust-enshrouded Star Formation Rate. *The Astrophysical Journal*, 556(2):562.

Chen, Y., Trager, S., Peletier, R., et al., 2011. XSL: The X-Shooter Spectral Library. In *Journal of Physics Conference Series*, volume 328 of *Journal of Physics Conference Series*, page 012023. IOP.

Chevallard, J. and Charlot, S., 2016. Modelling and interpreting spectral energy distributions of galaxies with BEAGLE. *Monthly Notices of the Royal Astronomical Society*, 462(2):1415.

Choi, J., Dotter, A., Conroy, C., et al., 2016. Mesa Isochrones and Stellar Tracks (MIST). I. Solar-scaled Models. *The Astrophysical Journal*, 823(2):102.

Ciardi, B. and Ferrara, A., 2005. The First Cosmic Structures and Their Effects. *Space Science Reviews*, 116(3-4):625.

Cid Fernandes, R., Mateus, A., Sodré, L., et al., 2005. Semi-empirical analysis of Sloan Digital Sky Survey galaxies - I. Spectral synthesis method. *Monthly Notices of the Royal Astronomical Society*, 358(2):363.

Cid Fernandes, R., Stasińska, G., Schlickmann, M.S., et al., 2010. Alternative diagnostic diagrams and the 'forgotten' population of weak line galaxies in the SDSS. *Monthly Notices of the Royal Astronomical Society*, 403(2):1036.

Ciesla, L., Charmandaris, V., Georgakakis, A., et al., 2015. Constraining the properties of AGN host galaxies with spectral energy distribution modelling. *Astronomy and Astrophysics*, 576:A10.

Ciesla, L., Gómez-Guijarro, C., Buat, V., et al., 2023. GOODS-ALMA 2.0: Last gigayear star formation histories of the so-called starbursts within the main sequence. *Astronomy and Astrophysics*, 672:A191.

Cimatti, A., Bianchi, S., Ferrara, A., et al., 1997. On the dust extinction in high-z galaxies and the case of extremely red objects. *Monthly Notices of the RAS*, 290(3):L43.

Cimatti, A., Fraternali, F., and Nipoti, C., 2020. *Introduction to galaxy formation and evolution: from primordial gas to present-day galaxies*. Cambridge University Press.

Cirasuolo, M. and MOONS Consortium, 2016. MOONS: A New Powerful Multi-Object Spectrograph for the VLT. In I. Skillen, M. Balcells, and S. Trager, editors, *Multi-Object Spectroscopy in the Next Decade: Big Questions, Large Surveys, and Wide Fields*, volume 507 of *Astronomical Society of the Pacific Conference Series*, page 109.

Clark, P.C., Glover, S.C.O., Klessen, R.S., et al., 2011a. Gravitational Fragmentation in Turbulent Primordial Gas and the Initial Mass Function of Population III Stars. *The Astrophysical Journal*, 727(2):110.

Clark, P.C., Glover, S.C.O., Smith, R.J., et al., 2011b. The Formation and Fragmentation of Disks Around Primordial Protostars. *Science*, 331(6020):1040.

Clarke, L., Shapley, A.E., Sanders, R.L., et al., 2024. The Star-forming Main Sequence in JADES and CEERS at z ¿ 1.4: Investigating the Burstiness of Star Formation. *The Astrophysical Journal*, 977(1):133.

Cochrane, R.K., Katz, H., Begley, R., et al., 2024. High-z stellar masses can be recovered robustly with JWST photometry. *arXiv e-prints*, arXiv:2412.02622.

Cochrane, R.K., Kondapally, R., Best, P.N., et al., 2023. The LOFAR Two-metre Sky Survey: the radio view of the cosmic star formation history. *Monthly Notices of the Royal Astronomical Society*, 523(4):6082.

Coelho, P., Barbuy, B., Meléndez, J., et al., 2005. A library of high resolution synthetic stellar spectra from 300 nm to 1.8 μm with solar and α-enhanced composition. *Astronomy and Astrophysics*, 443(2):735.

Coelho, P., Bruzual, G., Charlot, S., et al., 2007. Spectral models for solar-scaled and α-enhanced stellar populations. *Monthly Notices of the Royal Astronomical Society*, 382(2):498.

Collinson, J.S., Ward, M.J., Landt, H., et al., 2017. Reaching the peak of the quasar spectral energy distribution - II. Exploring the accretion disc, dusty torus and host galaxy. *Monthly Notices of the Royal Astronomical Society*, 465(1):358.

Comerford, J.M., Negus, J., Barrows, R.S., et al., 2022. Toward a More Complete Optical Census of Active Galactic Nuclei via Spatially Resolved Spectroscopy. *The Astrophysical Journal*, 927(1):23.

Condon, J.J., 1989. The 1.4 GHz Luminosity Function and Its Evolution. *The Astrophysical Journal*, 338:13.

Condon, J.J., 1992. Radio emission from normal galaxies. *Annual Review of Astronomy and Astrophysics*, 30:575.

Condon, J.J., 1996. Radio Luminosity Functions (Review). In R.D. Ekers, C. Fanti, and L. Padrielli, editors, *Extragalactic Radio Sources*, volume 175 of *IAU Symposium*, page 535.

Condon, J.J., 1999. Very Large Radio Surveys of the Sky. *Proceedings of the National Academy of Science*, 96(9):4756.

Condon, J.J., Cotton, W.D., Greisen, E.W., et al., 1998. The NRAO VLA Sky Survey. *The Astronomical Journal*, 115(5):1693.

Condon, J.J. and Mitchell, K.J., 1984. A deeper VLA survey of the alf = 08h52m15s, del = +17 16 field. *The Astronomical Journal*, 89:610.

Condon, J.J. and Ransom, S.M., 2016. *Essential Radio Astronomy*. Princeton University Press.

Conroy, C., 2013. Modeling the panchromatic spectral energy distributions of galaxies. *Annual Review of Astron and Astrophys*, 51(1):393.

Conroy, C., Gunn, J.E., and White, M., 2009. The Propagation of Uncertainties in Stellar Population Synthesis Modeling. I. The Relevance of Uncertain Aspects of Stellar Evolution and the Initial Mass Function to the Derived Physical Properties of Galaxies. *The Astrophysical Journal*, 699(1):486.

Cortese, L., Catinella, B., and Smith, R., 2021. The Dawes Review 9: The role of cold gas stripping on the star formation quenching of satellite galaxies. *Publications of the Astronomical Society of Australia*, 38:e035.

Cram, L., Hopkins, A., Mobasher, B., et al., 1998. Star Formation Rates in Faint Radio Galaxies. *The Astrophysical Journal*, 507(1):155.

Cranmer, K., Brehmer, J., and Louppe, G., 2020. The frontier of simulation-based inference. *Proceedings of the National Academy of Science*, 117(48):30055.

Croton, D.J., Springel, V., White, S.D.M., et al., 2006. The many lives of active galactic nuclei: cooling flows, black holes and the luminosities and colours of galaxies. *Monthly Notices of the Royal Astronomical Society*, 365(1):11.

Crummy, J., Fabian, A.C., Gallo, L., et al., 2006. An explanation for the soft X-ray excess in active galactic nuclei. *Monthly Notices of the Royal Astronomical Society*, 365(4):1067.

da Cunha, E., Charlot, S., and Elbaz, D., 2008. A simple model to interpret the ultraviolet, optical and infrared emission from galaxies. *Monthly Notices of the Royal Astronomical Society*, 388(4):1595.

da Cunha, E., Walter, F., Smail, I.R., et al., 2015. An ALMA Survey of Sub-millimeter Galaxies in the Extended Chandra Deep Field South: Physical Properties Derived from Ultraviolet-to-radio Modeling. *The Astrophysical Journal*, 806(1):110.

Daddi, E., Dickinson, M., Morrison, G., et al., 2007. Multiwavelength Study of Massive Galaxies at z~2. I. Star Formation and Galaxy Growth. *The Astrophysical Journal*, 670(1):156.

Dale, D.A., Helou, G., Contursi, A., et al., 2001. The Infrared Spectral Energy Distribution of Normal Star-forming Galaxies. *The Astrophysical Journal*, 549(1):215.

Dale, J.E., 2015. The modelling of feedback in star formation simulations. *New Astronomy Review*, 68:1.

Dalton, G., 2016. WEAVE: The Next Generation Spectroscopy Facility for the WHT. In I. Skillen, M. Balcells, and S. Trager, editors, *Multi-Object Spectroscopy in the Next Decade: Big Questions, Large Surveys, and Wide Fields*, volume 507 of *Astronomical Society of the Pacific Conference Series*, page 97.

Dalton, G., Trager, S.C., Abrams, D.C., et al., 2012. WEAVE: the next generation wide-field spectroscopy facility for the William Herschel Telescope. In I.S. McLean, S.K. Ramsay, and H. Takami, editors, *Ground-based and Airborne Instrumentation for Astronomy IV*, volume 8446 of *Society of Photo-Optical Instrumentation Engineers (SPIE) Conference Series*, page 84460P.

Das, S., Kharb, P., Morganti, R., et al., 2021. The peculiar WAT NGC 2329 with Seyfert/FR I-like radio lobes. *Monthly Notices of the Royal Astronomical Society*, 504(3):4416.

Das, S., Smith, D.J.B., Haskell, P., et al., 2024. The lofar two-metre sky survey: The nature of the faint source population and sfr-radio luminosity relation using prospector. *Monthly Notices of the Royal Astronomical Society*, 531(1):977.

Davé, R., Finlator, K., and Oppenheimer, B.D., 2012. An analytic model for the evolution of the stellar, gas and metal content of galaxies. *Monthly Notices of the Royal Astronomical Society*, 421(1):98.

Davies, L.J.M., Huynh, M.T., Hopkins, A.M., et al., 2017. Galaxy And Mass Assembly: the 1.4 GHz SFR indicator, SFR-M_* relation and predictions for ASKAP-GAMA. *Monthly Notices of the Royal Astronomical Society*, 466(2):2312.

Davis, M., Efstathiou, G., Frenk, C.S., et al., 1985. The evolution of large-scale structure in a universe dominated by cold dark matter. *The Astrophysical Journal*, 292:371.

de Gasperin, F., Williams, W.L., Best, P., et al., 2021. The LOFAR LBA Sky Survey. I. Survey description and preliminary data release. *Astronomy and Astrophysics*, 648:A104.

de Jong, R.S., Agertz, O., Berbel, A.A., et al., 2019. 4MOST: Project overview and information for the First Call for Proposals. *The Messenger*, 175:3.

de Jong, R.S., Bellido-Tirado, O., Chiappini, C., et al., 2012. 4MOST: 4-metre multi-object spectroscopic telescope. In I.S. McLean, S.K. Ramsay, and H. Takami, editors, *Ground-based and Airborne Instrumentation for Astronomy IV*, volume 8446 of *Society of Photo-Optical Instrumentation Engineers (SPIE) Conference Series*, page 84460T.

de Jong, T., Klein, U., Wielebinski, R., et al., 1985. Radio continuum and far-infrared emission from spiral galaxies : a close correlation. *Astronomy and Astrophysics*, 147:L6.

De Lucia, G. and Blaizot, J., 2007. The hierarchical formation of the brightest cluster galaxies. *Monthly Notices of the Royal Astronomical Society*, 375(1):2.

de Souza, R.S., Dantas, M.L.L., Costa-Duarte, M.V., et al., 2017. A probabilistic approach to emission-line galaxy classification. *Monthly Notices of the Royal Astronomical Society*, 472(3):2808.

de Zotti, G., Massardi, M., Negrello, M., et al., 2010. Radio and millimeter continuum surveys and their astrophysical implications. *Astronomy and Astrophysics Review*, 18(1-2):1.

Dekel, A., Birnboim, Y., Engel, G., et al., 2009. Cold streams in early massive hot haloes as the main mode of galaxy formation. *Nature*, 457(7228):451.

Delhaize, J., Smolčić, V., Delvecchio, I., et al., 2017. The VLA-COSMOS 3 GHz Large Project: The infrared-radio correlation of star-forming galaxies and AGN to $z \lesssim 6$. *Astronomy and Astrophysics*, 602:A4.

Delvecchio, I., Daddi, E., Sargent, M.T., et al., 2021. The infrared-radio correlation of star-forming galaxies is strongly $M_\star$-dependent but nearly redshift-invariant since $z \sim 4$. *Astronomy and Astrophysics*, 647:A123.

DESI Collaboration, Abareshi, B., Aguilar, J., et al., 2022. Overview of the Instrumentation for the Dark Energy Spectroscopic Instrument. *The Astronomical Journal*, 164(5):207.

DESI Collaboration, Abdul-Karim, M., Adame, A.G., et al., 2025. Data Release 1 of the Dark Energy Spectroscopic Instrument. *arXiv e-prints*, arXiv:2503.14745.

DESI Collaboration, Adame, A.G., Aguilar, J., et al., 2024. The Early Data Release of the Dark Energy Spectroscopic Instrument. *The Astronomical Journal*, 168(2):58.

DESI Collaboration, Aghamousa, A., Aguilar, J., et al., 2016a. The DESI Experiment Part I: Science,Targeting, and Survey Design. *arXiv e-prints*, arXiv:1611.00036.

DESI Collaboration, Aghamousa, A., Aguilar, J., et al., 2016b. The DESI Experiment Part II: Instrument Design. *arXiv e-prints*, arXiv:1611.00037.

Devecchi, B. and Volonteri, M., 2009. Formation of the First Nuclear Clusters and Massive Black Holes at High Redshift. *The Astrophysical Journal*, 694(1):302.

Dewdney, P.E., Hall, P.J., Schilizzi, R.T., et al., 2009. The Square Kilometre Array. *IEEE Proceedings*, 97(8):1482.

Dey, A., Schlegel, D.J., Lang, D., et al., 2019. Overview of the DESI Legacy Imaging Surveys. *The Astronomical Journal*, 157(5):168.

Dey, S., Goyal, A., Małek, K., et al., 2022. Low-frequency Radio Continuum Imaging and SED Modeling of 11 LIRGs: Radio-only and FUV to Radio Bands. *The Astrophysical Journal*, 938(2):152.

Diemer, B., Sparre, M., Abramson, L.E., et al., 2017. Log-normal Star Formation Histories in Simulated and Observed Galaxies. *The Astrophysical Journal*, 839(1):26.

Dome, T., Tacchella, S., Fialkov, A., et al., 2024. Mini-quenching of z = 4-8 galaxies by bursty star formation. *Monthly Notices of the RAS*, 527(2):2139.

Domínguez, A., Siana, B., Brooks, A.M., et al., 2015. Consequences of bursty star formation on galaxy observables at high redshifts. *Monthly Notices of the Royal Astronomical Society*, 451(1):839.

Domínguez, A., Siana, B., Henry, A.L., et al., 2013. Dust Extinction from Balmer Decrements of Star-forming Galaxies at 0.75 ¡= z ¡= 1.5 with Hubble Space Telescope/Wide-Field-Camera 3 Spectroscopy from the WFC3 Infrared Spectroscopic Parallel Survey. *The Astrophysical Journal*, 763(2):145.

Done, C., Davis, S.W., Jin, C., et al., 2012. Intrinsic disc emission and the soft X-ray excess in active galactic nuclei. *Monthly Notices of the Royal Astronomical Society*, 420(3):1848.

Donley, J.L., Koekemoer, A.M., Brusa, M., et al., 2012. Identifying Luminous Active Galactic Nuclei in Deep Surveys: Revised IRAC Selection Criteria. *Astrophysical Journal*, 748(2):142.

Dotter, A., 2016. MESA Isochrones and Stellar Tracks (MIST) 0: Methods for the Construction of Stellar Isochrones. *The Astrophysical Journal Supplement Series*, 222(1):8.

Draine, B.T., 2003. Interstellar Dust Grains. *Annual Review of Astronomy and Astrophysics*, 41:241.

Draine, B.T. and Lee, H.M., 1984. Optical Properties of Interstellar Graphite and Silicate Grains. *The Astrophysical Journal*, 285:89.

Draine, B.T. and Li, A., 2001. Infrared Emission from Interstellar Dust. I. Stochastic Heating of Small Grains. *The Astrophysical Journal*, 551(2):807.

Draine, B.T. and Li, A., 2007. Infrared Emission from Interstellar Dust. IV. The Silicate-Graphite-PAH Model in the Post-Spitzer Era. *The Astrophysical Journal*, 657(2):810.

Drake, A.B., Smith, D.J.B., Hardcastle, M.J., et al., 2024. The LOFAR two metre sky survey data release 2: probabilistic spectral source classifications and faint radio source demographics. *Monthly Notices of the RAS*, 534(2):1107.

Dressler, A., Rieke, M., Eisenstein, D., et al., 2024. Building the First Galaxies—Chapter 2. Starbursts Dominate the Star Formation Histories of 6 ¡ z ¡ 12 Galaxies. *The Astrophysical Journal*, 964(2):150.

Driver, S.P., Davies, L.J., Meyer, M., et al., 2016. The Wide Area VISTA Extra-Galactic Survey (WAVES). In N.R. Napolitano, G. Longo, M. Marconi, M. Paolillo, and E. Iodice, editors, *The Universe of Digital Sky Surveys*, volume 42 of *Astrophysics and Space Science Proceedings*, page 205.

Driver, S.P., Liske, J., Davies, L.J.M., et al., 2019. 4MOST Consortium Survey 7: Wide-Area VISTA Extragalactic Survey (WAVES). *The Messenger*, 175:46.

Duncan, K., Baker, A., Best, P., et al., 2023. Optical, Radio Continuum and HI Deep Spectroscopic Survey (ORCHIDSS). *The Messenger*, 190:25.

Duncan, K., Conselice, C.J., Mortlock, A., et al., 2014. The mass evolution of the first galaxies: stellar mass functions and star formation rates at 4 ¡ z ¡ 7 in the CANDELS GOODS-South field. *Monthly Notices of the Royal Astronomical Society*, 444(3):2960.

Duncan, K.J., Kondapally, R., Brown, M.J.I., et al., 2021. The LOFAR Two-meter Sky Survey: Deep Fields Data Release 1. IV. Photometric redshifts and stellar masses. *Astronomy and Astrophysics*, 648:A4.

Eddington, A.S., 1921. Das Strahlungsgleichgewicht der Sterne. *Zeitschrift fur Physik*, 7(1):351.

Edge, D.O., Shakeshaft, J.R., McAdam, W.B., et al., 1959. A survey of radio sources at a frequency of 159 Mc/s. *Memoirs of the Royal Astronomical Society*, 68:37.

Eisenstein, D.J., Willott, C., Alberts, S., et al., 2023. Overview of the JWST Advanced Deep Extragalactic Survey (JADES). *arXiv e-prints*, arXiv:2306.02465.

Elbaz, D., Daddi, E., Le Borgne, D., et al., 2007. The reversal of the star formation-density relation in the distant universe. *Astronomy and Astrophysics*, 468(1):33.

Eldridge, J.J., Stanway, E.R., Xiao, L., et al., 2017. Binary Population and Spectral Synthesis Version 2.1: Construction, Observational Verification, and New Results. *Publications of the Astronomical Society of Australia*, 34:e058.

Elmegreen, D.M., Elmegreen, B.G., Ravindranath, S., et al., 2007. Resolved Galaxies in the Hubble Ultra Deep Field: Star Formation in Disks at High Redshift. *The Astrophysical Journal*, 658(2):763.

Elvis, M., Wilkes, B.J., McDowell, J.C., et al., 1994. Atlas of Quasar Energy Distributions. *The Astrophysical Journal Supplement Series*, 95:1.

Emami, N., Siana, B., Weisz, D.R., et al., 2019. A Closer Look at Bursty Star Formation with L $_{H\alpha}$ and L $_{UV}$ Distributions. *The Astrophysical Journal*, 881(1):71.

Endsley, R., Stark, D.P., Chevallard, J., et al., 2021. The [O III]+H β equivalent width distribution at z $\simeq$ 7: implications for the contribution of galaxies to reionization. *Monthly Notices of the Royal Astronomical Society*, 500(4):5229.

Endsley, R., Stark, D.P., Whitler, L., et al., 2023. A JWST/NIRCam study of key contributors to reionization: the star-forming and ionizing properties of UV-faint z 7-8 galaxies. *Monthly Notices of the Royal Astronomical Society*, 524(2):2312.

Endsley, R., Stark, D.P., Whitler, L., et al., 2024. The star-forming and ionizing properties of dwarf z 6-9 galaxies in JADES: insights on bursty star formation and ionized bubble growth. *Monthly Notices of the Royal Astronomical Society*, 533(1):1111.

Erb, D.K., Shapley, A.E., Steidel, C.C., et al., 2003. Hα Spectroscopy of Galaxies at z ¿ 2: Kinematics and Star Formation. *The Astrophysical Journal*, 591(1):101.

Euclid Collaboration, Scaramella, R., Amiaux, J., et al., 2022. Euclid preparation. I. The Euclid Wide Survey. *Astronomy and Astrophysics*, 662:A112.

Evans, D.A., Worrall, D.M., Hardcastle, M.J., et al., 2006. Chandra and xmm-newton observations of a sample of low-redshift fr i and fr ii radio galaxy nuclei. *The Astrophysical Journal*, 642(1):96.

Faber, S.M., 1972. Quadratic programming applied to the problem of galaxy population synthesis. *Astronomy and Astrophysics*, 20:361.

Fabian, A.C., 2012. Observational Evidence of Active Galactic Nuclei Feedback. *Annual Review of Astronomy and Astrophysics*, 50:455.

Fabian, A.C., Lohfink, A., Kara, E., et al., 2015. Properties of AGN coronae in the NuSTAR era. *Monthly Notices of the Royal Astronomical Society*, 451(4):4375.

Faisst, A.L., Capak, P.L., Emami, N., et al., 2019. The Recent Burstiness of Star Formation in Galaxies at z $\sim$ 4.5 from Hα Measurements. *The Astrophysical Journal*, 884(2):133.

Fan, X., Carilli, C.L., and Keating, B., 2006a. Observational Constraints on Cosmic Reionization. *Annual Review of Astronomy and Astrophysics*, 44(1):415.

Fan, X., Strauss, M.A., Richards, G.T., et al., 2006b. A Survey of z¿5.7 Quasars in the Sloan Digital Sky Survey. IV. Discovery of Seven Additional Quasars. *The Astronomical Journal*, 131(3):1203.

Fanaroff, B., Lal, D.V., Venturi, T., et al., 2021. A new look at old friends - I. Imaging classical radio galaxies with uGMRT and MeerKAT. *Monthly Notices of the Royal Astronomical Society*, 505(4):6003.

Fanaroff, B.L. and Riley, J.M., 1974. The morphology of extragalactic radio sources of high and low luminosity. *Monthly Notices of the Royal Astronomical Society*, 167:31P.

Faucher-Giguère, C.A., 2018. A model for the origin of bursty star formation in galaxies. *Monthly Notices of the RAS*, 473(3):3717.

Fazio, G.G., Hora, J.L., Allen, L.E., et al., 2004. The infrared array camera (irac) for the spitzer space telescope. *Astrophysical Journal, Supplement*, 154(1):10.

Feltre, A., Hatziminaoglou, E., Fritz, J., et al., 2012. Smooth and clumpy dust distributions in AGN: a direct comparison of two commonly explored infrared emission models. *Monthly Notices of the Royal Astronomical Society*, 426(1):120.

Ferland, G.J., Chatzikos, M., Guzmán, F., et al., 2017. The 2017 Release Cloudy. *Revista Mexicana de Astronomia y Astrofisica*, 53:385.

Ferland, G.J., Porter, R.L., van Hoof, P.A.M., et al., 2013. The 2013 Release of Cloudy. *Revista Mexicana de Astronomia y Astrofisica*, 49:137.

Ferrara, A. and Tolstoy, E., 2000. The role of stellar feedback and dark matter in the evolution of dwarf galaxies. *Monthly Notices of the Royal Astronomical Society*, 313(2):291.

Filippenko, A.V., Ho, L.C., and Sargent, W.L.W., 1993. HST Observations of NGC 4395, the Least Luminous Seyfert 1 Nucleus: Evidence against the Starburst Hypothesis for Broad-lined Active Galactic Nuclei. *The Astrophysical Journal*, 410:L75.

Finkelstein, S.L., Dickinson, M., Ferguson, H.C., et al., 2017. The Cosmic Evolution Early Release Science (CEERS) Survey. JWST Proposal ID 1345. Cycle 0 Early Release Science.

Finkelstein, S.L., Leung, G.C.K., Bagley, M.B., et al., 2024. The Complete CEERS Early Universe Galaxy Sample: A Surprisingly Slow Evolution of the Space Density of Bright Galaxies at z $\sim$ 8.5–14.5. *The Astrophysical Journal*, 969(1):L2.

Fisher, R., Bowler, R.A.A., Stefanon, M., et al., 2025. REBELS-IFU: dust attenuation curves of 12 massive galaxies at z $\simeq$ 7. *Monthly Notices of the Royal Astronomical Society*, 539(1):109.

Fixsen, D.J., 2009. The Temperature of the Cosmic Microwave Background. *The Astrophysical Journal*, 707(2):916.

Flores Velázquez, J.A., Gurvich, A.B., Faucher-Giguère, C.A., et al., 2021. The time-scales probed by star formation rate indicators for realistic, bursty star formation histories from the fire simulations. *Monthly Notices of the RAS*, 501(4):4812.

Foreman-Mackey, D., Hogg, D.W., Lang, D., et al., 2013. emcee: The MCMC Hammer. *Publications of the Astronomical Society of the Pacific*, 125(925):306.

Frank, J., King, A., and Raine, D.J., 2002. *Accretion Power in Astrophysics: Third Edition*. Cambridge University Press.

Fritz, J., Franceschini, A., and Hatziminaoglou, E., 2006. Revisiting the infrared spectra of active galactic nuclei with a new torus emission model. *Monthly Notices of the Royal Astronomical Society*, 366(3):767.

Fujimoto, S., Arrabal Haro, P., Dickinson, M., et al., 2023. CEERS Spectroscopic Confirmation of NIRCam-selected z $\gtrsim$ 8 Galaxy Candidates with JWST/NIRSpec: Initial Characterization of Their Properties. *The Astrophysical Journal*, 949(2):L25.

Furlanetto, S.R. and Mirocha, J., 2022. Bursty star formation during the Cosmic Dawn driven by delayed stellar feedback. *Monthly Notices of the Royal Astronomical Society*, 511(3):3895.

Furlanetto, S.R., Oh, S.P., and Briggs, F.H., 2006. Cosmology at low frequencies: The 21 cm transition and the high-redshift Universe. *Physics Reports*, 433(4-6):181.

Galliano, F., Galametz, M., and Jones, A.P., 2018. The Interstellar Dust Properties of Nearby Galaxies. *Annual Review of Astronomy and Astrophysics*, 56:673.

Gamow, G., 1946. Expanding Universe and the Origin of Elements. *Physical Review*, 70(7-8):572.

Gao, F., Wang, L., Efstathiou, A., et al., 2021. The nature of hyperluminous infrared galaxies. *Astronomy and Astrophysics*, 654:A117.

Gardner, J.P., Mather, J.C., Abbott, R., et al., 2023. The James Webb Space Telescope Mission. *Publications of the Astronomical Society of the Pacific*, 135(1048):068001.

Gardner, J.P., Mather, J.C., Clampin, M., et al., 2006. The James Webb Space Telescope. *Space Science Reviews*, 123(4):485.

Garn, T., Green, D.A., Riley, J.M., et al., 2009. The relationship between star formation rate and radio synchrotron luminosity at 0 ¡ z ¡ 2. *Monthly Notices of the Royal Astronomical Society*, 397(2):1101.

Garrett, M.A., 2012. Radio Astronomy Transformed: Aperture Arrays - Past, Present & Future. In *From Antikythera to the Square Kilometre Array: Lessons from the Ancients*, page 41.

Garrington, S.T., Anderson, B., Baines, C., et al., 2004. e-MERLIN. In J.M. Oschmann Jr., editor, *Ground-based Telescopes*, volume 5489 of *Society of Photo-Optical Instrumentation Engineers (SPIE) Conference Series*, pages 332–343.

Garrison-Kimmel, S., Hopkins, P.F., Wetzel, A., et al., 2018. The origin of the diverse morphologies and kinematics of Milky Way-mass galaxies in the FIRE-2 simulations. *Monthly Notices of the Royal Astronomical Society*, 481(3):4133.

Georgantopoulos, I., Georgakakis, A., Rowan-Robinson, M., et al., 2008. Searching for mid-IR obscured AGN in the Chandra deep field North. *Astronomy and Astrophysics*, 484(3):671.

George, I.M. and Fabian, A.C., 1991. X-ray reflection from cold matter in Active Galactic Nuclei and X-ray binaries. *Monthly Notices of the Royal Astronomical Society*, 249:352.

Gibbons, G.W., Hawking, S.W., and Siklos, S.T.C., editors, 1983. *The Very early universe : proceedings of the Nuffield workshop, Cambridge, 21 June to 9 July, 1982*.

Gilmozzi, R. and Spyromilio, J., 2007. The European Extremely Large Telescope (E-ELT). *The Messenger*, 127:11.

Girardi, L., Bressan, A., Bertelli, G., et al., 2000. Evolutionary tracks and isochrones for low- and intermediate-mass stars: From 0.15 to 7 M_{sun}, and from Z=0.0004 to 0.03. *Astronomy and Astrophysics Supplement Series*, 141:371.

Gladders, M.D., Oemler, A., Dressler, A., et al., 2013. The IMACS Cluster Building Survey. IV. The Log-normal Star Formation History of Galaxies. *The Astrophysical Journal*, 770(1):64.

Glazebrook, K., Nanayakkara, T., Jacobs, C., et al., 2023. Early Results from GLASS-JWST. XV. Properties of the Faintest Red Sources in the NIRCAM Deep Fields. *The Astrophysical Journal*, 947(2):L25.

Glazebrook, K., Nanayakkara, T., Schreiber, C., et al., 2024. A massive galaxy that formed its stars at z $\approx$ 11. *Nature*, 628(8007):277.

Gloudemans, A.J., Duncan, K.J., Röttgering, H.J.A., et al., 2021. Low frequency radio properties of the z ¿ 5 quasar population. *Astronomy and Astrophysics*, 656:A137.

Greenberg, D.S., Nonnenmacher, M., and Macke, J.H., 2019. Automatic Posterior Transformation for Likelihood-Free Inference. *arXiv e-prints*, arXiv:1905.07488.

Greene, J., Bezanson, R., Ouchi, M., et al., 2022. The Prime Focus Spectrograph Galaxy Evolution Survey. *arXiv e-prints*, arXiv:2206.14908.

Greene, J.E., Strader, J., and Ho, L.C., 2020. Intermediate-Mass Black Holes. *Annual Review of Astronomy and Astrophysics*, 58:257.

Gregg, M.D., Silva, D., Rayner, J., et al., 2006. The HST/STIS Next Generation Spectral Library. In A.M. Koekemoer, P. Goudfrooij, and L.L. Dressel, editors, *The 2005 HST Calibration Workshop: Hubble After the Transition to Two-Gyro Mode*, page 209.

Greif, T.H., Glover, S.C.O., Bromm, V., et al., 2010. The First Galaxies: Chemical Enrichment, Mixing, and Star Formation. *The Astrophysical Journal*, 716(1):510.

Greif, T.H., Johnson, J.L., Klessen, R.S., et al., 2008. The first galaxies: assembly, cooling and the onset of turbulence. *Monthly Notices of the Royal Astronomical Society*, 387(3):1021.

Greif, T.H., Springel, V., White, S.D.M., et al., 2011. Simulations on a Moving Mesh: The Clustered Formation of Population III Protostars. *The Astrophysical Journal*, 737(2):75.

Griffin, M.J., Abergel, A., Abreu, A., et al., 2010. The Herschel-SPIRE instrument and its in-flight performance. *Astronomy and Astrophysics*, 518:L3.

Groves, B., Dopita, M.A., Sutherland, R.S., et al., 2008. Modeling the Pan-Spectral Energy Distribution of Starburst Galaxies. IV. The Controlling Parameters of the Starburst SED. *The Astrophysical Journal Supplement Series*, 176(2):438.

Gullieuszik, M., Falomo, R., Greggio, L., et al., 2016. Exploring high-z galaxies with the E-ELT. *Astronomy and Astrophysics*, 593:A24.

Gunn, J.E. and Peterson, B.A., 1965. On the Density of Neutral Hydrogen in Intergalactic Space. *The Astrophysical Journal*, 142:1633.

Guo, Y., Ferguson, H.C., Bell, E.F., et al., 2015. Clumpy Galaxies in CANDELS. I. The Definition of UV Clumps and the Fraction of Clumpy Galaxies at 0.5 ¡ z ¡ 3. *The Astrophysical Journal*, 800(1):39.

Guo, Y., Rafelski, M., Faber, S.M., et al., 2016. The Bursty Star Formation Histories of Low-mass Galaxies at 0.4 ¡ z ¡ 1 Revealed by Star Formation Rates Measured From Hβ and FUV. *Astrophysical Journal*, 833(1):37.

Guo, Z., Zhang, Z.Y., Yan, Z., et al., 2024. First Detection of CO Isotopologues in a High-redshift Main-sequence Galaxy: Evidence of a Top-heavy Stellar Initial Mass Function. *The Astrophysical Journal*, 970(2):136.

Gürkan, G., Hardcastle, M.J., Best, P.N., et al., 2019. LoTSS/HETDEX: Optical quasars. I. Low-frequency radio properties of optically selected quasars. *Astronomy and Astrophysics*, 622:A11.

Gürkan, G., Hardcastle, M.J., and Jarvis, M.J., 2014. The Wide-field Infrared Survey Explorer properties of complete samples of radio-loud active galactic nucleus. *Monthly Notices of the Royal Astronomical Society*, 438(2):1149.

Gürkan, G., Hardcastle, M.J., Smith, D.J.B., et al., 2018. LOFAR/H-ATLAS: the low-frequency radio luminosity-star formation rate relation. *Monthly Notices of the Royal Astronomical Society*, 475(3):3010.

Gürkan, G., Prandoni, I., O'Brien, A., et al., 2022. Deep ASKAP EMU Survey of the GAMA23 field: properties of radio sources. *Monthly Notices of the Royal Astronomical Society*, 512(4):6104.

Gurvich, A.B., Stern, J., Faucher-Giguère, C.A., et al., 2023. Rapid disc settling and the transition from bursty to steady star formation in Milky Way-mass galaxies. *Monthly Notices of the Royal Astronomical Society*, 519(2):2598.

Guth, A.H., 1981. Inflationary universe: A possible solution to the horizon and flatness problems. *Physical Review D*, 23(2):347.

Guy, J., Bailey, S., Kremin, A., et al., 2023. The Spectroscopic Data Processing Pipeline for the Dark Energy Spectroscopic Instrument. *The Astronomical Journal*, 165(4):144.

Haardt, F. and Maraschi, L., 1991. A Two-Phase Model for the X-Ray Emission from Seyfert Galaxies. *The Astrophysical Journal*, 380:L51.

Haiman, Z. and Loeb, A., 2001. What Is the Highest Plausible Redshift of Luminous Quasars? *The Astrophysical Journal*, 552(2):459.

Hale, C.L., Whittam, I.H., Jarvis, M.J., et al., 2023. Mightee: deep 1.4 ghz source counts and the sky temperature contribution of star-forming galaxies and active galactic nuclei. *Monthly Notices of the Royal Astronomical Society*, 520(2):2668.

Han, C. and Carlin, B.P., 2001. Markov chain monte carlo methods for computing bayes factors: A comparative review. *Journal of the American Statistical Association*, 96(455):1122.

Hardcastle, M.J. and Croston, J.H., 2020. Radio galaxies and feedback from AGN jets. *New Astronomy Reviews*, 88:101539.

Hardcastle, M.J., Evans, D.A., and Croston, J.H., 2007. Hot and cold gas accretion and feedback in radio-loud active galaxies. *Monthly Notices of the Royal Astronomical Society*, 376(4):1849.

Hardcastle, M.J., Gürkan, G., van Weeren, R.J., et al., 2016. LOFAR/H-ATLAS: a deep low-frequency survey of the Herschel-ATLAS North Galactic Pole field. *Monthly Notices of the Royal Astronomical Society*, 462(2):1910.

Hardcastle, M.J., Horton, M.A., Williams, W.L., et al., 2023. The LOFAR Two-Metre Sky Survey. VI. Optical identifications for the second data release. *Astronomy and Astrophysics*, 678:A151.

Hardcastle, M.J., Williams, W.L., Best, P.N., et al., 2019. Radio-loud AGN in the first LoTSS data release. The lifetimes and environmental impact of jet-driven sources. *Astronomy and Astrophysics*, 622:A12.

Harrison, C., 2014. *Observational constraints on the influence of active galactic nuclei on the evolution of galaxies*. Ph.D. thesis, Durham University, UK.

Harrison, C.M., Alexander, D.M., Mullaney, J.R., et al., 2014. Kiloparsec-scale outflows are prevalent among luminous AGN: outflows and feedback in the context of the overall AGN population. *Monthly Notices of the Royal Astronomical Society*, 441(4):3306.

Harwit, M. and Spaans, M., 2003. Chemical Composition of the Early Universe. *The Astrophysical Journal*, 589(1):53.

Haskell, P., Das, S., Smith, D.J.B., et al., 2024. Beware the recent past: a bias in spectral energy distribution modelling due to bursty star formation. *Monthly Notices of the Royal Astronomical Society*, 530(1):L7.

Haskell, P., Smith, D.J.B., Cochrane, R.K., et al., 2023. Energy balance SED modelling can be effective at high redshifts regardless of UV-FIR offsets. *Monthly Notices of the Royal Astronomical Society*, 525(1):1535.

Hayward, C.C. and Hopkins, P.F., 2017. How stellar feedback simultaneously regulates star formation and drives outflows. *Monthly Notices of the RAS*, 465(2):1682.

Hayward, C.C. and Smith, D.J.B., 2015. Should we believe the results of ultraviolet-millimetre galaxy spectral energy distribution modelling? *Monthly Notices of the RAS*, 446(2):1512.

Heckman, T.M. and Best, P.N., 2014. The Coevolution of Galaxies and Supermassive Black Holes: Insights from Surveys of the Contemporary Universe. *Annual Review of Astronomy and Astrophysics*, 52:589.

Heesen, V., Buie, E., I., Huff, C.J., et al., 2019. Calibrating the relation of low-frequency radio continuum to star formation rate at 1 kpc scale with LOFAR. *Astronomy and Astrophysics*, 622:A8.

Heesen, V., Staffehl, M., Basu, A., et al., 2022. Nearby galaxies in the LOFAR Two-metre Sky Survey. I. Insights into the non-linearity of the radio-SFR relation. *Astronomy and Astrophysics*, 664:A83.

Heger, A., Woosley, S., Baraffe, I., et al., 2002. Evolution and Explosion of Very Massive Primordial Stars. In M. Gilfanov, R. Sunyeav, and E. Churazov, editors, *Lighthouses of the Universe: The Most Luminous Celestial Objects and Their Use for Cosmology*, page 369.

Helfand, D.J., White, R.L., and Becker, R.H., 2015. The Last of FIRST: The Final Catalog and Source Identifications. *The Astrophysical Journal*, 801(1):26.

Helou, G., Soifer, B.T., and Rowan-Robinson, M., 1985. Thermal infrared and nonthermal radio : remarkable correlation in disks of galaxies. *The Astrophysical Journal*, 298:L7.

Heywood, I., Jarvis, M.J., Hale, C.L., et al., 2022. MIGHTEE: total intensity radio continuum imaging and the COSMOS/XMM-LSS Early Science fields. *Monthly Notices of the Royal Astronomical Society*, 509(2):2150.

Hickox, R.C. and Alexander, D.M., 2018. Obscured Active Galactic Nuclei. *Annual Review of Astronomy and Astrophysics*, 56:625.

Hickox, R.C., Jones, C., Forman, W.R., et al., 2009. Host Galaxies, Clustering, Eddington Ratios, and Evolution of Radio, X-Ray, and Infrared-Selected AGNs. *The Astrophysical Journal*, 696(1):891.

Higson, E., Handley, W., Hobson, M., et al., 2019. Dynamic nested sampling: an improved algorithm for parameter estimation and evidence calculation. *Statistics and Computing*, 29(5):891.

Ho, L.C., 2008. Nuclear activity in nearby galaxies. *Annual Review of Astronomy and Astrophysics*, 46:475.

Hopkins, P.F., Gurvich, A.B., Shen, X., et al., 2023. What causes the formation of discs and end of bursty star formation? *Monthly Notices of the RAS*, 525(2):2241.

Hopkins, P.F., Kereš, D., Oñorbe, J., et al., 2014. Galaxies on fire (feedback in realistic environments): stellar feedback explains cosmologically inefficient star formation. *Monthly Notices of the RAS*, 445(1):581.

Hopkins, P.F., Quataert, E., and Murray, N., 2012. Stellar feedback in galaxies and the origin of galaxy-scale winds. *Monthly Notices of the RAS*, 421(4):3522.

Hopkins, P.F., Wetzel, A., Kereš, D., et al., 2018. Fire-2 simulations: physics versus numerics in galaxy formation. *Monthly Notices of the RAS*, 480(1):800.

Hosokawa, T., Omukai, K., Yoshida, N., et al., 2011. Protostellar Feedback Halts the Growth of the First Stars in the Universe. *Science*, 334(6060):1250.

Hughes, P.A., 1991. *Beams and Jets in Astrophysics*. Cambridge University Press.

Hurley, P.D., Oliver, S., Betancourt, M., et al., 2017. HELP: XID+, the probabilistic de-blender for Herschel SPIRE maps. *Monthly Notices of the Royal Astronomical Society*, 464(1):885.

Ilbert, O., Arnouts, S., McCracken, H.J., et al., 2006. Accurate photometric redshifts for the cfht legacy survey calibrated using the vimos vlt deep survey. *Astronomy and Astrophysics*, 457(3):841.

Inayoshi, K., Visbal, E., and Haiman, Z., 2020. The Assembly of the First Massive Black Holes. *Annual Review of Astronomy and Astrophysics*, 58:27.

Iwata, I., Inoue, A.K., and Burgarella, D., 2005. Spectroscopy and stellar populations of star-forming galaxies at z ~3 in the Hubble Deep Field - South. *Astronomy and Astrophysics*, 440(3):881.

Iyer, K. and Gawiser, E., 2017. Reconstruction of Galaxy Star Formation Histories through SED Fitting:The Dense Basis Approach. *The Astrophysical Journal*, 838(2):127.

Iyer, K.G., Gawiser, E., Faber, S.M., et al., 2019. Nonparametric Star Formation History Reconstruction with Gaussian Processes. I. Counting Major Episodes of Star Formation. *The Astrophysical Journal*, 879(2):116.

Jackson, C., 2005. The Extragalactic Radio Sky at Faint Flux Densities. *Publications of the Astronomical Society of Australia*, 22(1):36.

Jackson, C.A., 2004. Deep radio continuum studies with the SKA: evolution of radio AGN populations. *New Astronomy Reviews*, 48(11-12):1187.

Jain, S., Tacchella, S., and Mosleh, M., 2024. The motivation for flexible star-formation histories from spatially resolved scales within galaxies. *Monthly Notices of the Royal Astronomical Society*, 527(2):3291.

Jannuzi, B.T. and Dey, A., 1999. The NOAO Deep Wide-Field Survey. In R. Weymann, L. Storrie-Lombardi, M. Sawicki, and R. Brunner, editors, *Photometric Redshifts and the Detection of High Redshift Galaxies*, volume 191 of *Astronomical Society of the Pacific Conference Series*, page 111.

Jansen, F., Lumb, D., Altieri, B., et al., 2001. XMM-Newton observatory. I. The spacecraft and operations. *Astronomy and Astrophysics*, 365:L1.

Jansky, K., 1933. Electrical disturbances apparently of extraterrestrial origin. *Proceedings of the Institute of Radio Engineers*, 21(10):1387.

Janssen, R.M.J., Röttgering, H.J.A., Best, P.N., et al., 2012. The triggering probability of radio-loud AGN. A comparison of high and low excitation radio galaxies in hosts of different colors. *Astronomy and Astrophysics*, 541:A62.

Jarvis, M., Taylor, R., Agudo, I., et al., 2016. The MeerKAT International GHz Tiered Extragalactic Exploration (MIGHTEE) Survey. In *MeerKAT Science: On the Pathway to the SKA*, page 6.

Jarvis, M.E., Harrison, C.M., Thomson, A.P., et al., 2019. Prevalence of radio jets associated with galactic outflows and feedback from quasars. *Monthly Notices of the Royal Astronomical Society*, 485(2):2710.

Jarvis, M.J., Smith, D.J.B., Bonfield, D.G., et al., 2010. Herschel-ATLAS: the far-infrared-radio correlation at z ¡ 0.5. *Monthly Notices of the Royal Astronomical Society*, 409(1):92.

Jelić, V., de Bruyn, A.G., Mevius, M., et al., 2014. Initial LOFAR observations of epoch of reionization windows. II. Diffuse polarized emission in the ELAIS-N1 field. *Astronomy and Astrophysics*, 568:A101.

Jiang, L., Fan, X., Bian, F., et al., 2009. A Survey of z ~6 Quasars in the Sloan Digital Sky Survey Deep Stripe. II. Discovery of Six Quasars at z $_{AB}$¿21. *The Astronomical Journal*, 138(1):305.

Jiang, Y.F., Stone, J.M., and Davis, S.W., 2019. Super-Eddington Accretion Disks around Supermassive Black Holes. *The Astrophysical Journal*, 880(2):67.

Jin, C., Done, C., and Ward, M., 2017. Super-Eddington QSO RX J0439.6-5311 - I. Origin of the soft X-ray excess and structure of the inner accretion flow. *Monthly Notices of the Royal Astronomical Society*, 468(3):3663.

Jin, S., Trager, S.C., Dalton, G.B., et al., 2023. The wide-field, multiplexed, spectroscopic facility WEAVE: Survey design, overview, and simulated implementation. *Monthly Notices of the RAS*.

Jin, S., Trager, S.C., Dalton, G.B., et al., 2024. The wide-field, multiplexed, spectroscopic facility WEAVE: Survey design, overview, and simulated implementation. *Monthly Notices of the Royal Astronomical Society*, 530(3):2688.

Johnson, B., Foreman-Mackey, D., Sick, J., et al., 2023. dfm/python-fsps: v0.4.6. Zenodo.

Johnson, B.D., 2019. SEDPY: Modules for storing and operating on astronomical source spectral energy distribution. Astrophysics Source Code Library, record ascl:1905.026.

Johnson, B.D., Leja, J., Conroy, C., et al., 2021. Stellar Population Inference with Prospector. *The Astrophysical Journal Supplement Series*, 254(2):22.

Johnston, S., Bailes, M., Bartel, N., et al., 2007. Science with the Australian Square Kilometre Array Pathfinder. *Publications of the Astronomical Society of Australia*, 24(4):174.

Jones, M.H. and Lambourne, R.J.A., 2004. *An Introduction to Galaxies and Cosmology*. Cambridge University Press.

Jones, T., Sanders, R., Chen, Y., et al., 2023. Early Results from GLASS-JWST. XXI. Rapid Asembly of a Galaxy at z = 6.23 Revealed by Its C/O Abundance. *The Astrophysical Journal*, 951(1):L17.

Jonsson, P., 2006. Sunrise: polychromatic dust radiative transfer in arbitrary geometries. *Monthly Notices of the RAS*, 372(1):2.

Juneau, S., Bournaud, F., Charlot, S., et al., 2014. Active Galactic Nuclei Emission Line Diagnostics and the Mass-Metallicity Relation up to Redshift z ~2: The Impact of Selection Effects and Evolution. *The Astrophysical Journal*, 788(1):88.

Juneau, S., Dickinson, M., Alexander, D.M., et al., 2011. A New Diagnostic of Active Galactic Nuclei: Revealing Highly Absorbed Systems at Redshift ¿0.3. *The Astrophysical Journal*, 736(2):104.

Juneau, S., Dickinson, M., Bournaud, F., et al., 2013. Widespread and Hidden Active Galactic Nuclei in Star-forming Galaxies at Redshift ¿0.3. *The Astrophysical Journal*, 764(2):176.

Kaiser, N., Burgett, W., Chambers, K., et al., 2010. The Pan-STARRS wide-field optical/NIR imaging survey. In L.M. Stepp, R. Gilmozzi, and H.J. Hall, editors, *Ground-based and Airborne Telescopes III*, volume 7733 of *Society of Photo-Optical Instrumentation Engineers (SPIE) Conference Series*, page 77330E.

Karlsson, T., Bromm, V., and Bland-Hawthorn, J., 2013. Pregalactic metal enrichment: The chemical signatures of the first stars. *Reviews of Modern Physics*, 85(2):809.

Kass, R.E. and Raftery, A.E., 1995. Bayes Factors. *Journal of the American Statistical Association*, 90(430):773.

Katsianis, A., Blanc, G., Lagos, C.P., et al., 2017. The evolution of the star formation rate function in the EAGLE simulations: a comparison with UV, IR and Hα observations from z $\sim$ 8 to z $\sim$ 0. *Monthly Notices of the Royal Astronomical Society*, 472(1):919.

Katz, H., Rosdahl, J., Kimm, T., et al., 2023. The sphinx public data release: Forward modelling high-redshift jwst observations with cosmological radiation hydrodynamics simulations. *The Open Journal of Astrophysics*, 6:44.

Katz, N., Keres, D., Dave, R., et al., 2003. How Do Galaxies Get Their Gas? In J.L. Rosenberg and M.E. Putman, editors, *The IGM/Galaxy Connection. The Distribution of Baryons at z=0*, volume 281 of *Astrophysics and Space Science Library*, page 185.

Kauffmann, G., Heckman, T.M., Tremonti, C., et al., 2003. The host galaxies of active galactic nuclei. *Monthly Notices of the Royal Astronomical Society*, 346(4):1055.

Kellermann, K.I., 1980. Radio galaxies and quasars. In J. Ehlers, J.J. Perry, and M. Walker, editors, *Ninth Texas Symposium on Relativistic Astrophysics*, volume 336, pages 1–11.

Kellermann, K.I. and Owen, F.N., 1988. Radio galaxies and quasars. In K.I. Kellermann and G.L. Verschuur, editors, *Galactic and Extragalactic Radio Astronomy*, pages 563–602. "Springer-Verlag".

Kennicutt, Robert C., J., 1998a. Star Formation in Galaxies Along the Hubble Sequence. *Annual Review of Astronomy and Astrophysics*, 36(2):189.

Kennicutt, Robert C., J., Hao, C.N., Calzetti, D., et al., 2009. Dust-corrected Star Formation Rates of Galaxies. I. Combinations of Hα and Infrared Tracers. *The Astrophysical Journal*, 703(2):1672.

Kennicutt, R.C. and Evans, N.J., 2012. Star Formation in the Milky Way and Nearby Galaxies. *Annual Review of Astronomy and Astrophysics*, 50:531.

Kennicutt, Jr., R.C., 1998b. The Global Schmidt Law in Star-forming Galaxies. *The Astrophysical Journal*, 498(2):541.

Kereš, D., Katz, N., Weinberg, D.H., et al., 2005. How do galaxies get their gas? *Monthly Notices of the Royal Astronomical Society*, 363(1):2.

Kewley, L.J., Dopita, M.A., Sutherland, R.S., et al., 2001. Theoretical Modeling of Starburst Galaxies. *The Astrophysical Journal*, 556(1):121.

Kewley, L.J., Groves, B., Kauffmann, G., et al., 2006. The host galaxies and classification of active galactic nuclei. *Monthly Notices of the Royal Astronomical Society*, 372(3):961.

Kewley, L.J., Nicholls, D.C., and Sutherland, R.S., 2019. Understanding Galaxy Evolution Through Emission Lines. *Annual Review of Astronomy and Astrophysics*, 57:511.

Khullar, G., Nord, B., Ćiprijanović, A., et al., 2022. DIGS: deep inference of galaxy spectra with neural posterior estimation. *Machine Learning: Science and Technology*, 3(4):04LT04.

Kim, C.G., Ostriker, E.C., and Kim, W.T., 2013. Three-dimensional Hydrodynamic Simulations of Multiphase Galactic Disks with Star Formation Feedback. I. Regulation of Star Formation Rates. *The Astrophysical Journal*, 776(1):1.

King, A. and Pounds, K., 2015. Powerful Outflows and Feedback from Active Galactic Nuclei. *Annual Review of Astronomy and Astrophysics*, 53:115.

Kirkpatrick, A., Pope, A., Sajina, A., et al., 2015. The Role of Star Formation and an AGN in Dust Heating of z = 0.3-2.8 Galaxies. I. Evolution with Redshift and Luminosity. *The Astrophysical Journal*, 814(1):9.

Klessen, R., 2019. Formation of the first stars. In M. Latif and D. Schleicher, editors, *Formation of the First Black Holes*, pages 67–97. World Scientific.

Klessen, R.S. and Glover, S.C.O., 2023. The First Stars: Formation, Properties, and Impact. *Annual Review of Astronomy and Astrophysics*, 61:65.

Kogut, A., Spergel, D.N., Barnes, C., et al., 2003. First-Year Wilkinson Microwave Anisotropy Probe (WMAP) Observations: Temperature-Polarization Correlation. *The Astrophysical Journal Supplement Series*, 148(1):161.

Kolb, E.W. and Turner, M.S., 1990. *The early universe*, volume 69. CRC Press.

Koleva, M., Prugniel, P., Bouchard, A., et al., 2009. ULySS: a full spectrum fitting package. *Astronomy and Astrophysics*, 501(3):1269.

Kondapally, R., Best, P.N., Cochrane, R.K., et al., 2022. Cosmic evolution of low-excitation radio galaxies in the LOFAR two-metre sky survey deep fields. *Monthly Notices of the RAS*, 513(3):3742.

Kondapally, R., Best, P.N., Duncan, K.J., et al., 2025. Radio-AGN activity across the galaxy population: dependence on stellar mass, star formation rate, and redshift. *Monthly Notices of the Royal Astronomical Society*, 536(1):554.

Kondapally, R., Best, P.N., Hardcastle, M.J., et al., 2021. The LOFAR Two-meter Sky Survey: Deep Fields Data Release 1. III. Host-galaxy identifications and value added catalogues. *Astronomy and Astrophysics*, 648:A3.

Koopmans, L.V.E., 2017. Current status of the lofar eor key science project. *Proceedings of the International Astronomical Union*, 12(S333):71–76.

Kormendy, J., 2013. Secular Evolution in Disk Galaxies. In J. Falcón-Barroso and J.H. Knapen, editors, *Secular Evolution of Galaxies*, page 1. Cambridge University Press.

Kormendy, J. and Ho, L.C., 2013. Coevolution (Or Not) of Supermassive Black Holes and Host Galaxies. *Annual Review of Astronomy and Astrophysics*, 51(1):511.

Kormendy, J. and Kennicutt, Jr., R.C., 2004. Secular Evolution and the Formation of Pseudobulges in Disk Galaxies. *Annual Review of Astronomy and Astrophysics*, 42(1):603.

Krawczyk, C.M., Richards, G.T., Mehta, S.S., et al., 2013. Mean Spectral Energy Distributions and Bolometric Corrections for Luminous Quasars. *The Astrophysical Journal Supplement Series*, 206(1):4.

Kriek, M. and Conroy, C., 2013. The Dust Attenuation Law in Distant Galaxies: Evidence for Variation with Spectral Type. *The Astrophysical Journal*, 775(1):L16.

Kroupa, P., 2001. On the variation of the initial mass function. *Monthly Notices of the Royal Astronomical Society*, 322(2):231.

Lacey, C. and Cole, S., 1993. Merger rates in hierarchical models of galaxy formation. *Monthly Notices of the Royal Astronomical Society*, 262(3):627.

Lacki, B.C., Thompson, T.A., and Quataert, E., 2010. The Physics of the Far-infrared-Radio Correlation. I. Calorimetry, Conspiracy, and Implications. *The Astrophysical Journal*, 717(1):1.

Lacy, M., Baum, S.A., Chandler, C.J., et al., 2016. The VLA Sky Survey (VLASS): Description and Science Goals. In *American Astronomical Society Meeting Abstracts #227*, volume 227 of *American Astronomical Society Meeting Abstracts*, page 324.09.

Lacy, M., Storrie-Lombardi, L.J., Sajina, A., et al., 2004. Obscured and Unobscured Active Galactic Nuclei in the Spitzer Space Telescope First Look Survey. *Astrophysical Journal, Supplement*, 154(1):166.

Laing, R.A., Jenkins, C.R., Wall, J.V., et al., 1994. Spectrophotometry of a Complete Sample of 3CR Radio Sources: Implications for Unified Models. In G.V. Bicknell, M.A. Dopita, and P.J. Quinn, editors, *The Physics of Active Galaxies*, volume 54 of *Astronomical Society of the Pacific Conference Series*, page 201.

Lamers, H.J.G.L.M. and Cassinelli, J.P., 1999. *Introduction to Stellar Winds*. Cambridge University Press.

Latif, M.A. and Ferrara, A., 2016. Formation of Supermassive Black Hole Seeds. *Publications of the Astronomical Society of Australia*, 33:e051.

Lawrence, A., Warren, S.J., Almaini, O., et al., 2007. The UKIRT Infrared Deep Sky Survey (UKIDSS). *Monthly Notices of the Royal Astronomical Society*, 379(4):1599.

Le Borgne, J.F., Bruzual, G., Pelló, R., et al., 2003. STELIB: A library of stellar spectra at R ~2000. *Astronomy and Astrophysics*, 402:433.

Leethochawalit, N., Trenti, M., Santini, P., et al., 2023. Early Results from GLASS-JWST. X. Rest-frame UV-optical Properties of Galaxies at 7 ¡ z ¡ 9. *The Astrophysical Journal*, 942(2):L26.

Leja, J., Carnall, A.C., Johnson, B.D., et al., 2019. How to Measure Galaxy Star Formation Histories. II. Nonparametric Models. *The Astrophysical Journal*, 876(1):3.

Leja, J., Johnson, B.D., Conroy, C., et al., 2017. Deriving Physical Properties from Broadband Photometry with Prospector: Description of the Model and a Demonstration of its Accuracy Using 129 Galaxies in the Local Universe. *The Astrophysical Journal*, 837(2):170.

Leja, J., Johnson, B.D., Conroy, C., et al., 2018. Hot Dust in Panchromatic SED Fitting: Identification of Active Galactic Nuclei and Improved Galaxy Properties. *The Astrophysical Journal*, 854(1):62.

Li, A., 2005. The Warm, Cold and Very Cold Dusty Universe. *arXiv e-prints*, astro-ph/0503571.

Li, A., 2007. Dust in Active Galactic Nuclei. In L.C. Ho and J.W. Wang, editors, *The Central Engine of Active Galactic Nuclei*, volume 373 of *Astronomical Society of the Pacific Conference Series*, page 561.

Li, A. and Draine, B.T., 2001. Infrared Emission from Interstellar Dust. II. The Diffuse Interstellar Medium. *The Astrophysical Journal*, 554(2):778.

Li, M., Li, X.D., Wang, S., et al., 2013. Dark energy: A brief review. *Frontiers of Physics*, 8(6):828.

Lisenfeld, U., Voelk, H.J., and Xu, C., 1996. A quantitative model of the FIR/radio correlation for normal late-type galaxies. *Astronomy and Astrophysics*, 306:677.

Lockman, F.J., Jahoda, K., and McCammon, D., 1986. The Structure of Galactic H i in Directions of Low Total Column Density. *The Astrophysical Journal*, 302:432.

Lodato, G. and Natarajan, P., 2006. Supermassive black hole formation during the assembly of pre-galactic discs. *Monthly Notices of the Royal Astronomical Society*, 371(4):1813.

Loeb, A. and Rasio, F.A., 1994. Collapse of Primordial Gas Clouds and the Formation of Quasar Black Holes. *The Astrophysical Journal*, 432:52.

Lonsdale, C.J., Smith, H.E., Rowan-Robinson, M., et al., 2003. SWIRE: The SIRTF Wide-Area Infrared Extragalactic Survey. *Publications of the Astronomical Society of the Pacific*, 115(810):897.

Looser, T.J., D'Eugenio, F., Maiolino, R., et al., 2023. Jades: Differing assembly histories of galaxies – observational evidence for bursty sfhs and (mini-)quenching in the first billion years of the universe. *arXiv e-prints*, arXiv:2306.02470.

Looser, T.J., D'Eugenio, F., Maiolino, R., et al., 2024a. A recently quenched galaxy 700 million years after the Big Bang. *Nature*, 629(8010):53.

Looser, T.J., D'Eugenio, F., Maiolino, R., et al., 2024b. A recently quenched galaxy 700 million years after the Big Bang. *Nature*, 629(8010):53.

Looser, T.J., D'Eugenio, F., Maiolino, R., et al., 2025. JADES: Differing assembly histories of galaxies: Observational evidence for bursty star formation histories and (mini-)quenching in the first billion years of the Universe. *Astronomy and Astrophysics*, 697:A88.

Lower, S., Narayanan, D., Leja, J., et al., 2020. How Well Can We Measure the Stellar Mass of a Galaxy: The Impact of the Assumed Star Formation History Model in SED Fitting. *The Astrophysical Journal*, 904(1):33.

Luisi, M., Anderson, L.D., Schneider, N., et al., 2021. Stellar feedback and triggered star formation in the prototypical bubble RCW 120. *Science Advances*, 7(15):eabe9511.

Ma, X., Hopkins, P.F., Garrison-Kimmel, S., et al., 2018. Simulating galaxies in the reionization era with FIRE-2: galaxy scaling relations, stellar mass functions, and luminosity functions. *Monthly Notices of the RAS*, 478(2):1694.

Macfarlane, C., Best, P.N., Sabater, J., et al., 2021. The radio loudness of SDSS quasars from the LOFAR Two-metre Sky Survey: ubiquitous jet activity and constraints on star formation. *Monthly Notices of the Royal Astronomical Society*, 506(4):5888.

Madau, P., 1995. Radiative Transfer in a Clumpy Universe: The Colors of High-Redshift Galaxies. *The Astrophysical Journal*, 441:18.

Madau, P., 1997. Cosmic star formation history. In S.S. Holt and L.G. Mundy, editors, *The Seventh Astrophysical Conference: Star formation, near and far*, volume 393 of *American Institute of Physics Conference Series*, pages 481–490. AIP.

Madau, P. and Dickinson, M., 2014. Cosmic Star-Formation History. *Annual Review of Astronomy and Astrophysics*, 52:415.

Madau, P., Haardt, F., and Dotti, M., 2014. Super-critical Growth of Massive Black Holes from Stellar-mass Seeds. *The Astrophysical Journal*, 784(2):L38.

Madau, P. and Rees, M.J., 2001. Massive Black Holes as Population III Remnants. *The Astrophysical Journal*, 551(1):L27.

Magliocchetti, M., 2022. Hosts and environments: a (large-scale) radio history of AGN and star-forming galaxies. *Astronomy and Astrophysics Review*, 30(1):6.

Magnelli, B., Ivison, R.J., Lutz, D., et al., 2015. The far-infrared/radio correlation and radio spectral index of galaxies in the SFR-M_* plane up to z~2. *Astronomy and Astrophysics*, 573:A45.

Mainieri, V., Anderson, R.I., Brinchmann, J., et al., 2024. The Wide-field Spectroscopic Telescope (WST) Science White Paper. *arXiv e-prints*, arXiv:2403.05398.

Mandal, S., Prandoni, I., Hardcastle, M.J., et al., 2021. Extremely deep 150 MHz source counts from the LoTSS Deep Fields. *Astronomy and Astrophysics*, 648:A5.

Maraston, C., Pforr, J., Renzini, A., et al., 2010. Star formation rates and masses of z ~2 galaxies from multicolour photometry. *Monthly Notices of the Royal Astronomical Society*, 407(2):830.

Marigo, P., Girardi, L., Bressan, A., et al., 2008. Evolution of asymptotic giant branch stars. II. Optical to far-infrared isochrones with improved TP-AGB models. *Astronomy and Astrophysics*, 482(3):883.

Markov, V., Gallerani, S., Pallottini, A., et al., 2023. Dust attenuation law in JWST galaxies at z ∼ 7-8. *Astronomy and Astrophysics*, 679:A12.

Marks, M., Kroupa, P., Dabringhausen, J., et al., 2012. Evidence for top-heavy stellar initial mass functions with increasing density and decreasing metallicity. *Monthly Notices of the Royal Astronomical Society*, 422(3):2246.

Mármol-Queraltó, E., Sánchez, S.F., Marino, R.A., et al., 2011. Integral field spectroscopy of a sample of nearby galaxies. I. Sample, observations, and data reduction. *Astronomy and Astrophysics*, 534:A8.

Martig, M., Bournaud, F., Teyssier, R., et al., 2009. Morphological Quenching of Star Formation: Making Early-Type Galaxies Red. *The Astrophysical Journal*, 707(1):250.

Martins, L.P., González Delgado, R.M., Leitherer, C., et al., 2005. A high-resolution stellar library for evolutionary population synthesis. *Monthly Notices of the Royal Astronomical Society*, 358(1):49.

Maseda, M.V., van der Wel, A., da Cunha, E., et al., 2013. Confirmation of Small Dynamical and Stellar Masses for Extreme Emission Line Galaxies at z ~2. *The Astrophysical Journal*, 778(1):L22.

Mathews, W.G. and Ferland, G.J., 1987. What Heats the Hot Phase in Active Nuclei? *The Astrophysical Journal*, 323:456.

Mathis, J.S., Mezger, P.G., and Panagia, N., 1983. Interstellar radiation field and dust temperatures in the diffuse interstellar medium and in giant molecular clouds. *Astronomy and Astrophysics*, 128:212.

Mauch, T. and Sadler, E.M., 2007. Radio sources in the 6dFGS: local luminosity functions at 1.4 GHz for star-forming galaxies and radio-loud AGN. *Monthly Notices of the Royal Astronomical Society*, 375(3):931.

Mauduit, J.C., Lacy, M., Farrah, D., et al., 2012. The Spitzer Extragalactic Representative Volume Survey (SERVS): Survey Definition and Goals. *Publications of the Astronomical Society of the Pacific*, 124(917):714.

Mayer, L., Mastropietro, C., Wadsley, J., et al., 2006. Simultaneous ram pressure and tidal stripping; how dwarf spheroidals lost their gas. *Monthly Notices of the Royal Astronomical Society*, 369(3):1021.

McCheyne, I., Oliver, S., Sargent, M., et al., 2022. The LOFAR Two-metre Sky Survey Deep fields. The mass dependence of the far-infrared radio correlation at 150 MHz using deblended Herschel fluxes. *Astronomy and Astrophysics*, 662:A100.

McGreer, I.D., Mesinger, A., and D'Odorico, V., 2015. Model-independent evidence in favour of an end to reionization by z $\approx$ 6. *Monthly Notices of the Royal Astronomical Society*, 447(1):499.

McKinney, J., Finnerty, L., Casey, C.M., et al., 2023. Broad Emission Lines in Optical Spectra of Hot, Dust-obscured Galaxies Can Contribute Significantly to JWST/NIRCam Photometry. *The Astrophysical Journal*, 946(2):L39.

McKinney, J.C., Tchekhovskoy, A., Sadowski, A., et al., 2014. Three-dimensional general relativistic radiation magnetohydrodynamical simulation of super-Eddington accretion, using a new code HARMRAD with M1 closure. *Monthly Notices of the Royal Astronomical Society*, 441(4):3177.

McNamara, B.R. and Nulsen, P.E.J., 2007. Heating Hot Atmospheres with Active Galactic Nuclei. *Annual Review of Astronomy and Astrophysics*, 45(1):117.

McNamara, B.R. and Nulsen, P.E.J., 2012. Mechanical feedback from active galactic nuclei in galaxies, groups and clusters. *New Journal of Physics*, 14(5):055023.

Mehta, V., Teplitz, H.I., Scarlata, C., et al., 2023. A Spatially Resolved Analysis of Star Formation Burstiness by Comparing UV and Hα in Galaxies at z $\sim$ 1 with UVCANDELS. *The Astrophysical Journal*, 952(2):133.

Meier, D.L., 2001. The Association of Jet Production with Geometrically Thick Accretion Flows and Black Hole Rotation. *The Astrophysical Journal*, 548(1):L9.

Messias, H., Afonso, J., Salvato, M., et al., 2012. A New Infrared Color Criterion for the Selection of 0 ¡ z ¡ 7 AGNs: Application to Deep Fields and Implications for JWST Surveys. *The Astrophysical Journal*, 754(2):120.

Meynet, G. and Maeder, A., 2000. Stellar evolution with rotation. V. Changes in all the outputs of massive star models. *Astronomy and Astrophysics*, 361:101.

Michel-Dansac, L., Blaizot, J., Garel, T., et al., 2020. RASCAS: RAdiation SCattering in Astrophysical Simulations. *Astronomy and Astrophysics*, 635:A154.

Mingo, B., Hardcastle, M.J., Croston, J.H., et al., 2014. An X-ray survey of the 2 Jy sample - I. Is there an accretion mode dichotomy in radio-loud AGN? *Monthly Notices of the Royal Astronomical Society*, 440(1):269.

Miyazaki, S., Komiyama, Y., Kawanomoto, S., et al., 2018. Hyper Suprime-Cam: System design and verification of image quality. *Publications of the Astronomical Society of Japan*, 70:S1.

Miyazaki, S., Komiyama, Y., Nakaya, H., et al., 2012. Hyper Suprime-Cam. In I.S. McLean, S.K. Ramsay, and H. Takami, editors, *Ground-based and Airborne Instrumentation for Astronomy IV*, volume 8446 of *Society of Photo-Optical Instrumentation Engineers (SPIE) Conference Series*, page 84460Z.

Mo, H., van den Bosch, F.C., and White, S., 2010. *Galaxy Formation and Evolution*. Cambridge University Press.

Mohan, N. and Rafferty, D., 2015. PyBDSF: Python Blob Detection and Source Finder. Astrophysics Source Code Library, record ascl:1502.007.

Molnár, D.C., Sargent, M.T., Leslie, S., et al., 2021. The non-linear infrared-radio correlation of low-z galaxies: implications for redshift evolution, a new radio SFR recipe, and how to minimize selection bias. *Monthly Notices of the Royal Astronomical Society*, 504(1):118.

Mor, R., Netzer, H., and Elitzur, M., 2009. Dusty Structure Around Type-I Active Galactic Nuclei: Clumpy Torus Narrow-line Region and Near-nucleus Hot Dust. *The Astrophysical Journal*, 705(1):298.

Morabito, L.K., Jackson, N.J., Mooney, S., et al., 2022. Sub-arcsecond imaging with the International LOFAR Telescope. I. Foundational calibration strategy and pipeline. *Astronomy and Astrophysics*, 658:A1.

Morabito, L.K., Kondapally, R., Best, P.N., et al., 2025. A hidden active galactic nucleus population: the first radio luminosity functions constructed by physical process. *Monthly Notices of the Royal Astronomical Society*, 536(1):L32.

Morganti, R., 2017. The many routes to AGN feedback. *Frontiers in Astronomy and Space Sciences*, 4:42.

Mortlock, D.J., Warren, S.J., Venemans, B.P., et al., 2011. A luminous quasar at a redshift of z = 7.085. *Nature*, 474(7353):616.

Mosby, G., Rauscher, B.J., Bennett, C., et al., 2020. Properties and characteristics of the Nancy Grace Roman Space Telescope H4RG-10 detectors. *Journal of Astronomical Telescopes, Instruments, and Systems*, 6:046001.

Moustakas, J., Scholte, D., Dey, B., et al., 2023. FastSpecFit: Fast spectral synthesis and emission-line fitting of DESI spectra. Astrophysics Source Code Library, record ascl:2308.005.

Muñoz Marín, V.M., Storchi-Bergmann, T., González Delgado, R.M., et al., 2009. On the nature of the near-UV extended light in Seyfert galaxies. *Monthly Notices of the Royal Astronomical Society*, 399(2):842.

Munari, U., Sordo, R., Castelli, F., et al., 2005. An extensive library of 2500 10 500 Å synthetic spectra. *Astronomy and Astrophysics*, 442(3):1127.

Muratov, A.L., Kereš, D., Faucher-Giguère, C.A., et al., 2015. Gusty, gaseous flows of FIRE: galactic winds in cosmological simulations with explicit stellar feedback. *Monthly Notices of the Royal Astronomical Society*, 454(3):2691.

Murgia, M., Parma, P., Mack, K.H., et al., 2011. Dying radio galaxies in clusters. *Astronomy and Astrophysics*, 526:A148.

Murphy, E.J., Condon, J.J., Schinnerer, E., et al., 2011. Calibrating Extinction-free Star Formation Rate Diagnostics with 33 GHz Free-free Emission in NGC 6946. *The Astrophysical Journal*, 737(2):67.

Mutch, S.J., Geil, P.M., Poole, G.B., et al., 2016. Dark-ages reionization and galaxy formation simulation - III. Modelling galaxy formation and the epoch of reionization. *Monthly Notices of the Royal Astronomical Society*, 462(1):250.

Muxlow, T.W.B., Richards, A.M.S., Garrington, S.T., et al., 2005. High-resolution studies of radio sources in the Hubble Deep and Flanking Fields. *Monthly Notices of the Royal Astronomical Society*, 358(4):1159.

Muzzin, A., Wilson, G., Yee, H.K.C., et al., 2009. Spectroscopic Confirmation of Two Massive Red-Sequence-Selected Galaxy Clusters at z ~1.2 in the SpARCS-North Cluster Survey. *The Astrophysical Journal*, 698(2):1934.

Myers, A.D., Moustakas, J., Bailey, S., et al., 2023. The Target-selection Pipeline for the Dark Energy Spectroscopic Instrument. *The Astronomical Journal*, 165(2):50.

Naab, T. and Ostriker, J.P., 2017. Theoretical Challenges in Galaxy Formation. *Annual Review of Astronomy and Astrophysics*, 55(1):59.

Nakamura, F. and Umemura, M., 2001. On the Initial Mass Function of Population III Stars. *The Astrophysical Journal*, 548(1):19.

Nanayakkara, T., Glazebrook, K., Jacobs, C., et al., 2024. A population of faint, old, and massive quiescent galaxies at 3 ¡z ¡4 revealed by JWST NIRSpec Spectroscopy. *Scientific Reports*, 14:3724.

Narayan, R., 2005. Black holes in astrophysics. *New Journal of Physics*, 7(1):199.

Narayan, R. and Yi, I., 1995a. Advection-dominated Accretion: Self-Similarity and Bipolar Outflows. *The Astrophysical Journal*, 444:231.

Narayan, R. and Yi, I., 1995b. Advection-dominated Accretion: Underfed Black Holes and Neutron Stars. *The Astrophysical Journal*, 452:710.

Narayanan, D., Lower, S., Torrey, P., et al., 2024. Outshining by Recent Star Formation Prevents the Accurate Measurement of High-z Galaxy Stellar Masses. *The Astrophysical Journal*, 961(1):73.

Nenkova, M., Sirocky, M.M., Ivezić, Ž., et al., 2008a. AGN Dusty Tori. I. Handling of Clumpy Media. *The Astrophysical Journal*, 685(1):147.

Nenkova, M., Sirocky, M.M., Nikutta, R., et al., 2008b. AGN Dusty Tori. II. Observational Implications of Clumpiness. *The Astrophysical Journal*, 685(1):160.

Netzer, H., 1990. AGN emission lines. In R.D. Blandford, H. Netzer, L. Woltjer, T.J.L. Courvoisier, and M. Mayor, editors, *Active Galactic Nuclei*, pages 57–160.

Netzer, H., 2015. Revisiting the Unified Model of Active Galactic Nuclei. *Annual Review of Astronomy and Astrophysics*, 53:365.

Noeske, K.G., Weiner, B.J., Faber, S.M., et al., 2007. Star Formation in AEGIS Field Galaxies since z=1.1: The Dominance of Gradually Declining Star Formation, and the Main Sequence of Star-forming Galaxies. *The Astrophysical Journal*, 660(1):L43.

Noll, S., Burgarella, D., Giovannoli, E., et al., 2009. Analysis of galaxy spectral energy distributions from far-UV to far-IR with CIGALE: studying a SINGS test sample. *Astronomy and Astrophysics*, 507(3):1793.

Norris, R.P., Hopkins, A.M., Afonso, J., et al., 2011. EMU: Evolutionary Map of the Universe. *Publications of the Astronomical Society of Australia*, 28(3):215.

Norris, R.P., Marvil, J., Collier, J.D., et al., 2021. The Evolutionary Map of the Universe pilot survey. *Publications of the Astronomical Society of Australia*, 38:e046.

O'Connell, R.W., 1999. Far-Ultraviolet Radiation from Elliptical Galaxies. *Annual Review of Astronomy and Astrophysics*, 37:603.

Ocran, E.F., Taylor, A.R., Vaccari, M., et al., 2017. The nature of the faint low-frequency radio source population. *Monthly Notices of the Royal Astronomical Society*, 468(1):1156.

Ocvirk, P., Pichon, C., Lançon, A., et al., 2006. STECKMAP: STEllar Content and Kinematics from high resolution galactic spectra via Maximum A Posteriori. *Monthly Notices of the Royal Astronomical Society*, 365(1):74.

Oke, J.B. and Gunn, J.E., 1983. Secondary standard stars for absolute spectrophotometry. *The Astrophysical Journal*, 266:713.

Oliver, S., Rowan-Robinson, M., Alexander, D.M., et al., 2000. The European Large Area ISO Survey - I. Goals, definition and observations. *Monthly Notices of the Royal Astronomical Society*, 316(4):749.

Oliver, S.J., Bock, J., Altieri, B., et al., 2012. The Herschel Multi-tiered Extragalactic Survey: HerMES. *Monthly Notices of the RAS*, 424(3):1614.

Orr, M.E., Hatchfield, H.P., Battersby, C., et al., 2021. Fiery Cores: Bursty and Smooth Star Formation Distributions across Galaxy Centers in Cosmological Zoom-in Simulations. *The Astrophysical Journal*, 908(2):L31.

Orr, M.E., Hayward, C.C., and Hopkins, P.F., 2019. A simple non-equilibrium feedback model for galaxy-scale star formation: delayed feedback and SFR scatter. *Monthly Notices of the Royal Astronomical Society*, 486(4):4724.

Osterbrock, D.E. and Ferland, G.J., 2006. *Astrophysics of gaseous nebulae and active galactic nuclei*. University Science Books.

Pacifici, C., Iyer, K.G., Mobasher, B., et al., 2023. The Art of Measuring Physical Parameters in Galaxies: A Critical Assessment of Spectral Energy Distribution Fitting Techniques. *The Astrophysical Journal*, 944(2):141.

Padovani, P., 2016. The faint radio sky: radio astronomy becomes mainstream. *Astronomy and Astrophysics Review*, 24(1):13.

Padovani, P., Alexander, D.M., Assef, R.J., et al., 2017. Active galactic nuclei: what's in a name? *Astronomy and Astrophysics Review*, 25(1):2.

Padovani, P., Bonzini, M., Kellermann, K.I., et al., 2015. Radio-faint AGN: a tale of two populations. *Monthly Notices of the Royal Astronomical Society*, 452(2):1263.

Papovich, C., Cole, J.W., Yang, G., et al., 2023. CEERS Key Paper. V. Galaxies at 4 ¡ z ¡ 9 Are Bluer than They Appear–Characterizing Galaxy Stellar Populations from Rest-frame ∼1 μm Imaging. *The Astrophysical Journal*, 949(2):L18.

Papovich, C., Dickinson, M., and Ferguson, H.C., 2001. The Stellar Populations and Evolution of Lyman Break Galaxies. *The Astrophysical Journal*, 559(2):620.

Park, M., Belli, S., Conroy, C., et al., 2024. Widespread Rapid Quenching at Cosmic Noon Revealed by JWST Deep Spectroscopy. *The Astrophysical Journal*, 976(1):72.

Peebles, P.J. and Ratra, B., 2003. The cosmological constant and dark energy. *Reviews of Modern Physics*, 75(2):559.

Peebles, P.J.E., 1984. Tests of cosmological models constrained by inflation. *The Astrophysical Journal*, 284:439.

Penzias, A.A. and Wilson, R.W., 1965. A Measurement of Excess Antenna Temperature at 4080 Mc/s. *The Astrophysical Journal*, 142:419.

Perley, R.A., Chandler, C.J., Butler, B.J., et al., 2011. The Expanded Very Large Array: A New Telescope for New Science. *The Astrophysical Journal*, 739(1):L1.

Peterken, T., Merrifield, M., Aragón-Salamanca, A., et al., 2021. SDSS-IV MaNGA: when is morphology imprinted on galaxies? *Monthly Notices of the Royal Astronomical Society*, 500(1):L42.

Pier, E.A. and Krolik, J.H., 1992. Infrared Spectra of Obscuring Dust Tori around Active Galactic Nuclei. I. Calculational Method and Basic Trends. *The Astrophysical Journal*, 401:99.

Pier, E.A. and Krolik, J.H., 1993. Infrared Spectra of Obscuring Dust Tori around Active Galactic Nuclei. II. Comparison with Observations. *The Astrophysical Journal*, 418:673.

Pietrinferni, A., Cassisi, S., Salaris, M., et al., 2004. A Large Stellar Evolution Database for Population Synthesis Studies. I. Scaled Solar Models and Isochrones. *The Astrophysical Journal*, 612(1):168.

Pietrinferni, A., Cassisi, S., Salaris, M., et al., 2013. The BaSTI Stellar Evolution Database: models for extremely metal-poor and super-metal-rich stellar populations. *Astronomy and Astrophysics*, 558:A46.

Piovan, L., Tantalo, R., and Chiosi, C., 2006. Modelling galaxy spectra in presence of interstellar dust - I. The model of interstellar medium and the library of dusty single stellar populations. *Monthly Notices of the Royal Astronomical Society*, 366(3):923.

Planck Collaboration, Ade, P.A.R., Aghanim, N., et al., 2016. Planck 2015 results. XIII. Cosmological parameters. *Astronomy and Astrophysics*, 594:A13.

Planck Collaboration, Aghanim, N., Akrami, Y., et al., 2020. Planck 2018 results. I. Overview and the cosmological legacy of Planck. *Astronomy and Astrophysics*, 641:A1.

Poglitsch, A., Waelkens, C., Geis, N., et al., 2010. The Photodetector Array Camera and Spectrometer (PACS) on the Herschel Space Observatory. *Astronomy and Astrophysics*, 518:L2.

Pope, A., Aretxaga, I., Hughes, D., et al., 2019. TolTEC/LMT Extragalactic Legacy Surveys: Completing our Census of Dust-Obscured Star Formation. In *American Astronomical Society Meeting Abstracts #233*, volume 233 of *American Astronomical Society Meeting Abstracts*, page 363.20.

Popescu, C.C., Misiriotis, A., Kylafis, N.D., et al., 2000. Modelling the spectral energy distribution of galaxies. I. Radiation fields and grain heating in the edge-on spiral NGC 891. *Astronomy and Astrophysics*, 362:138.

Popescu, C.C., Tuffs, R.J., Dopita, M.A., et al., 2011. Modelling the spectral energy distribution of galaxies. V. The dust and PAH emission SEDs of disk galaxies. *Astronomy and Astrophysics*, 527:A109.

Pozzetti, L., Bolzonella, M., Zucca, E., et al., 2010. zCOSMOS - 10k-bright spectroscopic sample. The bimodality in the galaxy stellar mass function: exploring its evolution with redshift. *Astronomy and Astrophysics*, 523:A13.

Pracy, M.B., Ching, J.H.Y., Sadler, E.M., et al., 2016. GAMA/WiggleZ: the 1.4 GHz radio luminosity functions of high- and low-excitation radio galaxies and their redshift evolution to z = 0.75. *Monthly Notices of the Royal Astronomical Society*, 460(1):2.

Prandoni, I., Gregorini, L., Parma, P., et al., 2001. The ATESP radio survey. III. Source counts. *Astronomy and Astrophysics*, 365:392.

Press, W.H. and Schechter, P., 1974. Formation of Galaxies and Clusters of Galaxies by Self-Similar Gravitational Condensation. *Astrophysical Journal*, 187:425.

Quataert, E., 2001. Low Radiative-Efficiency Accretion Flows. In B.M. Peterson, R.W. Pogge, and R.S. Polidan, editors, *Probing the Physics of Active Galactic Nuclei*, volume 224 of *Astronomical Society of the Pacific Conference Series*, page 71.

Rawlings, S., Abdalla, F.B., Bridle, S.L., et al., 2004. Galaxy evolution, cosmology and dark energy with the Square Kilometer Array. *New Astronomy Review*, 48(11-12):1013.

Rayner, J.T., Cushing, M.C., and Vacca, W.D., 2009. The Infrared Telescope Facility (IRTF) Spectral Library: Cool Stars. *The Astrophysical Journal Supplement Series*, 185(2):289.

Read, S.C., Smith, D.J.B., Gürkan, G., et al., 2018. The Far-Infrared Radio Correlation at low radio frequency with LOFAR/H-ATLAS. *Monthly Notices of the Royal Astronomical Society*, 480(4):5625.

Reber, G., 1940. Notes: Cosmic Static. *The Astrophysical Journal*, 91:621.

Reddy, N.A., Kriek, M., Shapley, A.E., et al., 2015. The MOSDEF Survey: Measurements of Balmer Decrements and the Dust Attenuation Curve at Redshifts z ~1.4-2.6. *The Astrophysical Journal*, 806(2):259.

Reed, D.S., Bower, R., Frenk, C.S., et al., 2005. The first generation of star-forming haloes. *Monthly Notices of the Royal Astronomical Society*, 363(2):393.

Richards, G.T., Lacy, M., Storrie-Lombardi, L.J., et al., 2006. Spectral Energy Distributions and Multiwavelength Selection of Type 1 Quasars. *The Astrophysical Journal Supplement Series*, 166(2):470.

Richards, J.W., Starr, D.L., Miller, A.A., et al., 2012. Construction of a Calibrated Probabilistic Classification Catalog: Application to 50k Variable Sources in the All-Sky Automated Survey. *The Astrophysical Journal Supplement Series*, 203(2):32.

Rieke, G.H., Young, E.T., Engelbracht, C.W., et al., 2004. The Multiband Imaging Photometer for Spitzer (MIPS). *The Astrophysical Journal Supplement Series*, 154(1):25.

Rieke, M.J., Kelly, D., and Horner, S., 2005. Overview of James Webb Space Telescope and NIRCam's Role. In J.B. Heaney and L.G. Burriesci, editors, *Cryogenic Optical Systems and Instruments XI*, volume 5904 of *Society of Photo-Optical Instrumentation Engineers (SPIE) Conference Series*, pages 1–8.

Robertson, B.E., 2022. Galaxy Formation and Reionization: Key Unknowns and Expected Breakthroughs by the James Webb Space Telescope. *Annual Review of Astronomy and Astrophysics*, 60:121.

Robertson, B.E., Ellis, R.S., Dunlop, J.S., et al., 2010. Early star-forming galaxies and the reionization of the Universe. *Nature*, 468(7320):49.

Robertson, B.E., Ellis, R.S., Furlanetto, S.R., et al., 2015. Cosmic Reionization and Early Star-forming Galaxies: A Joint Analysis of New Constraints from Planck and the Hubble Space Telescope. *The Astrophysical Journal*, 802(2):L19.

Robotham, A.S.G., Bellstedt, S., Lagos, C.d.P., et al., 2020. ProSpect: generating spectral energy distributions with complex star formation and metallicity histories. *Monthly Notices of the Royal Astronomical Society*, 495(1):905.

Rocca-Volmerange, B., Drouart, G., De Breuck, C., et al., 2013. Starburst and old stellar populations in the z $\simeq$ 3.8 radio galaxies 4C 41.17 and TN J2007-1316. *Monthly Notices of the Royal Astronomical Society*, 429(4):2780.

Rodighiero, G., Daddi, E., Baronchelli, I., et al., 2011. The Lesser Role of Starbursts in Star Formation at z = 2. *The Astrophysical Journal*, 739(2):L40.

Rodighiero, G., Renzini, A., Daddi, E., et al., 2014. A multiwavelength consensus on the main sequence of star-forming galaxies at z $\sim$ 2. *Monthly Notices of the Royal Astronomical Society*, 443(1):19.

Rosario, D.J., Burtscher, L., Davies, R., et al., 2013. The Mid-infrared Emission of Narrow-line Active Galactic Nuclei: Star Formation, Nuclear Activity, and Two Populations Revealed by Wise. *The Astrophysical Journal*, 778(2):94.

Rosen, A.L., Lopez, L.A., Krumholz, M.R., et al., 2014. Gone with the wind: Where is the missing stellar wind energy from massive star clusters? *Monthly Notices of the Royal Astronomical Society*, 442(3):2701.

Röttgering, H., Afonso, J., Barthel, P., et al., 2011. LOFAR and APERTIF Surveys of the Radio Sky: Probing Shocks and Magnetic Fields in Galaxy Clusters. *Journal of Astrophysics and Astronomy*, 32(4):557.

Rybicki, G.B. and Lightman, A.P., 1979. *Radiative processes in astrophysics*. Wiley-VCH.

Sabater, J., Best, P.N., Hardcastle, M.J., et al., 2019. The LoTSS view of radio AGN in the local Universe. The most massive galaxies are always switched on. *Astronomy and Astrophysics*, 622:A17.

Sabater, J., Best, P.N., Tasse, C., et al., 2021. The LOFAR Two-meter Sky Survey: Deep Fields Data Release 1. II. The ELAIS-N1 LOFAR deep field. *Astronomy and Astrophysics*, 648:A2.

Sadowski, A., Narayan, R., McKinney, J.C., et al., 2014. Numerical simulations of super-critical black hole accretion flows in general relativity. *Monthly Notices of the Royal Astronomical Society*, 439(1):503.

Salim, S., Boquien, M., and Lee, J.C., 2018. Dust Attenuation Curves in the Local Universe: Demographics and New Laws for Star-forming Galaxies and High-redshift Analogs. *The Astrophysical Journal*, 859(1):11.

Salim, S., Lee, J.C., Janowiecki, S., et al., 2016. GALEX-SDSS-WISE Legacy Catalog (GSWLC): Star Formation Rates, Stellar Masses, and Dust Attenuations of 700,000 Low-redshift Galaxies. *The Astrophysical Journal Supplement Series*, 227(1):2.

Salim, S. and Narayanan, D., 2020. The Dust Attenuation Law in Galaxies. *Annual Review of Astronomy and Astrophysics*, 58:529.

Salpeter, E.E., 1955. The Luminosity Function and Stellar Evolution. *The Astrophysical Journal*, 121:161.

Sánchez Almeida, J., Terlevich, R., Terlevich, E., et al., 2012. Qualitative Interpretation of Galaxy Spectra. *The Astrophysical Journal*, 756(2):163.

Sánchez-Blázquez, P., Peletier, R.F., Jiménez-Vicente, J., et al., 2006. Medium-resolution Isaac Newton Telescope library of empirical spectra. *Monthly Notices of the Royal Astronomical Society*, 371(2):703.

Sanders, D.B., Phinney, E.S., Neugebauer, G., et al., 1989. Continuum Energy Distributions of Quasars: Shapes and Origins. *The Astrophysical Journal*, 347:29.

Santini, P., Fontana, A., Castellano, M., et al., 2023. Early Results from GLASS-JWST. XI. Stellar Masses and Mass-to-light Ratio of z ¿ 7 Galaxies. *The Astrophysical Journal*, 942(2):L27.

Schaerer, D. and de Barros, S., 2009. The impact of nebular emission on the ages of z≈ 6 galaxies. *Astronomy and Astrophysics*, 502(2):423.

Schaerer, D. and de Barros, S., 2012. The importance of nebular emission for SED modeling of distant star-forming galaxies. In R.J. Tuffs and C.C. Popescu, editors, *The Spectral Energy Distribution of Galaxies - SED 2011*, volume 284 of *IAU Symposium*, pages 20–25.

Schaller, G., Schaerer, D., Meynet, G., et al., 1992. New Grids of Stellar Models from 0.8-SOLAR-MASS to 120-SOLAR-MASSES at Z=0.020 and Z=0.001. *Astronomy and Astrophysics Supplement Series*, 96:269.

Schechter, P., 1976. An analytic expression for the luminosity function for galaxies. *Astrophysical Journal*, 203:297.

Scheuer, P.A.G., 1965. A Sensitive Test for the Presence of Atomic Hydrogen in Intergalactic Space. *Nature*, 207(5000):963.

Schmidt, M., 1959. The Rate of Star Formation. *The Astrophysical Journal*, 129:243.

Schreiber, C., Pannella, M., Elbaz, D., et al., 2015. The Herschel view of the dominant mode of galaxy growth from z = 4 to the present day. *Astronomy and Astrophysics*, 575:A74.

Scoville, N., Aussel, H., Brusa, M., et al., 2007. The Cosmic Evolution Survey (COSMOS): Overview. *The Astrophysical Journal Supplement Series*, 172(1):1.

Seager, S., Sasselov, D.D., and Scott, D., 2000. How Exactly Did the Universe Become Neutral? *The Astrophysical Journal Supplement Series*, 128(2):407.

Sellwood, J.A., 2014. Secular evolution in disk galaxies. *Reviews of Modern Physics*, 86(1):1.

Shakura, N.I. and Sunyaev, R.A., 1973. Black holes in binary systems. Observational appearance. *Astronomy and Astrophysics*, 24:337.

Shang, Z., Brotherton, M.S., Green, R.F., et al., 2005. Quasars and the Big Blue Bump. *The Astrophysical Journal*, 619(1):41.

Shapley, A.E., Sanders, R.L., Reddy, N.A., et al., 2023. JWST/NIRSpec Balmer-line Measurements of Star Formation and Dust Attenuation at z 3-6. *The Astrophysical Journal*, 954(2):157.

Shimwell, T.W., Hardcastle, M.J., Tasse, C., et al., 2022. The LOFAR Two-metre Sky Survey. V. Second data release. *Astronomy and Astrophysics*, 659:A1.

Shimwell, T.W., Röttgering, H.J.A., Best, P.N., et al., 2017. The LOFAR Two-metre Sky Survey. I. Survey description and preliminary data release. *Astronomy and Astrophysics*, 598:A104.

Shimwell, T.W., Tasse, C., Hardcastle, M.J., et al., 2019. The LOFAR Two-metre Sky Survey. II. First data release. *Astronomy and Astrophysics*, 622:A1.

Shivaei, I., Reddy, N., Rieke, G., et al., 2020. The MOSDEF Survey: The Variation of the Dust Attenuation Curve with Metallicity. *The Astrophysical Journal*, 899(2):117.

Shivaei, I., Reddy, N.A., Steidel, C.C., et al., 2015. Investigating Hα, UV, and IR Star-formation Rate Diagnostics for a Large Sample of z $\sim$ 2 Galaxies. *Astrophysical Journal*, 804(2):149.

Silk, J., 2011. Feedback in Galaxy Formation. In C. Carignan, F. Combes, and K.C. Freeman, editors, *Tracing the Ancestry of Galaxies*, volume 277 of *IAU Symposium*, pages 273–281.

Silk, J., Di Cintio, A., and Dvorkin, I., 2014. Galaxy Formation. In *Proceedings of the International School of Physics 'Enrico Fermi' Course 186 'New Horizons for Observational Cosmology' Vol. 186*, volume 186, pages 137–187.

Silva, L., Granato, G.L., Bressan, A., et al., 1998. Modeling the Effects of Dust on Galactic Spectral Energy Distributions from the Ultraviolet to the Millimeter Band. *The Astrophysical Journal*, 509(1):103.

Simha, V., Weinberg, D.H., Conroy, C., et al., 2014. Parametrising Star Formation Histories. *arXiv e-prints*, arXiv:1404.0402.

Simpson, C., Martínez-Sansigre, A., Rawlings, S., et al., 2006. Radio imaging of the Subaru/XMM-Newton Deep Field - I. The 100-μJy catalogue, optical identifications, and the nature of the faint radio source population. *Monthly Notices of the Royal Astronomical Society*, 372(2):741.

Skilling, J., 2004. Nested sampling. *AIP Conference Proceedings*, 735(1):395.

Skilling, J., 2006. Nested sampling for general Bayesian computation. *Bayesian Analysis*, 1(4):833 .

Sklias, P., Schaerer, D., Elbaz, D., et al., 2017. Insights on star-formation histories and physical properties of 1.2 $\leq$z $\lesssim$ 4 Herschel-detected galaxies. *Astronomy and Astrophysics*, 605:A29.

Smit, R., Bouwens, R.J., Franx, M., et al., 2012. The Star Formation Rate Function for Redshift z ~4-7 Galaxies: Evidence for a Uniform Buildup of Star-forming Galaxies during the First 3 Gyr of Cosmic Time. *The Astrophysical Journal*, 756(1):14.

Smith, D.J.B., Best, P.N., Duncan, K.J., et al., 2016. The WEAVE-LOFAR Survey. In C. Reylé, J. Richard, L. Cambrésy, M. Deleuil, E. Pécontal, L. Tresse, and I. Vauglin, editors, *SF2A-2016: Proceedings of the Annual meeting of the French Society of Astronomy and Astrophysics*, pages 271–280.

Smith, D.J.B., Dunne, L., da Cunha, E., et al., 2012. Herschel-ATLAS: multi-wavelength SEDs and physical properties of 250 μm selected galaxies at z ¡ 0.5. *Monthly Notices of the Royal Astronomical Society*, 427(1):703.

Smith, D.J.B., Haskell, P., Gürkan, G., et al., 2021. The LOFAR Two-metre Sky Survey Deep Fields. The star-formation rate-radio luminosity relation at low frequencies. *Astronomy and Astrophysics*, 648:A6.

Smith, D.J.B. and Hayward, C.C., 2015. Deriving star formation histories from photometry using energy balance spectral energy distribution modelling. *Monthly Notices of the Royal Astronomical Society*, 453(2):1597.

Smith, D.J.B. and Hayward, C.C., 2018. Panchromatic SED modelling of spatially resolved galaxies. *Monthly Notices of the Royal Astronomical Society*, 476(2):1705.

Smith, D.J.B., Jarvis, M.J., Hardcastle, M.J., et al., 2014. The temperature dependence of the far-infrared-radio correlation in the Herschel-ATLAS. *Monthly Notices of the Royal Astronomical Society*, 445(3):2232.

Smolčić, V., 2009. The Radio AGN Population Dichotomy: Green Valley Seyferts Versus Red Sequence Low-Excitation Active Galactic Nuclei. *The Astrophysical Journal*, 699(1):L43.

Smolčić, V., Delvecchio, I., Zamorani, G., et al., 2017a. The VLA-COSMOS 3 GHz Large Project: Multiwavelength counterparts and the composition of the faint radio population. *Astronomy and Astrophysics*, 602:A2.

Smolčić, V., Novak, M., Bondi, M., et al., 2017b. The VLA-COSMOS 3 GHz Large Project: Continuum data and source catalog release. *Astronomy and Astrophysics*, 602:A1.

Smoot, G.F., Bennett, C.L., Kogut, A., et al., 1992. Structure in the COBE Differential Microwave Radiometer First-Year Maps. *The Astrophysical Journal*, 396:L1.

Snyder, G.F., Torrey, P., Lotz, J.M., et al., 2015. Galaxy morphology and star formation in the Illustris Simulation at z = 0. *Monthly Notices of the Royal Astronomical Society*, 454(2):1886.

Sokasian, A., Yoshida, N., Abel, T., et al., 2004. Cosmic reionization by stellar sources: population III stars. *Monthly Notices of the Royal Astronomical Society*, 350(1):47.

Somerville, R.S. and Davé, R., 2015. Physical Models of Galaxy Formation in a Cosmological Framework. *Annual Review of Astronomy and Astrophysics*, 53:51.

Sorba, R. and Sawicki, M., 2015. Missing stellar mass in SED fitting: spatially unresolved photometry can underestimate galaxy masses. *Monthly Notices of the Royal Astronomical Society*, 452(1):235.

Sparre, M., Hayward, C.C., Feldmann, R., et al., 2017. (Star)bursts of FIRE: observational signatures of bursty star formation in galaxies. *Monthly Notices of the Royal Astronomical Society*, 466(1):88.

Sparre, M. and Springel, V., 2016. Zooming in on major mergers: dense, starbursting gas in cosmological simulations. *Monthly Notices of the Royal Astronomical Society*, 462(3):2418.

Speagle, J.S., 2020. DYNESTY: a dynamic nested sampling package for estimating Bayesian posteriors and evidences. *Monthly Notices of the Royal Astronomical Society*, 493(3):3132.

Spergel, D.N., Bean, R., Doré, O., et al., 2007. Three-Year Wilkinson Microwave Anisotropy Probe (WMAP) Observations: Implications for Cosmology. *The Astrophysical Journal Supplement Series*, 170(2):377.

Spergel, D.N., Verde, L., Peiris, H.V., et al., 2003. First-Year Wilkinson Microwave Anisotropy Probe (WMAP) Observations: Determination of Cosmological Parameters. *The Astrophysical Journal Supplement Series*, 148(1):175.

Spinrad, H. and Taylor, B.J., 1971. The Stellar Content of the Nuclei of Nearby Galaxies. I. M31, M32, and M81. *The Astrophysical Journal Supplement Series*, 22:445.

Springel, V., White, S.D.M., Jenkins, A., et al., 2005. Simulations of the formation, evolution and clustering of galaxies and quasars. *Nature*, 435(7042):629.

Stacy, A. and Bromm, V., 2013. Constraining the statistics of Population III binaries. *Monthly Notices of the Royal Astronomical Society*, 433(2):1094.

Stacy, A., Greif, T.H., and Bromm, V., 2012. The first stars: mass growth under protostellar feedback. *Monthly Notices of the Royal Astronomical Society*, 422(1):290.

Stanway, E.R. and Eldridge, J.J., 2018. Re-evaluating old stellar populations. *Monthly Notices of the Royal Astronomical Society*, 479(1):75.

Stark, D.P., Topping, M.W., Endsley, R., et al., 2025. Observations of the First Galaxies in the Era of JWST. *arXiv e-prints*, arXiv:2501.17078.

Stein, W.A. and Soifer, B.T., 1983. Dust in galaxies. *Annual Review of Astronomy and Astrophysics*, 21:177.

Stern, D., Assef, R.J., Benford, D.J., et al., 2012. Mid-infrared Selection of Active Galactic Nuclei with the Wide-Field Infrared Survey Explorer. I. Characterizing WISE-selected Active Galactic Nuclei in COSMOS. *The Astrophysical Journal*, 753(1):30.

Stern, D., Eisenhardt, P., Gorjian, V., et al., 2005. Mid-Infrared Selection of Active Galaxies. *Astrophysical Journal*, 631(1):163.

Stern, J., Faucher-Giguère, C.A., Fielding, D., et al., 2021. Virialization of the Inner CGM in the FIRE Simulations and Implications for Galaxy Disks, Star Formation, and Feedback. *The Astrophysical Journal*, 911(2):88.

Strait, V., Brammer, G., Muzzin, A., et al., 2023. An Extremely Compact, Low-mass Galaxy on its Way to Quiescence at z = 5.2. *The Astrophysical Journal*, 949(2):L23.

Suess, K.A., Leja, J., Johnson, B.D., et al., 2022. Recovering the star formation histories of recently quenched galaxies: The impact of model and prior choices. *Astrophysical Journal*, 935(2):146.

Szokoly, G.P., Bergeron, J., Hasinger, G., et al., 2004. The Chandra Deep Field-South: Optical Spectroscopy. I. *The Astrophysical Journal Supplement Series*, 155(2):271.

Tabatabaei, F.S., Schinnerer, E., Krause, M., et al., 2017. The Radio Spectral Energy Distribution and Star-formation Rate Calibration in Galaxies. *The Astrophysical Journal*, 836(2):185.

Tacchella, S., Carollo, C.M., Renzini, A., et al., 2015. Evidence for mature bulges and an inside-out quenching phase 3 billion years after the Big Bang. *Science*, 348(6232):314.

Tacchella, S., Conroy, C., Faber, S.M., et al., 2022a. Fast, Slow, Early, Late: Quenching Massive Galaxies at z $\sim$ 0.8. *The Astrophysical Journal*, 926(2):134.

Tacchella, S., Finkelstein, S.L., Bagley, M., et al., 2022b. On the Stellar Populations of Galaxies at z = 9-11: The Growth of Metals and Stellar Mass at Early Times. *The Astrophysical Journal*, 927(2):170.

Tacchella, S., Smith, A., Kannan, R., et al., 2022c. H α emission in local galaxies: star formation, time variability, and the diffuse ionized gas. *Monthly Notices of the Royal Astronomical Society*, 513(2):2904.

Tadhunter, C., 2016. Radio AGN in the local universe: unification, triggering and evolution. *Astronomy and Astrophysics Review*, 24(1):10.

Tamura, N., 2016. Prime Focus Spectrograph: A very wide-field, massively multiplexed, optical & near-infrared spectrograph for Subaru Telescope. In S. Kaviraj, editor, *Galaxies at High Redshift and Their Evolution Over Cosmic Time*, volume 319 of *IAU Symposium*, pages 55–55.

Tanaka, M., 2012. A Method of Identifying AGNs Based on Emission-Line Excess and the Nature of Low-Luminosity AGNs in the Sloan Digital Sky Survey. I. A New Method. *Publications of the Astronomical Society of Japan*, 64:36.

Tasse, C., Best, P.N., Röttgering, H., et al., 2008. Radio-loud AGN in the XMM-LSS field. II. A dichotomy in environment and accretion mode? *Astronomy and Astrophysics*, 490(3):893.

Tasse, C., Shimwell, T., Hardcastle, M.J., et al., 2021. The LOFAR Two-meter Sky Survey: Deep Fields Data Release 1. I. Direction-dependent calibration and imaging. *Astronomy and Astrophysics*, 648:A1.

Teyssier, R., 2002. Cosmological hydrodynamics with adaptive mesh refinement. A new high resolution code called RAMSES. *Astronomy and Astrophysics*, 385:337.

Thompson, A.R., Moran, J.M., and Swenson, Jr., G.W., 2017. *Interferometry and Synthesis in Radio Astronomy, 3rd Edition*. Springer.

Thorne, J.E., Robotham, A.S.G., Bellstedt, S., et al., 2022a. DEVILS: cosmic evolution of SED-derived metallicities and their connection to star formation histories. *Monthly Notices of the Royal Astronomical Society*, 517(4):6035.

Thorne, J.E., Robotham, A.S.G., Bellstedt, S., et al., 2023. The long and the short of it: the benefits and leverage of ultraviolet-radio galaxy fitting. *Monthly Notices of the Royal Astronomical Society*, 522(4):6354.

Thorne, J.E., Robotham, A.S.G., Davies, L.J.M., et al., 2022b. Deep Extragalactic VIsible Legacy Survey (DEVILS): identification of AGN through SED fitting and the evolution of the bolometric AGN luminosity function. *Monthly Notices of the Royal Astronomical Society*, 509(4):4940.

Tinsley, B.M., 1968. Evolution of the Stars and Gas in Galaxies. *The Astrophysical Journal*, 151:547.

Tinsley, B.M., 1972. Galactic Evolution. *Astronomy and Astrophysics*, 20:383.

Tinsley, B.M., 1980. Evolution of the Stars and Gas in Galaxies. *Fundamentals of Cosmic Physics*, 5:287.

Tinsley, B.M. and Gunn, J.E., 1976. Evolutionary synthesis of the stellar population in elliptical galaxies. I. Ingredients, broad-band colors, and infrared features. *The Astrophysical Journal*, 203:52.

Tojeiro, R., Heavens, A.F., Jimenez, R., et al., 2007. Recovering galaxy star formation and metallicity histories from spectra using VESPA. *Monthly Notices of the Royal Astronomical Society*, 381(3):1252.

Tombesi, F., Cappi, M., Reeves, J.N., et al., 2013. Unification of X-ray winds in Seyfert galaxies: from ultra-fast outflows to warm absorbers. *Monthly Notices of the Royal Astronomical Society*, 430(2):1102.

Tranin, H., Godet, O., Webb, N., et al., 2022. Probabilistic classification of X-ray sources applied to Swift-XRT and XMM-Newton catalogs. *Astronomy and Astrophysics*, 657:A138.

Treu, T., Roberts-Borsani, G., Bradac, M., et al., 2022. The GLASS-JWST Early Release Science Program. I. Survey Design and Release Plans. *The Astrophysical Journal*, 935(2):110.

Trotta, R., 2008. Bayes in the sky: Bayesian inference and model selection in cosmology. *Contemporary Physics*, 49(2):71.

Tsujikawa, S., 2003. Introductory review of cosmic inflation. *arXiv e-prints*, hep-ph/0304257.

Urry, C.M. and Padovani, P., 1995. Unified Schemes for Radio-Loud Active Galactic Nuclei. *Publications of the Astronomical Society of the Pacific*, 107:803.

van Cappellen, W.A., Oosterloo, T.A., Verheijen, M.A.W., et al., 2022. Apertif: Phased array feeds for the Westerbork Synthesis Radio Telescope. System overview and performance characteristics. *Astronomy and Astrophysics*, 658:A146.

van de Voort, F., Schaye, J., Booth, C.M., et al., 2011. The rates and modes of gas accretion on to galaxies and their gaseous haloes. *Monthly Notices of the Royal Astronomical Society*, 414(3):2458.

van der Kruit, P.C., 1971. Observations of core sources in Seyfert and normal galaxies with the Westerbork synthesis radio telescope at 1415 MHz. *Astronomy and Astrophysics*, 15:110.

van Haarlem, M.P., Wise, M.W., Gunst, A.W., et al., 2013. LOFAR: The LOw-Frequency ARray. *Astronomy and Astrophysics*, 556:A2.

Vanzella, E., Loiacono, F., Bergamini, P., et al., 2023. An extremely metal-poor star complex in the reionization era: Approaching Population III stars with JWST. *Astronomy and Astrophysics*, 678:A173.

Veilleux, S. and Osterbrock, D.E., 1987. Spectral Classification of Emission-Line Galaxies. *The Astrophysical Journal Supplement Series*, 63:295.

Venemans, B.P., Findlay, J.R., Sutherland, W.J., et al., 2013. Discovery of Three z ¿ 6.5 Quasars in the VISTA Kilo-Degree Infrared Galaxy (VIKING) Survey. *The Astrophysical Journal*, 779(1):24.

Venemans, B.P., Verdoes Kleijn, G.A., Mwebaze, J., et al., 2015. First discoveries of z ∼ 6 quasars with the Kilo-Degree Survey and VISTA Kilo-Degree Infrared Galaxy survey. *Monthly Notices of the Royal Astronomical Society*, 453(3):2259.

Voit, G.M., Donahue, M., Bryan, G.L., et al., 2015. Regulation of star formation in giant galaxies by precipitation, feedback and conduction. *Nature*, 519(7542):203.

Volonteri, M., 2010. Formation of supermassive black holes. *Astronomy and Astrophysics Review*, 18(3):279.

Volonteri, M., Habouzit, M., and Colpi, M., 2021. The origins of massive black holes. *Nature Reviews Physics*, 3(11):732.

Volonteri, M., Habouzit, M., Pacucci, F., et al., 2016. The evolution of high-redshift massive black holes. In S. Kaviraj, editor, *Galaxies at High Redshift and Their Evolution Over Cosmic Time*, volume 319 of *IAU Symposium*, pages 72–79.

Walch, S.K., Whitworth, A.P., Bisbas, T., et al., 2012. Dispersal of molecular clouds by ionizing radiation. *Monthly Notices of the Royal Astronomical Society*, 427(1):625.

Walcher, C.J., Lamareille, F., Vergani, D., et al., 2008. The VVDS-SWIRE-GALEX-CFHTLS surveys: physical properties of galaxies at z below 1.2 from photometric data. *Astronomy and Astrophysics*, 491(3):713.

Walcher, J., Groves, B., Budavári, T., et al., 2011. Fitting the integrated spectral energy distributions of galaxies. *Astrophysics and Space Science*, 331:1.

Wang, B., Leja, J., Atek, H., et al., 2024. Quantifying the Effects of Known Unknowns on Inferred High-redshift Galaxy Properties: Burstiness, IMF, and Nebular Physics. *The Astrophysical Journal*, 963(1):74.

Wang, L., Gao, F., Duncan, K.J., et al., 2019. A LOFAR-IRAS cross-match study: the far-infrared radio correlation and the 150 MHz luminosity as a star-formation rate tracer. *Astronomy and Astrophysics*, 631:A109.

Weinberg, D.H., Mortonson, M.J., Eisenstein, D.J., et al., 2013. Observational probes of cosmic acceleration. *Physics Reports*, 530(2):87.

Weinberg, S., 2008. *Cosmology*. Oxford University Press.

Weisskopf, M.C., Tananbaum, H.D., Van Speybroeck, L.P., et al., 2000. Chandra X-ray Observatory (CXO): overview. In J.E. Truemper and B. Aschenbach, editors, *X-Ray Optics, Instruments, and Missions III*, volume 4012 of *Society of Photo-Optical Instrumentation Engineers (SPIE) Conference Series*, pages 2–16.

Whalen, D.J., Even, W., Frey, L.H., et al., 2013a. Finding the First Cosmic Explosions. I. Pair-instability Supernovae. *The Astrophysical Journal*, 777(2):110.

Whalen, D.J., Fryer, C.L., Holz, D.E., et al., 2013b. Seeing the First Supernovae at the Edge of the Universe with JWST. *The Astrophysical Journal*, 762(1):L6.

Whitaker, K.E., van Dokkum, P.G., Brammer, G., et al., 2012. The Star Formation Mass Sequence Out to z = 2.5. *The Astrophysical Journal*, 754(2):L29.

White, S.D.M. and Rees, M.J., 1978. Core condensation in heavy halos: a two-stage theory for galaxy formation and clustering. *Monthly Notices of the Royal Astronomical Society*, 183:341.

Whittam, I.H., Jarvis, M.J., Hale, C.L., et al., 2022. MIGHTEE: the nature of the radio-loud AGN population. *Monthly Notices of the Royal Astronomical Society*, 516(1):245.

Wilkes, B., 1999. The Spectral Energy Distributions of Active Galactic Nuclei. In G. Ferland and J. Baldwin, editors, *Quasars and Cosmology*, volume 162 of *Astronomical Society of the Pacific Conference Series*, page 15.

Williams, C.C., Tacchella, S., Maseda, M.V., et al., 2023. JEMS: A Deep Medium-band Imaging Survey in the Hubble Ultra Deep Field with JWST NIRCam and NIRISS. *The Astrophysical Journal Supplement Series*, 268(2):64.

Williams, R.E., Blacker, B., Dickinson, M., et al., 1996. The Hubble Deep Field: Observations, Data Reduction, and Galaxy Photometry. *The Astronomical Journal*, 112:1335.

Williams, W.L., Calistro Rivera, G., Best, P.N., et al., 2018. LOFAR-Boötes: properties of high- and low-excitation radio galaxies at 0.5 ¡ z ¡ 2.0. *Monthly Notices of the Royal Astronomical Society*, 475(3):3429.

Williams, W.L., Hardcastle, M.J., Best, P.N., et al., 2019. The LOFAR Two-metre Sky Survey. III. First data release: Optical/infrared identifications and value-added catalogue. *Astronomy and Astrophysics*, 622:A2.

Williams, W.L., van Weeren, R.J., Röttgering, H.J.A., et al., 2016. LOFAR 150-MHz observations of the Boötes field: catalogue and source counts. *Monthly Notices of the Royal Astronomical Society*, 460(3):2385.

Willott, C.J., Delorme, P., Omont, A., et al., 2007. Four Quasars above Redshift 6 Discovered by the Canada-France High-z Quasar Survey. *The Astronomical Journal*, 134(6):2435.

Wilman, R.J., Miller, L., Jarvis, M.J., et al., 2008. A semi-empirical simulation of the extragalactic radio continuum sky for next generation radio telescopes. *Monthly Notices of the Royal Astronomical Society*, 388(3):1335.

Wilson, A.S. and Colbert, E.J.M., 1995. The Difference between Radio-loud and Radio-quiet Active Galaxies. *The Astrophysical Journal*, 438:62.

Wilson, G., Muzzin, A., Yee, H.K.C., et al., 2009. Spectroscopic Confirmation of a Massive Red-Sequence-Selected Galaxy Cluster at z = 1.34 in the SpARCS-South Cluster Survey. *The Astrophysical Journal*, 698(2):1943.

Wilson, G.W., Abi-Saad, S., Ade, P., et al., 2020. The TolTEC camera: an overview of the instrument and in-lab testing results. In J. Zmuidzinas and J.R. Gao, editors, *Millimeter, Submillimeter, and Far-Infrared Detectors and Instrumentation for Astronomy X*, volume 11453 of *Society of Photo-Optical Instrumentation Engineers (SPIE) Conference Series*, page 1145302.

Windhorst, R.A., 2003. The microJansky and nanoJansky population. *New Astronomy Reviews*, 47(4-5):357.

Windhorst, R.A., Miley, G.K., Owen, F.N., et al., 1985. Sub-millijansky 1.4 GHz source counts and multicolor studies of weak rado galaxy populations. *The Astrophysical Journal*, 289:494.

Windhorst, R.A., van Heerde, G.M., and Katgert, P., 1984. A deep Westerbork survey of areas with multicolor Mayall 4 M plates. I. The 1412 MHz catalogue, source counts and angular size statistics. *Astronomy and Astrophysics Supplement Series*, 58:1.

Wise, J.H., 2019. Cosmic reionisation. *Contemporary Physics*, 60(2):145.

Wise, J.H. and Abel, T., 2007. Resolving the Formation of Protogalaxies. I. Virialization. *The Astrophysical Journal*, 665(2):899.

Wise, J.H. and Abel, T., 2008. Resolving the Formation of Protogalaxies. III. Feedback from the First Stars. *The Astrophysical Journal*, 685(1):40.

Wise, J.H., Regan, J.A., O'Shea, B.W., et al., 2019. Formation of massive black holes in rapidly growing pre-galactic gas clouds. *Nature*, 566(7742):85.

Wootten, A. and Thompson, A.R., 2009. The Atacama Large Millimeter/Submillimeter Array. *IEEE Proceedings*, 97(8):1463.

Wu, P.F., van der Wel, A., Gallazzi, A., et al., 2018. Stellar Populations of over 1000 z $\sim$ 0.8 Galaxies from LEGA-C: Ages and Star Formation Histories from D_n4000 and Hδ. *The Astrophysical Journal*, 855(2):85.

Wu, X.B., Wang, F., Fan, X., et al., 2015. An ultraluminous quasar with a twelve-billion-solar-mass black hole at redshift 6.30. *Nature*, 518(7540):512.

Wuyts, S., Förster Schreiber, N.M., Lutz, D., et al., 2011. On Star Formation Rates and Star Formation Histories of Galaxies Out to z ~3. *Astrophysical Journal*, 738(1):106.

Yang, G., Boquien, M., Brandt, W.N., et al., 2022. Fitting AGN/Galaxy X-Ray-to-radio SEDs with CIGALE and Improvement of the Code. *The Astrophysical Journal*, 927(2):192.

York, D.G., Adelman, J., Anderson, John E., J., et al., 2000. The sloan digital sky survey: Technical summary. *Astronomical Journal*, 120(3):1579.

Yu, S., Bullock, J.S., Gurvich, A.B., et al., 2023. Born this way: thin disc, thick disc, and isotropic spheroid formation in FIRE-2 Milky Way-mass galaxy simulations. *Monthly Notices of the Royal Astronomical Society*, 523(4):6220.

Yun, M.S., Reddy, N.A., and Condon, J.J., 2001. Radio Properties of Infrared-selected Galaxies in the IRAS 2 Jy Sample. *The Astrophysical Journal*, 554(2):803.

Zensus, J.A. and Ros, E., 2015. European VLBI Network: Present and Future. *arXiv e-prints*, arXiv:1501.05079.